UNIVERSITÀ DEGLI STUDI DI MILANO

Doctorate School in Physics, Astrophysics and Applied Physics

Physics Department

Doctorate Course in Physics, Astrophysics and Applied Physics

Ciclo XXX

Diagnostics of Partially Coherent Radiation from Ultrarelativistic Beams: the Heterodyne Near Field Speckle approach

MIUR subject (SSD) FIS/03

Supervisor: Dott. M. A. C. Potenza

Co-supervisor: Dott. B. Paroli

PhD Thesis of:

Mirko Siano

Academic Year 2016-2017

Commission of the final examination:

External Referees:
Dr. Stefano Mazzoni
Dr. Michele Manfredda

External Members:
Prof. Giacomo Ghirighelli
Prof. Mauro Nisoli

Internal Member:
Prof. Giorgio Rossi

Final examination:

Date: 19^{th} December, 2017

Università degli Studi di Milano, Dipartimento di Fisica, Milano, Italy

A Stefania,
"the brightest light source"
e il mio sogno più grande.

Cover illustration:

Two-dimensional spatial power spectrum of Heterodyne Near Field Speckles for the case of a narrowband Synchrotron Radiation beam. Circular Talbot oscillations are a clear manifestation of coherence and their decay to the shotnoise level allows to retrieve the information on the partial coherence properties of the radiation.

Internal illustrations:

Mirko Siano

Design:

UNIMI PhD Thesis template

MIUR subjects:

FIS/03

PACS:

41.50.+h

42.25.Fx

42.30.Kq

Contents

List of Figures

List of Tables

Introduction

X-ray radiation from relativistic beams has nowadays achieved unprecedented high brilliance and high degree of coherence [1], thanks to the recent advances in third-generation light sources [2] and Free-Electron Lasers (FELs) [3, 4].

The availability of high brilliance coherent photon beams has fostered the development of many coherence-based techniques, e.g. coherent diffractive imaging, photon correlation spectroscopy and phase contrast imaging [5], routinely implemented at large-scale facilities to investigate physical systems from the micrometer down to the subnanometer scale. In this framework, accurate characterization of spatial and temporal coherence properties of the radiation at the specimen position is fundamental both for proper planning of the experiments and for unbiased data reduction.

Knowledge of the evolution of the spatial coherence properties along the beamline also paves the way to non-invasive diagnostics techniques aimed at measuring the transverse emittance of the particle beam itself [6, 7, 8, 9], a fundamental quantity to characterize the performances of accelerators and colliders [10]. At the same time, effects from limited temporal coherence are envisioned to be a peculiar feature of the broad-spectrum betatron radiation emitted by relativistic electrons in laser-plasma accelerators [11]. In this respect, X-ray and gamma-ray betatron radiation has been recently studied both theoretically and experimentally [12, 13, 14, 15] to diagnose the particle beam inside the plasma through the emitted spectral density [15] and related temporal coherence properties [16].

Finally, an upgrade of large-scale facilities is expected to occur in the forthcoming years to reduce the beam emittance and to increase the coherence properties of the photon beam. This has renewed the interest of the scientific community towards coherence diagnostics techniques. Consequently, the characterization and control of spatial and temporal coherence properties of the radiation emitted by relativistic beams represents an increasingly challenging demand in modern synchrotron and laser-plasma-based light sources.

The most widespread techniques for the characterization of spatial coherence of synchrotron radiation at optical wavelengths are based on interference from a double aperture (Young's interferometer) or on Fresnel diffraction by a slit [17, 18, 19], while temporal coherence measurements are usually performed with amplitude-division interferometers based on the Michelson's scheme [20, 21]. For a complete characterization of spatial and temporal coherence, users have to continuously change the setup to adjust the apertures separation or the optical path differences. Furthermore, despite such measurements are well established in the visible range, they are more challenging at shorter wavelengths. Many solutions have been adopted to extend such techniques to

X-rays [22, 23, 24, 25, 26], requiring specially manufactured and engineered devices, severe alignment constraints and implementation of dedicated X-ray optics.

In this thesis we describe a novel diagnostics technique based on Fourier analysis of Heterodyne Near Field Speckles (HNFS) [27, 28] which overcomes the aforementioned limitations. It exploits the staggered interference between the weak spherical waves scattered by nanoparticles in a colloidal suspension and the strong transmitted partially-coherent beam to probe the spatial and temporal coherence properties of the impinging radiation, without any *a priori* assumption [29, 30, 31, 32, 33]. A criterion based on master curves of data acquired at different sample-detector distances is introduced, allowing to gauge spatial and temporal coherence properties separately by means of two different scaling laws. A single measurement is in principle enough, thus making the technique suitable for single-shot coherence measurements, but nevertheless scanning different sample-detector distances proves self-consistency of the results, besides increasing the finesse of data. The experimental setup is minimal and easy to implement, almost free of any alignment requirement. Finally, the fundamentals of the technique are wavelength independent and scalability to X-rays is straightforward, remarkably without any dedicated X-ray optics [34, 30, 35].

Outline

The thesis is organized as follows:

- Part I deals with the description of partially coherent Synchrotron Radition (SR) within the framework of Statistical Optics:
  - Chap. 1 provides an intoduction to Statistical Optics (Sect. 1.1 and Sect. 1.2) and to the theory of coherence of light waves (Sect. 1.3). Most of the material is based on the widespread reference textbooks by Goodman [36] and Mandel and Wolf [37];
  - Chap. 2 describes SR emission from ultrarelativistic charged particles with the classical electrodynamics approach (Sect. 2.1), focusing on the emission from bending magnets (Sect. 2.2) and from undulators (Sect. 2.3). Topics are discussed following the standard and widespread reference books by Hofmann [38] and Clarke [39]. Finally, in Sect. 2.4 we describe a newly-introduced formalism to SR based on the recent works by Geloni *et al.* [40, 41], providing analytic expressions for the electric field in the near zone as well as in the far zone and for electrons moving with offset and deflection;
  - in Chap. 3 we mix Statistical Optics and the theory of SR emission together with the description of partially coherent radiation from relativistic particle beams (Sect. 3.1). Temporal coherence of SR beams is dealt with in Sect. 3.2, while spatial coherence is addressed in Sect. 3.3. Here we review the main results according to the refurbished theory by Geloni *et al.* based on dimensionless quantities [42]. In particular, the applicability of the Van Cittert - Zernike theorem to third-generation light sources is discussed;
- in Part II we describe the Heterodyne Near Field Speckle technique:
  - Chap. 4, after an overview of speckle patterns under coherent illumination (Sect. 4.1), provides a simplified description of the HNFS technique for partially coherent radiation in terms of Fourier Optics (Sect. 4.2). We also report, for the first time to our knowledge, experimental results validating the

theory. Finally, the underlying physical principles of the technique are introduced and discussed, namely the inteference pattern from a single colloidal particle (Sect. 4.3) and the Fourier analysis of heterodyne speckle fields from colloidal suspensions (Sect. 4.4);

  - in Chap. 5 we provide a theoretical description of the technique (Sect. 5.1), dealing with spatial and temporal coherence separately in Sect. 5.2 and 5.3, respectively. Two different scaling laws and the concept of master curves are therein introduced;
  - Chap. 6 is dedicated to the description of the data reduction algorithm;

- in Part III we show experimental results obtained with table-top optical sources:
  - Chap. 7 reports the first experimental results regarding the sensitivity of the technique to very short longitudinal coherence lengths by characterizing different thermal broadband sources [43, 32, 44]. The temporal scaling law yielding to a single temporal master curve has been tested for the relatively simple case of thermal radiation since the classical Van Cittert-Zernike's theorem and Wiener-Khinchine's theorem certainly hold, thus providing a robust benchmark to validate the theory developed in Part II. We also provide the reader with an introduction to the concept of Analogical Optical Modeling, a fashinating aspect of the technique allowing to mimic the main features of X-ray beams with table-top optical sources;
  - in Chap. 8 we show results about coherence properties of the pulsed second-harmonic of a High Harmonic Generation (HHG) laser at the Laser Laboratory of the ELETTRA synchrotron, Trieste (Italy). Although partial spatial and temporal coherence concurrently contribute to shape the envelope of two-dimensional power spectra, the two different scaling laws allow to gauge the spatial and temporal coherence of the radiation separately. The full two-dimensional spatio-temporal coherence function of the HHG pulses is then retrieved;

- in Part IV we discuss the results obtained at the ALBA Synchrotron Light Source, Barcelona (Spain):
  - Chap. 9 briefly describes the ALBA facility;
  - in Chap. 10 we report the results about the measurements of temporal coherence properties of visible SR from a bending magnet at the Xanadu beamline (FE01), both for narrow-band and white radiation beams, also providing reliable and independent measurements of the radiation power spectral density by virtue of the Wiener-Khinchine's theorem. This represents, to our knowledge, the first time that the HNFS technique is applied to characterize temporal coherence properties of SR beams [45, 33]. Moreover, we investigate the possibility of measuring the wavefront curvature by scanning different sample-detector distances;
  - Chap. 11 contains preliminary results of the measurements of the transverse electron beam size through spatial coherence properties of X-ray undulator radiation at the NCD beamline (BL11). A free-propagation geometry is used, but many experimental limitations prevented to access the vertical coherence. Opposite to this case, the horizontal coherence at the usage point is gauged. Despite transverse coherence measurements with the HNFS technique have

been reported, this is the first time to our knowledge that the method is applied to access the transverse emittance of the particle beam. In this view, we have developed a GPU-accelerated $C/C++$ code to simulate the spatial coherence properties of undulator radiation. Theoretical expectations are consistent with experimental results;

- finally, we collect our conclusion and we summarize the future perspectives.

Part I

Partially Coherent Synchrotron Radiation

CHAPTER 1

Theory of coherence

1.1 Statistical Optics: electromagnetic fields meet stochastic processes

Optics ultimately inquires about the phenomena of generation and propagation of electromagnetic waves. Among the infinite varieties of optical disturbances, plane waves and spherical waves are of outermost importance owing to their simplicity and to their ubiquity in any branch of optics. Referring to the reference frame adopted in Fig. 1.1 and restricting our attention to propagation along the z direction, plane waves and spherical waves can be expressed respectively as

$$\vec{E}(\vec{x},t) = \vec{E}_0 e^{i(kz-\omega t+\phi)} \qquad \vec{E}(\vec{x},t) = \vec{E}_0 \frac{e^{i(kr-\omega t+\phi)}}{r}, \tag{1.1}$$

where $k = 2\pi/\lambda$ is the radiation wavenumber, λ is the radiation wavelength, $\omega = ck = 2\pi\nu$ being $\nu = c/\lambda$ the radiation frequency and c is the speed of light.

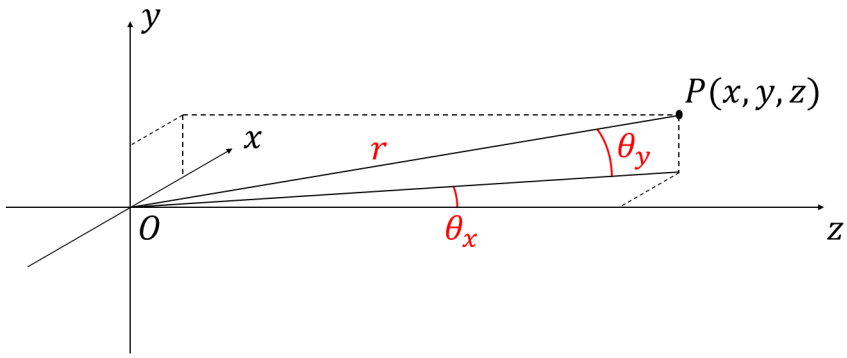

Figure 1.1: Reference frame adopted throughout the thesis. The z direction determines the optical axis of the system and the $(x$-$y)$ planes are perpendicular to it. A point P of coordinates (x, y, z) subtends the angles $\theta_x = \text{atan}(x/z)$ and $\theta_y = \text{atan}(y/z)$ to the origin O. When $\theta_x \ll 1$ and $\theta_y \ll 1$, paraxial conditions are fulfilled and the distance r of the point P from the origin O can be expressed as $r \approx z + (x^2 + y^2)/(2z)$.

The vector $\vec{x} = (x, y, z)$ denotes spatial coordinates while t stands for the temporal one. The z direction determines the optical axis of the system and the $(x$-$y)$ planes are perpendicular to it. Finally, r is the distance between the generic point P of coordinates (x, y, z) and the origin O of the adopted reference frame. The reader should start to

familiarize with the complex phasor representation of optical fields adopted in Eq. 1.1. The argument of the complex exponential is known as the phase of the wave while the other terms constitute the amplitude of the electric field. The initial phase ϕ determines the value of the field at the origin O at time $t = 0$. An example of the phase distributions of plane waves and spherical waves is reported in Fig. 1.2.

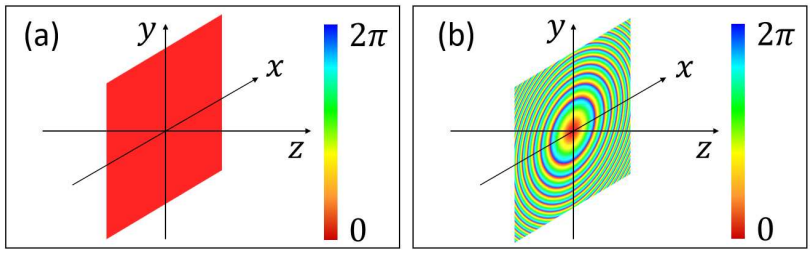

Figure 1.2: (a) Representation of a plane wave: from Eq. 1.1, the wavefronts are planes perpendicular to the optical axis. (b) Representation of a spherical wave: from Eq. 1.1, the wavefronts are spherical surfaces centered at the origin. The phase projected onto a plane perpendicular to the optical axis varies quadratically along the radial direction.

Free-space propagation and diffraction from an aperture or an opaque obstacle can be equivalently formulated in terms of the superposition of secondary spherical waves generated at each point of the incident field (Huygens-Fresnel's integral) [46] or in terms of the superposition of the propagated plane waves in which the incoming optical disturbance can be decomposed into (Fourier Optics) [47]. Optics phenomena are thus described in an entirely deterministic framework where light disturbances have an analytic representation in terms of plane waves or spherical waves which are subjected to perfectly predictable transformations upon propagation as in Eq. 1.1.

While plane waves and spherical waves provide simple expressions for the optical fields useful for a mathematical treatment of light phenomena, they unavoidably pose some problems from a physical viewpoint when we attempt to describe real light sources and emission processes. In fact, by definition, plane waves and spherical waves should have an infinite extent on any plane perpendicular to the propagation direction and they should exist from $t = -\infty$ to $t = +\infty$. Therefore they are only approximations to actual radiation fields valid within some degree of accuracy.

In real light sources radiation is generated by accelerated charges behaving as oscillating electric dipoles. The emitted field $\vec{E}_r$ is known as the radiant field, it is polarized in the direction of the charge acceleration $\vec{a}$ and its amplitude resembles that of a spherical wave:

$$\vec{E}_r \propto \frac{1}{r}\vec{a}. \tag{1.2}$$

The corresponding intensity $I = |\vec{E}|^2$ has the characteristic $\sin^2\theta$ directivity diagram of the radiation pattern from an oscillating dipole, as shown in Fig. 1.3. The total radiated power, i.e. the total radiated intensity per unit of time, integrated over a spherical surface of radius R centered on the emitting dipole is constant regardless of the value of R. This must imply an energy transfer from an external source to the charge. As a consequence, the radiative process eventually vanishes as soon as the excitation is turned off. Furthermore, the emission of the radiant field itself has a finite temporal duration: the

energy transferred to the electric charge is radiated in the form of optical pulses with a characteristic temporal scale ranging between 10^{-15} s and 10^{-12} s.

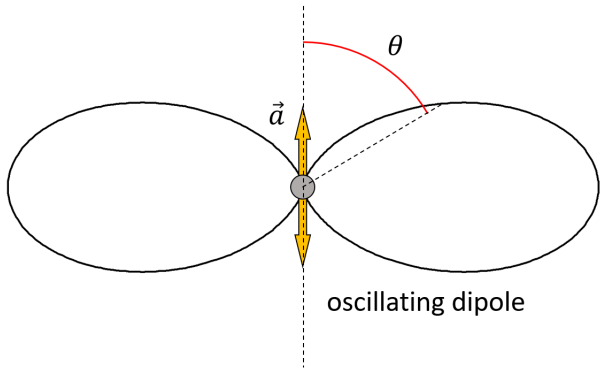

Figure 1.3: Directivity diagram of the radiation emitted by an oscillating dipole. It shows the characteristic $\sin^2\theta$ behavior, where the angle θ refers to the direction of the charge acceleration $\vec{a}$. The emitted radiation is polarized parallel to $\vec{a}$ and it is not emitted along the direction of the dipole oscillations.

When many independent emitters are considered, the total radiation results from the superposition of a number of emission processes by accelerated electric charges behaving as oscillating electric dipoles, for which each radiant field is emitted at a different time. The number of emitters and of the parameters involved is so large that it results in a complete lack of knowledge on the exact state of the system. From the point of view of an observer, this implies that the total electric field randomly fluctuates in time both in amplitude and phase on temporal scales comparable to the characteristic time of the emission processes. A statistical treatment is thus needed in order to gauge the properties of the radiation. Statistical Optics [37, 36] affords a convenient tool to deal with randomly fluctuating fields in the appropriate way.

1.2 Basic concepts of Statistical Optics

1.2.1 Ensamble averages

The branch of mathematics which deals with the analysis of random phenomena is known as the theory of stochastic processes. Introducing the concept of random variables as quantities for which the outcomes of an experiment cannot be predicted in advance, a stochastic process $U(A)$ is defined by assigning a function $u(A,t)$ of the independent variable t to each possible realization of the random variable A, together with a measure of their associated probabilities. The result of a measurement on the stochastic process $U(A)$ is not determined *a priori* due to the unpredictable structure of the function $u(A,t)$ inherited from the random variable A. Such functions play an important role in optics. As we have seen in Sect. 1.1, the field emitted by any real source undergoes random fluctuations in time and consequently it can be properly described within the framework of stochastic processes: the optical disturbance is modeled as a random variable A and $u(A,t)$ represents the set of all possible configurations of the corresponding

electric field as a function of time[1].

Suppose that many $u(t)$ are measured in similar experiments performed under the same conditions, producing the outcomes $u_1(t), u_2(t), \ldots, u_N(t)$, where the dependence on A has been dropped for the sake of simplicity. In the limit $N \to +\infty$, such a collection is called the ensamble of the stochastic process $U(A)$ and each individual $u_i(t)$ is called an ensamble realization. For each ensamble realization $u_i(t)$ and for any function $F[u_i(t)]$ of the ensamble realization $u_i(t)$ we define the temporal average $\langle \cdot \rangle_t$ as

$$\langle u_i(t) \rangle_t = \lim_{T \to +\infty} \frac{1}{2T} \int_{-T/2}^{+T/2} u_i(t)\, \mathrm{d}t \qquad \langle F[u_i(t)] \rangle_t = \lim_{T \to +\infty} \frac{1}{2T} \int_{-T/2}^{+T/2} F\left[u_i(t)\right]\, \mathrm{d}t. \tag{1.3}$$

Within the framework of stochastic processes, we can also define the ensamble average $\langle \cdot \rangle$ as the average over all the possible realizations:

$$\langle u(t) \rangle = \lim_{N \to +\infty} \sum_{k=1}^{N} u_k(t) \qquad \langle F[u(t)] \rangle = \lim_{N \to +\infty} \sum_{k=1}^{N} F[u_k(t)]. \tag{1.4}$$

Ensamble averages can be expressed in terms of the probability density function $p(u,t)$ associated to the stochastic process by recalling that $p(u,t)\,\mathrm{d}u$ represents by definition the probability that the stochastic process $U(A)$ will take on a value in the range $(u, u + \mathrm{d}u)$ at time t. Equations 1.4 can then be rephrased as

$$\langle u(t) \rangle = \int_{-\infty}^{+\infty} u(t)\, p(u,t)\, \mathrm{d}u \qquad \langle F[u(t)] \rangle = \int_{-\infty}^{+\infty} F[u(t)]\, p(u,t)\, \mathrm{d}u. \tag{1.5}$$

The probability density function $p(u,t)$ provides a description of the statistical behavior of a random variable at a single instant of time. In order to completely characterize the stochastic process $U(A)$, knowledge of the joint behavior of the underlying random variable at different instants of time $t_1, t_2, \ldots, t_n$ is also required. This leads to the introduction of the n-th order joint probability density $p_n(u_1, u_2, \ldots, u_n, t_1, t_2, \ldots, t_n)$ with the following meaning: the quantity $p_n(u_1, u_2, \ldots, u_n, t_1, t_2, \ldots, t_n)\, \mathrm{d}u_1\, \mathrm{d}u_2 \ldots \mathrm{d}u_n$ represents the joint probability that the stochastic process $U(A)$ will take on values in $(u_1, u_1 + \mathrm{d}u_1)$ at time t_1, $(u_2, u_2 + \mathrm{d}u_2)$ at time t_2, ... , $(u_n, u_n + \mathrm{d}u_n)$ at time t_n. The associated n-point ensamble average is known as the n-th order correlation function or the n-th order moment of the stochastic process:

$$\langle u_1(t_1)\, u_2(t_2) \ldots u_n(t_n) \rangle = \underbrace{\int_{-\infty}^{+\infty} \int_{-\infty}^{+\infty} \cdots \int_{-\infty}^{+\infty}}_{\mathrm{n-times}} u_1(t_1)\, u_2(t_2) \ldots u_n(t_n)\, p_n(u_1, u_2, \ldots, u_n, t_1, t_2, \ldots, t_n)\, \mathrm{d}u_1\, \mathrm{d}u_2 \ldots \mathrm{d}u_n. \tag{1.6}$$

[1] Although t reminds of the temporal coordinate, all the discussion and the derivations can be easily extended to the case of spatial coordinates. The notation and the terminology adopted here conform with those of the reference textbook on Statistical Optics by Goodman [36].

1.2.2 Stationarity

A random process is called strictly stationary when all the n-th order ensamble averages are independent on the origin of time[2]. Stated analitically, for all n and T we require that

$$\langle u_1(t_1)\, u_2(t_2) \ldots u_n(t_n)\rangle = \langle u_1(t_1 - T)\, u_2(t_2 - T) \ldots u_n(t_n - T)\rangle\,. \tag{1.7}$$

It is worth noting that for strictly stationary processes the first-order moment, i.e. the ensamble average, is independent on time and the second-order moment depends only on the time difference $\tau = t_2 - t_1$.

The concept of wide-sense stationarity is more general than strict stationarity since it involves only the first- and the second-order moments: a stochastic process is wide-sense stationary if the ensamble average is independent on time and the second-order moment depends only on the time difference $\tau = t_2 - t_1$. Every strictly stationary process is also wide-sense stationary, but the converse is not true.

As a consequence of the definition of stationarity, whether strict or wide-sense, a necessary condition for a stochastic process to be stationary is that the signal lasts forever.

1.2.3 Ergodicity

Ergodicity is a subtle concept dealing with the comparison of the statistical properties of an individual ensamble realization (temporal averages) with the properties of the entire ensamble (ensamble averages). A stochastic process is called ergodic if every sample function takes on values along the time axis with the same probability observed across the entire ensamble for any fixed instant of time. Heuristically, ergodicity implies that the n-th order temporal averages performed on every single ensamble realization are equal to the n-th order ensamble average over the entire collection of realizations. The statistical information about the ensamble is then already conveyed by each single realization: dividing a single sample function into many parts provides a collection of realizations which is representative of the entire ensamble. For ergodic processes temporal averages and ensamble averages are equal and they can thus be interchanged.

A necessary condition for ergodicity is strict stationarity. Figure 1.4 shows an example of non-ergodic stochastic process due to non-stationarity. The sample functions of such a process have the same relative frequency distribution along the time axis but they exhibit larger fluctuations at $t_2 \sim 250$ than at $t_1 \sim 200$. This implies that the statistical properties of each ensamble realization depend on time and the process is non-stationary. Furthermore, the relative frequencies observed across the ensamble at times t_1 and t_2 separately are not the same and they are not equal to the relative frequency observed along each single ensamble realization. Hence the stochastic process cannot be ergodic.

We stress that not every strictly stationary random process is ergodic. A trivial example is provided by the constant stochastic process where the functions $u_i(t)$ simply assume random constant values according to a given probability density function. Ensamble averages are independent on the origin of time and the process is strictly stationary. Nevertheless, a single sample function is not representative of the entire ensamble since the value assumed by a single realization does not reflect the occurence of the other random numbers.

[2]Within Statistical Optics, the concept of stationarity pertains to the time domain. The spatial analogue of stationarity is referred to as homogeneity. It implies that all the n-th order ensamble averages are invariant upon spatial translations.

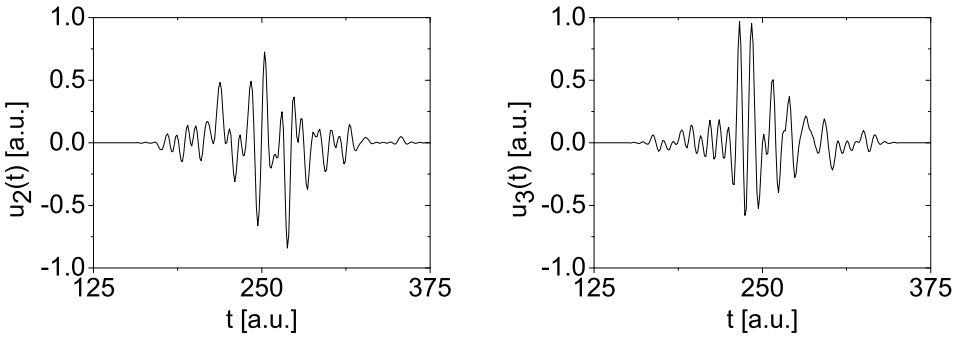

Figure 1.4: Example of a non-ergodic stochastic process due to non-stationarity. All the ensamble realizations have the same relative frequency distributions along the time axis and their random fluctuations are larger at $t_2 \sim 250$ than at $t_1 \sim 200$. The statistical properties across the entire ensamble are thus time-dependent and the process is non-stationary. As a consequence, the relative frequencies observed across the ensamble at a fixed instant of time are not equal to the relative frequencies observed along the time axis for each single sample function: the process is non-ergodic.

For convenience of the reader, we summarize in Fig. 1.5 the main classes of stochastic processes introduced, together with their hierarchical structure.

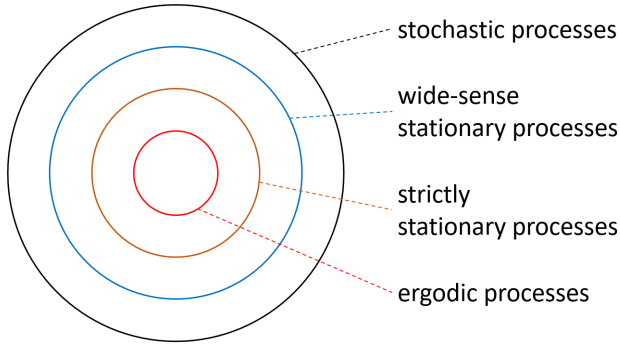

Figure 1.5: Hierarchy of stochastic processes.

1.2.4 Gaussian processes

A random process $U(A)$ is said to be a Gaussian random process if the associated random variable A has a Gaussian probability density function

$$p_A(u) = \frac{1}{\sqrt{2\pi}\sigma} e^{\frac{(u-\bar{u})^2}{2\sigma^2}}, \tag{1.8}$$

where $\bar{u} = \langle u \rangle$ is the ensamble average of the random variable A and $\sigma = \left\langle (u-\bar{u})^2 \right\rangle$ is the second-order central moment.

Gaussian processes have many useful properties [37, 36]:

- linearly filtered Gaussian random processes are also Gaussian random processes: despite the linear filter may alter the values of the n-th order moments of the process, the Gaussian statistics is retained;
- wide-sense stationarity implies strict stationarity;
- n-th order moments with $n > 2$ can be expressed in terms of first- and second-order moments (Gaussian Moment Theorem): only first- and second-order correlation functions are needed in order to characterize the statistical properties of the process.

1.2.5 An example from optics: thermal light

Thermal radiation results from the superposition of many contributions, each with a random amplitude and phase, emitted by a large number of independent radiating atoms. A large class of optical sources emits thermal light, as for example the Sun, the other stars or an incandescent lamp. By virtue of the Central Limit Theorem, the real and imaginary part of the total electric field are endowed with random fluctuations described by a Gaussian probability density function: thermal light is a Gaussian stochastic process.

The stochastic process associated to the emission of thermal light has (virtually) an infinite duration, at least on the characteristic time-scales of experiments, and its statistical properties are independent on time: thermal light is a stationary process.

Furthermore, it is straightforward to realize that the values of each single sample function occur with the same probability with which they appear across the ensamble realizations at any fixed instant of time. Thermal light is an ergodic process and temporal averages are equivalent to ensamble averages. Therefore, different measurements performed on the same (ideally infinite) sample function actually correspond to probing many ensamble realization.

Finally, the presence of a monochromator or of a band-pass filter, as well as of a spatial filter or a polarizer, does not change the Gaussian statistics of thermal light.

1.3 Coherence of light waves

1.3.1 What is coherence?

The theory of coherence of light deals with the correlations between the random fluctuations of the electromagnetic fields emitted by real sources. The amplitude and phase of the optical disturbances fluctuate in an unpredictable way due to the stochastic nature of the underlying emission processes. The random fluctuations of the fields occur over temporal scales comparable to those of the emission processes, ranging between 10^{-15} s and $- 10^{-12}$ s. None of the currently available detectors can achieve such a high temporal resolution and we can only access a statistical, time-integrated information. The stochastic fluctuations of the field and the correlations among them can thus be properly described with the formalism of correlation functions of Statistical Optics developed in the previous Sect. 1.2. Since for a large class of light sources the emitted radiation results from a number of independent contributions from many emitters, the field fluctuations are described by a Gaussian statistics. By means of the Gaussian Moment Theorem, first- and second-order moments suffice to provide a full statistical description of the stochastic process and we need need to investigate only the two-point correlation functions of the radiation.

Spatial coherence is concerned with the correlations of the field fluctuations at the same instant of time but at two different point on the same $(x\text{-}y)$ plane perpendicular to the propagation direction. In general, spatial coherence properties depend on the position on the $(x\text{-}y)$ plane. However, for homogeneous radiation the second-order spatial correlation function does not depend on the absolute position of the two points but only on their relative displacement. The second-order correlation function is invariant upon translations on the $(x\text{-}y)$ plane and the coherence properties do not change across the beam.

Temporal coherence provides the information on the correlations of the field fluctuations at the same spatial point but at two different instants of time. The radiation is said to be stationary if the second-order temporal correlation function depends only on the relative delay between the two instants of time. In this case the temporal coherence properties of light are invariant upon temporal shifts.

1.3.2 Probing coherence

The simplest manifestation of coherence is provided by the phenomenon of interference [46, 37, 36]. The instantaneous intensity distribution I_t arising from the superposition of two different optical disturbances $E_1 = |E_1| \exp(\phi_1)$ and $E_2 = |E_2| \exp(\phi_2)$ can be expressed as[3]

$$I_t = |E_1 + E_2|^2 = I_1 + I_2 + 2\Re\mathrm{e}\{E_1 E_2^*\} = I_1 + I_2 + 2\,|E_1| \cdot |E_2| \cos(\Delta\phi)\,, \tag{1.9}$$

where we have adopted the phasor representation for the electric fields E_1 and E_2, $I_1 = E_1 E_1^*$, $I_2 = E_2 E_2^*$ and $\Delta\phi = \phi_2 - \phi_1$. The first two terms represent the light intensity that would be generated independently by E_1 and E_2, as shown in Fig. 1.6(a) and Fig. 1.6(b). The last term describes an oscillatory intensity modulation responsible for the appearence of the interference fringes, as shown in Fig. 1.6(c).

Equation 1.9 describes the time-resolved intensity pattern that would be measured with a detector achieving a high temporal resolution. However, due to the stochastic processes associated to the emission of the radiation, the two interfering fields E_1 and E_2 fluctuate in an unpredictable way on temporal scales much shorter than the response time of any detection system and many interferograms contribute to the detected intensity pattern. The random fluctuations of the field amplitudes just induce variations in the overall background illumination (given by the sum $I_1 + I_2$ in Eq. 1.9) and in the absolute envelope of the interference fringes ($|E_1| \cdot |E_2|$ in Eq. 1.9). More importantly, the fluctuations of the relative phase $\Delta\phi$ are responsible for a lateral shift on the interference fringes. If the fluctuations of the two optical disturbances are correlated, the instantaneous interferograms of Eq. 1.10 are all similar and the detected intensity exhibits sharp interference fringes, as shown in Fig. 1.7(a),(d). Opposite to this case, when the random fluctuations of the two fields are uncorrelated, the superposition of many randomly laterally-shifted interferograms leads to a partial or to an almost complete cancellation of the interference fringes, as reported on Fig. 1.7(b),(e) and in Fig. 1.7(c),(f), respectively.

While the superposition of two electromagnetic fields always generates instantaneous interference fringes, the random fluctuations in the phases of the two optical

[3]Here we intentionally drop the dependence on spatial and temporal coordinates in order to keep the discussion on a general level. Detailed analysis of temporal coherence and spatial coherence will be properly addressed in the following Subsect. 1.3.3 and Subsect. 1.3.4, respectively.

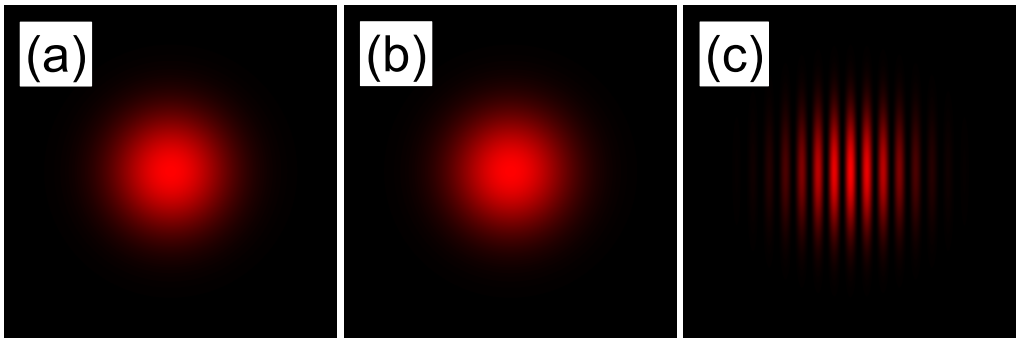

Figure 1.6: Simulated instantaneous interference between two optical beams. (a) Intensity distribution I_1 generated by the first beam. (b) Intensity distribution I_2 generated by the second beam. Without loss of generality, I_1 and I_2 have been described with the same two-dimensional Gaussian function. (c) The phase difference between the two optical disturbances has been assumed to vary only along the horizontal direction. The superposition of the two beams thus generates vertical interference fringes.

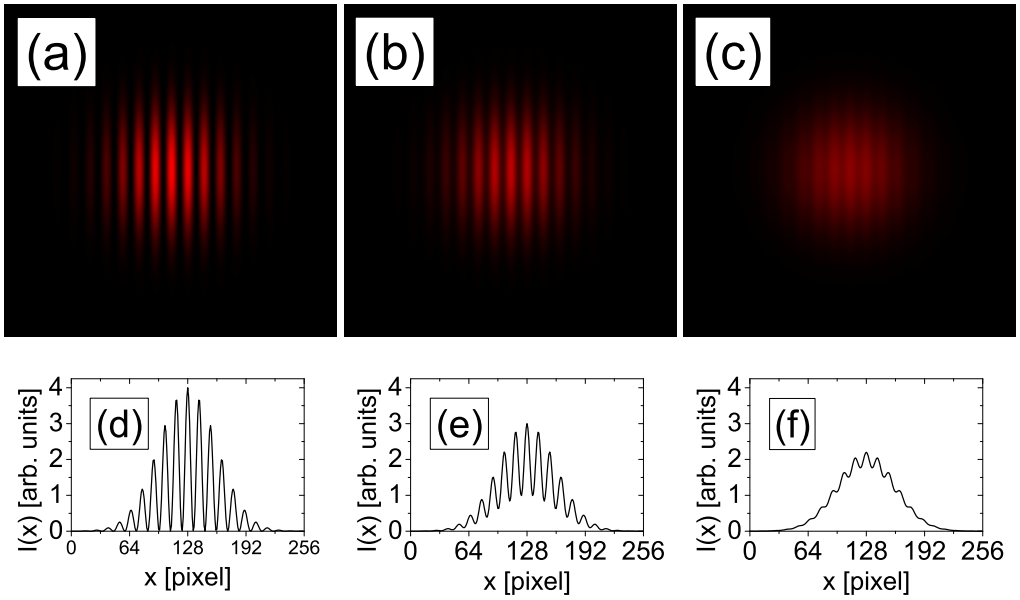

Figure 1.7: Simulated time-integrated interference between two partially coherent optical beams resulting from the superposition of 10^4 different instantaneous interferograms. The intensity distributions associated to E_1 and E_2 have been described with the same Gaussian functions as in Fig. 1.6. (a) Stable interference fringes arising from the superposition of two coherent beams. (b) The contrast of the interference fringes is reduced when the two beams are partially coherent. (c) In the case of incoherent beams, interference fringes are hardly visible and only the featureless intensity distribution $I_1 + I_2$ is left. Plots (d), (e) and (f) show the intensity profiles along the horizontal cuts indicated by the yellow lines. It is worth noting how zeros of intensity are reached only in the fully coherent case.

disturbances may prevent to measure such intensity modulation over a finite acquisition time. Analytically, the average over many ensamble realization gives the following expression for the detected intensity I:

$$I = \langle I_t \rangle = \langle I_1 \rangle + \langle I_2 \rangle + 2\Re\mathrm{e}\left\{\langle E_1 E_2^* \rangle\right\}. \tag{1.10}$$

Comparing Eq. 1.9 and Eq. 1.10, it can be seen that despite interference always occurs instantaneously, stable interference depends on the second-order correlation function of the optical field, namely on coherence properties of the radiation. The superposition of two fully coherent fieds generates interference fringes endowed with a high contrast. Conversely, stable interference does not occur with incoherent radiation and interference fringes do not appear due to the lack of any fixed phase relation between the two electromagnetic waves. We can thus restate coherence as the ability of the radiation to write stable interference fringes.

Owing to the relation between interference and coherence properties of the radiation, we can now reinterpret temporal coherence as the ability of the light to interfere with a delayed, but not spatially shifted, version of itself (amplitude splitting). Similarly, spatial coherence is the ability of the radiation to interfere with a spatially shifted, but not delayed, version of itself (wavefront splitting). In both cases the fundamental fact holds that the appearence of interference fringes and the degree of coherence of the radiation are intimately related. In fact, assuming $\langle I_1 \rangle = \langle I_2 \rangle = I_0$ for simplicity, we can define the visibility of the interference fringes as follows

$$V = \frac{I_{\max} - I_{\min}}{I_{\max} + I_{\min}} = |\mu|, \tag{1.11}$$

where

$$I_{\max} = 2I_0 + 2\left|\langle E_1 E_2^* \rangle\right| \tag{1.12}$$

and

$$I_{\min} = 2I_0 - 2\left|\langle E_1 E_2^* \rangle\right| \tag{1.13}$$

represent the intensity of the interferogram near a maximum of interference and near the corresponding minimum, respectively. The function $\mu = \langle E_1 E_2^* \rangle / I_0$ is the normalized coherence function of the radiation whose modulus varies between 0 and 1. Interference fringes thus have maximum visibility when $|\mu| = 1$, corresponding to the case of fully coherent radiation. Interference fringes have null visibility when the radiation is incoherent, in which case $|\mu| = 0$. The concept of fringe visibility thus quantitatively relates the features of the interferograms to the coherence properties of the radiation.

1.3.3 Temporal coherence

The Michelson's interferometer is an amplitude-division interferometer aimed at measuring the temporal coherence properties of the radiation [36, 37]. The scheme of the interferometer is depicted in Fig. 1.8. The light emerging from a localized source S is collimated by a converging lens and it is sent onto a beam splitter. Light is then divided into two beams following different paths. The transmitted radiation propagates along the horizontal arm of the interferometer and it is reflected back by the fixed mirror M_1. The second beam propagates along the vertical arm of the interferometer and it impinges onto the movable mirror M_2. Its position can be varied in order to tune the optical path difference $2h$ with respect to the fixed pathlength of the horizontal arm of the interferometer. The second beam then acquires a temporal delay $2h/c$ due to the propagation

along the extra path. After being reflected by M_1 and M_2, the two delayed beams are then recombined by the beam splitter and their interference pattern is measured with a detector.

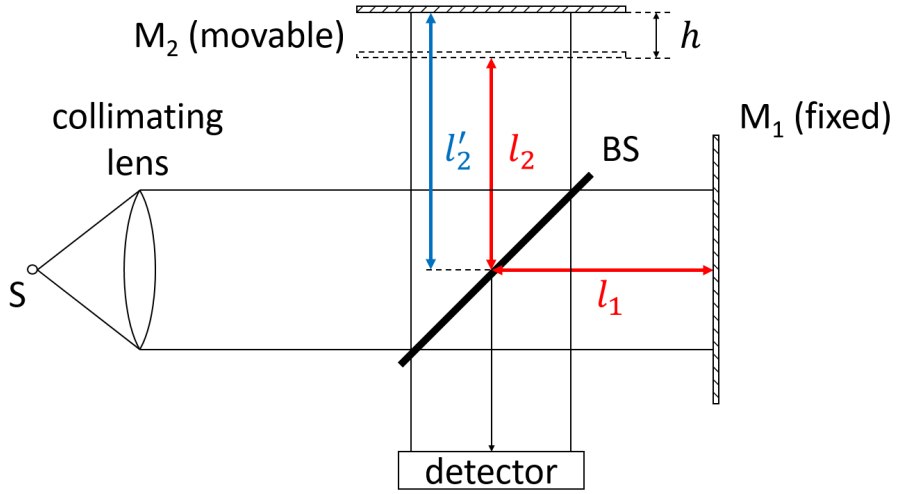

Figure 1.8: Scheme of the Michelson's interferometer including the light source S, the collimating lens, the beam splitter BS, the fixed mirror M_1, the movable mirror M_2 and the detector. In the configuration indicated by the dashed line, the lengths of the two arms of the interferometer l_1 and l_2 are equal. When M_2 is moved by the amount h, the pathlength l_2' of the vertical arm of the interferometer differs from the horizontal one by $2h$. Therefore the two beams interfere on the plane of the detector with a relative delay $\tau = 2h/c$.

Let $u(t)$ be the electric field of the light emitted by the source S. The intensity I on the detector as a function of the optical path difference h can be written as

$$I(h) = \left\langle \left| u(t) + u\left(t - \frac{2h}{c}\right)\right|^2 \right\rangle = \\ = \left\langle |u(t)|^2 \right\rangle + \left\langle \left| u\left(t - \frac{2h}{c}\right)\right|^2 \right\rangle + 2\Re\mathrm{e}\left\langle u(t)u^*\left(t - \frac{2h}{c}\right)\right\rangle, \tag{1.14}$$

where $2h/c$ takes into account the relative time delay induced by the movable mirror.

Under the assumption of stationarity, $\langle |u(t)|^2 \rangle = \langle |u(t-2h/c)|^2 \rangle = I_0$ and the second-order correlation function depends only on the time difference $\tau = 2h/c$. We can therefore introduce the Self Coherence Function

$$\Gamma(\tau) = \langle u(t)u^*(t-\tau)\rangle\,. \tag{1.15}$$

and the Complex Degree of self Coherence (CDC)

$$\gamma(\tau) = \frac{\Gamma(\tau)}{\Gamma(0)}, \tag{1.16}$$

where $\Gamma(0) = I_0$ from Eq. 1.15. The normalization in Eq. 1.16 and the Schwarz's inequality imply $\gamma(0) = 1$ and $|\gamma(\tau)| \leq 1$ for $\tau \geq 0$, respectively. Substituting Eq. 1.16 into Eq. 1.14 yield to

$$I(h) = 2I_0 \left\{ 1 + \Re\mathrm{e} \left[\gamma \left(\frac{2h}{c} \right) \right] \right\}. \tag{1.17}$$

The radiation CDC can be factorized in the following general form

$$\gamma(\tau) = |\gamma(\tau)| \exp\left\{ -i \left[2\pi\nu\tau - \alpha(\tau) \right] \right\}, \tag{1.18}$$

where $\nu = c/\lambda$ is the mean frequency of the radiation and $\alpha(\tau) = \mathrm{Arg}\{\gamma(\tau)\} + 2\pi\nu\tau$. The detected intensity then takes the final form

$$I(h) = 2I_0 \left[1 + \left| \gamma \left(\frac{2h}{c} \right) \right| \cos \left\{ 2\pi \left(\frac{2h}{\lambda} \right) - \alpha(\tau) \right\} \right]. \tag{1.19}$$

In the vicinity of zero pathlength difference $\gamma(2h/c) \approx 1$ and $\alpha(2h/c) \approx 0$. The interferogram developes as a fully modulated cosine with intensity varying from 0 to $4I_0$ with an average value of $2I_0$. As the relative pathlength difference h is increased, the depth of the interference modulation $|\gamma(2h/c)|$ decreases and fringes may suffer a phase shift induced by the term $\alpha(2h/c)$.

The visibility of the interference fringes at a fixed pathlength difference h allows to access the modulus of the radiation CDC:

$$V = \frac{I_{\max} - I_{\min}}{I_{\max} + I_{\min}} = \left| \gamma \left(\frac{2h}{c} \right) \right|, \tag{1.20}$$

where $I_{\max}$ and $I_{\min}$ are the maximum and minimum value of the interference fringes in the vicinity of the pathlength difference h.

The reduction in fringe visibility as the pathlength difference is increased is caused by the finite bandwidth $\Delta\nu$ of the source. In the ideal case of a monochromatic component described by a time-varying complex phasor of the form $A\exp(i\omega t)$, where $\omega = 2\pi\nu$ is the radiation angular frequency, the complex envelope of the electric field A would be constant over time and the corresponding signal would have an infinite duration. Opposite to this case, the presence of many independent monochromatic components induces a dependence on time in the complex envelope $A(t)$ of the emitted electric field. Increasing the bandwidth $\Delta\nu$ of the source makes the variations of $A(t)$ occur over shorter temporal scales. Owing to this relation between variables forming a Fourier couple, the electric field emitted by each atom has a pulsed structure with a characteristic duration $\Delta t \approx 1/\Delta\nu$. The total electric field is the result of the superposition of many randomly delayed pulses and the corresponding intensity exhibits stochastic fluctuations in time, as depicted in Fig. 1.9. Intensity spikes arise from the constructive interference among the emitted elementary fields. Their temporal duration thus sets the characteristic temporal scale over which the electric field is perfectly correlated, namely the coherence time of the radiation. By means of Fourier analysis on the complex envelope of the total electric field, the emitted radiation is expected to be correlated on a temporal scale smaller than or comparable to $1/\Delta\nu$. The drop of fringe visibility as the pathlength difference h increases is then a consequence of the superposition of many interferograms generated by two different uncorrelated pulses propagating along the two arms of the interferometer.

The dependence of the temporal coherence properties of the radiation on the emitted power spectral density of the source is quantitatively described by the Wiener-Khinchin's

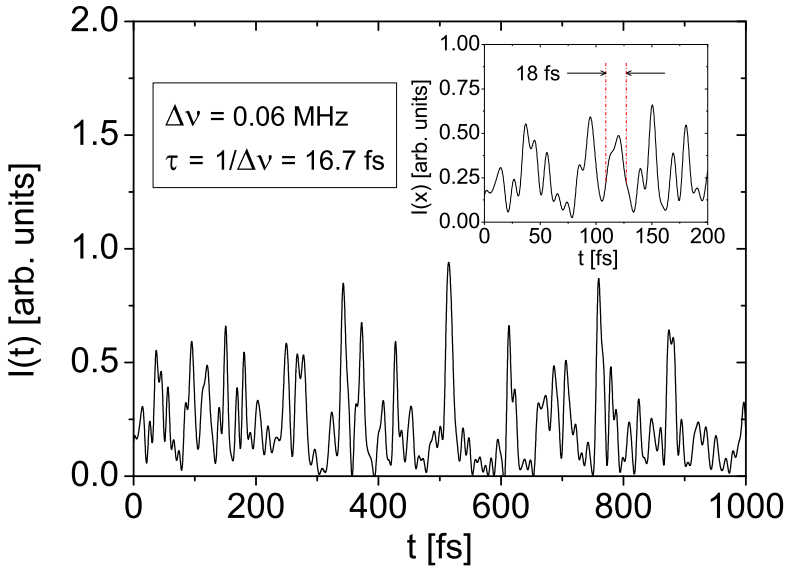

Figure 1.9: Simulated intensity of partially temporally coherent radiation with a finite bandwidth $\Delta\nu = 60$ THz, corresponding to $\Delta\lambda = 60$ nm at an average wavelength $\bar{\lambda} = 550$ nm. Intensity spikes arise from the coherent superposition of many light pulses of finite duration Δt emitted be the atoms at random times. The width of the intensity spikes determines the coherence time of the radiation and it is in agreement with the expected value $\Delta t = 1/\Delta\nu = 16.7$ fs from Fourier transform arguments (see inset).

theorem of stationary stochastic processes [36, 37]. It relates the temporal autocorrelation function of the process, i.e. the radiation CDC $\gamma(\tau)$, to the Fourier transform of the power spectral density $G(\nu)$ of the source:

$$\gamma(\tau) = \int_0^{+\infty} G(\nu) e^{i2\pi\nu\tau} \, \mathrm{d}\nu. \tag{1.21}$$

The characteristic time over which the optical disturbance is highly correlated is known as the coherence time of the radiation and it is related to the inverse bandwidth of the source spectrum by virtue of the Wiener-Khinchine's theorem. The calculation of the coherence time from the radiation CDC involses the introduction of a certain algorithm in order to extract a single number from the entire function. Among all the possible algorithms that can be implemented in order to reduce the radiation CDC into a single number, we follow Mandel and we define the coherence time τ_c of the radiation as [36, **?**]

$$\tau_c = \int_{-\infty}^{+\infty} |\gamma(\tau)|^2 \, \mathrm{d}\tau. \tag{1.22}$$

The coherence time just defined is of the same order of magnitude as $1/\Delta\nu$, as expected from simple Fourier transform arguments. The radiation is temporally coherent or partially temporally coherent depending on whether the coherence time is comparable to or smaller than the characteristic duration of the process, while temporally incoherent radi-

ation describes light whose phase fluctuations are complitely random and uncorrelated from instant to instant.

1.3.4 Spatial coherence

The Young's interferometer is a wavefront-division interferometer aimed at probing the spatial coherence properties of the radiation [36, 37]. The setup of the interferometer is depicted in Fig. 1.10. The light emerging from a localized source S is collimated by a converging lens and it is sent onto the $(\xi$-$\eta)$ plane where two apertures are present at positions $P_1 = (\xi_1, \eta_1)$ and $P_2 = (\xi_2, \eta_2)$, respectively. The interference of the two diffracted beams is then observed across the $(x$-$y)$ plane at a distance z downstream the opaque screen. The generic point $Q = (x, y)$ on the detection plane lies at a distance r_1 from P_1 and at a distance r_2 from P_2.

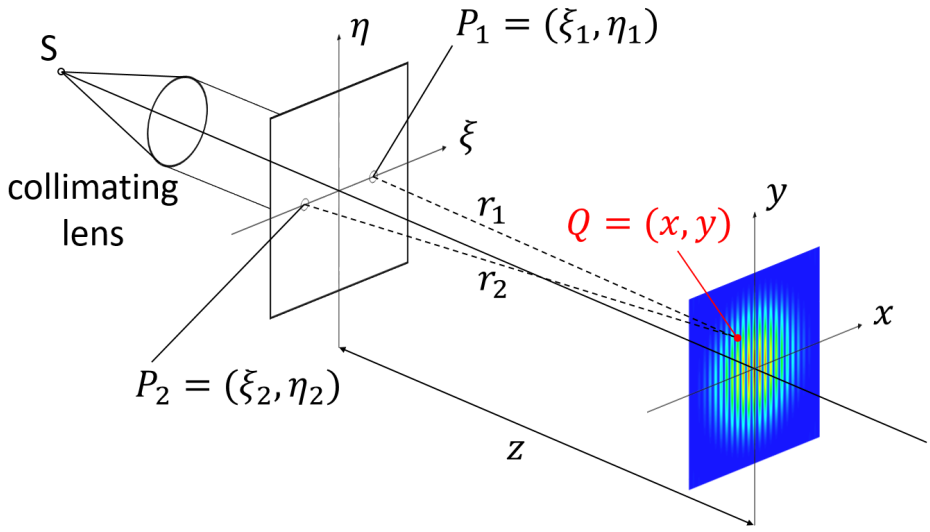

Figure 1.10: Scheme of the Young's interferometer including the light source S, the collimating lens and the opaque screen with the two apertures at positions $P_1 = (\xi_1, \eta_1)$ and $P_2 = (\xi_2, \eta_2)$. The detetction plane is located at a distance z downstream the plane of the apertures. The generic point $Q = (x, y)$ on the detection plane lies at a distance r_1 from P_1 and at a distance r_2 from P_2.

The optical disturbance at a point Q at time t is generated by the superposition of the light waves emerging from the two pinholes located at P_1 and P_2 at the earlier times $t - r_1/c$ and $t - r_2/c$, respectively:

$$u(Q,t) = K_1 u\left(P_1, t - \frac{r_1}{c}\right) + K_2 u\left(P_2, t - \frac{r_2}{c}\right). \tag{1.23}$$

Here K_1 and K_2 are purely imaginary numbers taking into account the shape and the finite size of the apertures [36, **?**]. The time-integrated intensity is then

$$I(Q) = |K_1|^2 \left\langle \left| u\left(P_1, t - \frac{r_1}{c}\right)\right|^2 \right\rangle + |K_2|^2 \left\langle \left| u\left(P_2, t - \frac{r_2}{c}\right)\right|^2 \right\rangle + \\ + 2|K_1||K_2| \Re\mathrm{e}\left\langle u\left(P_1, t - \frac{r_1}{c}\right) u^*\left(P_2, t - \frac{r_2}{c}\right)\right\rangle, \tag{1.24}$$

where we have noticed that $K_1K_2^* = K_1^*K_2 = |K_1||K_2|$. The first two terms represent the intensity distibutions $I^{(1)}(Q)$ and $I^{(2)}(Q)$ that would be generated at point Q by the pinhole P_1 and P_2 alone, respectively. We introduce the Mutual Coherence Function (MCF)

$$\Gamma_{12}(\tau) = \langle u(P_1,t)u^*(P_2,t-\tau)\rangle \tag{1.25}$$

and we rewrite Eq. 1.24 as

$$I(Q) = I^{(1)}(Q) + I^{(2)}(Q) + 2\,|K_1|\,|K_2|\,\Re\mathrm{e}\left[\Gamma_{12}\left(\frac{r_2-r_1}{c}\right)\right]. \tag{1.26}$$

From Schwarz's inequality, $|\Gamma_{12}(\tau)| \leq (\Gamma_{11}(0)\Gamma_{22}(0))^{1/2}$ where by definition $\Gamma_{11}(0)$ and $\Gamma_{22}(0)$ represent the intensities of the light incident on the two pinholes. The normalized Mutual Coherence Function, also known as the Complex Degree of Coherence, is then obtained as

$$\gamma_{12}(\tau) = \frac{\Gamma_{12}(\tau)}{|\Gamma_{11}(0)\Gamma_{22}(0)|^{1/2}}. \tag{1.27}$$

It describes the cross-correlation function of the radiation field taking into account spatial and temporal coherence effects and it plays a fundamental role in the theory of partial coherence. Finally, by exploiting the relation

$$I^{(\mathrm{i})}(Q) = |K_i|\,\Gamma_{\mathrm{ii}}(0) \tag{1.28}$$

for $i = (1,2)$, Eq. 1.26 takes the form

$$\begin{aligned} I(Q) &= I^{(1)}(Q) + I^{(2)}(Q) + \\ &+ 2\sqrt{I^{(1)}(Q)I^{(2)}(Q)}\left|\gamma_{12}\left(\frac{r_2-r_1}{c}\right)\right|\cos\left[2\pi\nu\left(\frac{r_2-r_1}{c}\right) + \alpha_{12}\left(\frac{r_2-r_1}{c}\right)\right], \end{aligned} \tag{1.29}$$

where $\alpha_{12}(\tau) = \mathrm{Arg}[\gamma_{12}(\tau)] - 2\pi\nu\tau$.

Equation 1.29 describes the interference of partially coherent light. Fringes are modulated in amplitude and phase by the complex degree of coherence of the radiation, which accounts for spatial coherence effects at the pinhole locations and temporal coherence effects related to the pathlength difference induced by the propagation fron the two apertures to the detection point Q.

When the coherence length of the radiation is much larger than the maximum pathlength difference encountered in the experimental setup, the radiation is said to be quasi-monochromatic and only spatial coherence effects are relevant. Under quasi-monochromatic conditions, the Mutual Coherence Function and the complex degree of coherence take the simplified forms [36, **?**]

$$\begin{aligned} \Gamma_{12}(\tau) &= J_{12}e^{-i2\pi\nu\tau} \\ \gamma_{12}(\tau) &= \mu_{12}e^{-i2\pi\nu\tau} \end{aligned} \tag{1.30}$$

where

$$J_{12} = \Gamma_{12}(0) = \langle u(P_1,t)u^*(P_2,t)\rangle \tag{1.31}$$

is called the Mutual Intensity of the radiation at points P_1 and P_2 and

$$\mu_{12} = \gamma_{12}(0) = \frac{J_{12}}{[I(P_1)I(P_2)]^{1/2}} \tag{1.32}$$

is known as the Complex Coherence Factor (CCF) of the radiation.

If the two pinholes are tiny enough in order to diffract light on a large angle, $I^{(1)}(Q) = I^{(1)}$ and $I^{(2)}(Q) = I^{(2)}$ are both constant over the region of interest on the detection plane. The interference pattern can then be expressed as

$$I(x,y) = I^{(1)} + I^{(2)} + 2\sqrt{I^{(1)}I^{(2)}}\,|\mu_{12}| \cos\left[\frac{2\pi}{\lambda z}\,(\Delta\xi \cdot x + \Delta\eta \cdot y) + \phi_{12}\right], \tag{1.33}$$

where $(\Delta\xi, \Delta\eta)$ denote the horizontal and vertical displacements of the two pinholes and $\phi_{12} = \mathrm{Arg}(\mu_{12}) - [2\pi/(\lambda z)](\Delta\xi \cdot x + \Delta\eta \cdot y)$.

Equation 1.33 describes interference fringes developing perpendicularly to the line joining P_1 and P_2. Their visibility is constant over the detected region and conveys the information on the modulus of the radiation CCF

$$V = \frac{2\sqrt{I^{(1)}I^{(2)}}}{I^{(1)} + I^{(2)}}\,|\mu_{12}| \tag{1.34}$$

while the information on the phase of the radiation CCF can be recovered by the position of the interference fringes. If $I^{(1)} = I^{(2)}$, the fringe visibility provides a direct measurement of $|\mu_{12}|$.

Similarly to the case of temporal coherence treated in Subsect.1.3.3, where we considered deviations from an ideal monochromatic field and the finite bandwidth of the radiation was taken into account, spatial coherence is a consequence of the finite extent of real light sources. A point-like source S_1 emits a perfect spherical wave and fully developed interference fringes are observed regardless on the separation between the two apertures. In fact, the phase relations over the spherical wavefront are fixed for any possible positions of the two pinholes, as it can be inferred from Eq. 1.1.

For a continuum of point-like sources spreading over a finite domain of linear extension D, the electric field across the plane of the two apertures is composed of many adjacent coherence patches (or coherence areas) within which the phase of the electric field is roughly constant, as depicted in Fig. 1.11. They are subjected to random changes in shape and position over temporal scales comparable to those of the emission processes. Fourier optics allows to decomposed the instantaneous electric field into the sum of many sinusoidal patterns generated by the interference between two tilted plane waves. The periodicity Λ of the sinusoidal modulation is related to the tilt angle θ by $\Lambda = \lambda/\theta$, while the absolute position of the pattern is determined by the phase difference between the two plane waves. The stochastic fluctuations of the coherence patches are thus interpreted in terms of the random fluctuations of the relative phase between the interfering plane waves, inducing random lateral shifts on the corresponding sinusoidal patterns. On average, the smallest region over which the phase of the field can be perfectly correlated is dictated by the angle $\theta_s = D/z_s$ subtended by the source at a distance z_s from the apertures plane. Radiation is thus regarded as spatially coherent over a length scale smaller than or comparable to

$$\Lambda = \frac{\lambda}{\theta_s} = \frac{\lambda z_s}{D}. \tag{1.35}$$

Equation 1.35 defines the linear extension of the coherence areas or the transverse coherence length of the radiation.

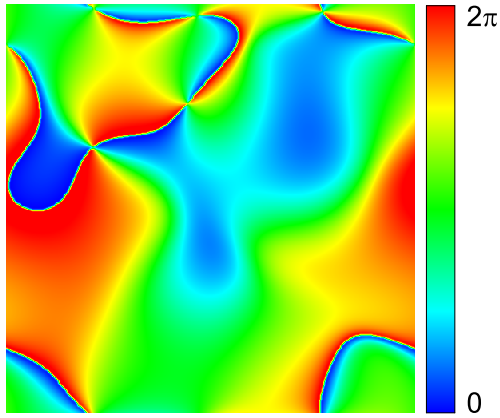

Figure 1.11: Instantaneous phase distribution of partially coherent radiation. It is composed of many adjacent patches within which the phase of the electric field is roughly constant. These coherence patches or coherence areas undergo random fluctuations over temporal scales comparable to those of the emission processes.

The dependence of the transverse coherence length of the radiation on the inverse of the angle subtended by the source suggests that the radiation CCF $\mu(\vec{x}_1, \vec{x}_2)$ and the source intensity distribution $I(\xi, \eta)$ form a Fourier couple. This relation is known in Statistical Optics as the Van Cittert-Zernike's theorem [36, **?**] and it constitutes the spatial analogue of the Wiener-Khinchine's theorem of Eq.1.21 in time domain:

$$\mu(x_1, x_2, y_1, y_2) = \frac{e^{-i\psi} \iint_{-\infty}^{+\infty} I(\xi, \eta) e^{i\frac{2\pi}{\lambda z}(\Delta x \cdot \xi + \Delta y \cdot \eta)} \, \mathrm{d}\xi \, \mathrm{d}\eta}{\iint_{-\infty}^{+\infty} I(\xi, \eta) \, \mathrm{d}\xi \, \mathrm{d}\eta}, \tag{1.36}$$

where $\psi = \pi(\rho_2^2 - \rho_1^2)/(\lambda z)$ being $\rho_1^2 = x_1^2 + y_1^2$ and $\rho_2^2 = x_2^2 + y_2^2$, $\Delta x = x_2 - x_1$ and $\Delta y = y_2 - y_1$.

An example of the experimental verification of the Van Cittert-Zernike's theorem is illustrated in Fig. 1.12 and Fig. 1.13. The radiation coming from a white Light Emitting Diode (LED) is filtered with a narrow band-pass filter by Thorlabs (average wavelength $\bar{\lambda} = 660$ nm, FWHM bandwidth $\Delta\lambda = 10$ nm) in order to increase the temporal coherence. A circular pinhole with diameter $D = 100$ μm determines the effective source size. The radiation is finally collimated by a converging lens with focal length $f = 7$ cm placed immediately upstream the Young's interferometer. According to the Van Cittert-Zernike's theorem expressed by Eq. 1.35, the transverse coherence length at the plane of the aperture is $\sigma_{\mathrm{coh}} = 1.22\lambda f/D \approx 500$ μm, where the multiplicative factor 1.22 comes from the circular shape of the source. A pair of rectangular slits is implemented in the Young's interferometer in place of the tiny pinholes to enhance the detected signal. The radiation CCF is probed at four points by increasing the slit separation, as shown in Fig. 1.12.

The measured values of the visibility have then been used to fit the expected radiation CCF according to the Van Cittert-Zernike's theorem stated in Eq. 1.36. The only free parameter was the radius of the pinhole used to limit the source size. The result of the

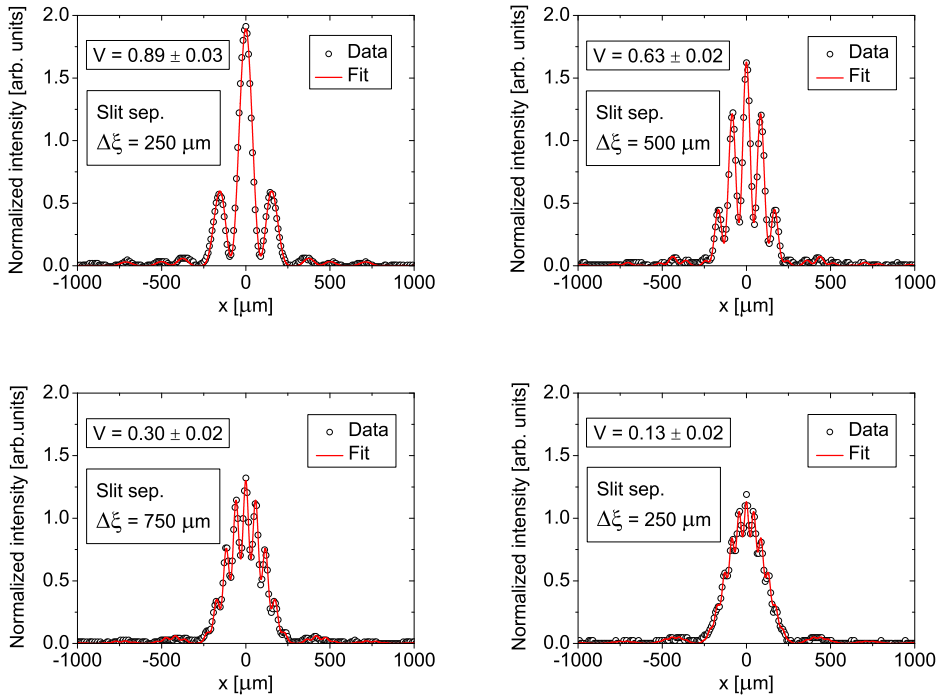

Figure 1.12: Horizontal profiles of the interferograms corresponding to four different pairs of rectangular slits with increasing separation: (a) 250 μm, (b) 500 μm, (c) 750 μm and (d) 1000 μm. The fringe visibility decreases as the slit separation is increased due to the limited transverse coherence of the incoming radiation. The modulation of the recorded interferograms is dictated by the diffraction patterns of the vertical slits.

fit is shown in Fig. 1.13. The fitted value $r_{\rm fit} = (50.7 \pm 1.6)\ \mu$m is in good agreement with the nominal one ($r_{\rm th} = 50.0\ \mu$m).

The radiation CCF in Eq. 1.36 generally depends on the absolute positions of the two pinholes through the phase factor $\exp(-i\psi)$. Nonetheless, its modulus is invariant upon lateral translations and it depends only on the pinhole separation. Similarly to the introduction of the coherence time, this allows to follow Mandel and define the coherence area as [36, **?**]

$$A_c = \int_{-\infty}^{+\infty} |\mu(\Delta x, \Delta y)|^2 \, \mathrm{d}\Delta x \, \mathrm{d}\Delta y. \tag{1.37}$$

Apart from inessential numerical constants depending on the particular shape of the source intensity profile, it can be proven to show the same dependences as in Eq. 1.35, obtained by means of Fourier Optics arguments. When the transverse coherence length of the radiation is comparable to the beam size, the field fluctuations are highly correlated and the beam is said to be spatially coherent. Conversely, incoherent radiation refers to the case in which the field fluctuations are completely random and uncorrelated from point to point.

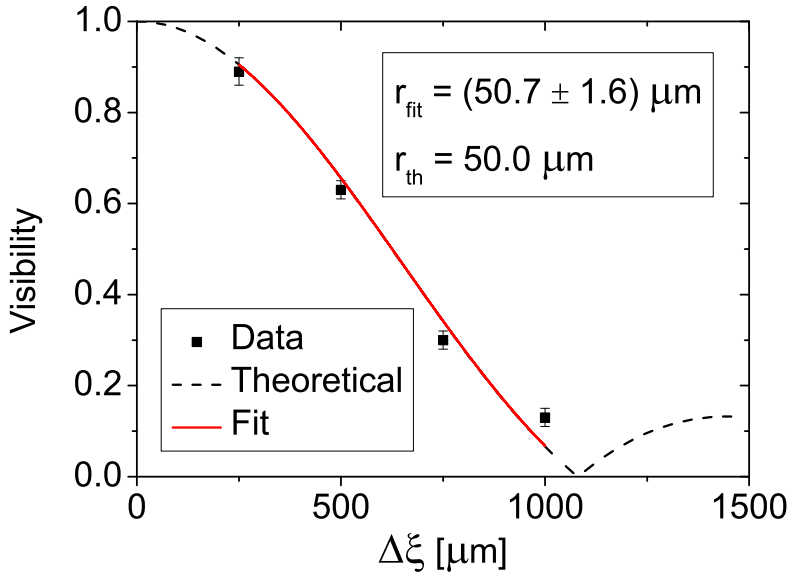

Figure 1.13: The visibilities of the interference fringes from Fig. 1.12 are used to fit the expected radiation CCF determined by the circular source, according to the Van Cittert-Zernike's theorem. The experimental value for the radius of the pinhole $r_{\mathrm{fit}} = (50.7 \pm 1.6)$ μm is in good agreement with the nominal value of $r_{\mathrm{th}} = 50.0$ μm. This proves how spatial coherence measurements can be exploited to retrieve the size of the radiation source.

In Tab. 1.1 we summarize the names and the definitions of the quantities introduced in this chapter and that are commonly used in characterizing coherence properties of the radiation.

Spatial and temporal coherence			
Mutual Coherence Function	MCF	$\Gamma_{12}(\tau)$	$\langle u(P_1,t)u^*(P_2,t-\tau)\rangle$
Complex Degree of Coherence	-	$\gamma_{12}(\tau)$	$\frac{\Gamma_{12}(\tau)}{[\Gamma_{11}(0)\Gamma_{22}(0)]^{1/2}}$
Temporal coherence			
Self Coherence Function	-	$\Gamma(\tau)$	$\langle u(t)u^*(t-\tau)\rangle$
Complex Degree of self Coherence	CDC	$\gamma(\tau)$	$\frac{\Gamma(\tau)}{\Gamma(0)}$
Spatial coherence			
Mutual Intensity	-	J_{12}	$\langle u(P_1,t)u^*(P_2,t)\rangle$
Complex Coherence Factor	CCF	μ_{12}	$\frac{J_{12}}{[I(P_1)I(P_2)]^{1/2}}$

Table 1.1: Names and mathematical definition of the functions used to characterize the coherence properties of the radiation. We also report some acronyms which will be used throughout the thesis.

CHAPTER 2

Synchrotron radiation from relativistic charges

2.1 Synchrotron Radiation: the classical electrodynamics approach

Synchrotron radiation (SR) is emitted by accelerated charged particles moving at relativistic velocities [38, 39]. It is endowed with peculiar features arising from the relativistic motion of the charge towards the observer:

- a strong beaming with respect to the direction of the instantaneous motion of the particle;
- a time compression of the radiation received by the observer: the particle and the emitted radiation travel with comparable velocities, hence the electric field generated over a relatively long period of time by the particle reaches the detection point within a much shorter period.

Due to the strong time compression, the spectrum of the SR short pulses is broad and it extends up to hundreds or thousands times the characteristic frequency of the particle motion.

As it will be seen, the angular width of the emission cone and the characteristic frequency of the emitted radiation can be described in term of the Lorentz factor

$$\gamma = \frac{1}{\sqrt{1-\beta^2}}, \tag{2.1}$$

where $\beta = v/c$ is the particle velocity v normalized to the speed of light. The Lorentz factor γ gives the ratio between the particle kinetic energy E and the particle rest energy:

$$E = \gamma m_0 c^2, \tag{2.2}$$

being m_0 the rest mass of the particle.

In this thesis we will restrict our attention to the radiation emitted by relativistic electrons (rest energy $m_0c^2 = 0.5$ GeV), for which the Lorentz factor assumes values much greater than one. This condition allows great simplifications in the development of the theory of SR by means of the ultrarelativistic approximation:

$$\gamma \gg 1 \qquad \beta \approx 1. \tag{2.3}$$

Finally, we would like to point out that the term Synchrotron Radiation is used in the currently adopted terminology to refer only to the radiation generated by a bending magnet, while throughout the rest of the thesis it also refers to emission processes by relativistic and ultrarelativistic charged particles in general. In this case, the reader should be able to extrapolate the proper meaning from the context.

2.1.1 The particle motion

The peculiar features of the electromagnetic fields emitted by an accelerated charge moving at relativistic or ultrarelativistic velocities have their basis in the finite propagation velocity c of light. Referring to Fig. 2.1, the radiation received by a stationary observer at P at time t was emitted by the particle at an earlier time t' when it was at position P'.

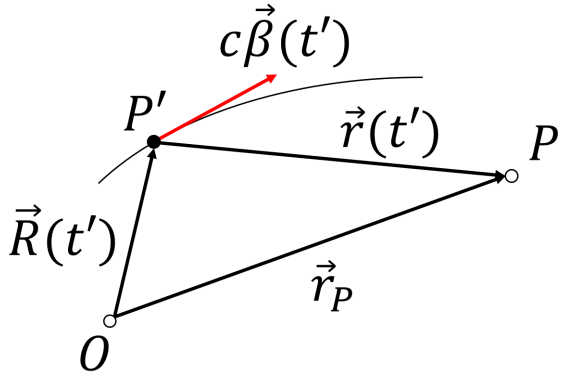

Figure 2.1: Geometry relating the detection time t to the emission time t'.

We indicate with $\vec{R}(t')$ the trajectory of the particle, with $\vec{r}_p$ the fixed position of observation and with $\vec{r}(t')$ the relative position of the observer with respect to the charge at the time t' when the radiation was emitted. The relation between the observation time t and the time t' at which the radiation was generated is given by

$$t = t' + \frac{r(t')}{c}, \tag{2.4}$$

where $r(t') = |\vec{r}(t')|$. Since

$$\vec{R}(t') + \vec{r}(t') = \vec{r}_p, \tag{2.5}$$

we obtain for the change of the vector $\vec{r}(t')$

$$\frac{\mathrm{d}\vec{r}(t')}{\mathrm{d}t'} = -\frac{\mathrm{d}\vec{R}(t')}{\mathrm{d}t'} = -c\vec{\beta}(t') \tag{2.6}$$

and for the corresponding change of its absolute value

$$r(t')\frac{\mathrm{d}r(t')}{\mathrm{d}t'} = \frac{1}{2}\frac{\mathrm{d}\left(\vec{r}(t')\cdot\vec{r}(t')\right)}{\mathrm{d}t'} = \vec{r}(t')\cdot\frac{\mathrm{d}\vec{r}(t')}{\mathrm{d}t'} = -\vec{r}(t')\cdot\vec{\beta}(t')c. \tag{2.7}$$

Introducing the unit vector $\hat{n}(t')$ pointing from the charge to the observer at the time t' of emission

$$\hat{n}(t') = \frac{\vec{r}(t')}{r(t')}, \tag{2.8}$$

we obtain the differentail relation between t and t' corresponding Eq. 2.4:

$$\mathrm{d}t = \left(1 + \frac{1}{c}\frac{\mathrm{d}r(t')}{\mathrm{d}t'}\right)\mathrm{d}t' = \left(1 - \hat{n}(t')\cdot\vec{\beta}(t')\right)\mathrm{d}t'. \tag{2.9}$$

2.1.2 The Liènard-Wiechert fields

Owing to the finite propagation velocity of light, the solutions of the Maxwell's equations for the electromagnetic fields $\vec{E}(\vec{r}_p, t)$ and $\vec{B}(\vec{r}_p, t)$ are determined by the characteristics of the charge motion at an earlier time t', with the retardation effect given by Eq. 2.4. Defining $\vec{\beta}(t')$ and $\dot{\vec{\beta}}$ as the instantaneous velocity and acceleration of the particle, respectively, the expressions for the retarded fields of a moving charge, or the Liènard-Wiechert fields, take the form [38, 39]

$$\begin{aligned}\vec{E}(\vec{r}_p, t) &= \frac{e}{4\pi\epsilon_0}\left\{\frac{(1-\beta^2)(\hat{n}-\vec{\beta})}{r^2(1-\hat{n}\cdot\vec{\beta})^3} + \frac{\hat{n}\times[(\hat{n}-\vec{\beta})\times\dot{\vec{\beta}}]}{cr(1-\hat{n}\cdot\vec{\beta})^3}\right\}_{\text{ret}} \\ \vec{B}(\vec{r}_p, t) &= \frac{\hat{n}_{\text{ret}}\times\vec{E}}{c},\end{aligned} \tag{2.10}$$

where the subscript ret indicates that the expressions between curly brackets have to be evaluated at the earlier time t'.

The electric and magnetic fields are composed of two terms showing a different dependence on the distance r between the source and the point of observation:

- the first term decreasing as r^{-2} does not depend on the charge acceleration but only on its velocity and position. It is therefore called the velocity field or the near field;
- the second term decreasing as r^{-1} is proportional to the particle acceleration and it is thus called the acceleration field or the radiation field.

The acceleration field is the only component of the Liènard-Wiechert fields which implies an energy transfer from the charge to the outside. In fact, the energy flow per unit of time is quantified by the Poynting vector $\vec{S}$

$$\vec{S}(\vec{r}_p, t) = \frac{\vec{E}(\vec{r}_p, t)\times\vec{B}(\vec{r}_p, t)}{\mu_0} = \frac{1}{c\mu_0}\left[\left|\vec{E}(\vec{r}_p, t)\right|^2 \hat{n}_{\text{ret}} - \left(\hat{n}_{\text{ret}}\cdot\vec{E}(\vec{r}_p, t)\right)\vec{E}(\vec{r}_p, t)\right], \tag{2.11}$$

whose modulus is proportional to $|\vec{E}(\vec{r}_p, t)|^2$. It has three main contribution with a different dependence on the distance r between the source and the observer: the term from the square of the velocity field decreases with distance as r^{-4}, the term from the square of the acceleration field decreases as r^{-2} and term from the cross products decreases as r^{-3}. The total power radiated by the charge is obtained by integrating Eq. 2.11 through a sphere of radius r around the source. Only the term from the acceleration field gives a non-vanishing contribution at large distances, thus implying an actual energy transfer to the outside. This explains why the acceleration field is also called the radiation field: only this term of the Liènard-Wiechert fields corresponds to energy being radiated at large distances. We also notice that the result of the integral is independent on the distance r, similarly to the case of the radiant field treated in Chap. 1.

2.1.3 The electric field in the frequency domain

The relation between the observation time t and the emission time t' may be very complicated for a general charge motion. It is sometimes more convenient to compute directly

the fields in the frequency domain:

$$\vec{\tilde{E}}(\vec{r}_p,\omega) = \frac{1}{\sqrt{2\pi}} \int_{-\infty}^{+\infty} \vec{E}(\vec{r}_p,t) e^{-i\omega t}\,\mathrm{d}t. \tag{2.12}$$

The integration involves the observation time as we are interested in the spectrum of the radiation as seen by the observer. From the discussion of the previous Subsect. 2.1.2, we are allowed to retain only the contribution from the radiation field:

$$\vec{\tilde{E}}(\vec{r},\omega) = \frac{e}{4\pi\epsilon_0 c}\frac{1}{\sqrt{2\pi}} \int_{-\infty}^{+\infty} \left\{ \frac{\hat{n}\times[(\hat{n}-\vec{\beta})\times\dot{\vec{\beta}}]}{r(1-\hat{n}\cdot\vec{\beta})^3} \right\}_{\mathrm{ret}} e^{-i\omega t}\,\mathrm{d}t. \tag{2.13}$$

A formal change of integration variable from t to t' leads to

$$\vec{\tilde{E}}(\vec{r}_p,\omega) = \frac{e}{4\pi\epsilon_0 c}\frac{1}{\sqrt{2\pi}} \int_{-\infty}^{+\infty} \frac{\hat{n}\times(\hat{n}-\vec{\beta})\times\dot{\vec{\beta}}}{r(1-\hat{n}\cdot\vec{\beta})^2}\, e^{-i\omega\left(t'+\frac{r(t')}{c}\right)}\,\mathrm{d}t', \tag{2.14}$$

where the subscript ret has been omitted since the integration variable is now t'. Notice the presence at the denominator of the factor $(1-\hat{n}\cdot\vec{\beta})^2$ instead of $(1-\hat{n}\cdot\vec{\beta})^3$: this is a consequence of the differential relation of Eq. 2.9 between the two time scales t and t'.

As long as the radiation is observed from large distances, we may consider $\vec{r}$ and $\hat{n}$ in the large fraction inside the integral in Eq. 2.14 as constants. Integrating by parts and neglecting the edge terms (the times $t' = \pm\infty$ have no influence on the radiation observed at time t), we obtain the following expression for the electric field in the frequency domain [38, 39]

$$\vec{\tilde{E}}(\vec{r_p},\omega) = \frac{i\omega e}{4\pi\sqrt{2\pi}\epsilon_0 c r_p} \int_{-\infty}^{+\infty} [\hat{n}\times(\hat{n}\times\vec{\beta})]\, e^{-i\omega\left(t'+\frac{r(t')}{c}\right)}\,\mathrm{d}t'. \tag{2.15}$$

2.2 Synchrotron Radiation

2.2.1 The opening angle

Let F be the reference frame of a fixed observer and let e be a charged particle moving along a curved trajectory inside a bending magnet. The trajectory is characterized by the radius of curvature ρ and the constant magnetic field is assumed to point outward from the plane of the page, as depicted in Fig. 2.2(a). The modulus of the particle velocity is constant and it is equal to βc. The reference frame F is chosen with its origin O corresponding to the half point of the particle trajectory, with the z-axis pointing along the line tangent to the orbit at the origin O and with the x-axis lying on the orbit plane along the radial direction at O. Without loss of generality, we will focus on the properties of the radiation emitted as the particle passes through the origin.

Referring to Fig. 2.2(a) and calling $\vec{v} = \beta c\hat{e}_z$ the instantaneous velocity of the partice at the origin O, we can introduce a reference frame F' moving with constant velocity $\vec{v}$, having the x'-, y'- and z'-axes parallel to those of the fixed reference frame F and such that its origin O' corresponds to the origin O of F at a certain instant of time t_0. Since the velocity of the moving frame F' is always greater than the z-component of the particle velocity, F' lags behind the particle for $t < t_0$, while the reverse happens for $t > t_0$. Moreover, by construction, the x'-coordinate of the particle in the moving frame F' is always negative, increasing for $t < t_0$ and decreasing for $t > t_0$. The situation is depicted

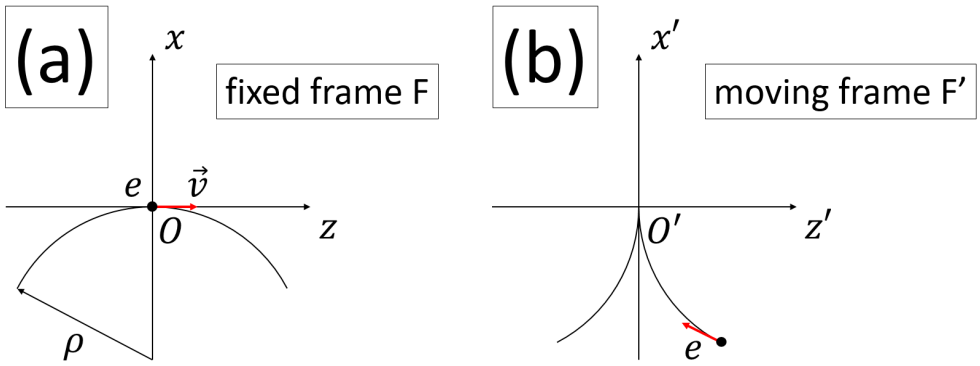

Figure 2.2: Geometric approach to the relativistic beaming effect. (a) A relativistic particle moving inside a bending magnet in the fixed laboratory frame. Radiation is beamed in the forward direction. (b) Particle motion in a co-moving frame. The trajectory resambles a cycloid and the particle emits isotropically. The beaming effect is a consequence of the Lorentz transformation back to the laboratory frame.

in Fig. 2.2(b), where it is shown how the trajectory of the charge in the moving frame F' thus resembles a portion of a cycloid with a cusp in the origin. When the particle is in O', it is momentarily at rest but it suffers an acceleration towards the negative x'-direction. This acceleration causes the charge to emit radiation with a dipole-like intensity pattern.

Going back to the reference frame F with a Lorentz transformation, the emitted radiation becomes beamed in the forward direction. In fact, a photon emitted along the x'-axis in the moving frame F' ($\theta' = \pi/2$) appears in the reference frame F of the stationary observer at an angle θ with respect to the z-direction given by [38]

$$\tan\theta = \frac{\sin\theta'}{\gamma\,(\cos\theta' + \beta)} \approx \frac{1}{\gamma} \qquad\qquad \theta \approx \frac{1}{\gamma}. \tag{2.16}$$

The typical opening angle of the emitted SR is thus of the order of $1/\gamma$ and the radiation is confined within a narrow cone in the forward direction (with respect to the instantaneous particle velocity), as shown in Fig. 2.3

2.2.2 The spectrum in a long magnet

Owing to the small opening angle $\theta \approx 1/\gamma$, an observer at a point P along the $z-$direction receives the radiation as a short pulse generated only from a small portion of the particle trajectory. Referring to Fig. 2.4, the portion of the trajectory from A to A'contributing to the field at P is determined by the condition that the instantaneous particle velocity is deflected by a maximum angle $\pm 1/\gamma$ with respect to the $z-$axis.

The particle takes approximately

$$t_e = \frac{2\rho}{\gamma\beta c} \tag{2.17}$$

to go from A to A'. The radiation emitted by the charge at A' is thus delayed with respect

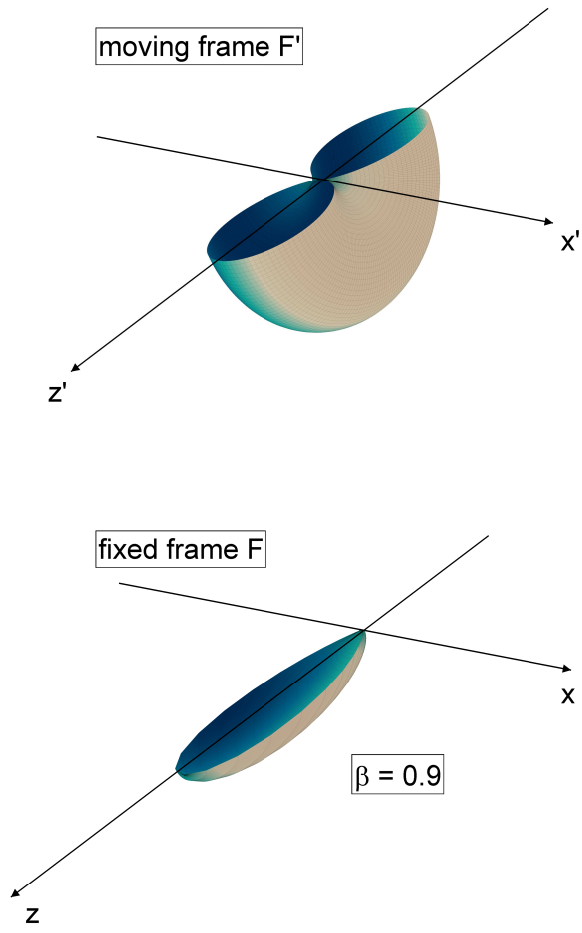

Figure 2.3: Radiation pattern from a relativistic charged particle accelerated perpendicularly to the instantaneous velocity. (a) In the reference frame K' of the particle, the angular distribution of the emitted radiation resembles that from an oscillating dipole. (b) Moving back to the reference frame of the stationary observer, a beaming effect in the forward direction is observed: the rear lobe of the dipole-like intensity pattern vanishes and the emitted radiation is confined within a narrow cone of aperture $1/\gamma$. The case $\beta = 0.9$ is reported. Drawings are not on scale for mere illustrative purposes.

to the field radiated at A by the amount

$$\Delta t = \frac{2\rho}{\gamma\beta c} - \frac{2\rho \sin\left(\frac{1}{\gamma}\right)}{c}. \tag{2.18}$$

In the ultrarelativistic approximation this delay gives the following expression for the

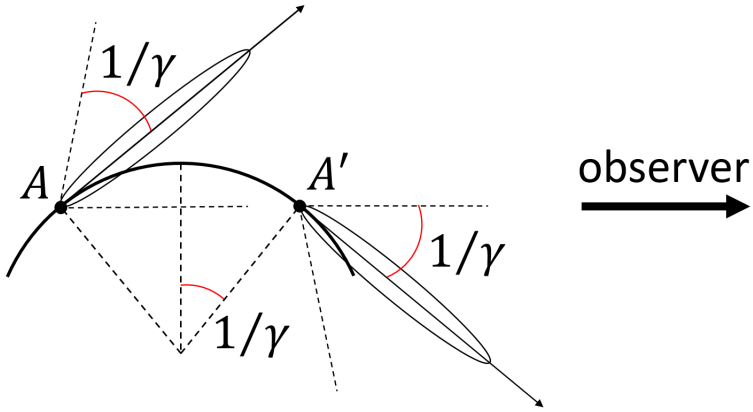

Figure 2.4: The ralativistic beaming affects the detected spectrum. An observer receives the radiation from a small portion of the particle orbit. Furthermore, due to the relativistic velocities, the electric field has a pulsed structure corresponding to a broad spectrum.

temporal duration of the radiation pulse:

$$\Delta t \approx \frac{2\rho}{\gamma\beta c} - \frac{2\rho}{c}\left(\frac{1}{\gamma} - \frac{1}{6\gamma^3}\right) = \frac{2\rho}{\gamma\beta c}\left(1 - \beta + \frac{\beta}{6\gamma^2}\right) = \frac{4}{3}\frac{\rho}{c}\frac{1}{\gamma^3}, \tag{2.19}$$

where in the last equality we have used the ultrarelativistic relation

$$1 - \beta = \frac{1-\beta^2}{1+\beta} \approx \frac{1}{2\gamma^2}. \tag{2.20}$$

From the radiation pulse duration Δt we obtain the typical frequency ω_{typ} of the spectrum by exploiting the relation between variables forming a Fourier couple:

$$\omega_{\mathrm{typ}} = \frac{1}{\Delta t} = \frac{3}{4}\frac{c}{\rho}\gamma^3, \tag{2.21}$$

where we recognize c/ρ as the fundamental cyclotron frequency $\omega_{\mathrm{cycl}} = \beta c/\rho$ in the ultrarelativistic case $\beta \approx 1$.

It is thus seen that for ultrarelativistic particles the radiation pulse becomes very short due to the small differences in travel times between the charge and the radiation. Furthermore, the emitted spectrum is broad, with frequences up to γ^3 times the fundamental frequency.

2.2.3 The angular-spectral power distribution

We choose a reference frame as depicted in Fig. 2.5, with the particle passing through the origin O at the time $t' = 0$. The described configuration evidences a cylindrical symmetry with respect to the axis passing through the center of the particle trajectory and perpendicular to the orbit plane. It is sufficient to compute the radiation received by an observer located on a plane tangent to the charge orbit at the origin. In fact, any observer P' on a vertical plane tangent to the particle orbit at a different point will receive the same electric field as the observer at P, apart from a finite temporal delay.

We refer the interested reader to standard textbooks dealing with Synchrotron Radiation in a classical electrodynamics framework for a detailed derivation of the properties

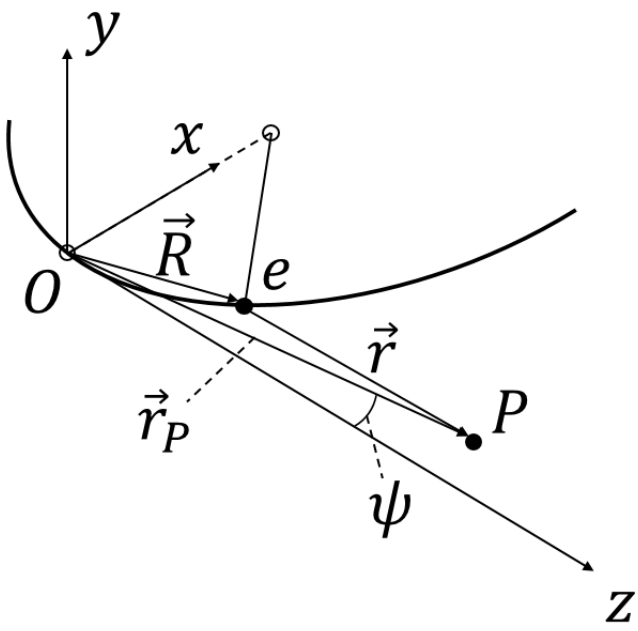

Figure 2.5: The ralativistic beaming affects the detected spectrum. An observer receives the radiation from a small portion of the particle orbit. Furthermore, due to the relativistic velocities, the electric field has a pulsed structure corresponding to a broad spectrum.

of SR (e.g. [38]). Here we just mention and exploit the general condition $\rho/(r_p\gamma) \ll 1$, which is fulfilled in most practical cases for ultrarelativistic particles, in order to reduce the expression of the radiation field in the frequency domain given by Eq.2.15 to

$$\tilde{E}_x(\vec{r}_p,\omega) = \frac{-\sqrt{3}e\gamma}{(2\pi)^{3/2}\epsilon_0 c r_p}\left(\frac{|\omega|}{2\omega_c}\right)(1+\gamma^2\psi^2)K_{2/3}\left\{\frac{\omega}{2\omega_c}(1+\gamma^2\psi^2)^{3/2}\right\}$$
$$\tilde{E}_y(\vec{r}_p,\omega) = \frac{i\sqrt{3}e\gamma}{(2\pi)^{3/2}\epsilon_0 c r_p}\left(\frac{\omega}{2\omega_c}\right)\gamma\psi\sqrt{1+\gamma^2\psi^2}K_{1/3}\left\{\frac{\omega}{2\omega_c}(1+\gamma^2\psi^2)^{3/2}\right\}, \qquad (2.22)$$

where we have introduced the critical frequency $\omega_c = 3c\gamma^2/2$ and $K_{2/3}$ and $K_{1/3}$ are the modified Bessel functions of order 2/3 and 1/3.

Equation 2.22 describes the two modes of linear polarization with the electric field parallel and perpendicular to the plane of the orbit. They are called the σ-mode and the π-mode, respectively. From the properties of the modified Bessel function, the electric field generated by the ultrarelativistic charge becomes negligible for $\xi \gg 1$, being $\xi = (\omega/(2\omega_c)) \cdot (1+\gamma^2\psi^2)^{3/2}$ the argument of the Bessel functions. This implies that at large angles only long wavelengths are radiated. Furthermore, if the frequency is too high, ξ is large at any angle and negligible radiation is generated at very short wavelengths. The cutoff frequency beyond which the radiated electric field becomes negligible for any value of the angle ψ may be identified by imposing $\xi = 0.5$ at $\psi = 0$, in which case it turns equal to the critical frequency ω_c.

We can now express the angular spectral power distribution radiated by the charged particle as the sum of the contributions from each of the two modes:

$$\frac{\mathrm{d}^2 P_\sigma}{\mathrm{d}\Omega\,\mathrm{d}\omega} = \frac{P_s\gamma}{\omega_c}\left(\frac{3}{2\pi}\right)^3\left(\frac{\omega}{2\omega_c}\right)^2(1+\gamma^2\psi^2)^2 K_{2/3}^2\left\{\frac{\omega}{2\omega_c}(1+\gamma^2\psi^2)^{3/2}\right\}$$
$$\frac{\mathrm{d}^2 P_\sigma}{\mathrm{d}\Omega\,\mathrm{d}\omega} = \frac{P_s\gamma}{\omega_c}\left(\frac{3}{2\pi}\right)^3\left(\frac{\omega}{2\omega_c}\right)^2\gamma^2\psi^2(1+\gamma^2\psi^2) K_{1/3}^2\left\{\frac{\omega}{2\omega_c}(1+\gamma^2\psi^2)^{3/2}\right\}, \qquad (2.23)$$

where P_s collects multiplicative factors together. It can be shown to represent the total power radiated by the relativistic charge. The two distribution are shown in Fig. 2.6. They are both symmetric with respect to the vertical angle ψ, being narrow at high frequencies and wide at low frequencies.

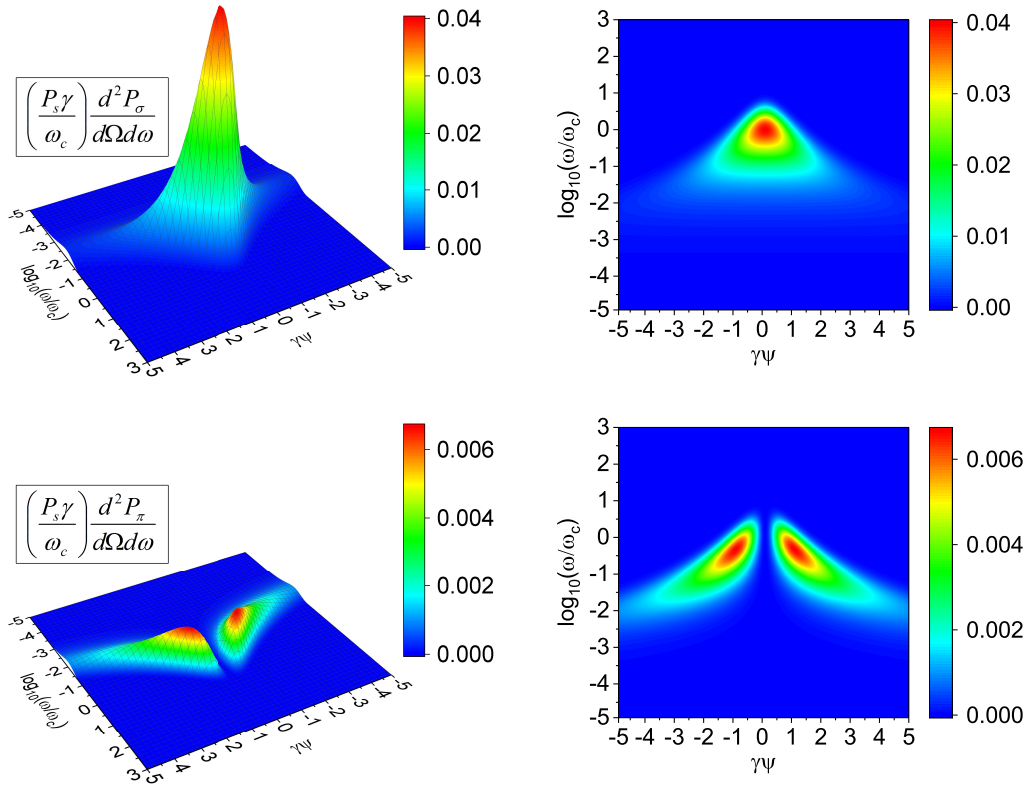

Figure 2.6: Angular-spectral power distribution for the π-mode and σ-mode of single-particle Synchrotron Radiation.

The σ-mode is large in the median plane while the π-mode is not radiated in the median plane.This is evident from the expression of the angular power distribution, obtained by integrating Eq. 2.23 over frequencies:

$$\frac{\mathrm{d}P_\sigma}{\mathrm{d}\Omega} = \int\frac{\mathrm{d}^2 P_\sigma}{\mathrm{d}\Omega\,\mathrm{d}\omega}\,\mathrm{d}\omega = \frac{P_s\gamma}{2\pi}\frac{21}{32}\frac{1}{(1+\gamma^2\psi^2)^{5/2}}$$
$$\frac{\mathrm{d}P_\pi}{\mathrm{d}\Omega} = \int\frac{\mathrm{d}^2 P_\pi}{\mathrm{d}\Omega\,\mathrm{d}\omega}\,\mathrm{d}\omega = \frac{P_s\gamma}{2\pi}\frac{15}{32}\frac{\gamma^2\psi^2}{(1+\gamma^2\psi^2)^{7/2}}. \qquad (2.24)$$

The angular power distribution of the σ-mode and of the π-mode are shown in Fig. 2.7, together with the total one.

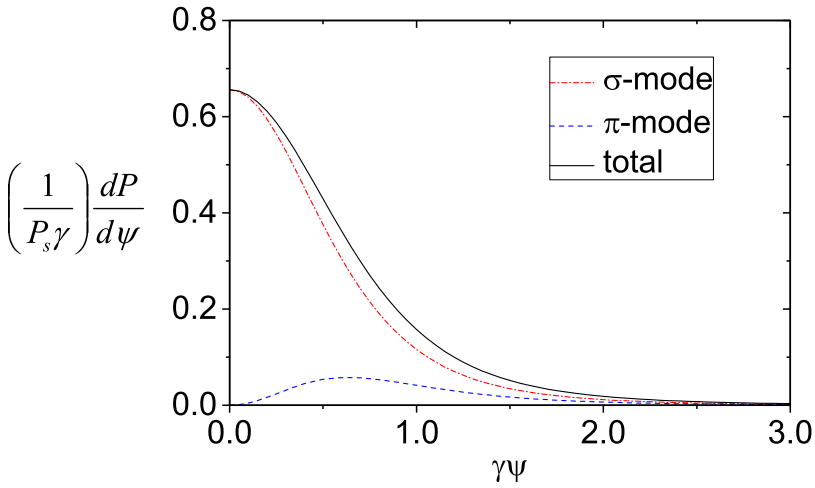

Figure 2.7: Angular power distribution for the π-mode and σ-mode of single-particle Synchrotron Radiation.

Integration of the angular spectral power distribution over the solid angle gives the spectral power distribution of the emitted SR:

$$\frac{\mathrm{d}P}{\mathrm{d}\omega} = \int \frac{\mathrm{d}^2P}{\mathrm{d}\Omega\,\mathrm{d}\omega}\,\mathrm{d}\Omega = \frac{P_s}{\omega_c} S_s\left(\frac{\omega}{\omega_c}\right) = \frac{P_s}{\omega_c}\left[S_{s\sigma}\left(\frac{\omega}{\omega_c}\right) + S_{s\pi}\left(\frac{\omega}{\omega_c}\right)\right], \tag{2.25}$$

where the universal functions $S_{s\sigma}$, $S_{s\pi}$, characterizing the properties of synchrotron radiation, are given by

$$\begin{aligned} S_{s\sigma}\left(\frac{\omega}{\omega_c}\right) &= \frac{9\sqrt{3}}{16\pi}\frac{\omega}{\omega_c}\left\{\int_{\omega/\omega_c}^{+\infty} K_{5/3}(z')\,\mathrm{d}z' + K_{2/3}\left(\frac{\omega}{\omega_c}\right)\right\} \\ S_{s\pi}\left(\frac{\omega}{\omega_c}\right) &= \frac{9\sqrt{3}}{16\pi}\frac{\omega}{\omega_c}\left\{\int_{\omega/\omega_c}^{+\infty} K_{5/3}(z')\,\mathrm{d}z' - K_{2/3}\left(\frac{\omega}{\omega_c}\right)\right\} \end{aligned} \tag{2.26}$$

and clearly

$$S_s\left(\frac{\omega}{\omega_c}\right) = \frac{9\sqrt{3}}{8\pi}\frac{\omega}{\omega_c}\int_{\omega/\omega_c}^{+\infty} K_{5/3}(z')\,\mathrm{d}z'. \tag{2.27}$$

They are shown in Fig. 2.8 on a double logarithmic scale and in Fig. 2.9 on a double linear scale.

The maxima of the universal functions occur below the critical frequency and the radiated spectrum is smooth and broad. Integration over all frequencies shows that the emitted SR is highly polarized, the total contribution from the σ-mode being seven times higher than that of the π-mode. Finally, integration up to the critical frequency gives half the total value. The critical frequency thus divides the spectrum into two parts having the same total power content.

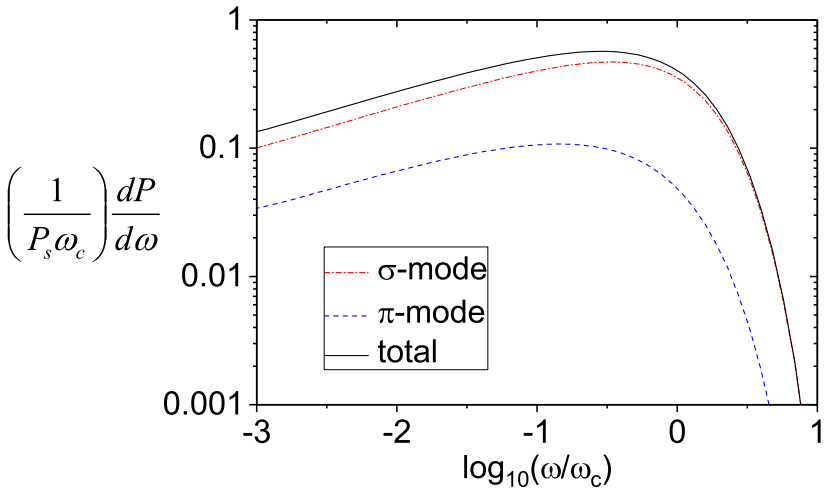

Figure 2.8: Spectral power distribution for the π-mode and σ-mode of single-particle Synchrotron Radiation on a double logarithmic scale.

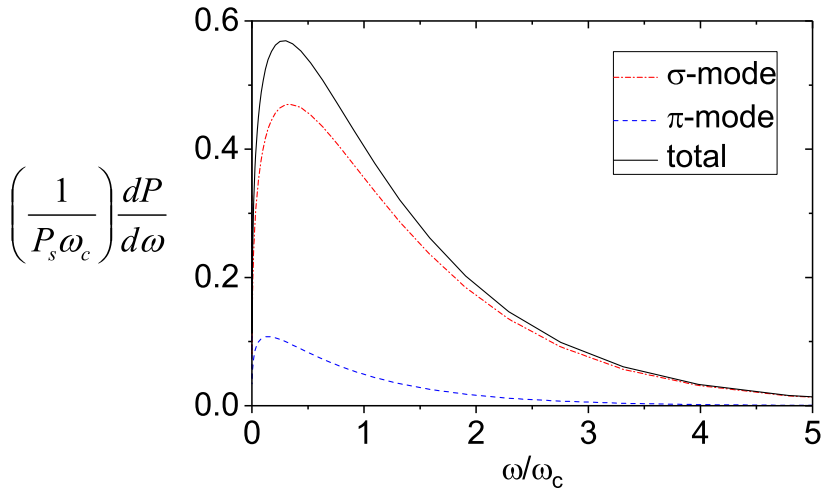

Figure 2.9: Spectral power distribution for the π-mode and σ-mode of single-particle Synchrotron Radiation on a double linear scale. They are obtained by integrating the angular-spectral power density shown in Fig. 2.6 over angles.

2.3 Undulator Radiation

2.3.1 Weak undulators and strong undulators

An undulator is a spatially periodic magnetic structure designed to produce high-brilliance quasi-monochromatic radiation from relativistic charged particles [38, 39]. A series of

N_w magnetic dipoles with alternating polarity generates a magnetic field of the form

$$\vec{B}(z) = B_0 \cos\left(\frac{2\pi}{\lambda_w} z\right) \hat{\epsilon}_y = B_0 \cos(k_w z)\, \hat{\epsilon}_y, \tag{2.28}$$

where λ_w is the period of the magnetic structure, also known as the wiggler wavelength, and N_w is the number of wigglers.

The magnetic field of Eq. 2.28 causes the electrons entering the magnetic structure to wiggle horizontally around the ideal rectilinear trajectory along the z-direction. At the exit of the undulator, the position and momentum of the particles are not significantly modified with respect to the entrance. For this reason, undulators are also called insertion devices.

The trajectory of an ultrarelativistic electron is characterized by the (maximum) deflection angle ψ_0 with respect to the z-axis. The properties of the Undulator Radiation (UR) strongly depend on the magnitude of the deflection angle with respect to the natural opening angle of the order of $1/\gamma$ of the emitted radiation. Their ratio defines a fundamental quantity known as the undulator parameter or the deflection parameter K:

$$K = \gamma \psi_0. \tag{2.29}$$

The two conditions $K < 1$ and $K > 1$ correspond to the so-called weak undulators and strong undulators, respectively [38]

- if $K < 1$, the observer sees a smoothly modulated field with a simple pattern and with quasi-monochromatic properties. This configuration identifies weak undulators;
- if $K > 1$, the observer sees a strongly modulated field composed of a train of short pulses, thus containing many harmonics. This configuration identifies strong undulators.

We will consider only the radiation from a strong undulator, for which the average drift velocity of the particle in the z-direction $\beta^* c$ is less than the instantaneous particle velocity βc due to the large deflection angle ψ_0. The non-uniform drift velocity has important consequences on the kinematics of an electron in an undulator and on the detailed angular and spectral distribution of the emitted radiation. We temporarily neglect the difference with respect to the instantaneous particle velocity βc without loss of generality in order to obtain the main features of UR by means of simple interference arguments.

2.3.2 The fundamental frequency and its harmonics

The fundamental frequency is obtained from the condition of constructive interference between the radiation emitted at successive periods [38, 39]. The charge takes the time $t_e = \lambda_w/(\beta c)$ to move forward by one period. During the same time interval, the wavefront of the radiation emitted at the earlier period has advanced by λ_w/β. An observer along the z-direction ($\theta = 0$) receives a periodic field of wavelength

$$\lambda = \lambda_w \left(\frac{1}{\beta} - 1\right) = \lambda_w \left(\frac{1-\beta}{\beta}\right) = \lambda_w \left[\frac{1-\beta^2}{\beta(1+\beta)}\right] \approx \frac{\lambda_w}{2\gamma^2}. \tag{2.30}$$

It can be seen that radiation with short wavelength in the UV and X-ray range can be obtained with wigglers with a period of the order of 10^{-2}-10^{-3} m.

The resonant frequency given by Eq. 2.30 can be generalized for the case of an observer located off-axis at an angle $\theta \neq 0$. While the wavefront emitted at the earlier period still advances by λ_w/β, the projection of the electron orbit along the θ-direction induces a further delay $\lambda_w \cos\theta$ on the wavefront emitted one period downstream. The wavelength of the radiation is then given by

$$\lambda = \frac{\lambda_w}{\beta}\left(1 - \beta\cos\theta\right) \approx \frac{\lambda_w}{\beta}\left(1 - \beta + \frac{\beta\theta^2}{2}\right) \approx \lambda_w\left(\frac{1}{2\gamma^2} + \frac{\theta^2}{2}\right) = \frac{\lambda_w}{2\gamma^2}(1 + \gamma^2\theta^2). \quad (2.31)$$

While the radiation wavelength changes with the observation position according to Eq. 2.31, at a fixed angle an ideally infinite undulator would generate a spectrum with sharp monochromatic lines at harmonics of the fundamental frequency given by the same Eq. 2.31. The effect of a finite number N_w of undulator periods is to broaden the frequency distribution at the fixed angle θ for each harmonic, with a frequency spread becoming narrower as the number of periods increases. For each harmonic number n, this can be seen by comparing the condition for constructive interference at the angle θ over N_w periods

$$N_w n\lambda = \frac{N_w\lambda_w}{\beta} - N_w\lambda_w\cos\theta \quad (2.32)$$

with the condition for destructive interference

$$N_w n\lambda' + \lambda' = \frac{N_w\lambda_w}{\beta} - N_w\lambda_w\cos\theta. \quad (2.33)$$

These two interference conditions give a relative bandwidth of the emitted radiation of the form

$$\frac{\Delta\lambda}{\lambda} = \frac{\lambda - \lambda'}{\lambda} = \frac{1}{1 + Nn} \approx \frac{1}{Nn}. \quad (2.34)$$

Typically, $N \sim 100$ hence the relative bandwidth is of the order of 1% for the first harmonic and even lower for higher harmonic numbers.

2.3.3 The central cone

Similar arguments allow to obtain the angular spread over which a particular wavelength is radiated. The condition for constructive interference is still given by

$$N_w n\lambda = \frac{N_w\lambda_w}{\beta} - N_w\lambda_w\cos\theta. \quad (2.35)$$

Since we are interested in the angular spread of a fixed harmonic, it has to be compared with the condition for destructive interference given by

$$N_w n\lambda + \lambda = \frac{N_w\lambda_w}{\beta} - N_w\lambda_w\cos\theta', \quad (2.36)$$

yielding under the small angle approximation to

$$\theta'^2 - \theta^2 = \frac{2\lambda}{N_w\lambda_w}. \quad (2.37)$$

For the radiation emitted on-axis ($\theta = 0$), the angle beyond which the intensity falls to zero is given by

$$\theta' = \frac{1}{\gamma\sqrt{N_w n}}. \tag{2.38}$$

For the first harmonic, Eq. 2.38 gives the angular width of the so-called central cone. It is modified as follows in order to take into account the average drift velocity of the particle $\beta^* c < \beta c$:

$$\theta' = \frac{1}{\gamma^*\sqrt{N_w n}}, \tag{2.39}$$

where $\gamma^* = 1/\sqrt{1-(\beta^*)^2}$.

2.3.4 Even and odd harmonics

A deeper insight into the angular and spectral distribution of the emitted UR can be obtained by considering a frame moving with the average drift velocity of the particle $\beta^* c$. In such reference frame, the period of the undulator moving towards the particle is Lorentz-contracted to $\lambda_w^* = \lambda_w/\gamma$. Since $\beta^* < \beta$, the particle follows a periodic figure-eight trajectory. It can be decomposed into an oscillation along the x'-axis occurring at odd harmonics of $\omega_w\gamma$ (here $\omega_w = 2\pi c/\lambda_w$) and an oscillation along the z'-axis at even harmonics of $\omega_w\gamma$. Both components of the charge trajectory are responsible for the emission of dipole radiation, though with a different angular orientation as depicted in Fig. 2.10(a) and in Fig. 2.10(c), respectively. In the laboratory frame, this results in the characteristic radiation beaming in the forward direction, with odd harmonics emitted on axis and even harmonics distributed in rings around them, as in Fig. 2.10(b) and in Fig. 2.10(d), respectively. The fundamental frequency of emission in the moving frame $\omega_w\gamma$ is Doppler-shifted by γ upon transformation back into the laboratory frame, resulting in the emitted resonant frequency $\omega_0 = \omega_w\gamma^2$. The overall spectrum containes many wavelengths, but at a fixed angle it consists of sharp lines at frequencies $n\omega_0$ multiple of the fundamental. In the forward direction, only odd harmonics are radiated.

2.3.5 The angular-spectral power distribution

In the case of strong undulators, the particle velocity along the z-direction consists of a constant drift at the average velocity

$$\langle \dot{z} \rangle = \beta c \left(1 - \frac{K^2}{4\beta^2\gamma^2}\right) = \beta^* c \tag{2.40}$$

superimposed to an oscillatory modulation with frequency $2\Omega_w = 2k_w\beta^* c$.

We restrict our attention to the far field, assuming that the radiation is observed from a distance r_p much larger than the undulator length $L_w = N_w\lambda_w$. Restricting our attention to the generic h-th harmonic and introducing $\Delta\omega_k = \omega - k\omega_1$, the angular spectral power distribution of the k-th harmonic is given by [38, 39]

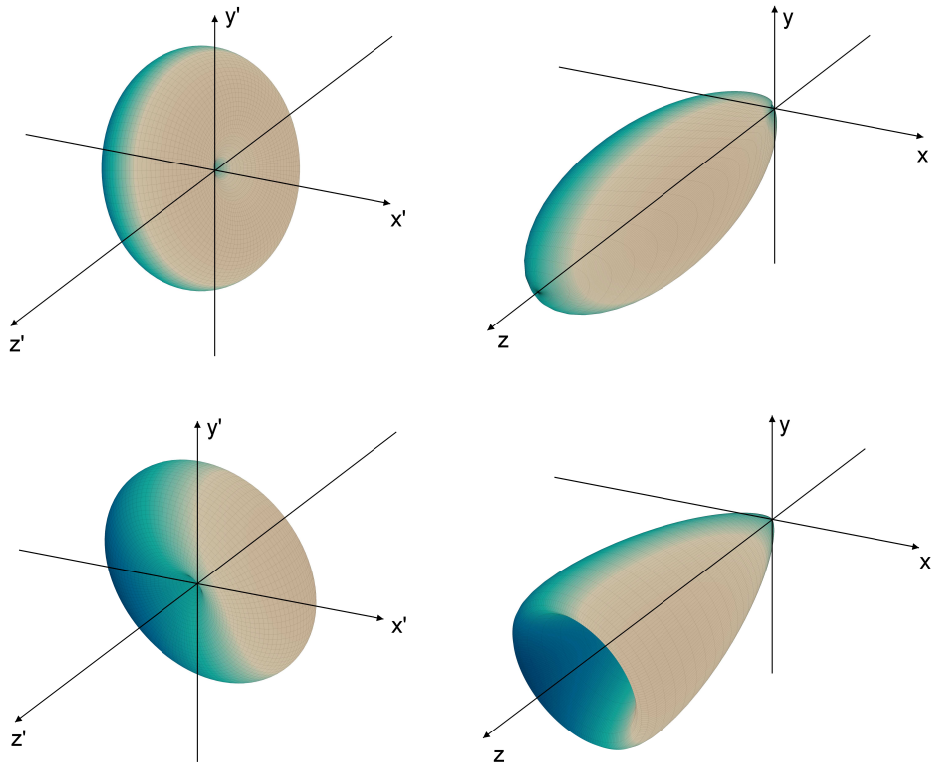

Figure 2.10: Undulator radiation pattern for even and odd harmonics. (a) Odd harmonics are due to the oscillatory motion in the horizontal direction suffered by the particle in its reference frame. (b) Moving back to the observer frame, the dipoel-like radiation is beamed in the forward direction. (c) Even harmonics arise from the longitudal oscillatory motion of the particle in its reference frame. It results in a dipole pattern with null emitted intensity along the z'-direction. (d) The Lorentz transformation to the reference frame of the observer shaped the emitted radiation in a narow cone in the forward direction. The resulting intensity distribution appears as a ring around the z-axis. Drawings are not on scale for mere illustrative purposes.

$$\frac{\mathrm{d}^2 W_k}{\mathrm{d}\Omega\,\mathrm{d}\omega} = P_u \left[\frac{\sin(\pi N_w \Delta\omega_k/\omega_1)}{\pi N_w \Delta\omega_k/\omega_1}\right]^2 \cdot \left| \hat{\epsilon}_x \left[\theta\cos\phi \sum_{\mathrm{m}=-\infty}^{+\infty} J_m(u) J_{k-2m}(v) e^{i\frac{\pi}{2}(k-2m)} + \right.\right.$$
$$+ \frac{iK}{2\gamma}\left(\sum_{\mathrm{m}=-\infty}^{+\infty} J_m(u) J_{k-2m+1}(v) e^{i\frac{\pi}{2}(k-2m+1)} - \sum_{\mathrm{m}=-\infty}^{+\infty} J_m(u) J_{k-2m-1}(v) e^{i\frac{\pi}{2}(k-2m-1)} \right) \Bigg] +$$
$$\left. + \hat{\epsilon}_y\,\theta\sin\phi \sum_{\mathrm{m}=-\infty}^{+\infty} J_m(u) J_{k-sm}(v) e^{i\frac{\pi}{2}(k-2m)} \right|^2, \tag{2.41}$$

where $P_u = r_e m_0 c N_w^2 \omega^2/(\gamma^2\Omega_w^2)$, $u = (\omega/\omega_1)C$, $v = (\omega/\omega_1)S$, $J_n(\cdot)$ is the Bessel function

of order n and we have introduced the following reduced parameters

$$\gamma^* = \frac{\gamma}{\sqrt{1+K^2/2}} \qquad K^* = \frac{K}{\sqrt{1+K^2/2}} \qquad C = \frac{2K^*\beta^*\gamma^*\theta\cos\phi}{1+\gamma^{*2}\theta^2} \qquad S = \frac{K^{*2}\beta^*}{1+\gamma^{*2}\theta^2}. \tag{2.42}$$

In most circumstances one does not have to compute the infinite sums with many terms. The first 10 or 20 terms about zero are enough to give adequate results, as reported in Fig. 2.11 for the horizontal profiles of the first four harmonics.

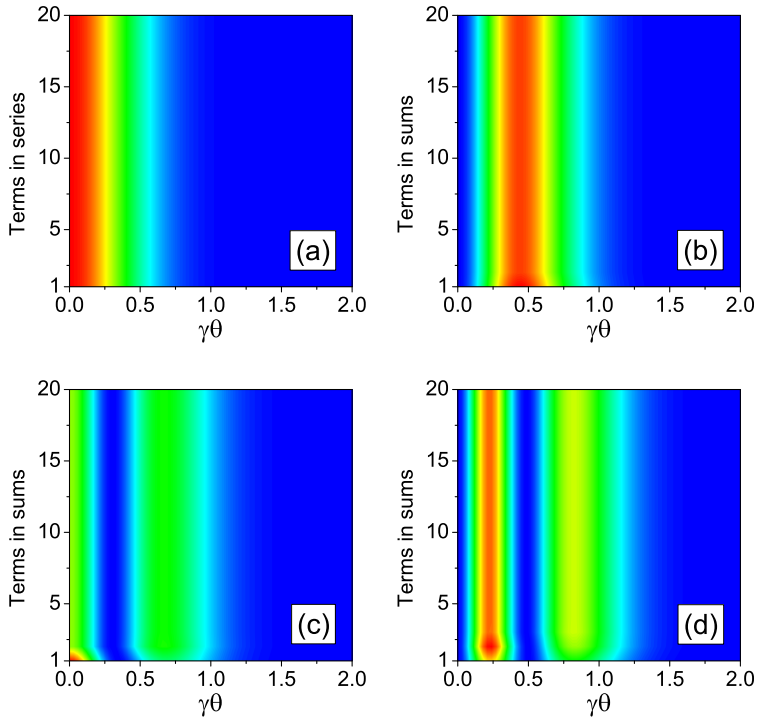

Figure 2.11: Convergence of the undulator sum in Eq. 2.41 for a finite number of terms for the first four harmonics. It can be seen that a number of $\approx$ 20 terms around zero in Eq. 2.41 ensures the convergence of the series.

Finally, Fig. 2.12 shows the 2-D angular power density of the first four harmonics. It is worth noting that such plots are not at a fixed wavelength: they show how the flux density of each harmonic varies with the observation position but the photon wavelength itself is changing with the angle.

One of the key features of wigglers and undulators is the narrow frequency distribution around the resonant frequency at a fixed angle. The bandwidth of the radiation at the observation angle θ is determined by $\Delta\omega_k$ through the resonant factor $\sin(\cdot)/(\cdot)$:

$$\frac{\sin(\pi N_w \Delta\omega_k/\omega_1)}{\pi N_w \Delta\omega_k/\omega_1} = 0 \quad \longrightarrow \quad \frac{\pi N_w \Delta\omega_k}{\omega_1} = \pi \quad \longrightarrow \quad \frac{\Delta\omega_k}{\omega_k} = \frac{1}{kN_w}. \tag{2.43}$$

In a similar way we can also determine the angular width of the peak of the k-th harmonic at an angle θ. We observe the radiation tuned at the resonant frequency $k\omega_1(\theta)$

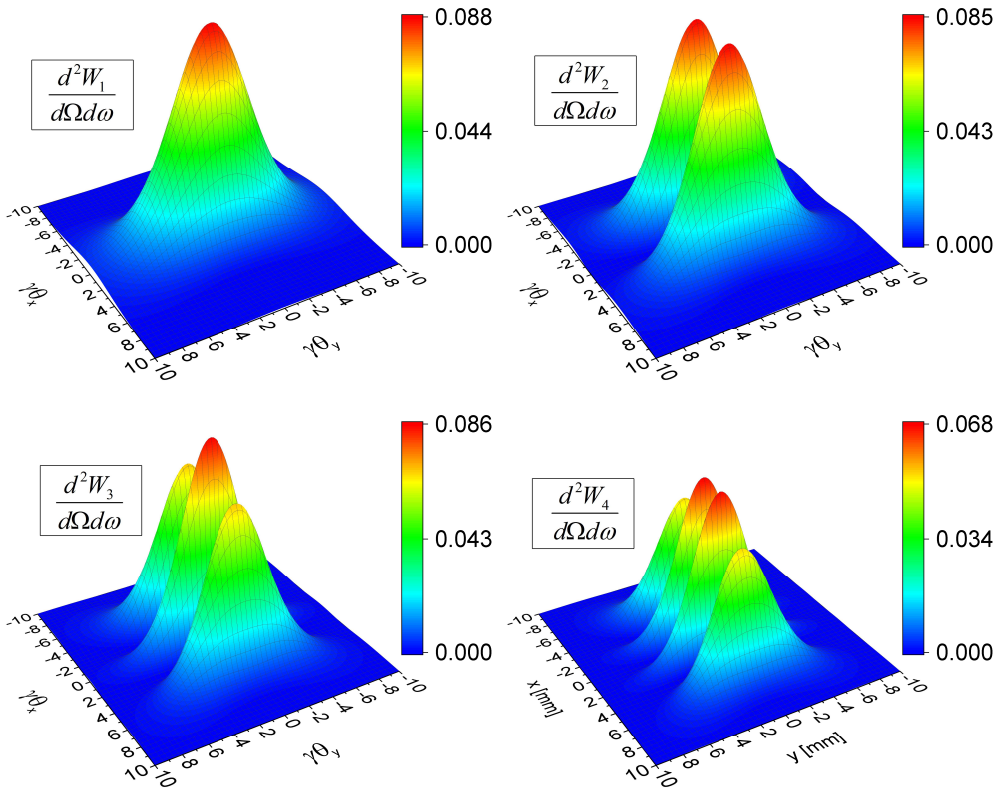

Figure 2.12: Undulator angular power distribution for the first four harmonics. It is worth remembering that such plots are not at a fixed wavelength due to the angle-dependent doppler shift $\lambda_n = [\lambda_w/(2\gamma^2 n)](1 + K^2/2 + \gamma^2\theta^2)$.

and then move to the angular position θ'. From the resonant factor, the angular width of the peak is given by

$$\pi = \frac{\pi N_w \Delta\omega_k(\theta')}{\omega_1(\theta')} = \pi N_w \frac{k\omega_1(\theta) - k\omega_1(\theta')}{\omega_1(\theta')} = \pi N_w k\gamma^2 \frac{\theta'^2 - \theta^2}{1 + K^2/2 + \gamma^2\theta^2}. \tag{2.44}$$

The angular width of the peak around $\theta = 0$ (central cone of radiation) for the k-th harmonic is then

$$\theta' = \frac{1}{\gamma^* \sqrt{kN_w}}. \tag{2.45}$$

2.4 Solution based on Paraxial Green's function

The properties of Synchrotron Radiation and of Undulator Radiation have been obtained so far in a classical electrodynamics framework, based on the far field expressions of the Lièнard-Wiechert fields [38, 39]. They are derived by solving the Maxwell's equations in the space-time domain and by Fourier-transforming the acceleration term to shift to the frequency representation of the electric field.

Recently [40, 41], a new formalism has been developed based on the solution of the paraxial Maxwell's equation in the space-frequency domain for a given harmonic of the electric field with the use of an appropriate Green's function. A general expression for the slowly-varying complex envelope $\vec{\tilde{E}}_\perp(z_o, \vec{r}_{\perp o}, \omega)$ of the Fourier component of the electric field is derived, remarkably valid in the near field as well as in the far field. Furthermore, it can be easily adapted to particles with offset and deflection with respect to the nominal trajectory, paving the way for an analytical or numerical investigation of finite emittance effects and of transverse coherence properties of the radiation beam.

Denoting with $\vec{r}_{\perp o} = (x_o, y_o)$ the transverse coordinates of an observer at the longitudinal position z_o and referring to the position and to the velocity of the particle with $(\vec{r}'_\perp, z') = (x', y', z')$ and $\vec{v} = (v_x, v_y)$, respectively, in the ultrarelativistic approximation $(1/\gamma^2 \ll 1)$ the slowly-varying envelope of the field in the space-frequency representation is expressed by the following general relation [40, 41]:

$$\vec{\tilde{E}}_\perp(z_o, \vec{r}_\perp, \omega) = -\frac{i\omega e}{c^2}\int_{-\infty}^{+\infty} \mathrm{d}z' \, \frac{e^{i\Phi_T}}{z_o - z'} \times \\ \times \left[\left(\frac{v_x(z')}{c} - \frac{x_o - x'(z')}{z_o - z'}\right)\hat{x} + \left(\frac{v_y(z')}{c} - \frac{y_o - y'(z')}{z_o - z'}\right)\hat{y}\right], \tag{2.46}$$

where the total phase Φ_T is given by

$$\Phi_T = \omega\left[\frac{s(z')}{v} - \frac{z'}{c}\right] + \omega\left[\frac{(x_o - x'(z'))^2 + (y_o - y'(z'))^2}{2c(z_o - z)}\right]. \tag{2.47}$$

The full derivation of Eq. 2.46 is reported in Appendix A for the convenience of the reader.

2.4.1 Bending magnet radiation

We consider a particle moving at constant velocity v along a circular trajectory with radius of curvature R inside a bending magnet. Under paraxial conditions, the following expressions for the particle trajectory and curvilinear abscissa hold:

$$s(z') = R\mathrm{arcsin}\left(\frac{z'}{R}\right) \approx z' + \frac{z'^3}{6R^2} \qquad\qquad \vec{r}'_\perp = -\frac{z'^2}{2R}\hat{x}. \tag{2.48}$$

The slowly-varying evelope of the electric field in the space-frequency domain and in far field conditions is obtained by expanding $(z_o - z')^{-1}$ around z_o. We keep terms up to the third power in the expression for the phase, while for the other factors it is sufficient to retain only first-order terms [40, 41]. We introduce the angles $\theta_x = x_o/z_o$ and $\theta_y = y_o/z_o$, yielding to the final result

$$\vec{\tilde{E}}_\perp(z_o, \theta_x, \theta_y, \omega) = \frac{i\omega e}{c^2 z_o} e^{i\Phi_s} e^{i\Phi_0} \times \\ \times \int_{-\infty}^{+\infty} \mathrm{d}z' \, \left(\frac{z'}{R}\hat{x} + \theta_y\hat{y}\right) \exp\left\{i\omega\left[\frac{z'}{2\gamma^2 c}(1 + \gamma^2\theta_y^2) + \frac{z'^3}{6R^2 c}\right]\right\}, \tag{2.49}$$

where

$$\Phi_s = \frac{\omega z_o}{2c}(\theta_x^2 + \theta_y^2) \qquad \Phi_0 = -\frac{\omega R \theta_x}{2c}\left(\frac{1}{\gamma^2} + \frac{\theta_x^2}{3} + \theta_y^2\right). \tag{2.50}$$

In order to compare the expression for the field just derived and the results of classical electrodynamics, we must put $\theta_x = 0$ and we set $z' = vt'$, since classical electrodynamics results are expressed in terms of integration over the retarded time t' of the particle. We thus obtain

$$\begin{aligned}\vec{\tilde{E}}_\perp(z_o, \theta_x, \theta_y, \omega) &= \frac{i\omega e}{cz_o} e^{i\Phi_s} \int_{-\infty}^{+\infty} \mathrm{d}t' \left(\frac{ct'}{R}\hat{x} + \theta_y \hat{y}\right) \exp\left\{i\omega\left[\frac{t'}{2\gamma^2}(1+\gamma^2\theta_y^2) + \frac{t'^3 c^2}{6R^2}\right]\right\} = \\ &= -\frac{\sqrt{3}e}{cz_o}\frac{2R\omega}{3\gamma^3 c} e^{i\Phi_s}\gamma(1+\gamma^2\theta_y^2)\left[K_{2/3}(\xi)\hat{x} - i\frac{\gamma\theta_y}{(1+\gamma^2\theta_y^2)^{1/2}}K_{1/3}(\xi)\right],\end{aligned} \tag{2.51}$$

where $K_{2/3}$ and $K_{1/3}$ are the modified Bessel function of second kind of fractional order $2/2$ and $1/3$, respectively, and $\xi = (R\omega/3\gamma^3 c)(1+\gamma^2\theta_y^2)^{3/2}$.

The phase term $\Phi_s = \omega z_o \theta_y^2/(2c)$, usually neglected in the standard electrodynamics derivation, represents the wavefront of a spherical wave propagating outward from the origin of the reference system. Nonetheless, the wavefront of the radiation emitted by a single particle does not resemble a spherical wave for nonzero values of θ_x due to the term Φ_0, as shown in Fig. 2.13. This term has no equivalent in the usual derivation with classical electrodynamics techniques and it describes in an analytical way the results of thorough simulations on single particle effects [48].

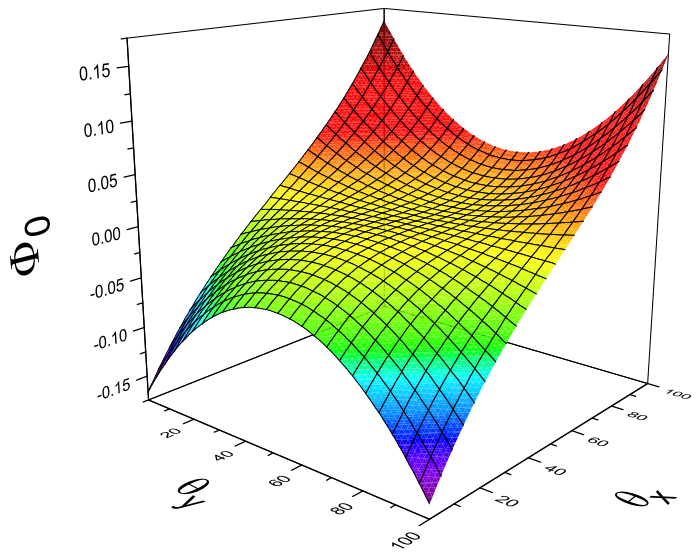

Figure 2.13: Non-spherical wavefront of single-particle Synchrotron Radiation.

The expression for the field can be easily generalized to the case of an electron with offset $\vec{l} = (l_x, l_y)$ and deflection $\vec{\eta} = (\eta_x, \eta_y)$. The offset $\vec{l}$ induces an overall transverse

shift of the detected electric field, while the particle deflection $\vec{\eta}$ causes a tilt in the radiation beam. Moreover, we notice that the phase profile of a spherical wave is not influenced by any angular tilt, as long as the observation plane is perpendicular to the z-axis. The generalized form of the electric field for a single particle with offset and deflection can thus be obtained by simply substituting θ_x with $\theta_x - l_x/z_o - \eta_x$ and θ_y with $\theta_y - l_y/z_o - \eta_y$ everywhere except in the spherical wave term, where they are replaced by $\theta_x - l_x/z_o$ and $\theta_y - l_y/z_o$, respectively:

$$\vec{\tilde{E}}_\perp(\vec{l},\vec{\eta},z_o,\theta_x,\theta_y,\omega) = \frac{i\omega e}{c^2 z_o} e^{i\Phi_s} e^{i\Phi_0} \int_{-\infty}^{+\infty} \mathrm{d}z' \left[\frac{z'}{R}\hat{x} + \left(\theta_y - \frac{l_y}{z_o} - \eta_y\right)\hat{y}\right] \times \\ \times \exp\left\{ i\omega \left[\frac{z'}{2\gamma^2 c}\left(1 + \gamma^2\left(\theta_y - \frac{l_y}{z_o} - \eta_y\right)^2\right) + \frac{z'^3}{6R^2 c}\right]\right\}, \quad (2.52)$$

where the phase factors Φ_s and Φ_0 are now given by

$$\Phi_s = \frac{\omega z_o}{2c}\left[\left(\theta_x - \frac{l_x}{z_o}\right)^2 + \left(\theta_y - \frac{l_y}{z_o}\right)^2\right] \\ \Phi_0 = -\frac{\omega R(\theta_x - l_x/z_o - \eta_x)}{2c}\left[\frac{1}{\gamma^2} + \left(\theta_y - \frac{l_y}{z_o} - \eta_y\right)^2 + \frac{(\theta_x - l_x/z_o - \eta_x)^2}{3}\right]. \quad (2.53)$$

2.4.2 Undulator radiation

We consider a planar undulator composed of N_w periods. The transverse position and velocity of the particle are given by

$$\vec{r}'_\perp(z') = \frac{K}{\gamma k_w}\cos(k_w z')\hat{x} \qquad \vec{v}_\perp(z') = -\frac{cK}{\gamma}\sin(k_w z')\hat{x}, \quad (2.54)$$

where K is the deflection parameter and $k_w = 2\pi/\lambda_w$, being λ_w the undulator period. The curvilinear abscissa is given in terms of the longitudinal particle coordinate as

$$s(z') = \frac{\beta}{\beta_{\mathrm{av}}} z' - \frac{K^2}{8\gamma^2 k_w}\sin(2k_w z'), \quad (2.55)$$

where $\beta_{\mathrm{av}} = \beta[1 - K^2/(4\gamma^2)]$ is the average velocity along the z-direction. In the limit for $z_o \gg L_w$, where $L_w = N_w\lambda_w$ is the undulator total length, the electric field has maxima at the resonant harmonics $\omega_h = h\omega_1$ of the fundamental frequency ω_1, the resonant terms being described by a $\sin(\cdot)/(\cdot)$ function. Once the observation angle θ is fixed, the corresponding resonant frequency $\omega_h(\theta)$ is defined. At an angular displacement $\Delta\theta$ the resonant frequency $\omega_h(\theta + \Delta\theta)$ may lie outside the radiation bandwidth determined by the width of the resonant term $\sin(\cdot)/(\cdot)$. For the case $\theta = 0$,this leads naturally to the definition of the central cone

$$\theta_c = \frac{1}{\gamma_z\sqrt{N_w h}}, \quad (2.56)$$

where $\gamma_z = \gamma/\sqrt{1+K^2/2}$. Under the resonant approximation ($N_w \gg 1$) and within the central cone ($\theta < \theta_c$), we obtain the following simple expression for the first harmonic of the electric field:

$$\vec{\tilde{E}}_{\perp,1}(z_o, \vec{r}_{\perp o}, \omega) = -\frac{K\omega e N_w \lambda_w e^{i\Phi_s}}{c^2 z_o \gamma} \frac{\sin(\pi N_w \Delta\omega_1/\omega_1)}{\pi N_w \Delta\omega_1/\omega_1} A_{\mathrm{JJ}} \left(\frac{K^2}{4+2K^2}\right) \hat{x}, \tag{2.57}$$

where $\Delta\omega_1 = \omega - \omega_1$, $A_{\mathrm{JJ}}(\cdot) = J_0(\cdot) - J_1(\cdot)$, J_p denotes the Bessel function of the first kind of order p and $\Phi_s = [\omega z_o/(2c)]\theta^2$ describes the phase front of a diverging spherical wave. Here

$$\omega_1^{-1} = \frac{1}{2ck_w\gamma^2}\left(1 + \frac{K^2}{2} + \gamma^2\theta^2\right). \tag{2.58}$$

Under the resonant approximation, the electric field is polarized in the horizontal direction and we can therefore refer to it with the scalar notation $\tilde{E}_{\perp,1}$. The argument in the resonant term can be rewritten as

$$\pi N_w \frac{\Delta\omega_1}{\omega_1} = \pi N_w \left[\frac{\omega - \omega_1(0)}{\omega_1(0)} + \frac{\omega\theta^2}{2k_w c}\right] = \left[\frac{L_w C}{2} + \frac{\omega L_w \theta^2}{4c}\right], \tag{2.59}$$

where $C = \omega/(2\gamma_z^2 c) - k_w$ is known as the detuning parameter. In the following, we will call $\omega_1(0) = \omega_0$. We also introduce the following dimensionless quantities

$$\begin{aligned} &\hat{E}_{\perp,1} = -\frac{c^2 z_o \gamma}{K\omega e L_w A_{JJ}} \tilde{E}_{\perp,1} \qquad && \hat{C} = L_w C = 2\pi N_w \Delta\omega_1/\omega_1 \\ &\hat{\theta} = \theta\sqrt{\frac{\omega L_w}{c}} \qquad && \vec{\hat{r}}_\perp = \vec{r}_\perp \sqrt{\frac{\omega}{cL_w}} \qquad && \hat{z} = \frac{z}{L_w} \end{aligned} \tag{2.60}$$

to cast the expression for the electric field in the more compact form

$$\hat{E}_{\perp,1}(z_o, \vec{r}_{\perp o}, \omega) = e^{i\Phi_s} \frac{\sin[\hat{C}/2 + \hat{\theta}^2/4]}{\hat{C}/2 + \hat{\theta}^2/4}. \tag{2.61}$$

The intensity profiles for the first harmonic and for different values of the detuning parameter $\hat{C}$ are reported in Fig. 2.14(a) and Fig. 2.14(b).

The introduction of dimensionless quantities, besides simplifying the expression for the electric field, provides a similarity technique to determine small and large parameters. In particular, from the dimensional analysis just introduced, it follows that angular and transverse coordinates (and quantities) are to be compared with the natural angle and with the natural transverse size of the single-particle undulator radiation, expressed respectively by $[c/(\omega L_w)]^{1/2}$ and $[cL_w/\omega]^{1/2}$, while the natural longitudinal distance is simply set by the undulator length L_w.

Similarly to the case of bending magnet radiation treated in Subsect. 2.4.1, we can easily generalize the expression of the electric field to the case of an electron with offset and deflection:

$$\hat{E}_{\perp,1,\vec{l},\vec{\eta}}(z_o, \vec{r}_{\perp o}, \omega) = e^{i\Phi_U} \frac{\sin(\zeta)}{\zeta}, \tag{2.62}$$

where

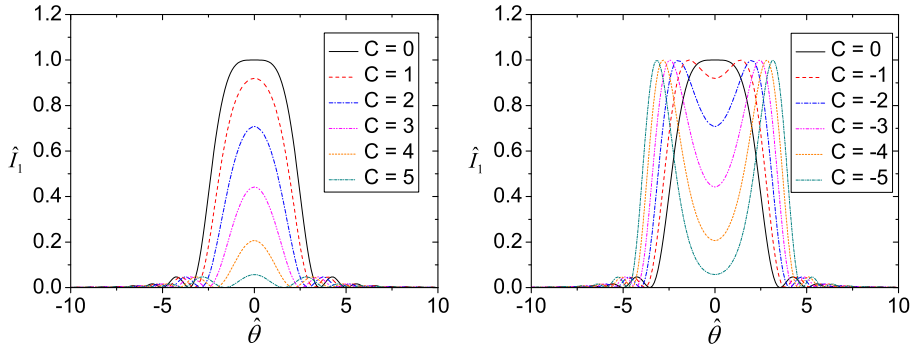

Figure 2.14: Effect of positive and negative detuning on the profile of undulator intensity. The symbol C in the legend should be read as $\hat{C}$.

$$\Phi_U = \left[\left(\hat{\theta}_x - \frac{\hat{l}_x}{\hat{z}_o}\right)^2 + \left(\hat{\theta}_x - \frac{\hat{l}_x}{\hat{z}_o}\right)^2\right]\frac{\hat{z}_o}{2}$$
$$\zeta = \frac{\hat{C}}{2} + \frac{1}{4}\left(\hat{\theta_x} - \frac{\hat{l}_x}{\hat{z}_o} - \hat{\eta}_x\right)^2 + \frac{1}{4}\left(\hat{\theta_y} - \frac{\hat{l}_y}{\hat{z}_o} - \hat{\eta}_y\right)^2 \tag{2.63}$$

and the offset $\vec{l}$ and the deflection $\vec{\eta}$ of the electron have been normalized according to the natural scalings of Eq. 2.60:

$$\vec{\hat{l}} = \vec{l}\sqrt{\frac{\omega}{cL_w}} \qquad\qquad \vec{\hat{\eta}} = \vec{\eta}\sqrt{\frac{L_w\omega}{c}}. \tag{2.64}$$

2.4.3 Undulator radiation as a laser-like beam

Synchrotron radiation can be described with the formalism of laser beam optics [41]. This parallelism stems from the fact that both the radiation from an ultrarelativistic electron and laser beams satisfy the paraxial wave equation. In particular, the Undulator Radiation from an ultrarelativistic particle appears as a laser-like beam generated by a virtual source with a plane wavefront, similarly to the case of the waist of a laser beam. Remarkably, the electric field distribution $\tilde{E}_\perp(0,\vec{r}_\perp)$ of this virtual waist is related to the Fourier transform of the far-field angular distribution of the emitted SR:

$$\tilde{E}_\perp(0,\vec{r}_\perp) = i\frac{K\omega e}{c^2\gamma}A_{JJ}\left[\pi - 2\mathrm{Si}\left(\frac{\omega r_\perp^2}{cL_w}\right)\right], \tag{2.65}$$

where $\vec{r}_\perp$ den otes transverse coordinates across the virtual source plane and $r_\perp = |\vec{r}_\perp|$. We refer the interested reader to Appendix B for further details. It can be seen that:

- the virtual waist is located in the center of the undulator, similarly to the waist of a laser beam located at the center of the optical cavity;

- both the UR virtual source and the waist of a laser beam have a plane wavefront;
- the UR virtual waist has a characteristic transverse extension $w_0 = [cL_w/\omega]^{1/2}$;
- the characteristic divergence of the UR beam is $c/(\omega w_0) = [c/(\omega L_w)]^{1/2}$;
- the UR Rayleigh range $z_R = (\omega/c)w_0^2 = L_w$ is related to the undulator geometrical factor.

We now have a deeper understanding regarding the scalings and dimensionless quantities of Eq. 2.60, having provided a physical meaning to the characteristic quantities therein introduced. Finally, the field at any longitudinal position z_o downstream the magnetic setup can then be obtained by means of the Fresnel propagation formula from the electric field of the virtual source:

$$\tilde{E}_\perp(z_o, \vec{r}_\perp) = \frac{K\omega e}{c^2\gamma} A_{JJ} \left[\mathrm{Ei}\left(\frac{i\omega r_\perp^2}{2z_o c - L_w c} \right) - \mathrm{Ei}\left(\frac{i\omega r_\perp^2}{2z_o c + L_w c} \right) \right], \tag{2.66}$$

being $\mathrm{Ei}(\cdot)$ the exponential integral function and $r_\perp = |\vec{r}_\perp|$, where $\vec{r}_\perp$ now indicates transverse coordinates across the observation plane at the longitudinal position z_o.

CHAPTER 3

Partially coherent synchrotron radiation from relativistic beams

3.1 Synchrotron Radiation as a stochastic process

Realistic electron beams have finite cross section and divergence. The electrons are randomly distributed within the beam and at a fixed position along the trajectory they travel with random deflection angles. Moreover, the shot noise in the electron beam induces fluctuations in the beam distribution which are random in time and space from bunch to bunch. As a consequence, the emitted Synchrotron Radiation has random amplitudes and phases and it is properly described as a stochastic process [42].

3.1.1 Synchrotron Radiation: a non-stationary process

Synchrotron Radiation is intrinsically a non-stationary process, being emitted in the form of short pulses: average over many ensamble realizations unavoidably yields to a time-varying intensity on a temporal scale comparable to the pulse duration. For this reason, averaging brackets $\langle\cdot\rangle$ will denote ensamble average over many electron bunches.

3.1.2 Synchrotron Radiation: a Gaussian process

We consider a fixed polarization component at the frequency ω of the Fourier transform of the electric field emitted by the electron bunch. At position $(z_o, \vec{r}_{\perp o})$ it is indicated as $\bar{E}_\perp(z_o, \vec{r}_{\perp o}, \omega)$. We will refer to it as the electric field for notational simplicity. The contribution to the total electric field from the k-th electron depends on the transverse offset $\vec{l}_k$ and on the deflection angle $\vec{\eta}_k$. Furthermore, the electric field in time domain is delayed by the time t_k with respect to some reference temporal instant. The arrival time t_k induces a phase shift $\exp(i\omega t_k)$ in the electric field in the frequency domain. The total eetric field can then be written as

$$\bar{E}_\perp(z_o, \vec{r}_{\perp o}, \omega) = \sum_{k=1}^{N} \bar{E}_\perp(\vec{l}_k, \vec{\eta}_k, z_o, \vec{r}_{\perp o}, \omega) e^{i\omega t_k}, \tag{3.1}$$

where N is the number of electrons in the bunch. We make the three following assumptions on the complex phasors composing the sum in Eq. 3.1, which are generally satisfied in Synchrotron Radiation from relativistic beams [42]

- the random variables t_k are independent of each other and of the random variables $\vec{l}_k$ and $\vec{\eta}_k$. This requirement is always fulfilled as the arrival times are due to the shot noise in the electron bunches and they do not depend on the offset and deflection of the electron;

- the random variables $|\bar{E}_\perp(\vec{lk}, \vec{\eta}_k, z_o, \vec{r}_{\perp o}, \omega)|$ are identically distributed for all k, with finite average and second-order moment. Also this requirement is fulfilled due to the properties of shotnoise in storage rings;

- the electron bunch duration σ_T is large enough in order to have $\omega\sigma_T \gg 1$. Under this assumption, generally fulfilled because ω refers is high enough in practical cases, the random phases ωt_k are uniformly distributed in the range $(0, 2\pi)$.

Under these three hypotheses, we can exploit the Central Limit Theorem to state that the real and imaginary part of $\bar{E}_\perp(z_o, \vec{r}_{\perp o}, \omega)$ follow a Gaussian statistics. As a result, Synchrotron Radiation is a non-stationary Gaussian stochastic process and its statistical characterization requires only the second-order field correlation function in frequency domain:

$$\Gamma_\omega(z_o, \vec{r}_{\perp o1}, \vec{r}_{\perp o2}, \omega_1, \omega_2) = \left\langle \bar{E}_\perp(z_o, \vec{r}_{\perp o1}, \omega_1)\bar{E}^*_\perp(z_o, \vec{r}_{\perp o2}, \omega_2)\right\rangle . \tag{3.2}$$

3.2 Theory of second-order field correlation function in space-frequency domain

Our starting point is the expression for the second-order correlation function given in Eq. 3.2. The ensamble average is given in temrs of the probability density distribution $P(\vec{l_k}, \vec{\eta}_k, t_k)$ of the joint random variables $\vec{l_k}$, $\vec{\eta}_k$ and t_k. Since the random variables t_k are independent on $\vec{l_k}$ and $\vec{\eta}_k$, P can be factorized as

$$P(\vec{l_k}, \vec{\eta}_k, t_k) = F_{l_x,\eta_x}(l_{x,k}, \eta_{x,k})F_{l_y,\eta_y}(l_{y,k}, \eta_{y,k})F_t(t_k), \tag{3.3}$$

where we have also assumed that the horizontal and vertical distributions are not correlated.

Substitution of Eq. 3.1 into Eq. 3.2 and expansion of the resulting expression give

$$\begin{aligned}
&\Gamma_\omega(z_o, \vec{r}_{\perp o1}, \vec{r}_{\perp o2}, \omega_1, \omega_2) = \\
&= \sum_{m=1}^{N} \left\langle \bar{E}_\perp(\vec{l}_m, \vec{\eta}_l, z_o, \vec{r}_{\perp o1}, \omega_1)\bar{E}^*_\perp(\vec{l}_m, \vec{\eta}_l, z_o, \vec{r}_{\perp o2}, \omega_2)e^{i(\omega_1-\omega_2)t_m}\right\rangle + \\
&+ \sum_{m\neq n} \left\langle \bar{E}_\perp(\vec{l}_m, \vec{\eta}_m, z_o, \vec{r}_{\perp o1}, \omega_1)e^{i\omega_1 t_m}\right\rangle \left\langle \bar{E}^*_\perp(\vec{l}_n, \vec{\eta}_n, z_o, \vec{r}_{\perp o2}, \omega_2)e^{-i\omega_2 t_n}\right\rangle .
\end{aligned} \tag{3.4}$$

The ensamble average $\langle\exp(i\omega t_k)\rangle$ can be rephrased in terms of the Fourier transform on the bunch longitudinal profile $F_t(t_k)$:

$$\left\langle e^{i\omega t_k}\right\rangle = \int_{-\infty}^{+\infty} \mathrm{d}t_k\, F_t(t_k)e^{i\omega t_k} = F_\omega(\omega), \tag{3.5}$$

so that

$$\Gamma_\omega(z_o,\vec{r}_{\perp o1},\vec{r}_{\perp o2},\omega_1,\omega_2) \qquad =$$
$$= \sum_{m=1}^{N} F_\omega(\omega_1-\omega_2)\left\langle \bar{E}_\perp(\vec{l}_m,\vec{\eta}_m,z_o,\vec{r}_{\perp o1},\omega_1)\bar{E}^*_\perp(\vec{l}_m,\vec{\eta}_m,z_o,\vec{r}_{\perp o2},\omega_2)\right\rangle +$$
$$+ \sum_{m\neq n} F_\omega(\omega_1)F_\omega(-\omega_2)\left\langle \bar{E}_\perp(\vec{l}_m,\vec{\eta}_m,z_o,\vec{r}_{\perp o1},\omega_1)\right\rangle\left\langle \bar{E}^*_\perp(\vec{l}_n,\vec{\eta}_n,z_o,\vec{r}_{\perp o2},\omega_2)\right\rangle . \tag{3.6}$$

For radiation wavelengths much shorter than the bunch length we can neglect the second term, since the product $F_\omega(\omega_1)F_\omega(\omega_2)$ goes to zero for frequencies larger than the inverse bunch duration. Conversely, the first term $F_\omega(\omega_1-\omega_2)$ cannot be neglected since it depends on the difference between ω_1 and ω_2. We therefore arrive at

$$\Gamma_\omega(z_o,\vec{r}_{\perp o1},\vec{r}_{\perp o2},\omega_1,\omega_2) =$$
$$= \sum_{m=1}^{N} F_\omega(\omega_1-\omega_2)\left\langle \bar{E}_\perp(\vec{l}_m,\vec{\eta}_m,z_o,\vec{r}_{\perp o1},\omega_1)\bar{E}^*_\perp(\vec{l}_m,\vec{\eta}_m,z_o,\vec{r}_{\perp o2},\omega_2)\right\rangle =$$
$$= NF_\omega(\omega_1-\omega_2)\left\langle \bar{E}_\perp(\vec{l},\vec{\eta},z_o,\vec{r}_{\perp o1},\omega_1)\bar{E}^*_\perp(\vec{l},\vec{\eta},z_o,\vec{r}_{\perp o2},\omega_2)\right\rangle . \tag{3.7}$$

Each electron is correlated only with itself. Correlations between different electrons are described by the second term in Eq. 3.6, which has been neglected. Finally, if the dependence of $\bar{E}_\perp(\vec{l},\vec{\eta},z_o,\vec{r}_\perp,\omega)$ on the frequency is slow enough on the characteristic scale of $F_\omega(\omega)$, we can replace $\bar{E}_\perp(\vec{l},\vec{\eta},z_o,\vec{r}_{\perp o2},\omega_2)=\bar{E}_\perp(\vec{l},\vec{\eta},z_o,\vec{r}_{\perp o2},\omega_1)$[1]. We can thus separate the correlation in frequency from the spatial correlation

$$\Gamma_\omega(z_o,\vec{r}_{\perp o1},\vec{r}_{\perp o2},\omega_1,\omega_2) = NF_\omega(\omega_1-\omega_2)\left\langle \bar{E}_\perp(\vec{l},\vec{\eta},z_o,\vec{r}_{\perp o1},\omega_1)\bar{E}^*_\perp(\vec{l},\vec{\eta},z_o,\vec{r}_{\perp o2},\omega_1)\right\rangle . \tag{3.8}$$

In particular, spatial coherence is described by the cross-spectral density function $G_\omega(z_o,\vec{r}_{\perp o1},\vec{r}_{\perp o2},\omega)$ defined by

$$G_\omega(z_o,\vec{r}_{\perp o1},\vec{r}_{\perp o2},\omega) = \left\langle \bar{E}_\perp(\vec{l},\vec{\eta},z_o,\vec{r}_{\perp o1},\omega)\bar{E}^*_\perp(\vec{l},\vec{\eta},z_o,\vec{r}_{\perp o2},\omega)\right\rangle , \tag{3.9}$$

or equivalently by the spectral degree of coherence $g(z_o,\vec{r}_{\perp o1},\vec{r}_{\perp o2},\omega)$:

$$g(z_o,\vec{r}_{\perp o1},\vec{r}_{\perp o2},\omega) = \frac{G_\omega(z_o,\vec{r}_{\perp o1},\vec{r}_{\perp o2},\omega)}{\sqrt{\left\langle \left|\bar{E}_\perp(\vec{l},\vec{\eta},z_o,\vec{r}_{\perp o1},\omega)\right|^2\right\rangle}\sqrt{\left\langle \left|\bar{E}_\perp(\vec{l},\vec{\eta},z_o,\vec{r}_{\perp o1},\omega)\right|^2\right\rangle}}. \tag{3.10}$$

Angular brackets $\langle\cdot\rangle$ denote averages over electron bunches. They are equivalent in form to integrals over the transverse phase space distribution of the particle beam, given in normalized units by

[1] We consider here the relevant case of undulator radiation. The characteristic scale of $F_\omega(\omega)$ is determined by the inverse bunch duration $1/\sigma_T$. The on-axis bandwidth of the single particle radiation (filament beam) at resonance with the frequency ω_0 is given by ω_0/N_w. For the case of an electron beam with finite emittance, the spectrum exhibits longer tails [40, 41] which ensures that ω_0/N_w is a minimum for the radiation bandwidth. Comparison with $1/\sigma_T$ for realistic cases (e.g. $\lambda = 1$ Å, $N_w \approx 10^2$, $\sigma_T \approx$ 10-100 ps) shows that the introduced approximation is valid.

$$
\begin{aligned}
F_{\hat{\eta}_x}(\hat{\eta}_x) &= \frac{1}{\sqrt{2\pi\hat{D}_x}} \exp\left(-\frac{\hat{\eta}_x^2}{2\hat{D}_x}\right) \\
F_{\hat{\eta}_y}(\hat{\eta}_y) &= \frac{1}{\sqrt{2\pi\hat{D}_y}} \exp\left(-\frac{\hat{\eta}_y^2}{2\hat{D}_y}\right) \\
F_{\hat{l}_x}(\hat{l}_x) &= \frac{1}{\sqrt{2\pi\hat{N}_x}} \exp\left(-\frac{\hat{l}_x^2}{2\hat{N}_x}\right) \\
F_{\hat{l}_y}(\hat{l}_y) &= \frac{1}{\sqrt{2\pi\hat{N}_y}} \exp\left(-\frac{\hat{l}_y^2}{2\hat{N}_y}\right),
\end{aligned} \tag{3.11}
$$

where $\hat{N}_{\mathrm{x,y}}$ and $\hat{D}_{\mathrm{x,y}}$ represent the normalized rms transverse dimension and angular spread of the electron bunch:

$$
\begin{aligned}
\hat{N}_{\mathrm{x,y}} &= \sigma_{\mathrm{x,y}}^2 \frac{\omega}{L_w c} \\
\hat{D}_{\mathrm{x,y}} &= \sigma_{\mathrm{x,y}}'^2 \frac{\omega L_w}{c}.
\end{aligned} \tag{3.12}
$$

We recall that $\sigma_{\mathrm{diffr}} = (cL_w/\omega)^{1/2}$ represents the transverse size of the virtual waist generating the laser-like single-particle undulator radiation and that $\sigma'_{\mathrm{diffr}} = [c/(\omega L_w)]^{1/2}$ is the associated photon beam divergence. Therefore, when $\sigma_{\mathrm{x,y}} \ll \sigma_{\mathrm{diffr}}$ and $\sigma'_{\mathrm{x,y}} \ll \sigma'_{\mathrm{diffr}}$, corresponding to $\hat{N}_{\mathrm{x,y}} \ll 1$ and $\hat{D}_{\mathrm{x,y}} \ll 1$, radiation is diffraction-limited and it is endowed with full coherence. The opposite case $\hat{N}_{\mathrm{x,y}} \gg 1$ and $\hat{D}_{\mathrm{x,y}} \gg 1$ is equivalent to an homogeneous source within the framework of Statistical Optics. Hence the Van Cittert-Zernike's theorem can be applied to predict the transverse coherence properties of the undulator radiation provided that the observer is sufficiently far from the source. In particular, the coherence patches of the radiation beam at a distance z are determined by the angular size $\sigma_{\mathrm{x,y}}/z$ of the source as long as $\sigma_{\mathrm{x,y}}/z \ll \sigma'_{\mathrm{diffr}}$. In dimensionless units, this is equivalent to state that the Van Cittert-Zernike's theorem is valid for observation distances $\hat{z}_o \gg (\hat{N}_{\mathrm{x,y}}/\hat{D}_{\mathrm{x,y}})^{1/2}$. Performing the full calculation (reported in Appendix C for the interested reader), the transverse coherence length $\hat{\xi}_c$ normalized to the diffraction length $(cL_w/\omega)^{1/2}$ is given by [42]

$$
\hat{\xi}_c(\hat{z}_o) = \sqrt{\pi}\left(\frac{1}{\hat{A}_{\mathrm{x,y}}} + \frac{1}{\hat{D}_{\mathrm{x,y}}}\right)^{1/2}, \tag{3.13}
$$

where $\hat{A}_{\mathrm{x,y}} = \hat{N}_{\mathrm{x,y}}/\hat{z}_o^2$ represents the squared angular size of the source in dimensionless units at the observer position. Results for the case $\hat{N} = 1000$ and $\hat{D} = 100$ are reported in Fig 3.1.

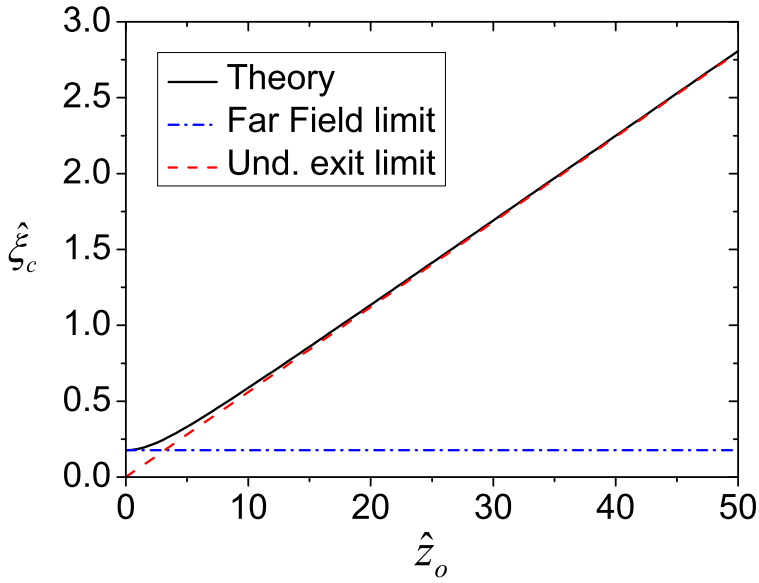

Figure 3.1: Evolution of the reduced coherence length downstream the undulator exit. The case $\hat{N} = 1000$ and $\hat{D} = 100$ is reported, as well as the asymptotic behaviors corresponding to the undulator exit limit and to the far field limit.

Part II

The Heterodyne Near Field Speckle Technique

CHAPTER 4

The Heterodyne Near Field Speckle technique

4.1 Overview of speckle patterns with fully coherent radiation

Whenever a coherent wavefront impinges onto a rough surface, a stochastic intensity distribution known as speckle pattern is observed [49, 50], as shown in Fig. 4.1. It arises from the interference among the randomly dephased contributions generated by and propagating from each point of the surface. Perhaps the most common case is that of a ground glass enlightened by a coherent laser beam.

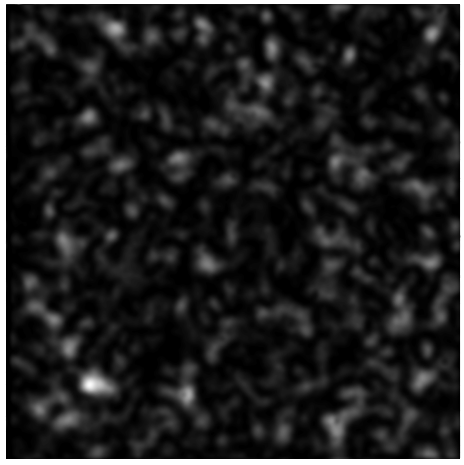

Figure 4.1: Speckle field arising from scattering of a laser beam by a ground glass.

The total electric field E downstream the random surface is given by the sum of the individual scattered waves $E_{\mathrm{s,i}}$ generated by each point i of the scattering surface:

$$E = \sum_{\mathrm{i}=1}^{N} E_{\mathrm{s,i}}, \tag{4.1}$$

where N denotes the number of scattering elements on the surface contributing to the propagated field. Since there is no contribution from the transmitted incident field, Eq. 4.1 describes the so-called homodyne speckles. Owing to the stochastic nature of the scattering surface inducing random phase shifts to each elementary contribution $E_{\mathrm{s,i}}$, the field and the intensity distributions of speckle patterns can be properly described as random variables within the framework of Statistical Optics.

The total electric field arising from the sum of Eq. 4.1 shows a random, non-uniform distribution composed by many adjacent patches of constant amplitude and phase. The problem arises of determining the average area over which the electric field is constant hence highly correlated, namely the average speckle size. The analogy with the task of finding the transverse coherence length of partially coherent radiation composed by many adjacent coherence areas[1] suggests that the speckle size can be inferred from the width of the field spatial autocorrelation function Γ_E [49, 50]

$$\Gamma_E(\Delta x) = \langle E(x)E^*(x+\Delta x)\rangle\,. \tag{4.2}$$

Due to the homodyne conditions, we can only access the intensity autocorrelation function

$$\Gamma_I(\Delta x) = \langle I(x)I^*(x+\Delta x)\rangle \tag{4.3}$$

However, assuming that a large number of scattering elements contributes to the total electric field ($N \to +\infty$ in Eq. 4.1) and that the random phases of the elementary contributions $E_{\mathrm{s,i}}$ are uniformly distributed between 0 and 2π (the optical path differences introduced by the rough surface are larger then the radiation wavelength), the Central Limit Theorem can be applied and the sum in Eq. 4.1 describes a random walk endowed with Gaussian statistics. Therefore, the modulus of $\Gamma_E(\Delta x)$ can be retrieved from the measured autocorrelation function of the intensity by means of the Siegert relation [49, 50]

$$\Gamma_I = \langle I\rangle^2 + |\Gamma_E|^2\,, \tag{4.4}$$

where $\langle I\rangle$ is the average value of the intensity across the detection plane.

4.1.1 Diffraction-limited speckles

In addition to the formalism introduced by Eq. 4.1, homodyne speckles can be described within the framework of Fourier Optics [47] as the superposition of a number of sinusoidal fringes with different orientations and different periodicities Λ. The inverse period $q = 2\pi/\Lambda$ detrmines the spatial frequency of the sinusoidal intensity modulation. Each of these modulations is equivalent to the interference pattern generated by two plane waves superimposing at an angle $\theta = \lambda/\Lambda$. For an incident beam of linear extension D, it follows that the maximum spatial frequency is determined by the angle $\theta_s = D/z$ subtended by the source at a distance z downstream the scattering plane, where z lies in the far field of the source. The corresponding interference fringes have a minimum periodicity

$$\Lambda = \frac{\lambda}{\theta_s} \tag{4.5}$$

which therefore sets the spatial scale of the finest intensity modulation appearing in the speckle field. The average speckle size d_{sp} is then given by

$$d_{\mathrm{sp}} = \frac{\lambda z}{D}. \tag{4.6}$$

[1] The analogy stems from the same physical phenomenology shared by homodyne speckles and partially coherent radiation beams. In both cases, the stochastic process arises from the superposition of many randomly dephased contributions from a number of independent emitters. However, opposite to the case of speckle fields arising from the scattering of coherent radiation from a static rough surface, the coherence patches of partially coherent radiation fluctuate from instant to instant.

This relation is analogous to the Van Cittert-Zernike's theorem and it states the well-known fact that the autocorrelation function of speckle patterns is given by the Fourier transform of the intensity distribution of the source [49, 50]. Far field speckles are diffraction-limited and they do not provide any quantitative characterization of the random system of scatterers: their behavior resembles that of the diffraction spot by an aperture, with the speckle size increasing linearly with the distance z and scaling as the inverse of the source size D. Figure 4.2 reports the experimental verification of the Van Cittert-Zernike's theorem for the case of homodyne speckles generated by a ground glass enlightened with a Gaussian laser beam. For a Gaussian intensity profile of the form $I(r) = I_0 \exp(-r^2/\sigma_I^2)$, the speckle size is given by $d_{\rm sp} = \lambda z/(\pi\sigma_I)$. The fitted value $\sigma_I = 1227$ μm is in good agreement with independent measurements performed with the edge scan technique[2] and giving a value of 1142 μ.

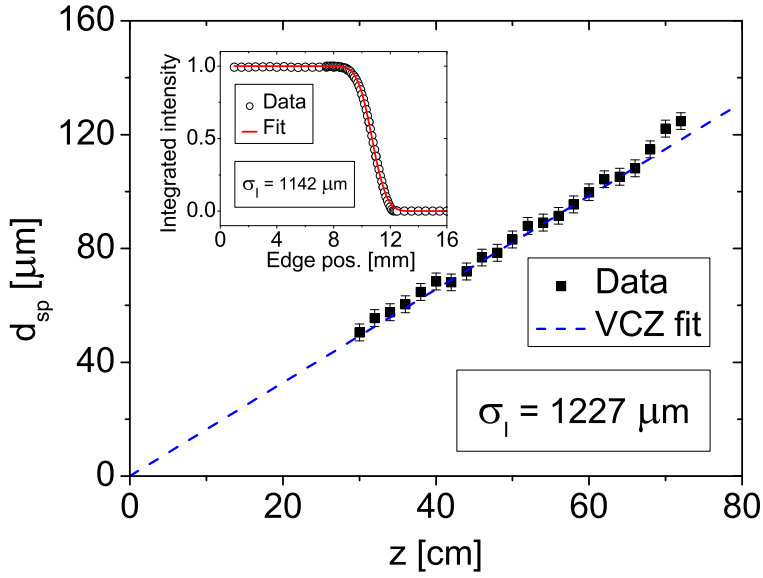

Figure 4.2: Measurements of the speckle size at different distances z from a ground glass enlightened with a Gaussian laser beam ($\lambda = 632.8$ nm). The good linearity allows to fit the experimental data (square black dots) with the theoretical curve $d_{\rm sp} = \lambda z/(\pi\sigma_I)$ predicted by the Van Cittert-Zernike's theorem (VCZ, dashed blue line). The fitted value $\sigma_I = 1227$ μm is in agreement with independent beam size measurements performed with the edge scan technique (inset).

[2]The edge scan technique works by gradually inserting a razor blade along the horizontal direction to intercept an ever-increasing portion of the laser beam. The trasmitted intensity is then measured by scanning different edge positions. The normalized transmitted intensity is given by

$$f_{\sigma_I, X_0}(\eta) = 1 - \frac{1}{\pi\sigma_I^2}\int_{-\infty}^{\eta} {\rm d}x \int_{-\infty}^{+\infty} {\rm d}y\, e^{-\frac{(x-X_0)^2+y^2}{\sigma_I^2}} = 1 - \frac{1+{\rm erf}\left(\frac{\eta - X0}{\sigma_I}\right)}{2},$$

where η and X_0 represent the absolute position of the edge and of the center of the laser beam, respectively. By fitting the experimental data through the erf function, the transverse size σ_I of the laser beam can be measured with high accuracy since it represents the only free parameter involved.

4.1.2 Homodyne Near Field Speckles (ONFS)

The Van Cittert-Zernike's theorem is strictly valid under the assumption of point-like emitters scattering light isotropically [36, 37]. However, real scatterers have a finite linear size d and the radiation is confined within the scattering angle $\theta_{\rm sc} = \lambda/d$. As long as $\theta_{\rm sc} > \theta_s$, each point on the detector receives light from the entire source and the theory developed in the previous Subsect. 4.1.1 is valid. The Van Cittert-Zernike's theorem can be applied to predict the size of the speckle and the field autocorrelation function. Moving the detector closer to the scattering surface causes the angle subtended by the source to increase. Below a certain distance $z_{\rm FF}$ that will be determined shortly, the limiting viewing angle is represented by $\theta_{\rm sc}$ and each point on the detector receives radiation only from a region $D^* = \theta_{\rm sc} z < D$, as depicted in Fig. 4.3 [51, 52]. The resulting speckle size is

$$d_{\rm sp} = \frac{\lambda z}{D^*} = \frac{\lambda}{\theta_{\rm sc}} = \frac{\lambda}{\lambda/d} = d \tag{4.7}$$

and it does not change with distance, being equal to the size of the scatterers. This regime has been named the deep Near Field or the deep Fresnel regime [51, 52], hence the name Homodyne Near Field Speckle (ONFS) of the technique. It occurs as long as the following near field condition is fulfilled:

$$\theta_{sc} < \theta_s \qquad \longrightarrow \qquad z_{\rm FF} < \frac{Dd}{\lambda}. \tag{4.8}$$

In the Near Field regime there is a deep connection between the emission cone of the radiating sources and the size of the speckles. The comparison between the characteristic emission cone of the scatterers and the angle subtended by the radiating system allows to define three regions of space downstream the random emitters:

- deep Near Field region (or deep Fresnel region), where $\theta_{\rm sc} < \theta_s$, corresponding to distances from the scattering plane $z < Dd/\lambda$. The speckle size is equal to the size of the scatterers and it does not change with the distance. Near Field speckles convey the information on the system of scatterers;
- near field region (or Fresnel region), corresponding to distances $Dd/\lambda < z < D^2/\lambda$. The speckle size increases as a function of the distance from the scattering plane, generally following non-trivial laws;
- far field region, where $\theta_s < \theta_{sc}$, corresponding to $z > D^2/\lambda$. Speckles are diffraction-limited and the Van Cittert-Zernike's theorem holds, implying $d_{\rm sp} = \lambda z/D$. The speckle pattern is determined by the intensity distribution of the source and it does not convey the information on the system of scatterers.

Figure 4.4 shows experimental results regarding the transition from near field speckles to diffraction-limited speckles. The same experimental setup as in Fig. 4.2 was adopted, but the detector was allowed to move closer to the scattering plane. Experimental data have been fitted with the following relation

$$d_{\rm sp} = \sigma_0 \sqrt{1 + \left(\frac{z\lambda}{\pi \sigma_I \sigma_0} \right)^2}, \tag{4.9}$$

in order to extract the speckle size σ_0 in the deep Fresnel regime, i.e. the average size of the scatterers. It is worth noticing how the correct laser beam size is retrieved from

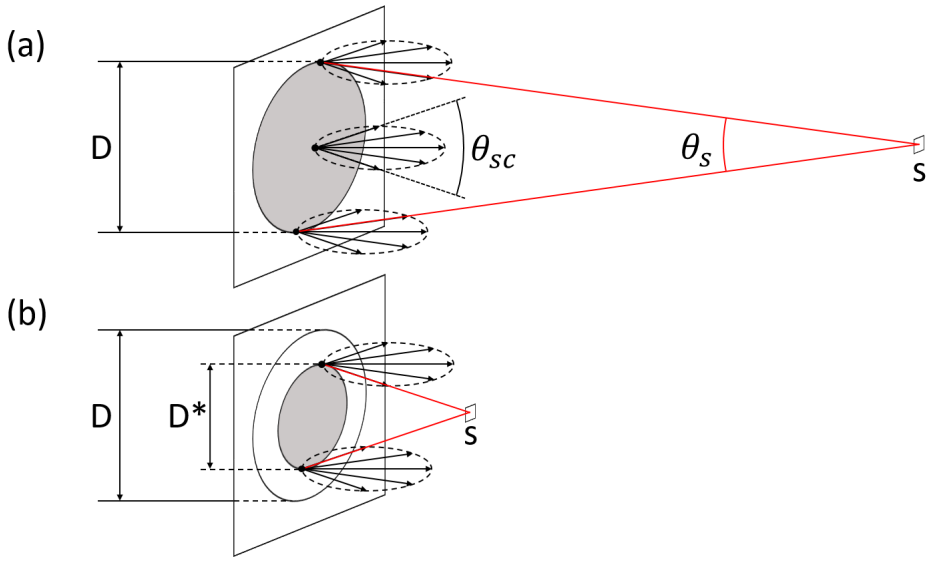

Figure 4.3: (a) A laser beam with transverse dimension D impinges onto the ensamble of scatterers with diameter d. As long as the emission cone of the scatterers $\theta_{\rm sc} = \lambda/d$ is larger than the angle subtended by the source $\theta_s = D/z$, where z is the distance between the scattering surface and the detector, each point s on the detector receives light from the entire beam and speckles are diffraction-limited. (b) When the detector is moved close to the scattering system, the limiting viewing angle is represented by the emission cone of the radiators. Each point s on the detector is illuminated by the light coming from a region $D^* < D$ and the speckle size is equal to the dimension of the scatterers.

the asymptotic diffraction-limited speckle, providing an internal check of consistency for the experiment. Furthermore, the transition from the deep Fresnel region to the far field occurs at $z_{\rm FF} \sim 10$ cm, in good agreement with Eq. 4.8 for scatterers of linear dimension $d = 17$ μm (a multiplicative factor π must be taken into account due to the Gaussian beam profile, as it can be notice from Eq. 4.9).

4.1.3 Heterodyne Near Field Speckles (HNFS)

Near field speckles can be also operated in the so-called heterodyne conditions. In this case the technique is named Heterodyne Near Field Scattering (HNFS) [53, 54, 55]. Opposite to the case of homodyne speckles, the incident field E_0 is let propagate beyond the scattering plane and it interferes with the scattered radiation E_s. The total electric field is then given by

$$E_t = E_0 + E_s, \tag{4.10}$$

and the corresponding intensity distribution is

$$I = |E_0|^2 + 2\Re\mathrm{e}\{E_0 E_s^*\} + |E_s|^2 . \tag{4.11}$$

Assuming $|E_s| \ll |E_0|$ (heterodyne conditions), the last term can be neglected. The resulting faint speckle field arise from the interference between the weak scattered waves

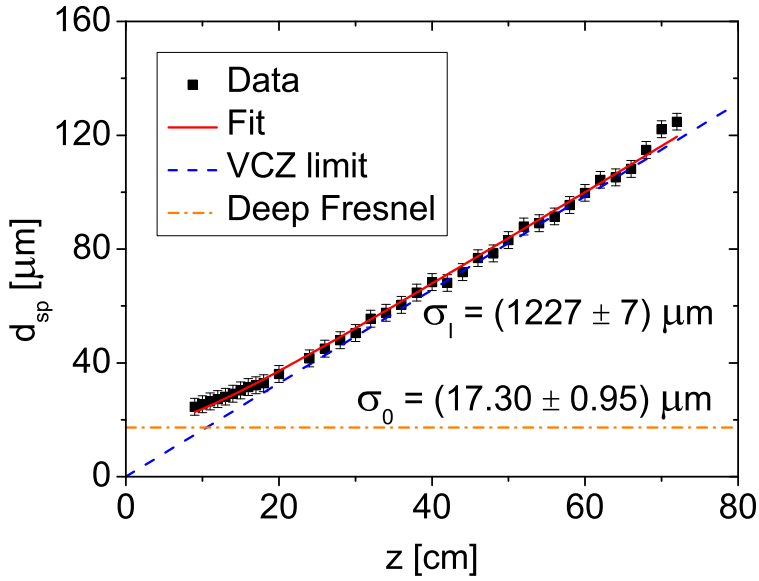

Figure 4.4: Speckles below $z \approx 20$ cm show deviations from the prediction of the Van Cittert-Zernike's theorem (dashed blue line). The asymptotically constant speckle size σ_0 (dash-dotted orange line) is equal to the transverse dimension of the emitters. Data (square black dots) have been fitted with Eq. 4.9 (solid red line) and a value $\sigma_0 = 17$ μm is found for the deep Near Field speckles. The distance $z_{\mathrm{FF}} \sim 10$ cm marks the transition from the Near Field to the Far Field. It is agreement with the expression given in Eq. 4.8, apart from a factor π due to the Gaussian intensity profile of the laser.

and the strong transmitted field (the term $2\Re\mathrm{e}\{E_0 E_s^*\}$ in Eq. 4.11), without any significant contribution from the interference among different scatterers (the term $|E_s|^2$ in Eq. 4.11).

The paradigmatic layout to generate heterodyne speckles is composed by a diluted suspension of monodispersed spherical nanoparticles scattering many almost perfect spherical waves[3].

One may ask whether the speckle size given in Eq. 4.7 is altered by the interference between the weak spherical waves scattered by the colloidal suspension and the strong transmitted field, assumed to be a fully coherent plane wave for the time being. From Fourier Optics arguments, the stochastic heterodyne speckle field is the result of the superposition of many sinusoidal patterns with periodicity $\Lambda = \lambda/\theta$ arising from the interference of the transmitted plane wave with the plane waves scattered by the particles at the angle θ. Since the scattered radiation is confined within the scattering angle

[3]The amount of light removed from the incident beam by the nanoparticles is quantified by the extinction cross section σ. For spherical nanoparticles, it can be computed by means of the exact Mie theory of scattering. The transmitted intensity I is then given by the Lambert-Beer's law:

$$I = I_0 e^{-n\sigma\Delta z}, \tag{4.12}$$

where Δz denotes the thickness of the sample and n is the particle number density to be found. At visible wavelengths, volume fraction of the order of 10^{-5} w/w ensure a transmissivity I/I_0 ranging between 80% and 90%.

$\theta_{\rm sc}$, the finest sinusoidal modulation determining the speckle size has a periodicity given by $\Lambda = \lambda/\theta_{\rm sc} = d$. HNFS with fully coherent radiation provides the information on the scattering system and it can be exploited for particle sizing [53, 54, 55]. This shows that HNFS and ONFS are equivalent, despite the interference phenomena determining the speckle fields are different.

4.2 Heterodyne Near Field Speckles with partially coherent light

One of the major advantages of the HNFS technique is the ability to probe the coherence properties of the incoming radiation, since heterodyne speckles arise from the interference of the scattered spherical waves with the transmitted incident field.

In fact, the speckle size $d_{\rm sp}$ is determined by the minimum periodicity $\Lambda = \lambda/\theta_{\rm max}$ associated to the sinusoidal intensity modulation arising from the stable interference between the transmitted radiation beam and the plane waves scattered at $\theta_{\rm max}$. Since partial coherence reduces the ability of the system of writing high-frequency fringes, it must be effective in reducing the viewing angle $\theta_{\rm max}$. Furthermore, since high-frequency fringes generate small-scale intensity modulation, the size of heterodyne speckles under partially coherent radiation increases with respect to the fully coherent case.

We can quantitatively relate the size $d_{\rm sp}$ of heterodyne speckles to the coherence properties of the radiation by a Fourier Optics approach. For the case of spatial coherence, stable interference occurs on a spatial region whose extension is comparable to the transverse coherence length $\sigma_{\rm coh}$ of the radiation. It follows that $\theta_{\rm max} = \sigma_{\rm coh}/z$, corresponding to the angle subtended by the coherence areas at a distance z from the scattering plane. The situation is depicted in Fig. 4.5(a). The speckle size is then given by $d_{\rm sp} = \lambda/\theta_{\rm max} = \lambda z/\sigma_{\rm coh}$. This relation is valid as long as the transverse coherence length of the radiation is unchanged upon propagation from the scattering plane to the detector, thus limiting the distance z to the near field of the coherence areas ($z < \sigma_{\rm coh}^2/\lambda$).

Regarding temporal coherence, stable interference requires that the optical path differences Δl between the scattered spherical wave and the transmitted plane wave are shorter than the longitudinal coherence length $l_{\rm coh}$ of the radiation. Referring to Fig. 4.5(b) and adopting paraxial conditions, a given angle θ corresponds to an optical path difference $\Delta l = z\theta^2/2$, where z is the distance between the scatterer and the detection plane. Therefore, stable interference occurs as long as $\theta < \sqrt{2l_{\rm coh}/z}$. The transverse size of the speckles is then determined by $d_{\rm sp} = \lambda/\theta_{\rm max} = \sqrt{\lambda^2 z/(2l_{\rm coh})}$. This relation holds as long as spatial coherence effects can be neglected. This requirement is fulfilled for coherence areas larger than the n-th Fresnel zone, where $n = l_c/\lambda$:

$$\sigma_{\rm coh} > (n\lambda z)^{1/2}. \tag{4.13}$$

Either for limited spatial or temporal coherence, the size of heterodyne speckles changes as a function of the sample-detector distance, opposite to the case of Near Field speckles under fully coherent illumination treated in Subsect. 4.1.3. Furthermore, two different laws are found allowing to distinguish spatial coherence and temporal coherence effects.

Figure 4.6 and Fig. 4.7 show for the first time the experimental results regarding a systematic study of the effects of limited spatial and temporal coherence on the speckle size. Referring to Fig. 4.6, the light from a halogen lamp has been used, coupled to a circular pinhole 250 μm in diameter to increase the transverse coherence length of the emitted thermal radiation. A converging lens with a focal length $f = 75$ mm sets the size of the coherence areas: $\sigma_{\rm coh} = 1.22\lambda f/d_{\rm ph} = 200$ μm, being $d_{\rm ph}$ the pinhole

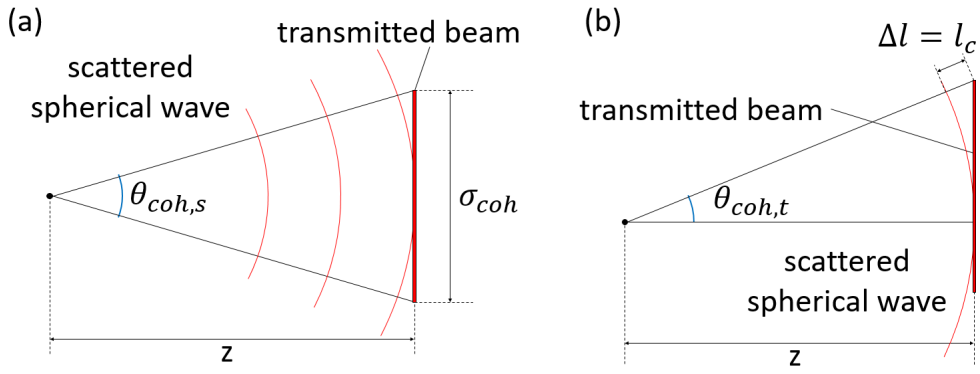

Figure 4.5: Fourier Optics approach to partially coherent Heterodyne Near Field Speckle. Partial coherence (either spatial or temporal) prevents the formation of high-frequency interference fringes thus being effective in limiting the viewing angle $\theta_{\max}$ of the system. (a) Case of limited spatial coherence. The limiting angle is given by $\theta_{\max} = \sigma_{\rm coh}/z$, where $\sigma_{\rm coh}$ denotes the transverse coherence length of the radiation and z is the sample-detector distance. (b) Case of limited spatial coherence. The limiting angle is given by $\theta_{\max} = \sqrt{2l_c/z}$, where l_c denotes the longitudinal coherence length of the radiation and z is the sample-detector distance.

diameter. Light has been filtered by means of a narrow band pass filter by Thorlabs with a FWHM bandwidth $\Delta\lambda_{\rm FWHM} = 10$ nm at a central wavelength $\lambda = 550$ nm. The longitudinal coherence length $l_c = \lambda^2/\Delta\lambda_{\rm FWHM} = 30$ μm corresponds to the n-th Fresnel zone with $n = \lambda/\Delta\lambda_{\rm FWHM} = 55$, allowing to probe spatial coherence as long as $z > \sigma_{\rm coh}^2/(n\lambda) = 13$ μm which is always fulfilled in practice. Different sample-detector distances have been probed, ranging between 1 mm and 25 mm. For each distance, a set of 100 images is acquired and the speckle size is evaluated from the FWHM of the autocorrelation function od single frames. Averages and standard deviations are then computed and three different experimental runs are performed in order to increase statistics. The linear behaviour as a function of z is observed and the experimental value for the transverse coherence length $\sigma_{\rm coh} = (200 \pm 5)$ μm is in good agreement with expectations.

Temporal coherence effects have been evidenced by removing the band pass filter and by spatially filtering the halogen lamp with a pinhole 80 μm in diameter. Coherence areas are now as large as $\sigma_{\rm coh} = 630$ μm. By exploiting a grating spectrometer, the measured FWHM of the halogen broad spectrum is $\Delta\lambda_{\rm FWHM} = 280$ nm corresponds to a longitudinal coherence length $l_c = 1.1$ μm, i.e. $n = 2$ wavelengths. Spatial coherence effects can then be neglected as long as $z < \sigma_{\rm coh}^2/(2\lambda) = 36$ cm. We performed measurements at sample-detector distances ranging between 1 mm and 50 mm and results are shown in Fig. 4.7. The power law $d_{\rm sp} \propto z^{1/2}$ is observed and the fitted value of the longitudinal coherence length $l_c = (1.3 \pm 0.1)$ μm is compatible with the inverse bandwidth predicted by the Wiener-Khinchine's theorem.

Finally, it is worth anticipating that the presence of a cutoff spatial frequency $q_{\rm cutoff} = 2\pi/\Lambda = k\theta_{\max}$ allows to advantageously characterize coherence properties of the radiation by means of Fourier analysis of heterodyne speckle field. This can be seen as a direct application of the Wiener-Khinchine's theorem of homogeneous stochastic processes to heterodyne speckles, relating the field autocorrelation function to the Fourier transform of the spatial power spectrum. As a consequence, the latter extends up to a characteristic

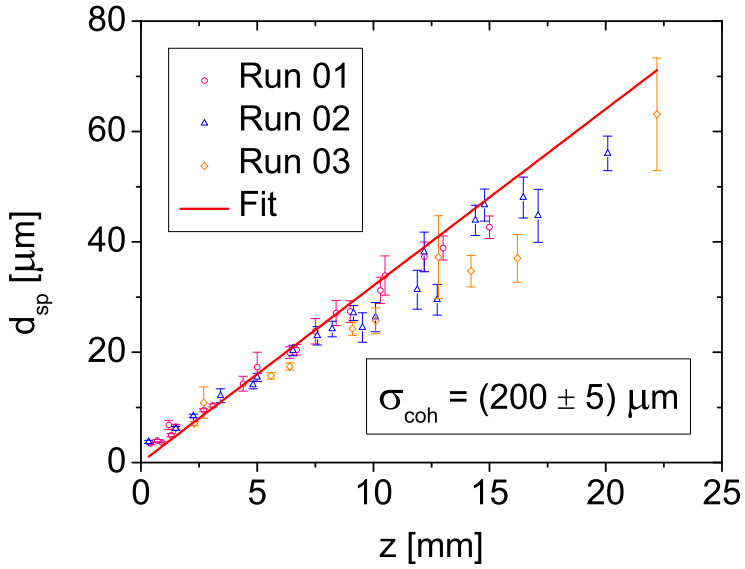

Figure 4.6: Size of heterodyne speckle with partially spatially coherent light. The expected linear behavior as a function of the sample-detector distance is observed. The fitted value for the coherence area $\sigma_{\rm coh} = (200 \pm 5)$ μm is in agreement with theoretical expectations by virtue of the Van Cittert-Zernike's theorem. See text for details.

Fourier wavevector $q_{\rm cutoff} = k\sigma_{\rm coh}/z$ for the case of partial spatial coherence and up to $q_{\rm cutoff} = k(2c\tau_c/z)^{1/2}$ for the case of limited temporal coherence. The reader should start to familiarize with these relations as they will be fundamental in the following.

4.3 Scattering from single particle

Referring to Fig. 4.8, we consider a spherical nanoparticle with diameter d enlightened with partially coherent radiation. We denote with (ξ-η) the plane perpendicular to the optical axis z at the position of the particle. Without loss of generality, we assume the scattering particle to be located at the origin of the (ξ-η)-plane. Assuming that the coherence areas are much larger than the particle, the latter scatters an almost perfect spherical wave [56] which interferes with the propagated incident field on the (x-y)-plane at a distance z downstream the particle.

The total electric field E_T on the (x-y)-plane at a time t is given by the superposition between the strong transmitted field E_0 and the weak scattered spherical wave E_s, each properly delayed owing to the finite propagation velocity of optical disturbances:

$$E_0(x,y,z,t) = E_0\left(x,y,z=0,t-\frac{z}{c}\right)e^{ikz}$$
$$E_s(x,y,z,t) = E_0\left(0,0,z=0,t-\frac{\rho}{c}\right)S(\theta)\frac{e^{ik\rho}}{\rho} \approx E_0\left(0,0,z=0,t-\frac{\rho}{c}\right)S(\theta)\frac{e^{ikz+ik\frac{x^2+y^2}{2z}}}{z}, \tag{4.14}$$

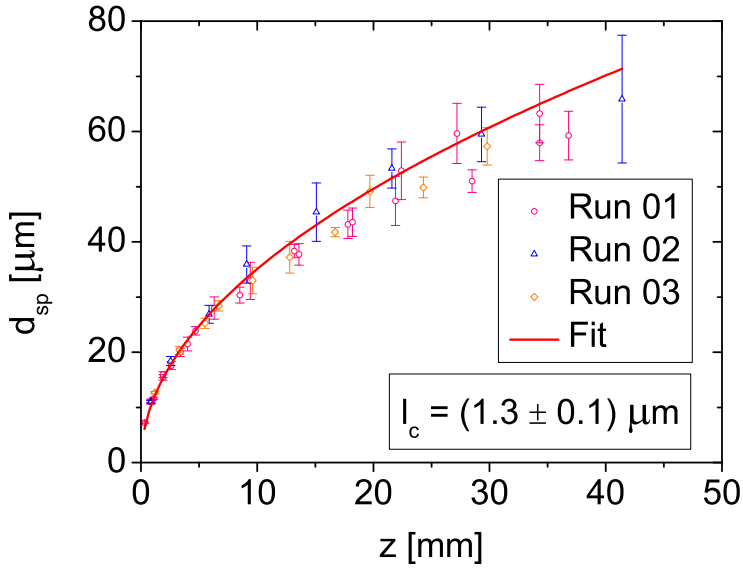

Figure 4.7: Size of heterodyne speckle with partially temporally coherent light. The expected power law behavior $d_{\mathrm{sp}} \propto z^{1/2}$ is observed. The fitted value for the longitudinal coherence length $l_c = (1.3 \pm 0.1)$ μm is in agreement with theoretical expectations by virtue of the Wiener-Khinchine's theorem. See text for details.

where we have applied the paraxial approximation to the phase of the scattered spherical wave. Here $S(\theta)$ is a complex function describing the angular distribution of the radiation scattered by the particle and it is known in the theory of light scattering as the particle form factor [56]. Finally, the angle θ is given by $\theta = (\sqrt{x^2+y^2})/z$ in paraxial approximation. As a rule of thumb, the scattering amplitude $S(\theta)$ for a particle of diameter d takes non-negligible values up to the scattering angle $\theta_s = \lambda/d$. In the following we will understand the longitudinal position $z = 0$ of the scattering particle for notational simplicity.

The instantaneous intensity $I_{\mathrm{tot}}^{\mathrm{inst}}$ is given by

$$\begin{aligned} I_{\mathrm{tot}}^{\mathrm{inst}}(x,y,z,t) &= |E_0(x,y,t)|^2 + 2\Re\mathrm{e}\left\{E_0(x,y,t)E_s^*(x,y,t)\right\} + |E_s(x,y,t)|^2 \\ &\approx I_0\left(x,y,t-\frac{z}{c}\right) + \frac{2|S(\theta)|}{z}\times \\ &\times \Re\mathrm{e}\left\{E_0\left(x,y,t-\frac{z}{c}\right)E_0^*\left(0,0,t-\frac{r}{c}\right)e^{-ik\frac{x^2+y^2}{2z}-i\sigma}\right\}, \end{aligned} \tag{4.15}$$

being $I_0(x,y,t-z/c) = |E_0(x,y,t-z/c)|^2$ and having factorized the complex scattering amplitude of the particle as $S(\theta) = |S(\theta)|\exp(i\sigma)$. The last term in the first row has been neglected assuming $|E_s| \ll |E_0|$ (heterodyne condition).

Equation 4.15 describes the time-resolved single-particle interferogram. Apart from the background contribution of the transmitted incoming beam $I_0(x,y,t-z/c)$, it shows instantaneous interference fringes whose amplitude and position depend on the modulus and on the phase of the complex field product $E_0(x,y,t-z/c)E_0^*(0,0,t-r/c)$, re-

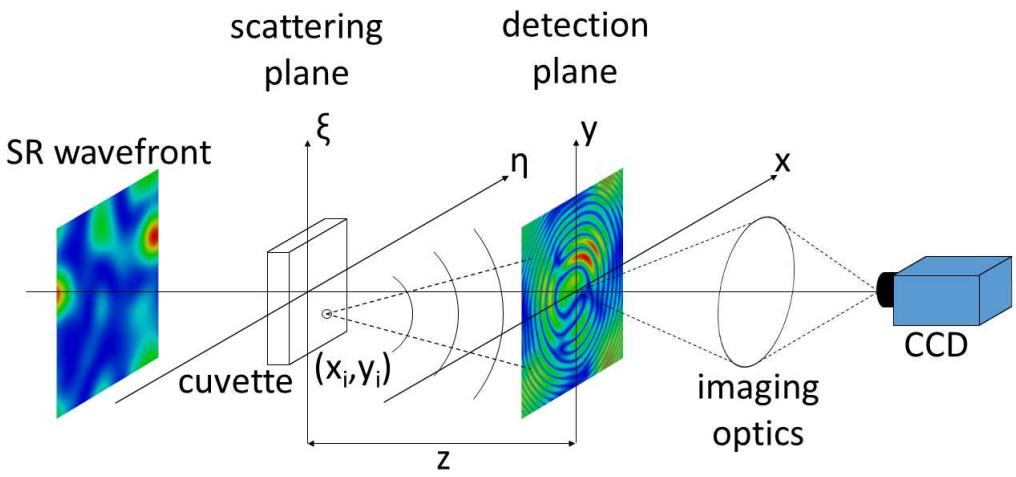

Figure 4.8: Typical HNFS experimental setup. A SR wavefront impinges onto a quartz cuvette containing many scattering particles suspended in a liquid at random positions (x_i, y_i). The interference between the scattered spherical waves and the transmitted radiation is observed at the detection plane $(x\text{-}y)$ at a distance z downstream the scattering plane $(\eta\text{-}\xi)$ by means of a CCD camera. Magnifying optics may be used, depending on the spatial resolution to be achieved.

spectively. Therefore, detection of the instantaneous single-particle interferogram would probe the phase distribution of the incoming electric field by means of the features of the distorted fringes, as depicted in Fig. 4.9.

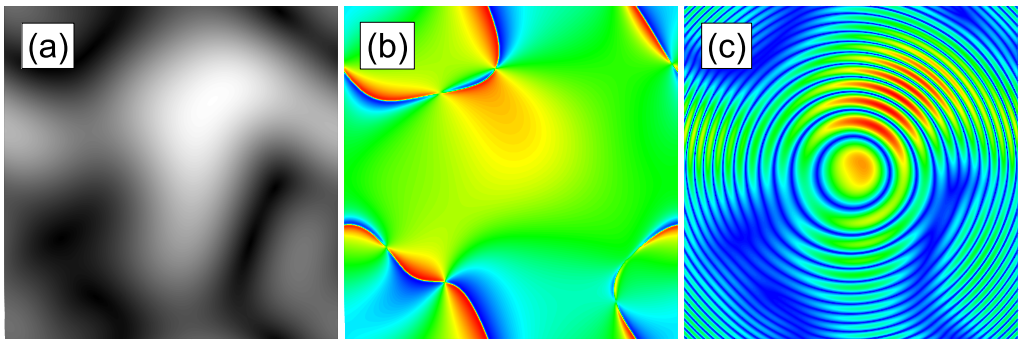

Figure 4.9: (a) Amplitude and (b) phase of a partially coherent wavefront impinging onto the scattering sample. (c) Simulated time-resolved single-particle interferogram. Information on the amplitude and phase of the coherence patches of the radiation can be retrieved from the features of the distorted fringes.

However, the incoming SR beams are composed by many adjacent coherence patches randomly changing in amplitude and phase over temporal scales comparable to the characteristic emission time of the electrons ranging between 10^{-15} s and 10^{-12} s [42, 36], thus inducing random fluctuations in the complex field product. Such short exposure

times are not achievable by any currently available detector and the time-resolved interference fringes described by Eq. 4.15 cannot be detected. We can only access the time-integrated information obtained by averaging a number of ensamble realizations of the partially coherent incident field. The ensamble average of Eq. 4.15 yields to the following expression for the detected intensity $I(x,y)$:

$$I(x,y) = \langle I_0\left(x,y,t-\frac{z}{c}\right)\rangle + \frac{2|S(\theta)|}{z}\times \\ \times \Re\mathrm{e}\left\{\left\langle E_0\left(x,y,t-\frac{z}{c}\right)E_0^*\left(0,0,t-\frac{\rho}{c}\right)\right\rangle e^{-i\sigma}e^{-ik\frac{x^2+y^2}{2z}}\right\}. \tag{4.16}$$

By calling $I_0(x,y) = \langle I_0\left(x,y,t-\frac{z}{c}\right)\rangle$ and by introducing the Mutual Coherence Function

$$\Gamma(x,y,\tau) = |\Gamma(x,y,\tau)|e^{i\phi(x,y,\tau)} = \langle E_0\left(x,y,t\right)E_0^*\left(0,0,t-\tau\right)\rangle, \tag{4.17}$$

where $\tau = (\rho - z)/c \approx (x^2+y^2)/(2zc) = z\theta^2/(2c)$, we finally arrive at the following expression for the detected intensity:

$$I(x,y) = I_0(x,y) + \frac{2|S(\theta)|}{z}|\Gamma(x,y,\tau)|\cos\left[\frac{k\left(x^2+y^2\right)}{2z} + \sigma + \phi(x,y,\tau)\right]. \tag{4.18}$$

The time-integrated interferogram of Eq. 4.18 describes perfect circular interference fringes modulated by the modulus of the Mutual Coherence Function of the incoming SR beam. This is shown in Fig. 4.10, where we report the results of a thorough simulation of time-integrated single-particle interference patterns. Stable circular interference fringes arise from the superposition of a number of ensamble realizations and their visibility allows to gauge the spatio-temporal coherence properties of the radiation.

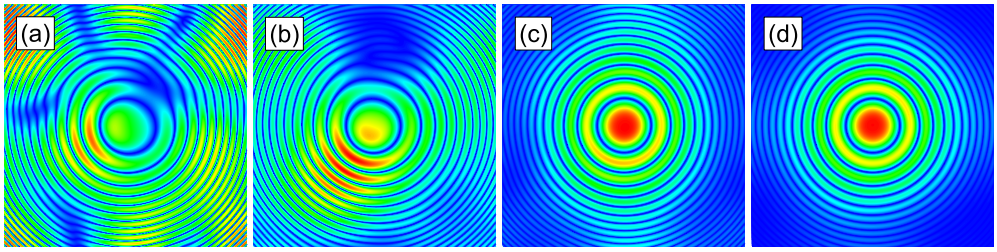

Figure 4.10: Simulated time-integrated single-particle interferogram for different ensamble realizations N of the incident partially coherent field: (a) $N = 1$, (b) $N = 10$, (c) $N = 100$ and (d) $N = 1000$. It can be noticed how uneven distorted fringes for a single realization of the radiation beam progressively become circularly symmetric as more ensable realizations are added. Furthermore, instantaneous high-frequency interference fringes disappear as a clear manifestation of partial coherence.

4.4 Scattering from colloidal suspension

Implementation of the HNFS technique with a single particle is neither efficient nor feasible. Even if it were possible to isolate and control a single spherical nanoparticle, the

associated interference pattern would be hardly detectable due to the extremely weak scattered radiation [56]. Conversely, the method is advantageously operated by using an ensamble of spherical nanoparticles suspended in a liquid, namely a colloidal suspension since the huge number N of colloidal particles results in a signal enhancement. Furthermore, the continuous Brownian motion of the particles guarantees a complete statistical renewal of the sample on temporal scales that can be easily set larger in order to not affect each single measurement, but shorter with respect to subsequent acquisitions [55].

The particles have random positions (x_i, y_i) inside the suspension and the scattered field E_s can be written as

$$E_s(x,y,z,t) = \sum_{i=1}^{N} E_{\mathrm{s,i}}(x,y,z,t), \tag{4.19}$$

where $E_{\mathrm{s,i}}(x,y,z,t)$ represents the contribution to the scattered field at the position (x,y,z) and at time t generated by the i-th particle. The detected intensity distribution is thus given by

$$\begin{aligned} I(x,y,z) = \langle I(x,y,z,t)\rangle &= \left\langle |E_0(x,y,z,t) + E_s(x,y,z,t)|^2 \right\rangle = \\ &= \left\langle I_0(x,y,z,t) + 2Re\sum_{i=1}^{N} E_0(x,y,z,t)E^*_{\mathrm{s,i}}(x,y,z,t) + \left|\sum_{i=1}^{N} E_{\mathrm{s,i}}(x,y,z,t)\right|^2 \right\rangle . \end{aligned} \tag{4.20}$$

The first term describes the contribution of the transmitted incident field to the total intensity. The second term is known as the heterodyne term and it is given by the interference between the weak scattered spherical waves and the strong transmitted field. The last term is known as the homodyne term and it describes the interference among the weak scattered spherical waves. It is usually neglected under the assumption that the scattered field is much weaker than the transmitted one (heterodyne conditions). In practice, at visible wavelengths this condition is fulfilled if the colloidal suspension is diluted enough in order to prevent multiple scattering. Opposite to this case, multiple scattering at X-ray wavelengths does not occur owing to the much lower scattering efficiencies of the particles. Remarkably, the ensamble average of the homodyne term of Eq. 4.20 is exactly null at X-ray wavelengths due to the small coherence areas involved, preventing the formation of stable interference fringes between the spherical waves scattered by different particles.

Neglecting the homodyne term, the detected intensity can be written as

$$\begin{aligned} I(x,y,z) &= \left\langle I_0(x,y,z,t) + 2Re\sum_{i=1}^{N} E_0(x,y,z,t)E_{\mathrm{s,i}}(x,y,z,t) \right\rangle \\ &= I_0(x,y,z) + 2Re\sum_{i=1}^{N} \langle E_0(x,y,z,t)E_{\mathrm{s,i}}(x,y,z,t)\rangle , \end{aligned} \tag{4.21}$$

where $I_0(x,y,z) = \langle I_0(x,y,z,t)\rangle$. Equation 4.21 describes the superposition of many single-particle interferograms generated by the interference of the scattered spherical waves with the transmitted incident beam. Comparing Fig. 4.11(a) to Fig. 4.11(b), a

small number of colloidal particles allows to probe coherence properties of the incoming radiation from the visibility and position of the single-particle circular interference fringes. The more realistic case of a colloidal suspension composed of many spherical nanoparticles is shown in Fig. 4.11(c): the random superposition of a number of single-particle interferograms results in a stochastic heterodyne speckle field and information on circular fringes is lost.

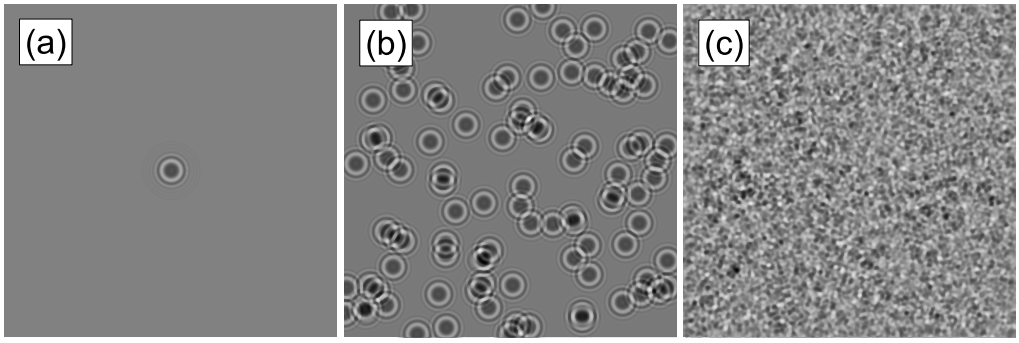

Figure 4.11: Fundamentals of the Heterodyne Near Field Speckle technique. (a) The superposition of the spherical wave scattered by a colloidal particle with the transmitted partially coherent radiation generates time-integrated circular interference fringes modulated by the Mutual Intensity of the radiation. (b) Simulation of the intensity resulting from the sum of $N = 100$ heterodyne interferograms: interference fringes are still visible and coherence properties of the radiation can be probed by means of visibility measurements. (c) Simulated speckle field from $N = 10000$ colloidal partiles: despite interference fringes are no more visible, the information of coherence can be gauged by moving to the reciprocal space to perform spatial power spectra analysis.

Nonetheless, the information on coherence properties of the radiation can be retrieved by moving to the reciprocal Fourier space:

- in direct space, the heterodyne speckle field is the result of N identical circular interfrence fringe systems, randomly displaced one with respect to the other; in Fourier space, each corresponding contribution acquires a random phase factor which however can be compensated by computating the power spectrum; the compensation of the phase factors in the power spectrum of heterodyne speckle fields is equivalent in direct space to superimposing all the single-particle interferograms, thus retrieving the interferometric information on coherence;
- in direct space, each single-particle interferogram exhibits circular fringes whose spatial frequency increases along the radial direction due to the quadratic phase term in Eq. 4.18; in Fourier space, this implies that maxima appear in the power spectrum at the corresponding spatial frequencies (actually, the number of maxima in Fourier space is doubled to account for the increasing spatial frequency of interference minima as well); power spectra of heterodyne speckles show a characteristic oscillatory behavior which is reminescent of the single-particle interference fringes. The appearence of these power spectrum oscillations (known as the Talbot oscillations) stems for the heterodyne term and it is a signature of coherence;
- in direct space, the intensity of higher-order interference maxima is lowered by the loss of coherence; in Fourier space, this implies that the Talbot oscillations are modulated according to the coherence function of the radiation.

The previous discussion shows that a statistical approach to heterodyne speckles based on power spectra analysis yields the mean square value of the fluctuations around any spatial frequency $\vec{q}$, while the information about the fringe centers is lost. Owing to the heterodyne conditions, the mean square fluctuations are a signature of the interference between the scattered spherical waves and the transmitted radiation and are thus proportional to the visibility of fringes. As it will be shortly proven here below [33] and more rigorously in the next section, the power spectrum of heterodyne speckle fields is proportional to the squared value of the radiation coherence function. In fact, recalling that

$$\begin{aligned} E_0(x,y,z,t) &= E_0\left(x,y,t-\frac{z}{c}\right)e^{ikz} \\ E_{\mathrm{s,i}}(x,y,z,t) &= E_0\left(x_i,y_i,t-\frac{\rho_i}{c}\right)S(\theta_i)\frac{e^{ikz}e^{ik\frac{(x-x_i)^2+(y-y_i)^2}{2z}}}{z}, \end{aligned} \tag{4.22}$$

the heterodyne term of Eq. 4.21 (we will call it from now on $s(x,y,z,t)$) can be rewritten as

$$s(x,y,z,,t) = \sum_{i=1}^{N}\frac{2}{z}\left\langle E_0\left(x,y,t-\frac{z}{c}\right)E_0^*\left(x_i,y_i,t-\frac{\rho_i}{c}\right)\right\rangle S^*(\theta_i)e^{-ik\frac{(x-x_i)^2+(y-y_i)^2}{2z}} + c.c, \tag{4.23}$$

where $\rho_i = \sqrt{(x-x_i)^2+(y-y_i)^2+z^2}$, $\theta_i = \sqrt{(x-x_i)^2+(y-y_i)^2}/z$ and $c.c$ denotes complex conjugate.

Under the assumptions of spatial homogeneity and of temporal stationarity, the correlation function can be expressed in terms of the difference between spatial coordinates and in term of the relative time delay τ, yielding to

$$s(x,y,z,\tau) = \sum_{i=1}^{N}\frac{2}{z}\left\langle E_0\left(x-x_i,y-y_i,\tau=\frac{\rho_i-z}{c}\right)E_0^*(0,0,0)\right\rangle S^*(\theta_i)e^{-ik\frac{(x-x_i)^2+(y-y_i)^2}{2z}} + c.c, \tag{4.24}$$

which can be rephrased in a more convenient way by means of Dirac δ-functions:

$$\begin{aligned} &s(x,y,z,\tau) = \\ &= \frac{2}{z}\left[\left\langle E_0\left(x,y,\tau=\frac{x^2+y^2}{2zc}\right)E_0(0,0,0)\right\rangle S^*(\theta)e^{-ik\frac{x^2+y^2}{2z}}\right]\otimes\left[\sum_{i=1}^{N}\delta(x-x_i,y-y_i)\right] + c.c. = \\ &= \frac{2}{z}I\left(x,y,\tau=\frac{x^2+y^2}{2zc}\right)\otimes\left[\sum_{i=1}^{N}\delta(x-x_i,y-y_i)\right] + c.c.. \end{aligned} \tag{4.25}$$

We now take the Fourier transfrom of the heterodyne signal and we apply the convolution theorem:

$$F\left[s(x,y,z)\right](\vec{q}) = F\left[I\left(x,y,\tau=\frac{x^2+y^2}{2zc}\right)\right](\vec{q})\cdot F\left[\sum_{i=1}^{N}\delta(x-x_i,y-y_i)\right](\vec{q}) + c.c., \tag{4.26}$$

where $I(x, y, \tau = (x^2 + y^2)/(2zc))$ represents the single-particle interferogram of Eq. 4.18.

The second term of the product is easy to compute:

$$F\left[\sum_{i=1}^{N}\delta(x-x_i, y-y_i)\right](\vec{q}) = \sum_{i=1}^{N} e^{i\vec{q}\cdot\vec{x}_i}. \tag{4.27}$$

The computation of the first term instead requires a deeper investigation,. In direct space, it is given by the product of three terms (the mutual intensity of the radiation, the particle form factor and the complex exponential), as it can be seen from Eq. 4.18. This results in a three-fold convolution in the reciprocal space. For small particles, the angular distribution of the scattered radiation is roughly uniform on the detection region and the Fourier transform of the scattering amplitude can be brougth out of the convolution integral as $S(\vec{q})$. Under certain assumption that will be discussed in the next section, the same arguments hold for the mutual intensity of the radiation, which therefore acts multiplicatively on the Fourier transform of the intensity distribution of heterodyne speckles. Finally, the complex exponential and its complex conjugate describe the Talbot oscillations in the power spectrum previously discussed. The power spectrum of the heterodyne term can thus be expressed as

$$\begin{aligned}
I(\vec{q}, z) &= |F[s(x, y, z)](\vec{q}, z)|^2 = \\
&= \frac{4}{z^2}\left|F\left\{I\left(x, y, \tau(x, y)\right) \otimes \left[\sum_{i=1}^{N}\delta(\Delta x_i, \Delta y_i)\right]\right\}(\vec{q}, z)\right|^2 = \\
&= \frac{4}{z^2}\left|F\left\{I(x, y, \tau(x, y))\right\}(\vec{q}, z)\right|^2 \times \left|F\left\{\sum_{i=1}^{N}\delta(\Delta x_i, \Delta y_i)\right\}(\vec{q}, z)\right|^2 = \\
&= S(\vec{q})C(\vec{q}, z)T(\vec{q}, z),
\end{aligned} \tag{4.28}$$

where $C(\vec{q}, z) = |J(\vec{q}, z)|^2$ is the squared modulus of the Mutual Intensity of the incoming radiation. Remarkably, the squared modulus of the Mutual Intensity is measured from the envelope of the Talbot oscillations appearing in the power spectrum of heterodyne near field speckles, as shown in Fig. 4.12. Talbot oscillations are described by the function $T(\vec{q}, z)$ (the Talbot transfer function) given by

$$T(\vec{q}, z) = \sin^2\left[\frac{q^2 z}{2k} + \sigma + \phi(\vec{q})\right]. \tag{4.29}$$

Here $q = |\vec{q}|$, σ denotes the phase of the complex scattering amplitude and ϕ is the phase of the Mutual Intensity.

The dependence on the distance z from the colloidal suspension of the Talbot function comes from the quadratic phase term of the scattered spherical wave appearing in the convolution integral. The dependence on z of the squared modulus of the coherence function is more subtle. Partial coherence, either spatial or temporal, affects the single-particle interferogram by preventing the formation of higher-order interference fringes. The power spectrum thus vanishes beyond a certain $\vec{q}_{\max}$, implying that the curve $C(\vec{q})$ enveloping the Talbot oscillations extends up to such value. The maximum Fourier wavevector $\vec{q}_{\max}$ depends on the coherence area or on the coherence time, as well as on the sample-detector distance, as it was proven in Subsect. 4.2 by means of

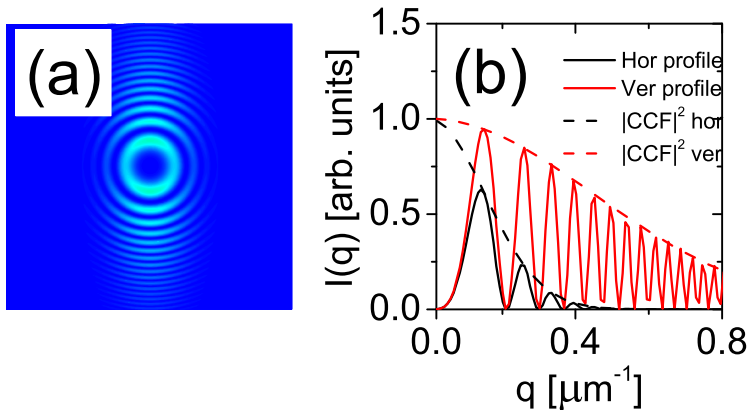

Figure 4.12: (a) Simulated 2-D power spectrum $I(\vec{q}, z)$ of heterodyne speckle and (b) radial profiles along the horizontal and vertical direction. Without loss of generality, the case of quasi-monochromatic radiation has been simulated, hence the Mutual Intensity reduces to the radiation CCF. The horizontal and vertical profiles show the characteristic Talbot oscillations enveloped by the squared modulus of the radiation CCF. A 2-D Gaussian coherence factor of the form $\exp(-x^2/\sigma^2_{\mathrm{coh,x}})\exp(-y^2/\sigma^2_{\mathrm{coh,y}})$ has been used, with $\sigma_{\mathrm{coh,x}} = 30$ μm and $\sigma_{\mathrm{coh,y}} = 90$ μm. The other relevant parameters are $\lambda = 440$ nm and $z = 2$ mm. A flat particle form factor $s(\vec{q})$ has been assumed for simplicity.

Fourier Optics arguments. Therefore power spectra corresponding to heterodyne speckles at different z vanish at different Fourier wavevector, with $\vec{q}_{\max}$ decreasing as the sample-detector distance z increases. However, the function $C(\vec{q}, z)$ describes the coherence properties of the radiation at the sample position. Hence, it must reduce to a unique function independent on z when it is expressed in terms of transverse displacements $\Delta\vec{r}$ (spatial coherence) or in terms of temporal delays τ (temporal coherence). This implies the possibility of introducing scaling laws that brings all the curves obtained at different distances onto the same master curve [30, 31, 29, 32, 33]. The scaling laws can be obtained by means of Fourier Optics treatment of heterodyne speckle fields. In fact, the contribution to the power spectrum at the Fourier wavevector $\vec{q}$ is generated by the interference between two plane waves superimposing at an angle $\vec{\theta}$ given by the relation $\vec{q} = k\vec{\theta}$. The angle θ is then related to trasverse displacements (of interest for the case of spatial coherence) by $\theta = \Delta\vec{r}/z$ and to temporal delays (for the case of temporal coherence) by $\theta = \sqrt{2\tau c/z}$.For the case of spatial coherence, the scaling is [30, 31, 29]

$$\Delta\vec{r} = \vec{q}\frac{z}{k} \tag{4.30}$$

and it causes the envelope of the Talbot oscillations to generate the master curve $C(\Delta r)$ describing the squared modulus of the radiation CCF, as shown in Fig. 4.13(a),(b). It is also worth noting that since $\vec{q}_{\max}$ depends on the transverse coherence length of the radiation, it may take on different value depending on the particular direction in the $(x$-$y)$ plane. Consequently, power spectra may show azymuthal asymmetry, as depicted in Fig. 4.13(c) for the case of a vertically-elongated CCF.

For temporal coherence the scaling is [32, 33]

$$\tau = \frac{zq^2}{2k^2c}. \tag{4.31}$$

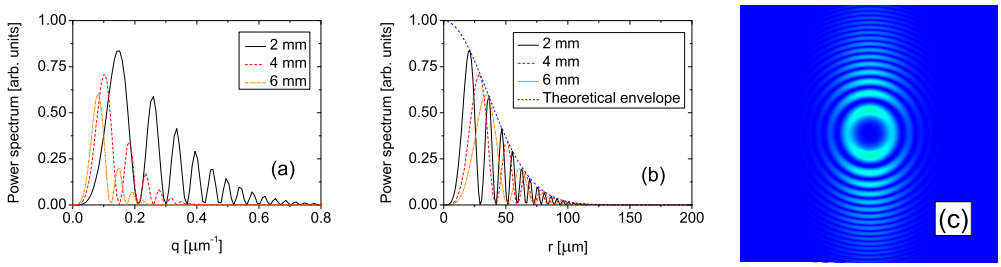

Figure 4.13: (a) Simulated horizontal profiles of power spectra of heterodyne speckles for different sample-detector distances z. It can be noticed how they progressively shrink as z increases. (b) Master curve $C(\Delta r)$ for spatial coherence obtained through the scaling of Eq. 4.30. The common envelope of the Talbot oscillations fits the theoretical squared modulus of the radiation CCF of the form $\exp(-\Delta x^2)/\sigma_{\mathrm{coh}}^2$. The parameters of the simulation are $\lambda = 440$ nm and $\sigma_{\mathrm{coh}} = 50$ μm. (c) Simulated 2-D power spectrum corresponding to a 2-D Gaussian CCF of the form $\exp(-x^2/\sigma_{\mathrm{coh,x}}^2)\exp(-y^2/\sigma_{\mathrm{coh,y}}^2)$, where $\sigma_{\mathrm{coh,x}} = 50$ μm and $\sigma_{\mathrm{coh,y}} = 150$ μm. The resulting envelope of the Talbot oscillation is elongated in the vertical direction as expected.

Under this scaling, the curves $C(\vec{q}, z)$ measured at different distances generate the master curve $C(\tau)$ describing the radiation CDC. Opposite to the case of spatial coherence, Talbot oscillations superimpose, as shown in Fig. 4.14(a),(b). Finally, since $\vec{q}_{\mathrm{max}}$ depends only on the scalar quantity τ_{coh}, it is independent on the orientation in the $(x$-$y)$ plane and power spectra, as well as the Talbot oscillation, are endowed with circular symmetry, as depicted in Fig. 4.14(c). It is worth noting how this property of the temporal master curve is due to the circularly symmetric spherical wavefronts scattered by the particles and probing the transmitted incident field.

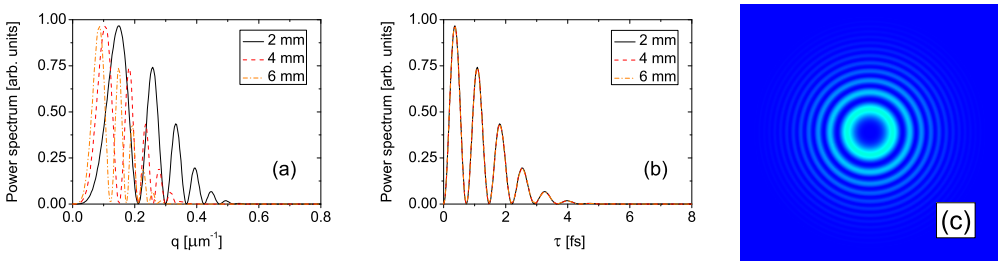

Figure 4.14: (a) Simulated radial profiles of power spectra of heterodyne speckles for different sample-detector distances z. It can be noticed how they progressively shrink as z increases. (b) Master curve $C(\tau)$ for temporal coherence obtained through the scaling of Eq. 4.31. The common envelope of the Talbot oscillations fits the theoretical squared modulus of the radiation CDC of the form $\exp(-t^2)/\tau_{\mathrm{coh}}^2$. The parameters of the simulation are $\lambda = 440$ nm and $\tau_{\mathrm{coh}} = 2$ fs. Opposite to the case of spatial coherence reported in Fig. 4.13, Talbot oscillation superimpose. (c) Simulated 2-D power spectrum corresponding to a Gaussian CDC of the form $\exp(-t^2/\tau_{\mathrm{coh}}^2)$, where $\tau_{\mathrm{coh}} = 2$ fs as before. Due to the spherical wavefront scattered by the particles, temporal delays are the same regardless of the azymuthal angle and the power spectrum exhibit a peculiar circular symmetry.

We would like to remark that the possibility of introducing scaling laws for the spatial and temporal coherence and hence the possibility to generate the master curves $C(\Delta r)$ and $C(\tau)$ from power spectra of heterodyne speckle fields is intimately related to the spherical nature of the scattered wavefront. In fact, despite the squared modulus of

the Fourier transform does not preserve the information on spatial localization of the interference fringes, the quadratic term in the phase of the scattered waves causes the spatial frequency of the interference fringes to increase as a function of the distance from the scattering center. This implies that spatial frequencies can be mapped into transverse displacements (for the case of spatial coherence) or into into temporal delays (for the case of temporal coherence).

CHAPTER 5

Theoretical basis of the HNFS technique

5.1 Mathematical description

The intensity distribution of heterodyne speckle fields generated by an ensamble of N scattering particles is given by

$$I(x,y,z) = I_0(x,y,z) + 2Re\langle E_0(x,y,z,t)E_s^*(x,y,z,t)\rangle, \tag{5.1}$$

where (x,y) denote transverse coordinates across the detection plane at a distanze z downstream the colloidal suspension. E_0 denotes the incoming radiation, I_0 is the corresponding intensity distribution and E_s is the field scattered by the spherical nanoparticles.

The two terms in Eq. 5.1 have substantially different temporal behaviors. The first term is time-independent, being related to the detected intensity distribution of the incoming radiation. The second term instead represents a time-varying contribution, owing to the Brownian motion of the particles inside the suspension. The static component $I_0(x,y,z)$ can thus be removed by acquiring and comparing different frames[1], yielding the heterodyne signal

$$i(x,y,z) = 2Re\langle E_0(x,y,z,t)E_s^*(x,y,z,t)\rangle. \tag{5.2}$$

5.1.1 Plane-wave approximation

Inspection of Eq. 5.2 reveals that the transmitted incoming field, which is the object of our study, is evaluated at a distance z from the sample. Since we want to investigate the coherence properties of the radiation at the scattering plane, this in general introduces undesired variation of the field phases. However, assuming $z < \sigma_{\rm coh}^2/\lambda$ with $\sigma_{\rm coh}$ indicating the transverse coherence length, diffraction effects can be neglected. This condition is equivalent to the requirement that the coherence areas of the radiation beam subtend an angle much larger than their natural diffraction angle $\theta_{\rm diffr} = \lambda/\sigma_{\rm coh}$. The transmitted field at the sensor plane is thus related to the field at the scattering plane by a simple phase shift given by the following plane-wave relation:

$$E_0(x,y,z,t) = E_0\left(x,y,z=0,t-\frac{z}{c}\right)e^{ikz}, \tag{5.3}$$

where we have also taken into account that the field at the detection plane at time t is determined by the incoming field at the earlier time $t - z/c$ due to the finite propagation velocity of optical signals.

[1] We will see in the next chapter how to properly reduce HNFS data by means of two different procedures [54] exploting the computation of the mean frame (Single-Frame Analysis, SFA) or of image differences (Double-Frame Analysis, DFA), respectively.

5.1.2 Paraxial approximation

Exploting the Huygens-Fresnel's principle [46], the scattered field from all scatterers at positions (x_i, y_i) can be written as

$$E_s(x,y,z,t) = \sum_{i=1}^{N} E_{\mathrm{s,i}}(x,y,z,t) = \sum_{i=1}^{N} E_0\left(x_i, y_i, z=0, t-\frac{\rho_i}{c}\right) S(\theta_i)\frac{e^{ik\rho_i}}{\rho_i}, \tag{5.4}$$

where ρ_i is the distance between the i-th particle and the detection point, θ_i is the corresponding angle and $S(\theta_i)$ is the particle form factor of scattering theory [56]. Under paraxial conditions,

$$\rho_i = z + \frac{(x-x_i)^2+(y-y_i)^2}{2z} \qquad \theta_i = \frac{\sqrt{(x-x_i)^2+(y-y_i)^2}}{z}, \tag{5.5}$$

and the field scattered by the i-th particle can be written as

$$E_{\mathrm{s,i}} = E_0\left(x_i, y_i, z=0, t-\frac{\rho_i}{c}\right) S\left(\theta_i\right) \frac{e^{ikz}}{z} e^{ik\frac{(x-x_i)^2+(y-y_i)^2}{2z}}. \tag{5.6}$$

In the following, we will omit the dependence on the longitudinal coordinate $z = 0$ for the fields evaluated at the scatering plane for notational simplicity.

Substituing Eq. 5.3 and Eq. 5.4 into Eq. 5.2, the heterodyne signal takes the form

$$\begin{aligned}
i(x,y,z) &= 2Re\left\langle E_0(x,y,z,t)\sum_{i=1}^{N} E^*_{\mathrm{s,i}}(x,y,z,t)\right\rangle = \\
&= 2Re\sum_{i=1}^{N}\left\langle E_0(x,y,z,t)E^*_{\mathrm{s,i}}(x,y,z,t)\right\rangle = \\
&= \frac{2}{z}Re\sum_{i=1}^{N}\left\langle E_0\left(x,y,t-\frac{z}{c}\right)E_0^*\left(x_i,y_i,t-\frac{\rho_i}{c}\right)\right\rangle S(\theta_i)e^{-ik\frac{(x-x_i)^2+(y-y_i)^2}{2z}} = \\
&= \frac{1}{z}\sum_{i=1}^{N}\left\langle E_0\left(x,y,t-\frac{z}{c}\right)E_0^*\left(x_i,y_i,t-\frac{\rho_i}{c}\right)\right\rangle S(\theta_i)e^{-ik\frac{(x-x_i)^2+(y-y_i)^2}{2z}} + c.c.,
\end{aligned} \tag{5.7}$$

where $c.c.$ denotes complex conjugate. Taking the spatial Fourier transform of Eq. 5.7 we obtain

$$\begin{aligned}
i(\vec{q},z) = &\frac{1}{z}\sum_{i=1}^{N}\int \mathrm{d}\vec{r}\, e^{i\vec{q}\cdot\vec{r}}\left\langle E_0\left(x,y,t-\frac{z}{c}\right)E_0^*\left(x_i,y_i,t-\frac{\rho_i}{c}\right)\right\rangle S(\theta_i)e^{-ik\frac{(x-x_i)^2+(y-y_i)^2}{2z}} + \\
&+\frac{1}{z}\sum_{i=1}^{N}\int \mathrm{d}\vec{r}\, e^{i\vec{q}\cdot\vec{r}}\left\langle E_0^*\left(x,y,t-\frac{z}{c}\right)E_0\left(x_i,y_i,t-\frac{\rho_i}{c}\right)\right\rangle S^*(\theta_i)e^{ik\frac{(x-x_i)^2+(y-y_i)^2}{2z}},
\end{aligned} \tag{5.8}$$

where $\vec{q} = (q_x, q_y)$ and $\vec{r} = (x, y)$.

The x-component of the complex exponential in the first row of Eq. 5.8 (and similarly for the y-component) can be rewritten as

$$\begin{aligned} iq_x x - ik\frac{(x-x_i)^2}{2z} &= iq_x x - \frac{ik}{2z}x^2 + \frac{ik}{z}xx_i - \frac{ik}{2z}x_i^2 = \\ &= -\frac{ik}{2z}\left[x^2 - 2x\left(x_i + \frac{q_x z}{k}\right) + x_i^2\right] = \\ &= -\frac{ik}{2z}\left(x - x_i - \frac{q_x z}{k}\right)^2 + i\frac{q_x^2 z}{2k} + iq_x x_i. \end{aligned} \tag{5.9}$$

A similar procedure can be applied to the x-component of the complex exponential in the second row of Eq. 5.8 (and similarly for the y-component):

$$\begin{aligned} iq_x x + ik\frac{(x-x_i)^2}{2z} &= iq_x x + \frac{ik}{2z}x^2 - \frac{ik}{z}xx_i + \frac{ik}{2z}x_i^2 = \\ &= \frac{ik}{2z}\left[x^2 - 2x\left(x_i - \frac{q_x z}{k}\right) + x_i^2\right] = \\ &= \frac{ik}{2z}\left(x - x_i + \frac{q_x z}{k}\right)^2 - i\frac{q_x^2 z}{2k} + iq_x x_i. \end{aligned} \tag{5.10}$$

Introducing the squared modulus of the Fourier wavevector $q^2 = q_x^2 + q_y^2$, we can rewrite Eq. 5.8 in the following form:

$$\begin{aligned} i(\vec{q}, z) = &\frac{1}{z}e^{i\frac{q^2 z}{2k}}\sum_{i=1}^{N} e^{iq_x x_i + iq_y y_i} \times \\ &\times \int \mathrm{d}\vec{r}\, e^{-\frac{ik}{2z}\left(x - x_i - \frac{q_x z}{k}\right)^2} e^{-\frac{ik}{2z}\left(y - y_i - \frac{q_y z}{k}\right)^2} \times \\ &\times \left\langle E_0\left(x, y, t - \frac{z}{c}\right) E_0^*\left(x_i, y_i, t - \frac{\rho_i}{c}\right)\right\rangle S(\theta_i) + \\ &+ \frac{1}{z}e^{-i\frac{q^2 z}{2k}}\sum_{i=1}^{N} e^{iq_x x_i + iq_y y_i} \times \\ &\times \int \mathrm{d}\vec{r}\, e^{\frac{ik}{2z}\left(x - x_i + \frac{q_x z}{k}\right)^2} e^{\frac{ik}{2z}\left(y - y_i + \frac{q_y z}{k}\right)^2} \times \\ &\times \left\langle E_0^*\left(x, y, t - \frac{z}{c}\right) E_0\left(x_i, y_i, t - \frac{\rho_i}{c}\right)\right\rangle S^*(\theta_i) = \\ &= i_1(\vec{q}, z) + i_2(\vec{q}, z). \end{aligned} \tag{5.11}$$

In the first and second integral we perform the following changes of integration variable:

$$\begin{aligned} &\xi_x = x - x_i - \frac{q_x z}{k} \qquad \xi_y = y - y_i - \frac{q_y z}{k} \qquad \text{in } i_1(\vec{q}, z) \\ &\xi_x = x - x_i + \frac{q_x z}{k} \qquad \xi_y = y - y_i + \frac{q_y z}{k} \qquad \text{in } i_2(\vec{q}, z) \end{aligned} \tag{5.12}$$

thus obtaining

$$i_1(\vec{q},z) = \frac{1}{z} e^{i\frac{q^2 z}{2k}} \sum_{\mathrm{i}=1}^{N} e^{i\vec{q}\cdot\vec{x}_i} \int \mathrm{d}\vec{\xi}\, e^{-\frac{ik}{2z}\xi^2} \times$$
$$\times \left\langle E_0\left(\vec{\xi}+\vec{x}_i+\frac{\vec{q}z}{k}, t-\frac{z}{c}\right) E_0^*\left(\vec{x}_i, t-\frac{z}{c}-\frac{\left(\xi_x+\frac{q_x z}{k}\right)^2+\left(\xi_y+\frac{q_y z}{k}\right)^2}{2zc}\right)\right\rangle \times$$
$$\times S\left(\frac{\sqrt{\left(\xi_x+\frac{q_x z}{k}\right)^2+\left(\xi_y+\frac{q_y z}{k}\right)^2}}{z}\right). \tag{5.13}$$

$$i_2(\vec{q},z) = \frac{1}{z} e^{-i\frac{q^2 z}{2k}} \sum_{\mathrm{i}=1}^{N} e^{i\vec{q}\cdot\vec{x}_i} \int \mathrm{d}\vec{\xi}\, e^{\frac{ik}{2z}\xi^2} \times$$
$$\times \left\langle E_0^*\left(\vec{\xi}+\vec{x}_i-\frac{\vec{q}z}{k}, t-\frac{z}{c}\right) E_0\left(\vec{x}_i, t-\frac{z}{c}-\frac{\left(\xi_x-\frac{q_x z}{k}\right)^2+\left(\xi_y-\frac{q_y z}{k}\right)^2}{2zc}\right)\right\rangle \times$$
$$\times S^*\left(\frac{\sqrt{\left(\xi_x-\frac{q_x z}{k}\right)^2+\left(\xi_y-\frac{q_y z}{k}\right)^2}}{z}\right). \tag{5.14}$$

5.1.3 Stationary phase approximation

The field correlation function conveying the information on spatial and temporalcoherence properties of the radiation appear under an integral sign which convolves the information over many transverse displacements and temporal delays. We notice that the complex exponential in ξ^2 makes the integrand fastly oscillating over scales $\xi \gg \sqrt{\lambda z}$. Therefore the integrand gives non-negligible contribution up to values of ξ of the order of $\sqrt{\lambda z}$. If the field correlation function does not vary appreciably for ξ of the order of $\sqrt{\lambda z}$, it can be brought out of the integral, thus acting as a multiplicative factor on the power spectrum.

5.1.4 The particle form factor

The dependence on ξ in the particle form factor can be neglected if $\xi < (\ll) qz/k$. Since in the stationary phase approximation the integration is carried up to $\xi \simeq \sqrt{\lambda z}$, the dependence on ξ can be neglected for reduced spatial frequencies satisfying

$$\frac{1}{q} < (\ll)\sqrt{\lambda z}. \tag{5.15}$$

In practice, we require the colloidal particles to be small enough in order to scatter light roughly isotropically over the range of angles $\theta \sim q/k$ of interest, in order to have $S(\vec{q}) \approx 1$. Under these assumptions, often fulfilled in practice, the particle form factor can be brought out of the integral (and also out of the sum) simply as simply $S(\vec{q})$.

5.2 Spatial coherence

We now assume the incident radiation to be fully temporally coherent: the field at time $t - z/c$ and the field at time $t - \rho_i/c$ are exact replica one of the other. This allows us to drop the dependence on temporal coordinates in both $i_1(\vec{q}, z)$ and $i_2(\vec{q}, z)$:

$$i_1(\vec{q}, z) = \frac{1}{z} S(\vec{q}) e^{i\frac{q^2 z}{2k}} \sum_{i=1}^{N} e^{i\vec{q}\cdot\vec{x}_i} \int \mathrm{d}\vec{\xi}\, e^{-\frac{ik}{2z}\xi^2} \left\langle E_0\left(\vec{\xi} + \vec{x}_i + \frac{\vec{q}z}{k}\right) E_0^*(\vec{x}_i)\right\rangle$$

$$i_2(\vec{q}, z) = \frac{1}{z} S^*(\vec{q}) e^{-i\frac{q^2 z}{2k}} \sum_{i=1}^{N} e^{i\vec{q}\cdot\vec{x}_i} \int \mathrm{d}\vec{\xi}\, e^{\frac{ik}{2z}\xi^2} \left\langle E_0^*\left(\vec{\xi} + \vec{x}_i - \frac{\vec{q}z}{k}\right) E_0(\vec{x}_i)\right\rangle. \tag{5.16}$$

It is seen from Eq. 5.16 that the field correlation function $\langle E_0(\vec{\xi} + \vec{x}_i + \vec{q}z/k) E_0^*(\vec{x}_i)\rangle$, conveying the information on the spatial coherence properties of the radiation at points $\vec{x}_i$ and $\vec{xi} + \vec{x}_i + \vec{q}z/k$, is convolved all over the $\vec{\xi}$-space. However, due to the stationary phase approximation, integration over $\vec{\xi}$ is limited to values less than or of the order of $\sqrt{\lambda z}$. The near field condition for the coherence areas stated via the plane-wave approximation of Eq. 5.3 requires $z < \sigma_{\mathrm{coh}}^2/\lambda$, therefore implying $\xi < (\ll)\sigma_{\mathrm{coh}}$. Since the width of the field correlation function is of the order of σ_{coh}, the stationary phase approximation and the near field condition for the coherence areas allows to neglect the dependence on $\vec{\xi}$ inside the spatial coherence function of the radiation which can then be taken out of the convolution integral. Obviously, the same reasoning applies to field correlation function $\langle E_0^*(\vec{\xi} + \vec{x}_i - \vec{q}z/k) E_0(\vec{x}_i)\rangle$ in the second integral, thus yielding to

$$i_1(\vec{q}, z) = \frac{1}{z} S(\vec{q}) e^{i\frac{q^2 z}{2k}} \sum_{i=1}^{N} e^{i\vec{q}\cdot\vec{x}_i} \left\langle E_0\left(\vec{x}_i + \frac{\vec{q}z}{k}\right) E_0^*(\vec{x}_i)\right\rangle \int \mathrm{d}\vec{\xi}\, e^{-\frac{ik}{2z}\xi^2}$$

$$i_2(\vec{q}, z) = \frac{1}{z} S^*(\vec{q}) e^{-i\frac{q^2 z}{2k}} \sum_{i=1}^{N} e^{i\vec{q}\cdot\vec{x}_i} \left\langle E_0^*\left(\vec{x}_i - \frac{\vec{q}z}{k}\right) E_0^*(\vec{x}_i)\right\rangle \int \mathrm{d}\vec{\xi}\, e^{\frac{ik}{2z}\xi^2}. \tag{5.17}$$

The integrals appearing in Eq. 5.17 are recognized to be Fresnel integrals, thus giving a contribution

$$\int \mathrm{d}\vec{\xi}\, e^{\pm i\left(\frac{k}{2z}\right)\xi^2} = \int \mathrm{d}\xi_x\, e^{\pm i\left(\frac{k}{2z}\right)\xi_x^2} \int \mathrm{d}\xi_y\, e^{\pm i\left(\frac{k}{2z}\right)\xi_y^2} = \pm\frac{2i\pi z}{k}. \tag{5.18}$$

Substituting this result into Eq. 5.17 yields to

$$i_1(\vec{q}, z) = \frac{2i\pi}{k} S(\vec{q}) e^{i\frac{q^2 z}{2k}} \sum_{i=1}^{N} e^{i\vec{q}\cdot\vec{x}_i} \left\langle E_0\left(\vec{x}_i + \frac{\vec{q}z}{k}\right) E_0^*(\vec{x}_i)\right\rangle$$

$$i_2(\vec{q}, z) = \frac{2i\pi}{k} S^*(\vec{q}) e^{-i\frac{q^2 z}{2k}} \sum_{i=1}^{N} e^{i\vec{q}\cdot\vec{x}_i} \left\langle E_0^*\left(\vec{x}_i - \frac{\vec{q}z}{k}\right) E_0(\vec{x}_i)\right\rangle. \tag{5.19}$$

We recall the definition of the Complex Coherence Factor (CCF):

$$\mu(\vec{x}_1, \vec{x}_2) = \frac{\langle E_0(\vec{x}_1) E_0^*(\vec{x}_2)\rangle}{\sqrt{\langle |E_0(\vec{x}_1)|^2\rangle}\sqrt{\langle |E_0(\vec{x}_2)|^2\rangle}}. \tag{5.20}$$

It can be conveniently rephrased in terms of the average position $\vec{\bar{x}} = (\vec{x}_1 + \vec{x}_2)/2$ and of the relative displacement $\Delta\vec{x} = \vec{x}_2 - \vec{x}_2$:

$$\mu(\vec{\bar{x}}, \Delta\vec{x}) = \frac{\langle E_0(\vec{\bar{x}} - \Delta\vec{x}/2) E_0^*(\vec{\bar{x}} + \Delta\vec{x}/2)\rangle}{\sqrt{\langle |E_0(\vec{\bar{x}} - \Delta\vec{x}/2)|^2\rangle}\sqrt{\langle |E_0(\vec{\bar{x}} + \Delta\vec{x}/2)|^2\rangle}}. \tag{5.21}$$

We now make the following assumptions on the spectral degree of coherence:

- polar symmetry with respect to $\Delta\vec{x}$: $\mu(\vec{\bar{x}}, \Delta\vec{x}) = \mu(\vec{\bar{x}}, -\Delta\vec{x})$;
- homogeneity: $\mu(\vec{\bar{x}}, \Delta\vec{x}) = \mu(\Delta\vec{x})$ and $\langle |E_0(\vec{\bar{x}} - \Delta\vec{x}/2)|^2\rangle = \langle |E_0(\vec{\bar{x}} + \Delta\vec{x}/2)|^2\rangle = I_0$.

Under these assumptions, and considering $S(\vec{q})$ real (which is the case of spherical particles), we have

$$s(\vec{q}, z) = \frac{4\pi}{k}\mu\left(\frac{\vec{q}z}{k}\right)\sin\left(\frac{q^2 z}{2k}\right)F(\vec{q}), \tag{5.22}$$

where

$$F(\vec{q}) = S(\vec{q})\sum_{i=1}^{N} e^{i\vec{q}\cdot\vec{x}_i}. \tag{5.23}$$

Taking the square modulus of Eq. 5.22 yields to the following expression for the power spectrum $I(\vec{q}, z)$ of speckle fields:

$$I(\vec{q}, z) = S(\vec{q})T(\vec{q}, z)C(\vec{q}, z), \tag{5.24}$$

where

- $C(\vec{q}, z) = |\mu(\vec{q}z/k)|^2$ is the squared modulus of the radiation CCF;
- $T(\vec{q}, z) = \sin^2(q^2 z/(2k))$ is the Talbot transfer function;
- $S(\vec{q})$ is the squared modulus of the ensamble-averaged particle form factor given in Eq. 5.23.

In order to account for instrumental effects, we introduce the two following contributions:

- the instrumental transfer function $H(\vec{q})$: it arises from the convolution of Eq. 5.2 with the Point Spread Function of the detection system and it determines the maximum spatial frequency (i.e. the smallest intensity modulation) that can be detected;
- the power spectrum of the image shotnoise and of the readout noise $P(\vec{q})$.

Finally, the power spectrum of the heterodyne speckle field is

$$I(\vec{q}, z) = S(\vec{q})T(\vec{q}, z)C(\vec{q}, z)H(\vec{q}) + P(\vec{q}). \tag{5.25}$$

5.3 Temporal coherence

We now assume the incident radiation to be fully spatially coherent in order to drop the dependence on spatial coordinates in both $i_1(\vec{q},z)$ and $i_2(\vec{q},z)$:

$$
\begin{aligned}
i_1(\vec{q},z) &= \frac{1}{z}S(\vec{q})e^{i\frac{q^2 z}{2k}}\sum_{i=1}^{N}e^{i\vec{q}\cdot\vec{x}_i}\times \\
&\times\int \mathrm{d}\vec{\xi}\, e^{-\frac{ik}{2z}\xi^2}\left\langle E_0\left(t-\frac{z}{c}\right)E_0^*\left(t-\frac{z}{c}+\frac{\left(\xi_x+\frac{q_x z}{k}\right)^2+\left(\xi_y+\frac{q_y z}{k}\right)^2}{2zc}\right)\right\rangle \\
i_2(\vec{q},z) &= \frac{1}{z}S^*(\vec{q})e^{-i\frac{q^2 z}{2k}}\sum_{i=1}^{N}e^{i\vec{q}\cdot\vec{x}_i}\times \\
&\times\int \mathrm{d}\vec{\xi}\, e^{\frac{ik}{2z}\xi^2}\left\langle E_0^*\left(t-\frac{z}{c}\right)E_0\left(t-\frac{z}{c}-\frac{\left(\xi_x-\frac{q_x z}{k}\right)^2+\left(\xi_y-\frac{q_y z}{k}\right)^2}{2zc}\right)\right\rangle .
\end{aligned}
\tag{5.26}
$$

The presence of $\vec{\xi}$ inside the field correlation function $\langle E_0(t-z/c)E_0^*(t-z/c+[(\xi_x+q_xz/k)^2+(\xi_y+q_yz/k)^2]/[2zc])\rangle$ convolves the information on temporal coherence over any temporal delay from the $\vec{\xi}$-space to the detection plane. The points on the ξ-plane contributing to the temporal coherence function of width $l_c=\tau_c c$ are those lying within an angle $\theta_c=\sqrt{2l_c/z}$ corresponding to an area of linear extent $\xi_c=\sqrt{2l_c z}$. Owing to the stationary phase approximation, the dependence on $\vec{\xi}$ inside the temporal coherence function can be neglected if $\sqrt{\lambda z}<\sqrt{2l_c z}$ or equivalently $l_c>\lambda/2$. This condition implies that the radiation is able to write at least one interference fringes and is always fulfilled for broadband light, for which interferogram display a few fringes. The same reasoning applies to field correlation function $\langle E_0^*(t-z/c)E_0(t-z/c-[(\xi_x-q_xz/k)^2+(\xi_y-q_yz/k)^2]/[2zc])\rangle$ and allows to take the field correlation functions out of the integrals in both $i_1(\vec{q},z)$ and $i_2(\vec{q},z)$:

$$
\begin{aligned}
i_1(\vec{q},z) &= \frac{1}{z}S(\vec{q})e^{i\frac{q^2 z}{2k}}\sum_{i=1}^{N}e^{i\vec{q}\cdot\vec{x}_i}\times \\
&\times\left\langle E_0(t-\frac{z}{c})E_0^*(t-\frac{z}{c}+\frac{(\xi_x+\frac{q_x z}{k})^2+(\xi_y+\frac{q_y z}{k})^2}{2zc})\right\rangle\int \mathrm{d}\vec{\xi}\, e^{-\frac{ik}{2z}\xi^2} \\
i_2(\vec{q},z) &= \frac{1}{z}S^*(\vec{q})e^{-i\frac{q^2 z}{2k}}\sum_{i=1}^{N}e^{i\vec{q}\cdot\vec{x}_i}\times \\
&\times\left\langle E_0^*(t-\frac{z}{c})E_0(t-\frac{z}{c}-\frac{(\xi_x-\frac{q_x z}{k})^2+(\xi_y-\frac{q_y z}{k})^2}{2zc})\right\rangle\int \mathrm{d}\vec{\xi}\, e^{\frac{ik}{2z}\xi^2}.
\end{aligned}
\tag{5.27}
$$

We introduce the Complex Degree of self Coherence (CDC)

$$
\mu(t_1,t_2)=\frac{\langle E_0(t_1)E_0^*(t_2)\rangle}{\sqrt{\langle|E_0(t_1)|^2\rangle}\sqrt{\langle|E_0(t_2)|^2\rangle}} \tag{5.28}
$$

and we make the following assumptions:

- symmetry with respect to $\tau=t_2-t_1$;

- stazionarity: $\mu(t_1, t_2) = \mu(\tau)$ and $\langle |E_0(t_1)|^2 \rangle = \langle |E_0(t_2)|^2 \rangle = I_0$.

Under these assumptions, and considering $S(\vec{q})$ real (which is the case of spherical particles), we have

$$s(\vec{q}, z) = \frac{4\pi}{k} \mu \left(\frac{q^2 z}{2ck^2} \right) \sin \left(\frac{q^2 z}{2k} \right) F(\vec{q}), \tag{5.29}$$

where $F(\vec{q})$ has already been defined in Eq. 5.23. Accounting for the instrumental response and for the shotnoise and readout noise contribution, the power spectrum $I(\vec{q}, z)$ of speckle fieldshas an identical expression cmpared to the case of spatial coherence

$$I(\vec{q}, z) = S(\vec{q}) T(\vec{q}, z) C(\vec{q}, z) H(\vec{q}) + P(\vec{q}), \tag{5.30}$$

where now $C(\vec{q}, z) = |\mu(q^2 z / (2ck^2))|^2$ is the squared modulus of the radiation CDC.

CHAPTER 6

Data reduction

6.1 Image pre-processing

For each distance z a stack of $N = 100$ images I_i separated by a time lag of 1 s is acquired. A square area of 900×900 pixels is selected from each frame and pre-processed by subtracting the dark noise i_{dark} and by normalizing to the intensity average value $\langle\cdot\rangle_{\mathrm{pixel}}$:

$$i_i = \frac{I_i - i_{\mathrm{dark}}}{\langle I_i - i_{\mathrm{dark}}\rangle_{\mathrm{pixels}}}. \tag{6.1}$$

6.2 Static background subtraction

The use of a dynamical sample ensures a continual renewal of the speckle pattern owing to the stochastic brownian motion of the particles. This allows to separate the static background contribution from the time-varying heterodyne scattered signal.

6.2.1 Single-Frame Analysis (SFA)

In Single-Frame Analysis (SFA) [54] we exploit the fact that the average of the scattered signal over N acquired images reduces to zero in the limit of large N. The static background contribution i_0 is then computed as

$$i_0 = \frac{1}{N}\sum_{i=1}^{N} i_i \tag{6.2}$$

and the heterodyne signal $i_{\mathrm{s,j}}$ of the j-th image generated by the brownian nanoparticles is obtained as

$$i_{\mathrm{s,j}} = i_j - i_0. \tag{6.3}$$

The power spectrum with SFA $I_{\mathrm{SFA,j}}(\vec{q})$ directly conveys the information on the fluctuating part of the signal for each image:

$$I_{\mathrm{SFA,j}}(\vec{q}) = \left|\mathscr{F}[i_{\mathrm{s,j}}](\vec{q})\right|^2. \tag{6.4}$$

6.2.2 Double-Frame Analysis

Under certain assumptions that will be discussed in the following, we may gauge the information on coherence by subtracting two different images I_{j_1} and i_{j_2} acquired at different instants of time (Double-Frame Analysis, DFA [54]). This procedure allows to exactly compensate for the static contribution, leaving the difference between the scattered signals:

$$i_{rms,j_1,j_2} = i_{j_1} - i_{j_2}. \tag{6.5}$$

The power spectrum with DFA has a third term describing the correlation between the two subtracted images:

$$I_{\mathrm{DFA,j_1,j_2}}(\vec{q}) = |\mathscr{F}[i_{j_1}](\vec{q})|^2 + |\mathscr{F}[i_{j_2}](\vec{q})|^2 + 2\Re\mathrm{e}\mathscr{F}[i_{j_1}](\vec{q})\mathscr{F}^*[i_{j_2}](\vec{q}). \tag{6.6}$$

This term can be neglected if the acquisition delay between the two images is large enough to guarantee that the two speckle fields are completely uncorrelated one with respect to the other. In our case, a total temporal separation of at least 50 s is sufficient. The power spectrum with DFA is then twice the power spectrum with SFA:

$$I_{\mathrm{DFA,j_1,j_2}}(\vec{q}) = |\mathscr{F}[i_{j_1}](\vec{q})|^2 + |\mathscr{F}[i_{j_2}](\vec{q})|^2 = 2\,|\mathscr{F}[i_{j_1}](\vec{q})|^2 = 2I_{\mathrm{SFA,j_1}}(\vec{q}). \tag{6.7}$$

6.3 Normalization by local oscillator

In case of uneven illumination, the non-uniform intensity distribution can be (partially) compensate by dividing the heterodyne signal by the average intenisty distribution prior to power spectrum computation. For DFA this is equivalent to

$$i_{\mathrm{s,DFA,j_1,j_2}} = \frac{i_{j_1} - i_{j_2}}{i_{j_1} + i_{j_2}}, \tag{6.8}$$

while for SFA this is done by computing

$$i_{\mathrm{s,SFA,j}} = \frac{i_j - i_0}{i_0}. \tag{6.9}$$

6.4 Shotnoise

Shotnoise arises from the stochastic fluctuations in the photoelectron counts. Due to its random nature, it can be removed in the reciprocal space. The shotnoise contribution can be estimated by computing the power spectrum of a series of images corresponding to the scattering cell filled with only water. In most circumstances, the shotnoise contribution to power spectrum is almostconstnt over the range of Fourier wavevector of interest.

6.5 The instrumental transfer function

The instrumental transfer function determines the response of the detection system to interference fringes of a certain spatial frequencies. It arises from the finite Point Spread Function of the detection device limiting the resolution of any imaging configuration.

At optical wavelengths, it is mainly dictated by the numerical aperture of the microscope objective employed as a magnifying optics. The finite acceptance angle of the

objective determines a cutoff spatial frequency $q_{\max}$ beyond which the system response drop to zero. The instrumental transfer function of such a detection system can be measured independently by using a coherent illumination ($C(\vec{q}) = 1$ by definition) and particle of known size. According to Eq. 5.25 and to Eq. 5.30, the envelope of the Talbot oscillations of the resulting power spectrum reduces to the product $S(\vec{q})H(\vec{q})$. Knowledge of the partcle form factor $S(\vec{q})$ then allows to measure the spatialfrequency response of the detection optics.

For X-ray wavelength, the instrumental transfer function is mainly determined by the scintillator used to convert the incident X-ray photons into visible light [34, 29]. In this case, the response function of the scintillator can be measured with the same HNFS technique exploiting the scaling $\Delta r = qz/k$. In fact, acquiring heterodyne speckle fields sufficiently close to the sample allows to approximate $C(\Delta r) \approx C(0) = 1$, thus providing a direct measurement of $H(\vec{q})$ from the envelopeof the Talbot oscillations. Remarkably, the hypothesis $C(\Delta r) \approx 1$ can be checked by comparing the envelope of power spectra acquired at different sample-detector distances [29] the curves should fit a single master curve in q-coordinates, thus describing a single calibration function. Opposite to this case, when coherence effects are not negligible the envelopes of the power spectra do not superimpose anymore in q. Finally, despite in principle a single measurement at a fixed distance is sufficient to obtain the scintillator calibration function, measurements at many distances improve data quality and the accuracy of the calibration procedure by means of the master curve arising in q-coordinates.

Part III
Results with Table-Top sources

CHAPTER 7

Temporal coherence characterization of visible thermal radiation

7.1 Motivations and experimental layout

While spatial coherence measurements of SR beams with the HNFS technique have already been reported [30, 31, 29], this work constitute the first time that the method is applied to the characterization of temporal coherence properties as well. In this view, we have preliminary tested and validated the temporal scaling and the temporal master curve criterion on a paradigmatic system in Statical Optics, namely thermal radiation from halogen lamps and white Light Emitting Diodes (LEDs) [32, 44]. Thermal radiation from such kind of sources represents a robust and reliable benchmark for the technique since the underlying stochastic process is stationary and homogeneous. This implies that the classical Van Cittert-Zernike's theorem can be applied to infer transverse coherence properties from the intensity profile of the source, while temporal coherence properties are determined by the emitted spectrum by virtue of the Wiener-Khinchine's theorem. Remarkably, it also implies that spatial coherence can be controlled by properly shaping the transverse profile of the source with suitable masks, while the coherence time of the radiation can be increased with narrow band pass filters. Finally, the broad spectrum of such sources allows to test the sensitiviy of the technique to extremely short longitudinal coherence lengths of the order of a few wavelengths (equivalently, coherence times are of the order of a few optical cycles).

The broadband source, either an halogen lamp or a white LED, is placed behind a circular pinhole with a diameter $d = 80$ μm to increase the tranverse coherence length of the emitted radiation. The pinhole lies in the rear focal plane of a converging lens having a focal length $f = 75$ mm. This configuration results in coherence areas of transverse size $\sigma_{\rm coh} = 1.22\lambda f/d = 630$ μm at $\lambda = 550$ nm. Downstream the collimating lens, they behave as laser beams with a Rayleigh range $z_{\rm ff} = \sigma_{\rm coh}^2/\lambda = 720$ mm setting the transition from the Near Field to the Far Field of the coherence areas. The scattering cell is placed immediately after the lens and the resulting heterodyne speckle fields are collected at a maximum sample-detector distance $z_{\rm max} = 70$ mm lying in the Near Field of the coherence areas. The colloidal suspension consists of polystyrene spheres 1 μm in diameter suspended in water. Dilution down to a volume fraction of the order of 10^{-5} w/w ensures heterodyne conditions. Images are acquired with a PCO1600 CCD camera with a resolution of 1600×1200 pixels and with a pixel size of 7.1 μm.

Within the range of distances probed, coherence areas induce optical path differences between the transmitted radiation beam and the scattered spherical waves larger than $\Delta l = \sigma_{\rm coh}^2/(2z_{\rm max}) = 3$ μm. Temporal coherence of broadband white light source can then be accessed, since typical longitudinal coherence lengths rarely exceed 2 μm. Equivalently, the first Fresnel zone reaches its maximum transverse size $\sqrt{\lambda z} \sim 200$ μm at

$z = 70$ mm. This value is smaller than the transverse coherence length of the radiation by a factor 3, implying that $n = 9$ Fresnel zones lie within a coherence area (the squared term $9 = 3^2$ comes from the $\sqrt{n}$ dependence for the n-th order Fresnel zone). Therefore temporal coherence effects are dominant as long as the longitudinal coherence length of the radiation is shorter than $9\lambda \sim 5$ μm .

7.2 Probing temporal coherence of thermal radiation: results

7.2.1 Results for broad-spectrum halogen lamps

An example of two-dimensional power spectrum of the acquired heterodyne speckle fields for the case of a broad-spectrum halogen lamp is shown in Fig. 7.1. It exhibits perfect circular symmetry and few Talbot oscillations, thus denoting an extremely short longitudinal coherence length of the order of a few radiation wavelengths.

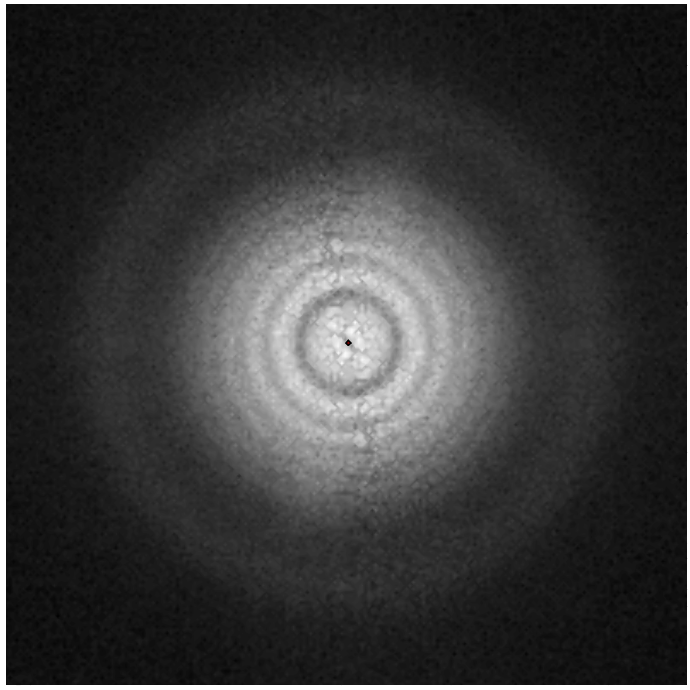

Figure 7.1: Two-dimensional power spectrum of broadband thermal radiation from an halogen lamp. Perfect azymuthal symmetry is a signature of partial temporal coherence. The small number of visible Talbot oscillations implies an extremely short longitudinal coherence length.

Power spectra at larger sample-detector distances gradually shrink towards lower q as a consequence of the limited temporal coherence, as expected from the theory developed in Chap. 4 and Chap. 5. This is confirmed by Fig. 7.2, where angular averages at different sample-detector distances are reported, and by Fig. 7.3, showing how Talbot oscillations superimpose under the temporal scaling of Eq. 4.31.

Upon reduction for the particle form factor and for the instrumental transfer function of the magnifying optics, average of the upper and lower envelopes of Talbot oscillations finally provides a direct measurement of the squared modulus of the radiation CDC.

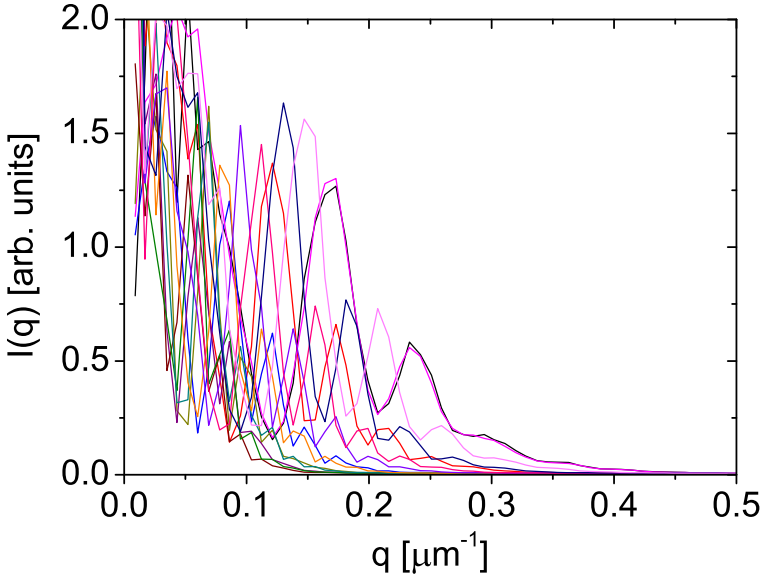

Figure 7.2: Collection of angular averages of power spectra of broadband thermal radiation.

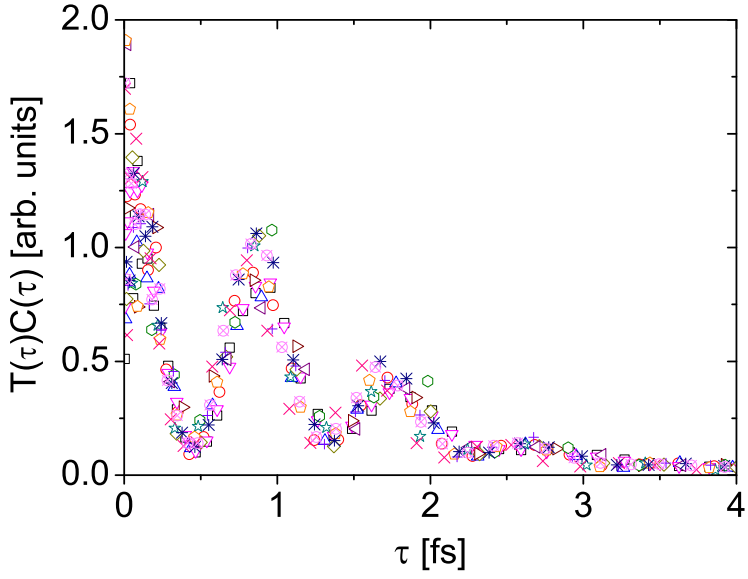

Figure 7.3: Talbot oscillations of broadband thermal radiation superimpose under the temporal scaling revealing partial temporal coherence of the emitted thermal radiation.

Results are reported in Fig. 7.4 and in Fig. 7.5, showing the upper and lower envelopes of the Talbot oscillations and the temporal master curve $C(\tau)$, respectively.

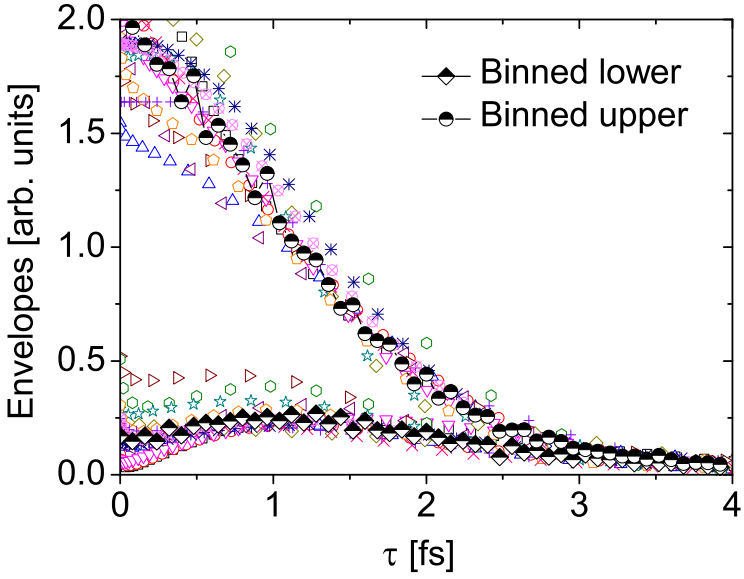

Figure 7.4: Superposition of the upper and lower envelopes of Talbot oscillations for thermal radiation under the temporal scaling.

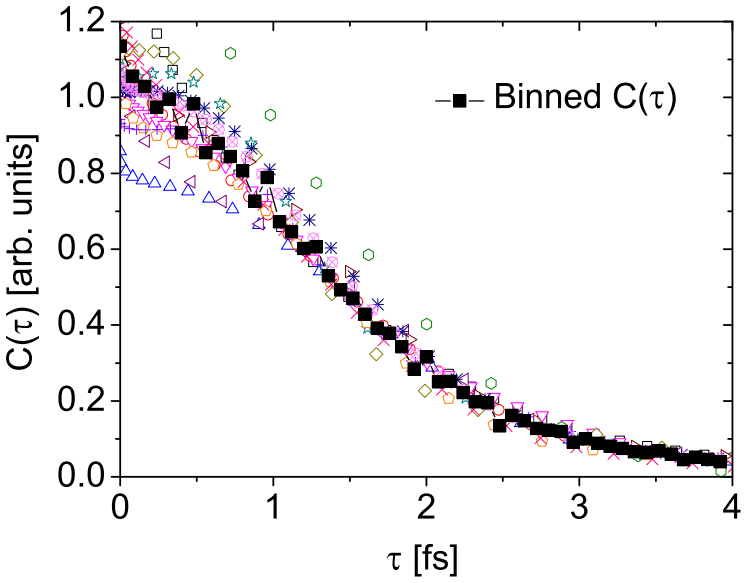

Figure 7.5: Temporal master curve for broadband thermal radiation by an halogen lamp.

Following Mandel, the coherence time of the radiation is

$$\tau_{\mathrm{coh}} = \int_{-\infty}^{+\infty} |\gamma(\tau)|^2 \, \mathrm{d}\tau = 2 \int_{0}^{+\infty} C(\tau) \, \mathrm{d}\tau = 2.82 \text{ fs}. \tag{7.1}$$

Results are in good agreement with independent measurements performed with a grating spectrometer by Hamamatsu with a wavelength resolution of about 2 nm. From the measured power spectral density reported in Fig. 7.6, the FWHM bandwidth corresponds to a coherence time $\tau_c = 0.664\lambda^2/(c\Delta\lambda) = 2.89$ fs (the multiplicative factor 0.664 stems for the Gaussian-like shape of the emitted spectrum [36]), which compares to the value from the HNFS temporal master curve.

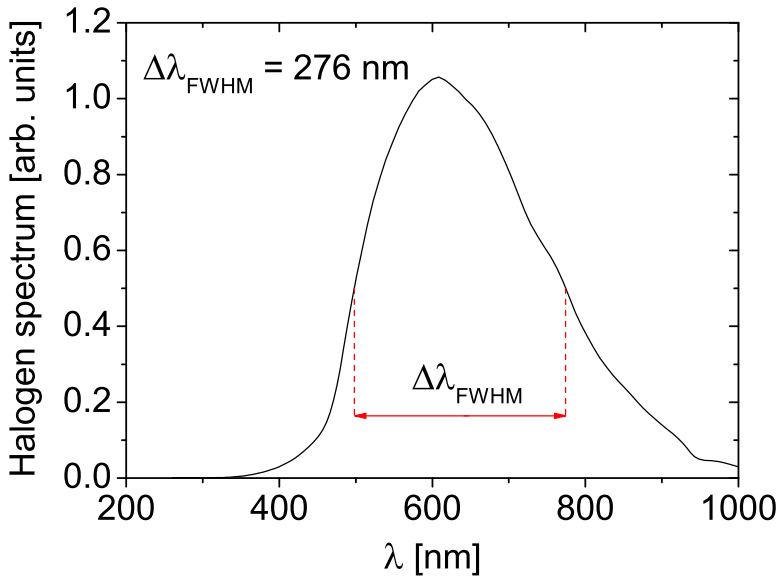

Figure 7.6: Power spectral density emitted by the halogen lamp measured with a grating spectrometer. The FWHM inverse bandwidth is in agreement with the coherence time measured with the HNFS method.

7.2.2 Results for white Light Emitting Diodes

Interesting results regarding the degree of accuracy of the technique have been obtained for the case of a white LED source. In fact, power spectra exhibit a peculiar renewal of Talbot oscillations beyond the decay to shotnoise level, as shown in Fig. 7.7 where data at different sample-detector distances superimpose under the temporal scaling. The squared root of data is visualized to enhance the renewal of the temporal master curve and to directly provide the modulus of the radiation CDC.

The echo in the temporal coherence function can be ascribed to the presence of two sharp peaks in the LED spectrum. It is analogous to the beating effects between two superimposing sound waves at slightly different frequencies. Therefore, from the position $\tau = 7$ fs of the secondary maximum we can retrieve the wavelength separation $\Delta\lambda$ between the peaks as $\Delta\lambda = \lambda^2/(c\tau) = 119$ nm at an average wavelength $\lambda = 500$ nm. Results are in agreement with the LED power spectral density measured with the grating spectometer and reported in Fig. 7.8.

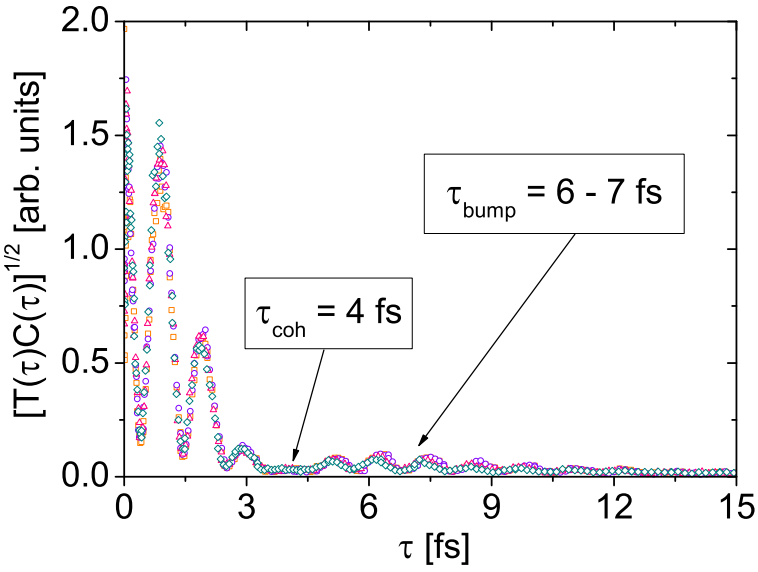

Figure 7.7: Echoes in the Talbot oscillations for the thermal light coming from a LED. Beyond the decay to shotnoie level at around $\tau = 4$ fs, a renewal of Talbot oscillations is observed at $\tau \approx 7$ fs. The good fit to the temporal master curve proves that it is an intrinsic feature of the radiation CDC.

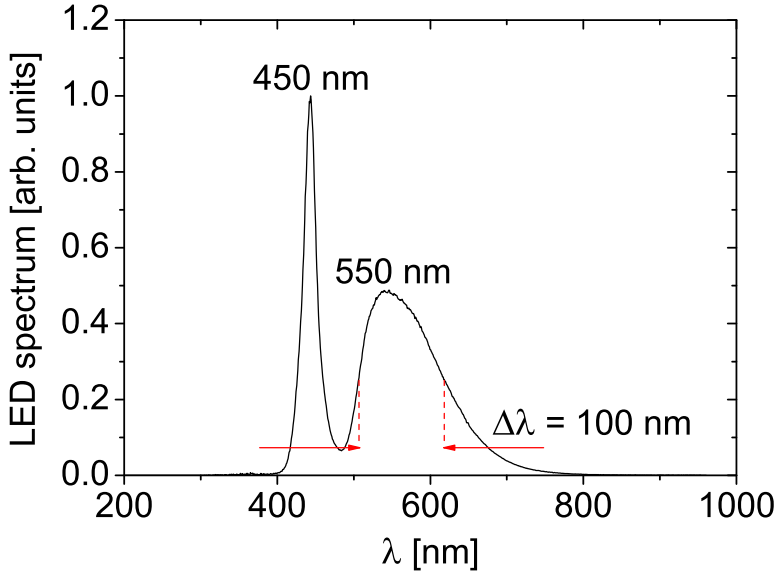

Figure 7.8: Power spectral density of the radiation emitted by the LED, showing a double peak responsible for the echo of the radiation CDC visible in Fig. 7.7.

7.3 Analogical Optical Modeling

A fashinating outcome of the HNFS technique is the possiility of performing Analogical Optical Modeling with visible table-top setups for a variety of cases, as for example for

much complex and expensive X-ray radiation sources. In particular, as it will be discussed in details below, there is a strong similarity between our experiments with visible light source and the broad-spectrum X-ray betatron radiation emitted in laser-driven accelerators. Therefore, the parameters of our experimental setpu previously described have been properly scaled to reproduce the main features of the X-ray betatron radiation emitted in the laser-plasma accelerator under development at the SPARC_LAB facility in Frascati, Rome (Italy) [57, 14].

We notice that maxima of the Talbot transfer function (enveloped by the radiation Mutual Coherence Function) appear at wavevector q related to the other experimental parameters by $z\lambda q^2/(4\pi) = \text{const}$. Since the Fourier wavevector q are entirely determined by the detector, the distance z can be set according to the working wavelength in order to keep Talbot maxima at the same position for both the experiments at X-ray wavelengths and the experiments with table-top visible sources. Typically, z is of the order of a few millimeters for visible radiation, while it ranges between a few centimeters and a few meters at X-ray wavelengths.

The longitudinal coherence length of the broadband betatron radiation is envisioned to be of the order of two or three wavelengths. The comparison between the n-th order Fresnel zone for $n = 3$ and the transverse coherence length of the betatron radiation then sets the working distance z to probe temporal coherence properties, according to Eq. 4.13. It is then scaled to visible wavelengths as previously discussed. By filtering the broad-spectrum thermal radiation from an halogen lamp or from a white LED with suitable band-pass filters, we set in a condition to have $n = \lambda/\Delta\lambda \sim 3$. The corresponding n-th order Fresnel zone determines the minimum transverse coherence length to probe the radiation CDC by inverting Eq. 4.13. It can then be set by a proper combination of apertures and converging lens, as discussed in Sect. 7.1.

This procedure ensures that in both cases Talbot oscillations are progressively depressed by the limited coherence length of the radiation. Furthermore, the same number of observable oscillations at the same positions can be used to retrieve temporal coherence properties of the X-ray betatron radiation, as well as of thermal radiation.

Analogical Optical Modeling thus represents a powerful tool for reproducing the experimental conditions of current and future X-ray sources. The behaviour of Talbot oscillations can be accurately reproduced, in order to mimic the data and therefore the analysis procedures to extract the coherence information. For the case of betatron radiation, this has been demonstrated to be advantageous to characterize the acceleration process inside the plasma [11, 12, 13, 14, 15, 16]

CHAPTER 8

Coherence properties of a VIS-UV High Harmonic Generation (HHG) laser

We performed HNFS coherence measurements on the High Harmonic Generation (HHG) laser at the Laser Laboratory of the ELETTRA Synchrotron Light Source, Trieste. The laser light source exploits an Optical Parametric Amplifier (OPA) to generate radiation with tunable wavelength in the visible and ultraviolet range. Characterization of the transverse and temporal coherence properties of the photon beam is fundamental in view of coherent non-linear pump-probe experiments on electronic and spin systems, as well as for future four-wave mixing experiments with seeded Free-Electron Lasers. The main parameters of the HHG laser are summarized in Tab. 8.1.

Pulse duration	σ_T	300 fs
Energy per pulse	-	400 μJ
Max rep. rate	-	1 MHz
Min rep. rate	-	single shot
Operational rep. rate	-	50 kHz
Beam size	σ	5 mm

Table 8.1: Main parameters of the HHG pulsed laser at the ELETTRA synchrotron.

8.1 Results for the second harmonic at 630 nm

Visible radiation at $\lambda = 630$ nm is obtained directly from the OPA as the second harmonic of the fundamental wavelength at 1260 nm (infrared region). The radiation beam directly reaches the HNFS diagnostics without passing through any optical components. The sample consisted of polystyrene spherical particles 1 μm in diameter suspended in water and stored in a 1-mm-thick quartz cuvette. Dilution down to a volume fraction $\sim 10^{-5}$ w/w ensures heterodyne conditions ($\sim$ 90-95 % transmitted intensity). Speckle fields have been acquired with a PCO1600 CCD camera coupled to a 10X microscope objective at distances downstream the sample ranging between 10 mm and 90 mm. For each distance, a stack of 100 images with a temporal lag of 1 s is recorded and then processed with DFA. Examples of speckle fields for the second harmonic of the HHG laser are reported in Fig. 8.1. The increase in speckle size as the detection plane is farther from the sample is a clear signature of partial coherence.

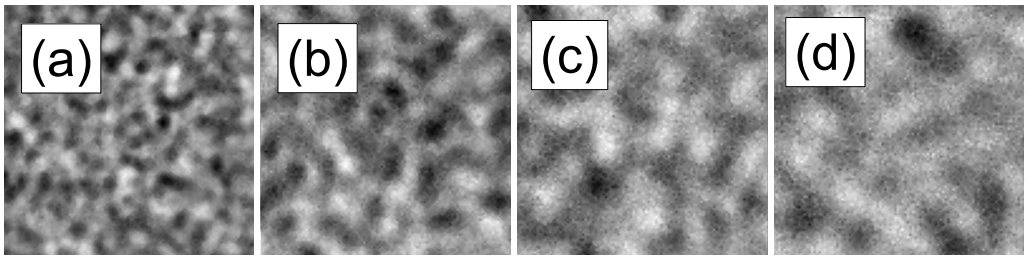

Figure 8.1: Raw images of heterodyne speckle fields generated by the HHG laser second harmonic acquired at different sample-detector distances: (a) 7 mm, (b) 17 mm, (c) 27 mm and (d) 37 mm. Operational wavelength is 630 nm. The increase in speckle size as a function of the sample-detector distance is a signature of partial coherence. Each image shows a selected region of 100×100 pixels of the entire 1024×1024 processed frame.

Two-dimensional power spectra have azymithal symmetry allowing to compute the curves $I(q)$ as angular averages over the whole range $[0, 2\pi]$. They exhibit tapered Talbot oscillations at lower q due to the walkoff effect induced by the finite sensor size [58, 59, 60]. This prevents to generate the master curves upon the scalings described in Eq. 4.30 or in Eq. 4.31 unless the average of the upper and lower envelopes is computed. However, the dacay of the power spectrum to shotnoise level is caused by the limited coherence of the radiation since the curves $I(q)$ do not superimpose in q. Results are reported in Fig. 8.2.

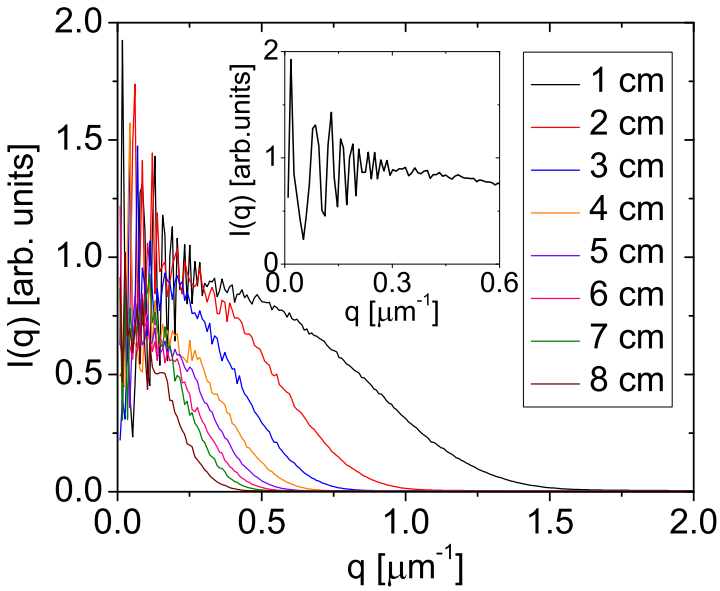

Figure 8.2: Angular averages of heterodyne speckle power spectra for the HHG laser second harmonic. Tapered Talbot oscillations are clearly visible at lower q. Partial coherence prevents power spectra to properly fit a single master curve. (inset) Enlarged view of the profile corresponding to $z = 1$ mm to better evidence the effects of the Talbot transfer function.

The inset in Fig. 8.2 shows an enlarged view of the curve $I(q)$ for the sample-detector distanze $z = 1$ cm to better evidence the tapered Talbot oscillations. The functions $C(q)$ at lower q are then retrieved by computing the average between the upper and the lower envelopes of the Talbot oscillations. The resulting coherence functions $C(q)$ are reported in Fig. 8.3 under the spatial scaling and in Fig. 8.4 under the temporal scaling. Interestingly, data do not fit neither the spatial master curve nor the temporal one, thus impliying both limited spatial and temporal coherence.

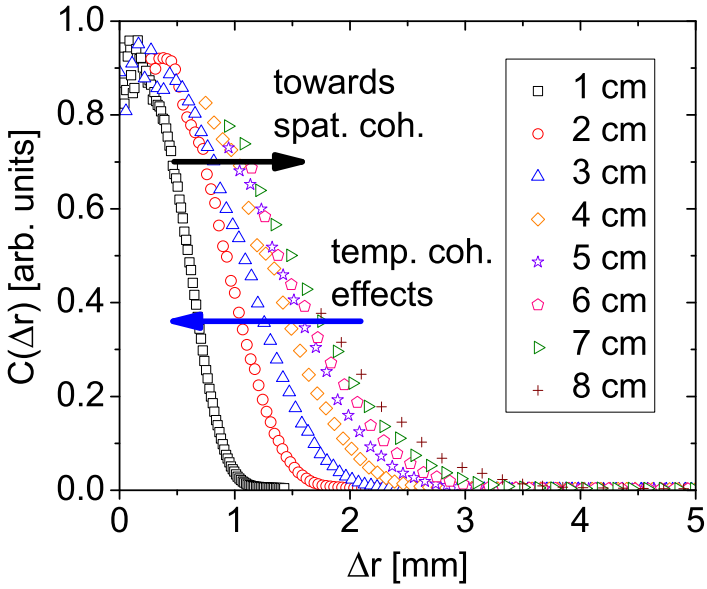

Figure 8.3: Effects of the spatial scaling on power spectra profiles of the HHG laser second harmonic. Data fail to fit a single master curve, denoting the presence of limited temporal coherence effects (blue arrow). Curves are expected to better superimpose at ever larger z (black arrow), since the optical path differences Δl within a coherence area σ_{coh} decrease as $\Delta l = \sigma_{\mathrm{coh}}^2/(2z)$.

With reference to Fig. 8.4, the only exception is represented by the two shortest sample-detector distances $z_1 = 1$ cm and $z_2 = 2$ cm, which succeed in fitting the temporal master curve. Results are reported in Fig. 8.5, together with the binned $C(\tau)$. Integration of the measured squared modulus of the radiation CDC yields to a coherence time of

$$\tau_{\mathrm{coh}} = \int_{-\infty}^{+\infty} |\gamma(\tau)|^2 \, \mathrm{d}\tau = 2 \int_{0}^{+\infty} C(\tau) \, \mathrm{d}\tau = 190 \text{ fs}, \tag{8.1}$$

roughly corresponding to half the pulse duration $\sigma_T = 300$ fs. This is compatible with nearly Fourier-transform-limited radiation pulses and it provides evidence of two longitudinal modes per pulse. Furthermore, temporal coherence effects can only be measured under (nearly) full spatial coherence over the corresponding probed transverse displacements Δr, i.e. roughly 2 mm referring to the horizontal scale in Fig. 8.3 and considering only the curves at z_1 and z_2. This value compares with the radiation beam size, thus probing large coherence areas and a high degree of spatial coherence for the second harmonic of the HHG laser.

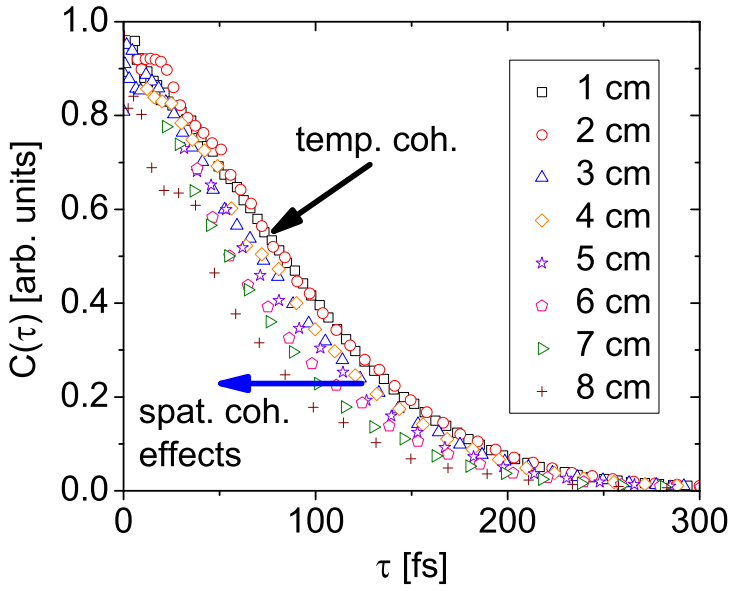

Figure 8.4: Effects of the temporal scaling on power spectra profiles of the HHG laser second harmonic. Data fail to fit a single master curve thus implying partial spatial coherence (blue arrow). Exception is represented by the two shortest sample-detector distances for which the curves $C(\tau)$ effectively superimpose (black arrow).

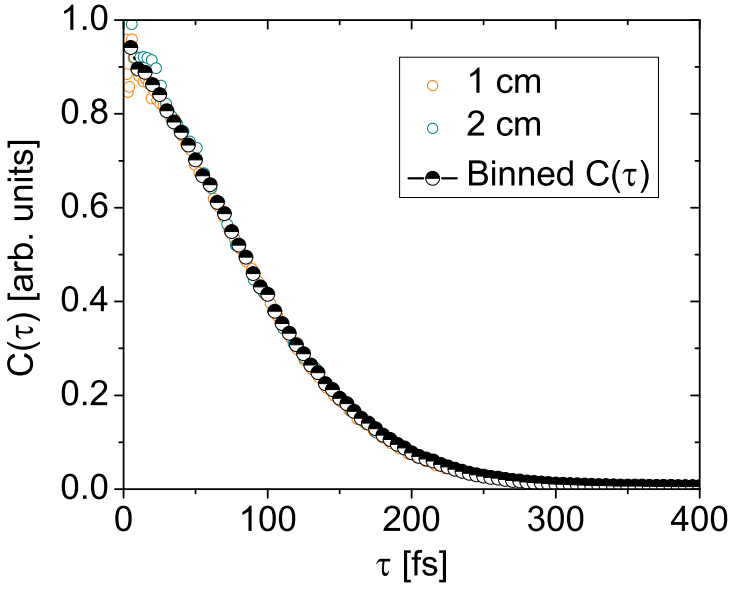

Figure 8.5: Temporal master curve of the HHG laser second harmonic generated by the two shortest sample-detector distances. It is related to a coherence time $\tau_{\mathrm{coh}} = 190$ fs, roughly half the pulse duration $\sigma_T = 300$ fs. Each pulse carries two longitudinal modes.

Knowledge of the laser beam CDC as in Fig. 8.5 allows to retrieve the radiation CCF from the measured spatio-temporal coherence function. One has to firstly express the temporal coherence function $C(\tau)$ in terms of Fourier wavevectors q by inverting the temporal scaling law. Secondly, the power spectra envelopes $C(q)$ are divided by the squared modulus of the radiation CDC rescaled $C(q = q(\tau))$. Finally, the reduced envelope $C_{\mathrm{red}}(q)$ are rescaled according to the spatial scaling in order to fit the spatial master curve. The results of this procedure are summarized in Fig. 8.6, where a fair superposition of the reduced envelopes for the different sample-detector distances is shown. The binned master curve $C(\Delta r)$ is also reported, together with a Gaussian fit to better estimate the transverse coherence length. Following Mandel, the transverse coherence length is given by

$$\sigma_{\mathrm{coh}} = \int_{-\infty}^{+\infty} |\mu(\Delta r)|^2 \, \mathrm{d}\Delta r = 2 \int_{0}^{+\infty} C_{\mathrm{fit}}(\Delta r) \, \mathrm{d}\Delta r = 3.83 \, \mathrm{mm}, \tag{8.2}$$

comparable to the transverse beam size. From the measured value of the transverse coherence length we can thus estimate the degree of transverse coherence of the HHG laser as

$$\zeta = \frac{\int_{-\infty}^{+\infty} |\mu(\Delta r)|^2 \, \mathrm{d}\Delta r}{\int_{-\infty}^{+\infty} I(x) \, \mathrm{d}x} = \frac{\sigma_{\mathrm{coh}}}{\sigma} = 0.77. \tag{8.3}$$

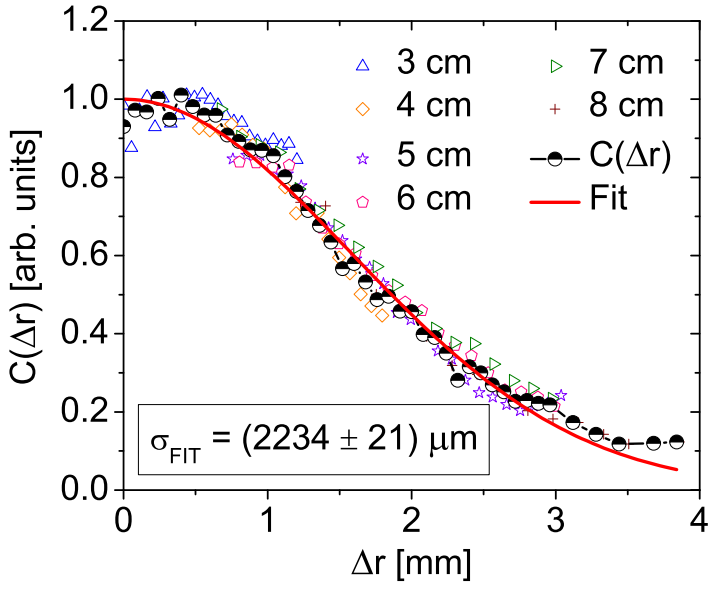

Figure 8.6: Spatial master curve of the HHG laser second harmonic obtained by reducing data at different distances by the measured temporal master curve $C(\tau)$. The good fit to the spatial master curve experimentally proves reducibility of the Mutual Coherence Function of the HHG laser second harmonic. A Gaussian fit to the function $\exp(-\Delta r^2/\sigma_G^2)$ is also reported (solid red curve) to better estimate the dimension of the transverse coherence areas. The transverse coherence length $\sigma_{\mathrm{coh}} = 3.83$ mm, compared to the beam size $\sigma = 5$ mm, implies 1.3 transverse modes.

Finally, we can reconstruct the full two-dimensional Mutual Coherence Function (MCF) of HGG pulses by merging the measured CCF and CDC. In fact, the good fit of the spatial master curve as in Fig. 8.6 upon reduction of power spectra for the temporal master curve in Fig. 8.5 provides an experimental verification of MCF reducibility:

$$\gamma_{12}(\tau) = \mu(\Delta r)\gamma(\tau). \tag{8.4}$$

The two-dimensional MCF can then be reconstructed from the product of the spatial and temporal master curves. Results are shown in Fig. 8.7(a), where we have assumed symmetry properties $\mu(-\Delta r) = \mu(\Delta r)$ and $\gamma(-\tau) = \gamma(\tau)$) for the radiation CCF and CDC, respectively, while Fig. 8.7(b) shows a 3-D view of the HHG spatio-temporal coherence function.

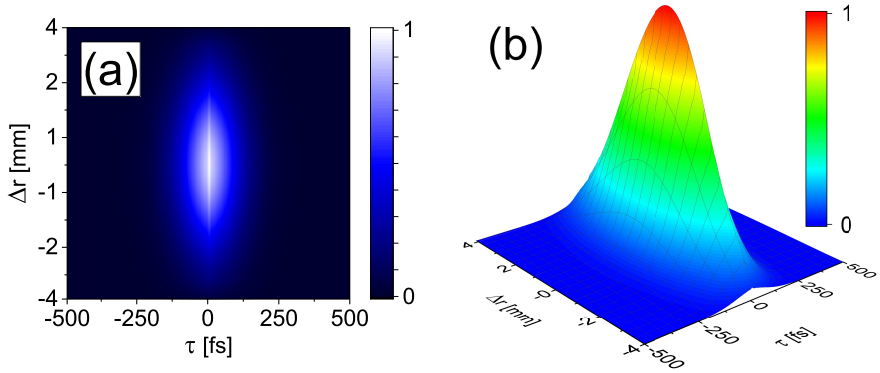

Figure 8.7: (a) Two-dimensional Mutual Coherence Function $\gamma_{12}(\tau)$ of the HHG laser second harmonic and (b) a 3-D view.

8.2 Results for the fourth harmonic at 248 nm

The fourth harmonic is obtained from the second harmonic generated by the OPA and using a non-linear crystal (NL-XTAL) for an additional second harmonic generation. A prism is placed downstream to separate the angularly separate the co-propagating second and fourth harmonic. The radiation wavelength has been tuned to the value $\lambda = 248$ nm (VIS-UV range) from the fundamental wavelength of 992 nm.

Opposite to the case described in the previous section, the HNFS diagnostics could not be effectively operated due to an unexpected speckle-like distorsion in the laser wavefront, as reported in Fig. 8.8. Such wavefront modulation is similar to homodyne speckles arising from scattering of a highly coherent radiation from a rough surface, whose roughness is comparable or larger than the incident wavelength. By definition, the transverse coherence length is determined by the transverse extent of such diffraction-limited speckle patches, thus considerably lowering the spatial coherence properties of the HHG fourth harmonic. In fact, an ideal lens without aberrations would focus down to diffraction limit only an area of the order of the average speckle size.

The optical component affecting the transverse beam quality can be precisely determined by studying the transverse size of the speckle patches as a function of the distance. In fact, diffraction-limited speckles grow linearly in size as the distance z from the scattering surface is increased, with ideally null size at $z = 0$ (Van Cittert - Zernike's

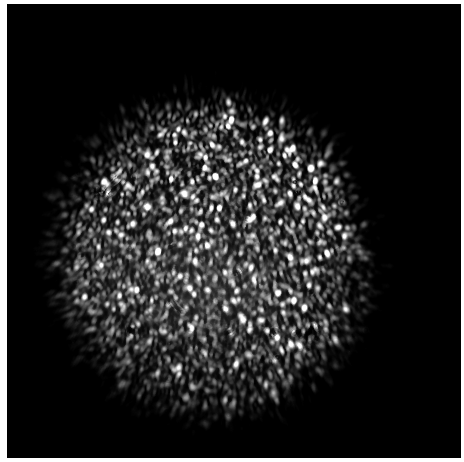

Figure 8.8: The wavefront of the HHG laser fourth harmonic tuned at 248 nm (VIS-UV wavelength range) has a speckled appearance. Speckle patches are generated by a surface whose roughness is comparable to, or larger than, the incident wavelength.

theorem). Three different optical elements may generate the observed speckled distortion: the non-linear crystal, the prism or the mirror used to deflect light towards the HNFS diagnostics. The one generating the speckle patches is recognized by the aforementioned zero-offset criterion for the speckle size as a function of the distance from each of the three elements. Results are shown in Fig. 8.9 and they identify the deflecting mirror as the rough scattering surface. It shall be replaced by an optical component with a higher flatness in order to restore the transverse coherence properties of the HHG fourth harmonic.

Remarkably, coherence properties of the wavefront before impinging on the rough mirror could be evaluated from the first-order statistics of the speckled wavefront. For the case of scattering of fully coherent radiation, it would exhibit a negative exponential distribution of the form

$$p_I(I) = \frac{1}{\langle I \rangle} e^{-\frac{I}{\langle I \rangle}}, \tag{8.5}$$

where $\langle I \rangle$ denotes the average intensity across the detection plane. The case of partially coherent radiation is described by a Rician distribution where the only free parameter is the number of independent transverse and longitudinal modes M:

$$p_I(I) = \frac{\Gamma(I+M)}{\Gamma(M)\Gamma(I+1)} \left(1 + \frac{M}{\langle I \rangle}\right)^{-I} \left(1 + \frac{\langle I \rangle}{M}\right)^{-M}, \tag{8.6}$$

being $\Gamma(\cdot)$ the Euler Gamma function. Figure 8.10 shows the fitted value for the total number of modes at different observation distances, as well as the result obtained with a standard HeNe laser for which full spatial and temporal coherence can be safely assumed. As it can be seen, the total number of modes fluctuates between 4 and 5.

A deeper and profitable survey was not possible due to the lack of beamtime, but the following explanations have been attempted:

- the second harmonic generation inside the NL-XTAL changes either the coherence

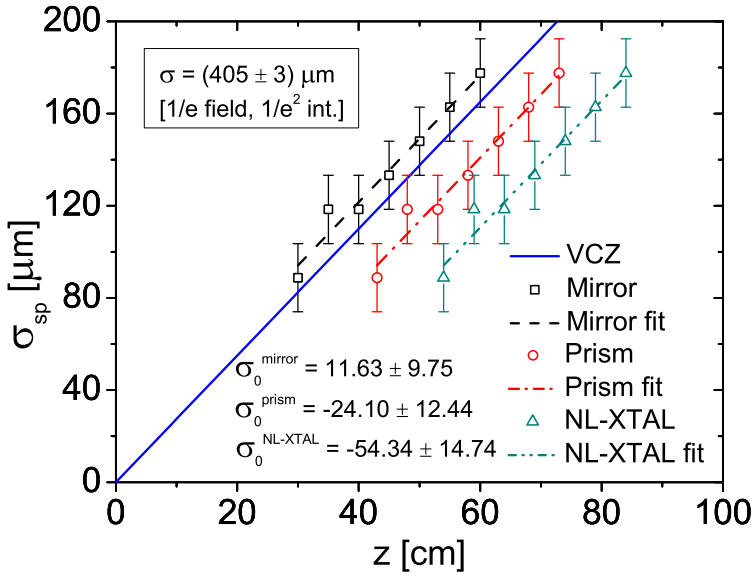

Figure 8.9: Transverse size of the speckle patches as a function of the observation distance from three different optical components: the non-linear crystal (NL-XTAL), the prism and the mirror. The scattering element is identified as the mirror by a linear fit of data through the zero-offset criterion following from the Van Cittert-Zernike's theorem. The three fitted values of the offsets are reported as $\sigma_0^{\mathrm{NL-XTAL}}$, $\sigma_0^{\mathrm{prism}}$ and $\sigma_0^{\mathrm{mirror}}$. The slope of the linear fit also gives a transverse beam size at the mirror position of 0.4 mm.

time of the radiation or the pulse duration, resulting in four purely longitudinal modes;

- longitudinal coherence properties are not changed by the non-linear processes inside the NL-XTAL, but the fourth harmonic of the HHG laser has lowered spatial coherence properties corresponding to 2 or 3 additional transverse modes;
- the non-linear process generates a transversally fully coherent beam, but either the NL-XTAL or the prism induce random wavefront distortion due to the finite roughness of their optical surfaces: in this case, the divergence of the speckle patched within the wavefront of the fourth harmonic laser beam is still determine by scattering from the rough mirror, but the impinging distorted wavefront reduces the measured speckle contrast resulting in an increased number of modes.

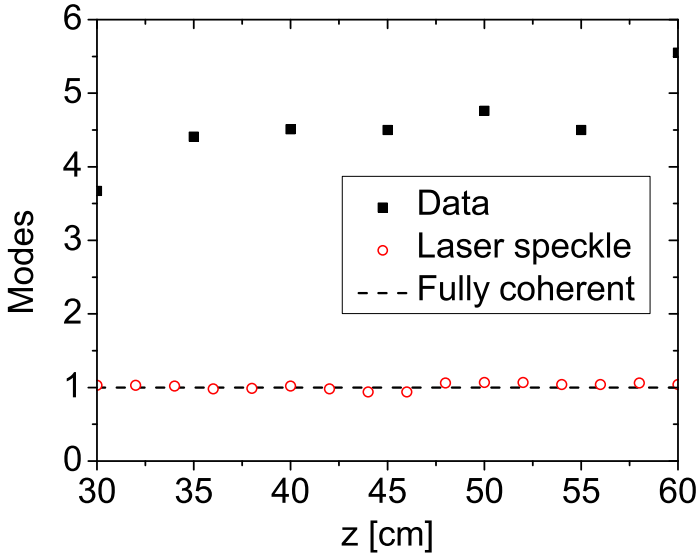

Figure 8.10: First-order statistics of the speckled intensity allows to retrieve information on the coherence properties of the laser pulses before impinging onto the rough mirror. A total number of modes fluctuating between 4 and 5 is found (see text for further details). We also reported experimental results obtained with a standard HeNe laser for comparison.

Part IV

Results at the ALBA Synchrotron Light Source

CHAPTER 9

The ALBA Synchrotron Light Source

9.1 Introduction on Synchrotron Light Sources

Synchrotron Light Sources (SLSs) are particle accelerators designed and optimized for the production of brilliant X-ray radiation for scientific and industrial purposes.

The term Synchrotron Radiation (SR) is used to denote the radiation emitted by a relativistic charged particle undergoing a transverse acceleration. It was first observed at the synchrotron accelerator of the General Electric in 1947. Since the emission of SR photons causes a loss of the particle beam energy, it was initially considered as a drawback of electron accelerators.

Eventually, SR started to be exploited parasitically for mterial science experiments in accelerators devoted to particle physics. These facilities are now referred to as the first-generation SLSs.

The ever-increasing demand of SR for scinentific purposes required the design and realization of specific accelerators to provide thescientific community with high-quality radiation. These first SR-oriented facilities are called second-generation SLSs.

Third-generation light sources are the machine in operation nowadays. SR is produced by small-emittance electron beams and is endowed with a high-brilliance photon flux. Third-generation SLSs are also equipped with straight section to locate Insertion Devices, mainly undulators and wigglers. The radiation coming from IDs is highly coherent and quasi-monochromatic and it is exploited and chracterized in dedicated beamlines.

Finally, fourth-generation light sources are under development and optimization nowadays. The term refers to Free-Electron Lasers (FELs), linear accelerators equipped with long undulators capable of producing extremely short, highly coherent photon pulses.

9.2 The ALBA facility

The ALBA facility is a high flux, high brightness third-generation SLS located in Cerdanyola del Vallès, near Barcelona (Spain). It consists of a 100 MeV Linac followed by a Booster that accelerates electrons up to their final energy of 3 GeV before they are transferred to the Storage Ring. The low emittance of the Booster (10 nm·rad) ensures a high transmission efficiency to the Storage Ring, were electrons are kept circulating to produce hard X-ray SR through bending dipoles and insertion devices. ALBA is design to have a small emittance of 4.6 nm·rad and a maximum beam current of 250 mA. During normal operations, the stored current amounts to 130 mA. The main parameters of the machine are reported in Tab. 9.1.

Linac	
Extraction energy	110 MeV
Emittance	150 nm·rad
Energy spread	0.20%
Booster	
Circumference	249.6 m
Emittance at 3 GeV	9 nm·rad
Energy spread at 3 GeV	0.10%
Maximum horizontal β-function	11.2 m
Maximum vertical β-function	11.7 m
Maximum dispersion	0.47 m
Reptition rate	3.125 Hz
Storage Ring	
Circumference	268.8 m
Maximum current	250 mA
Electron energy	3 GeV
Emittance	4.6 nm·rad
Energy spread	0.105%
Maximum horizontal β-function	17.89 m
Maximum vertical β-function	24.93 m
Maximum dispersion	0.247 m
Minimum bunch length	16 ps

Table 9.1: Main parameters of the ALBA Synchrotron Light Source.

The Storage Ring is divided into four quadrants and it thus has a 4-fold symmetry. It has 24 straight sections to locate Insertion Devices. Three sections are dedicated to the RF cavities, two sections are used to locate the diagnostics and one long sections hosts the Booster-to-Ring transfer line. A technical drawing of the facility is reported in Fig. 9.1.

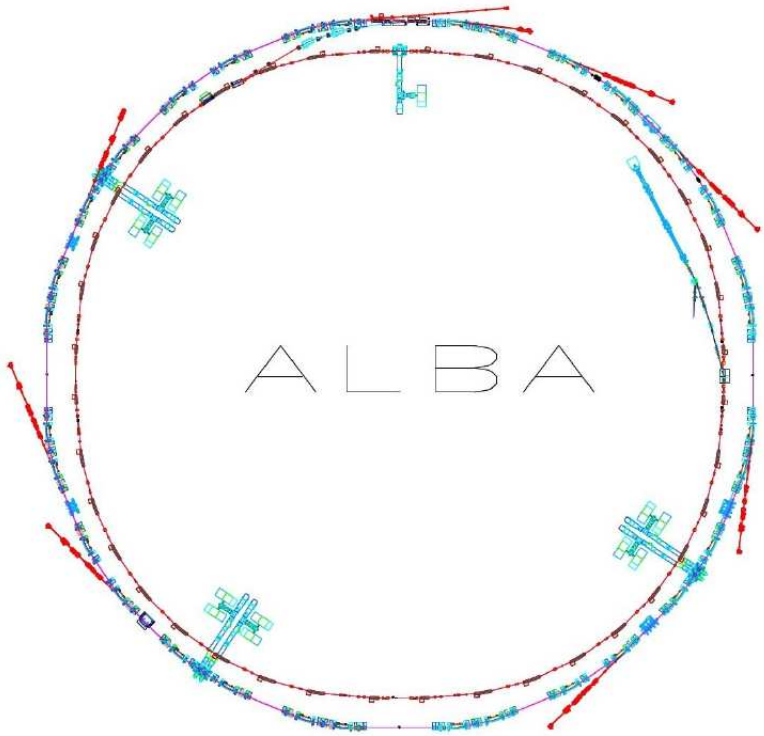

Figure 9.1: Technical drawing of the ALBA Synchrotron Light Source. The Linac, the Booster (interior ring), the Storage Ring (external ring), the Booster-to-Storage Ring transfer line and six RF cavities can be easily recognized.

CHAPTER 10

Probing temporal coherence of Synchrotron Radation

10.1 The Xanadu beamline (FE01)

Temporal coherence measurements with the HNFS technique have been performed at the Xanadu diagnostics beamline, located downstream the Front-End 01 (FE01). The aim of the beamline is to provide reliable measurements of the transverse electron beam size by means of the Synchrotron Radiation Interferometry (SRI) exploiting the classical Young's scheme to perform spatial coherence measurements on the visible part of the emitted SR [7].

Synchrotron radiation is generated by a bending magnet (BM01) and it is selected by a photon shutter at 1.684 m downstream the source point. The angular acceptance of the photon shutter is ± 1.84 mrad in the horizontal plane and ± 3.2 mrad in the vertical plane. The main parameters of the electron beam at the source point BM01 are summarized in Tab. 10.1.

Magnetic field	B	1.42 T
Hor. beam size	σ_x	54 μm
Ver. beam size	σ_y	23 μm
Hor. divergence	σ'_x	136 μrad
Ver. divergence	σ'_y	0.37 μrad
Hor. β-function	β_x	0.249 m
Ver. β-function	β_y	24.741 m
Hor. emittance	ϵ_x	4.6 nm·rad
Ver. emittance	ϵ_y	0.023 nm·rad
Coupling		0.5%
Hor. dispersion	D_x	0.04 m
Ver. dispersion	D_y	0.0
Energy spread	$\Delta E/E$	0.00105
Tilt angle		-0.26 rad

Table 10.1: Main parameters of the ALBA electron beam at the source point BM01.

The visible part of the emitted SR spectrum is selected by a motorized in-vacuum mirror located inside the tunnel at a distance of 8.635 m from the source point. The mirror is controlled with a motor which allows to insert it from 25 mm down to 7 mm above the orbit plane. In addition to selecting the visible wavelengths of the emitted spectrum, it is designed to reflect only the upper lobe of the SR beam hence the setup is

usually referred to as "half-mirror". The vertical position of the in-vacuum mirror also avoids the interaction with the hard X-ray components thus preventing the device to suffer from overheating and contaminations due to long exposure to ionizing radiation. Visible SR is then extracted out of the vacuum chamber through a dedicated extraction window and it is guided through a hole drilled in the shielding wall onto the optical table by a system of seven flat mirrors.

The HNFS diagnostics has been installed at a distance from the source point of 15 m. It consists of a quartz cuvette storing a colloidal suspension of polystyrene spherical nanoparticles with diameter of 1 μm. Dilution down to a volume fraction of approximately 10^{-5} w/w guarantees heterodyne conditions. The speckle fields are collected by a 4X magnifying microscope objective and imaged onto the sensor of a Basler sc1300-32cm/gc camera. The CCD camera has 1296×966 pixels and the pixel size is 3.75 μm. The sample detector distance z can be changed through a micrometer translational stage and it ranges between 1 mm and 30 mm. The experimental setup is sketched in Fig. 10.1.

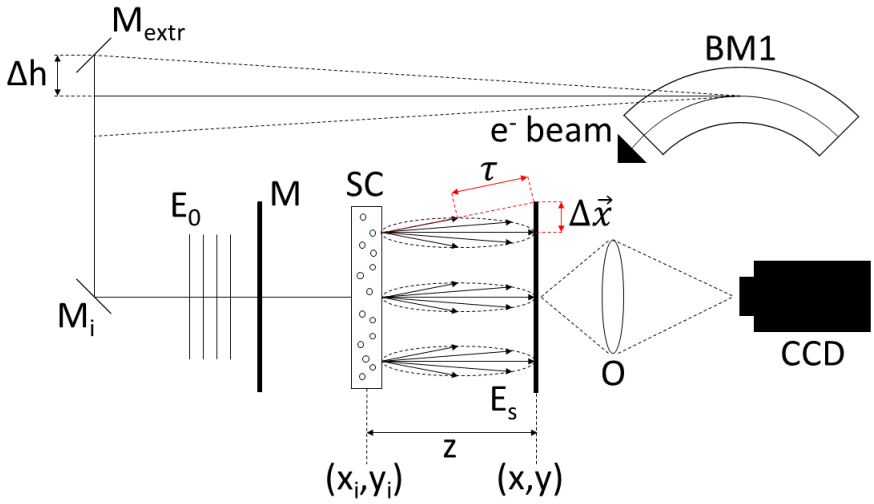

Figure 10.1: HNFS experimental setup at ALBA: SR is emitted at Bending Magnet 1 (BM1) and visible light is selected by an extraction mirror M_{extr} that can be inserted from 25 mm to 7 mm from the orbit plane (Δh). A system of flat mirrors M_i delivers the radiation (E_0) to the scattering cell SC and the interference with the scattered field E_s is imaged by the microscope objective O onto the CCD. A micrometric translation stage allows to scan the distance z from the particle plane (x_i,y_i) to the image plane (x,y). Whether the monochromator M is used defines narrow-band or broad-band conditions, respectively. The dashed red lines allow to relate the parameter Δx of the radiation CCF and the parameter τ of the radiation CDC to the geometry of the HNFS setup.

10.2 Results and discussion

Coherence areas at $z_s = 15$ m from the source point are of the order of a few centimeters at visible wavelengths according to the Van Cittert-Zernike's theorem (e.g. $\sigma_{\mathrm{coh,x}} = \lambda z_s/(\pi\sigma_x) = 4$ cm and $\sigma_{\mathrm{coh,y}} = \lambda z_s/(\pi\sigma_y) = 9$ cm at $\lambda = 440$ nm). This implies that fully spatially coherent radiation impinges onto the colloidal suspension, the scattering

cell having a transverse extension of less than 2 cm. Moreover, the transverse coherence length exceeds by more than an order of magnitude the accessible range of transverse displacements $\Delta r_{\max} = 2$ mm given by the spatial scaling of Eq. 4.30 for a typical value of $q_{\max} = 1\ \mu\text{m}^{-1}$ at the maximum sample-detector distance $z_{\max} = 3$ cm. The Mutual Coherence Function $\Gamma(\Delta x, \Delta y, \tau)$ describing the simultaneous effects of partial spatial and temporal coherence can then be reduced to the Self Coherence Function $\Gamma(\tau)$ conveying the information on temporal coherence only.

A subtlety is involved in the definition of the Self Coherence Function for SR from electron bunches as we must ensure that the underlying stochastic process is stationary. This in turn requires the comparison between the inverse bandwidth of the emitted single-particle SR and the electron bunch duration [42]. We have computed the single-particle SR spectrum from the well-known expression of the angular-spectral power density [38] for a point-like aperture positioned at the average vertical angle $\psi_0 = (16$ mm$)/(8.635$ m$) = 1.853$ mrad of the in-vacuum mirror. The result is reported in Fig. 10.2.

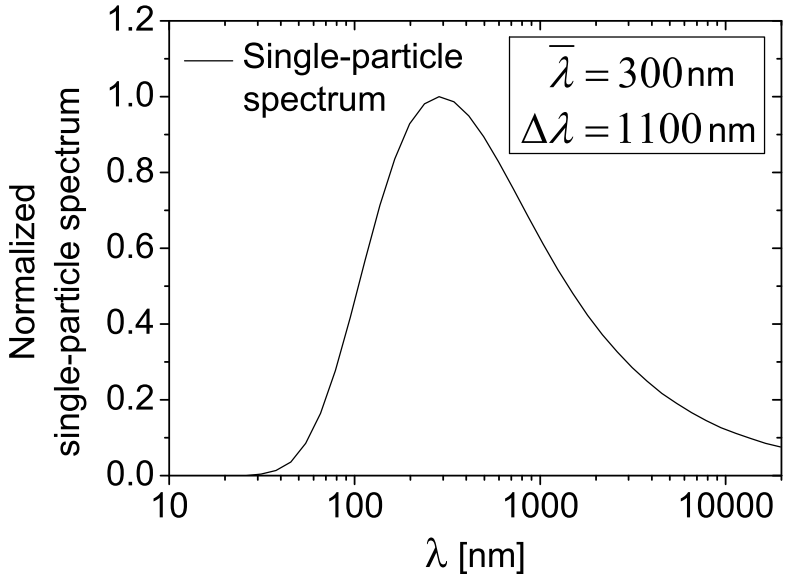

Figure 10.2: Computed single-electron spectrum for the ALBA case (radius of curvature $\rho = 7.05$ m and Lorentz factor $\gamma = 6000$) at the vertical angle $\psi_0 = 1.835$ mrad corresponding to the average vertical position of the in-vacuum extraction mirror. The inverse bandwidth $1/\Delta\nu_{\text{FWHM}} = \bar{\lambda}^2/(c\Delta\lambda_{\text{FWHM}}) = 0.33$ fs is much shorter than the bunch duration $\tau_{\text{bunch}} = 16$ ps. This ensures the validity of the Wiener-Khinchine theorem and temporal coherence properties are thus determined by the incident SR spectrum.

The single-particle spectrum is peaked at $\bar{\lambda} = 300$ nm and it has a FWHM bandwidth of $\Delta\lambda_{\text{FWHM}} \approx 1100$ nm. The inverse bandwidth of the radiation is thus $1/\Delta\nu_{\text{FWHM}} = \bar{\lambda_{\text{th}}}^2/(c\Delta\lambda_{FWHM}) = 0.27$ fs, much shorter than the electron bunch duration $\tau_{\text{bunch}} = 15.8$ ps. The stochastic process associated to the SR emission from the electrons inside the bunch is stationary and temporal coherence can be properly investigated through the Self Coherence Function.

The actual SR spectrum reaching the Xanadu experimental optical table differs from

the one reported in Fig. 10.2. Since the synchrotron spectrum emitted by a single electron is angle-dependent, this is due to the finite angular acceptance of the in-vacuum mirror and of extraction line, as well as to finite emittance effects. The presence of the extraction line itself contributes to shaping the actual SR spectrum, as the reflectivity of the mirrors is optimized for visible wavelengths. Mirrors are also out of plane and oriented at different angles one with respect to the other, thus affecting the power spectral density of the extracted SR since the reflectivity of each mirror at a fixed wavelength depends on the state of polarization of the corresponding incident component. Finally, the extraction windows generally acts as a spectral filter.

10.2.1 Temporal coherence of narrowband SR beams

Narrowband SR beams are obtained by inserting a band pass filter by Thorlabs with FWHM bandwidth $\Delta\lambda = 10$ nm centered at the mean wavelength $\bar{\lambda} = 440$ nm upstream the HNFS setup. The expected coherence time and longitudinal coherence length are then $\tau_{\mathrm{coh}} = 0.664\,\bar{\lambda}^2/(c\Delta\lambda) = 43$ fs and $l_{\mathrm{coh}} = c\tau_{\mathrm{coh}} = 12.9$ μm, respectively. The multiplicative factor 0.664 takes into account the Gaussian-like shape of the spectral response of the filter [36]. The requirements for the stationarity of the stochastic process and for the validity of the stationary phase approximation are fulfilled. This ensures that the envelope of the power spectra of heterodyne speckle fields conveys the information on the Complex Degree of Coherence of the impinging SR beam.

Two-dimensional power spectra exhibit perfect azymuthal symmetry, allowing to compute angular averages of power spectra as

$$I(q,z) = \frac{1}{2\pi}\int_0^{2\pi} I(q,\theta,z)\,\mathrm{d}\theta, \tag{10.1}$$

where the Fourier wavevector $\vec{q} = (q_x, q_y)$ has been expressed in polar coordinates:

$$\vec{q} = (q_x, q_y) = (q\cos\theta, q\sin\theta). \tag{10.2}$$

The power spectra profiles are plotted in Fig. 10.3. It can be noticed how the envelopes shrink as the distance z is increased. This is due to the partial coherence of the impinging radiation, in agreement with the theory developed in Chap. 4 and in Chap. 5. Profiles have already been reduced for the shotnoise term $P(q)$, for the instrumental transfer function $H(q)$ and for the particle form factor $S(q)$.

Perfect azymuthal symmetry of the power spectra is the signature of limiting temporal coherence of the incident radiation. This is confirmed in Fig. 10.4 and Fig. 10.5, which show the different power spectra under the spatial scaling of Eq. 4.30 and the temporal scaling of Eq. 4.31, respectively. If we attempt to reduce the power spectra by means of the spatial scaling, angular averages at different distances z fail to generate the master curve $C(\Delta r) = C(zq/k)$. Opposite to this case, power spectra at different sample-detector distances build the master curve $C(\tau) = C(zq^2/(2ck^2))$. Notice how the Talbot oscillations superimpose, as predicted by the theory developed in Chap. 4 and in Chap 5. The good fit to the temporal master curve indirectly proves full spatial coherence over the accessible transverse displacements of roughly 1 mm, referring to the baseline of Fig. 10.4.

The Talbot oscillations reported in Fig. 10.5 display an evident tapering for $\tau < 10$ fs. Such an effect is induced by the finite thickness of the sample holder, making the scatterers arrangement a 3-D system, and by the walkoff effect related to the limited sensor size [58, 59, 60]. These effects prevent to obtain the radiation CDC properly from

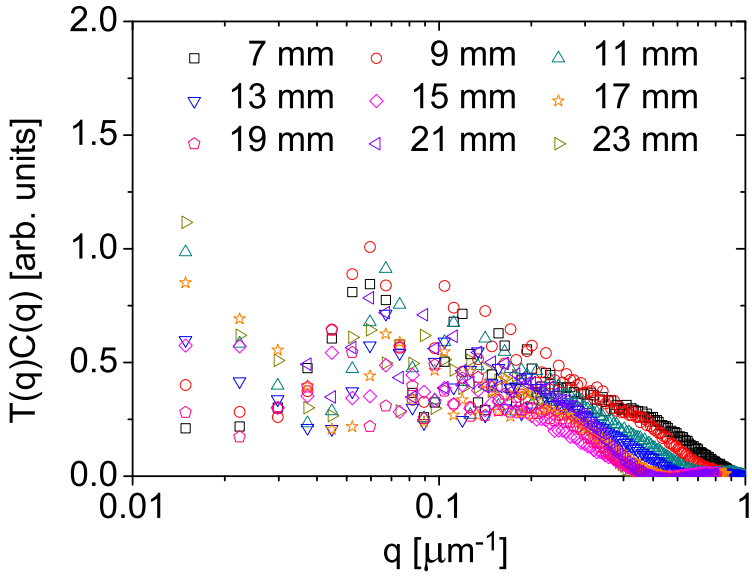

Figure 10.3: Raw power spectra for narrowband SR beams at the ALBA facility.

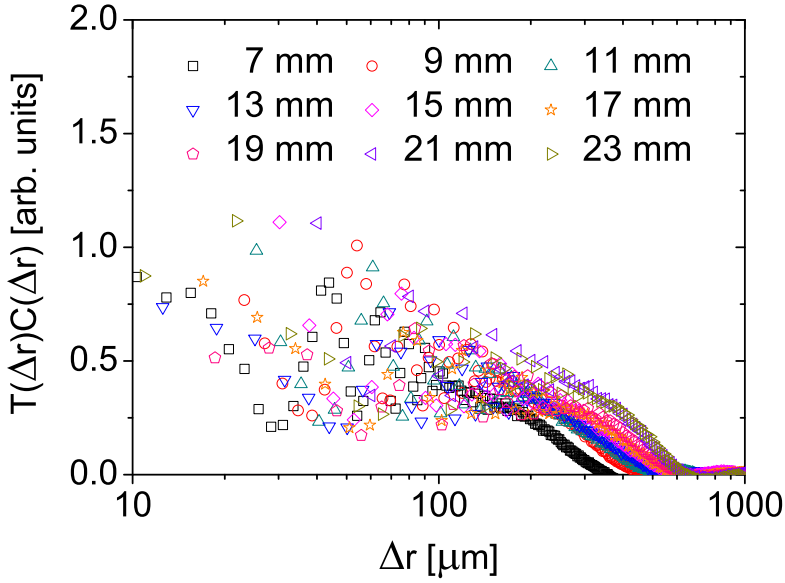

Figure 10.4: Power spectra fail to fit the master curve under the spatial scaling of Eq. 4.30.

the envelope of the master curve $C(\tau)T(\tau)$, unless the average of the upper and lower envelopes is computed. This procedure allows to exactly compensate for the Talbot ta-

pering, as reported in Fig. 10.6 which shows the squared modulus of the radiation CDC obtained from the experimental curves by averaging the upper and lower envelopes of the curves $C(\tau)T(\tau)$ displayed in the inset for completeness.

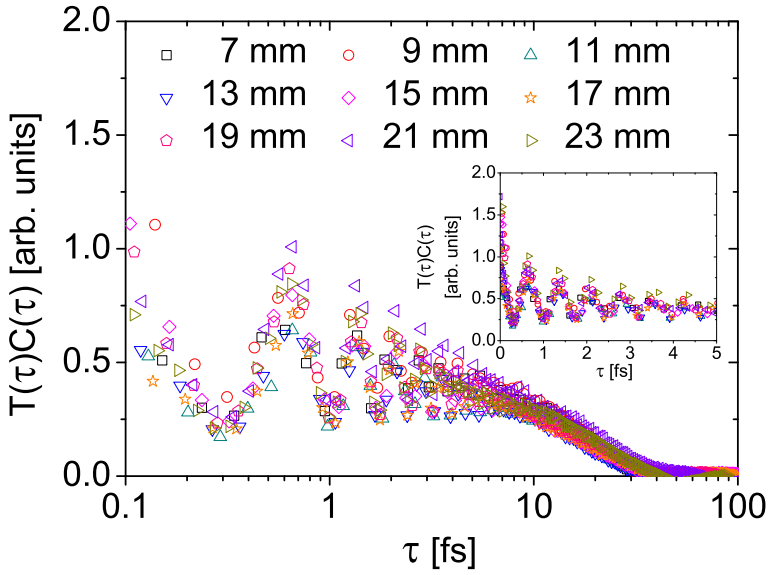

Figure 10.5: Power spectra fit the master curve under the scaling of Eq. 4.31. Inset shows the enlarged region corresponding to $\tau < 5$ fs to evidence the fine superposition of Talbot oscillations.

Following the definition given by Mandel, the measured squared modulus of the radiation CDC is related to a coherence time

$$\tau_{\mathrm{coh}} = \int_{-\infty}^{+\infty} |\gamma(\tau)|^2 \, \mathrm{d}\tau = 2 \int_{0}^{+\infty} C(\tau) \, \mathrm{d}\tau = 40 \pm 10 \text{ fs}, \tag{10.3}$$

in good agreement with the value of 43 fs given by the filter inverse bandwidth. The error bar stems from the dispersion of data around the binned curve.

Despite a full measurement of SR spatial coherence is not feasible with the HNFS technique at visible wavelengths, useful information on the coherence area can be obtained by analyzing narrowband Talbot oscillations. In fact, the Talbot transfer function bears the information on the phase of the Mutual Coherence Function. Owing to the Wiener-Khinchine theorem, the Gaussian-like linewidth of the band pass filter should result in a purely real temporal coherence function [36, 37]. Any phase term in the Talbot transfer function can then be ascribed to a complex spatial coherence function. The phase distribution of the coherence areas can then be retrieved from the position of Talbot extremants. In particular, Fourier Optics predicts that far field coherence areas should carry the information on the local wavefront curvature [61]. In fact, far field coherence patches are homothetic and their divergence is comparable to that of the wavefront. Contrarily, near field coherence areas behave as diffraction-limited Gaussian laser beams with a plane wavefront and a large Rayleigh range, thus carrying no information on the wavefront curvature. For a source of linear size D, the transition from the near field to the far

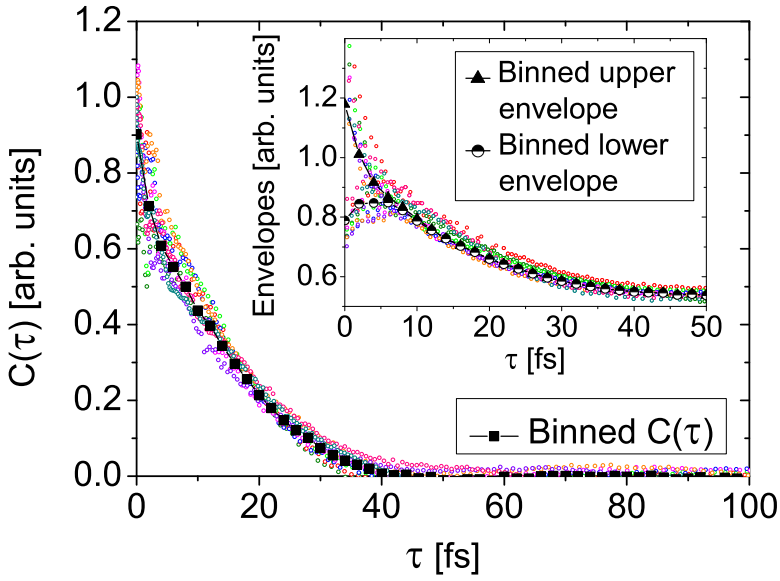

Figure 10.6: Squared modulus of the radiation CDC as measured with the HNFS technique. Data from the different 9 sample-detector distances shown in Fig. 10.3 have been merged through Eq. 4.31 and binned. Inset shows the corresponding upper and lower envelopes. The tapering effect on Talbot oscillations is clearly visible for $\tau < 10$ fs.

field occurs at $z_{\rm FF} \approx D^2/\lambda$. In our case $z_{\rm FF} = 7$ mm and the scattering sample lies in the Fraunhofer zone of the source, hence it is enlightened by SR whose coherent patches are endowed with a phase distribution reflecting the curvature of the wavefront. It is worth noting that for X-ray wavelengths the situation would be reversed as $z_{\rm FF}$ would be of the order of tens or hundreds of meters: the sample would be located within the Fresnel zone of the source and coherence areas would carry a vanishing curvature.

The effects on the Talbot oscillations of heterodying the scattered spherical waves with a wavefront endowed with a non-vanishing curvature can be easily described in the single-particle regime. Assuming that the incident wavefront has a radius of curvature R at the sample position and neglecting inessential amplitude constant without loss of generality, the superposition of the scattered spherical wave and of the transmitted incident wave at a distance z downstream the sample results in

$$E_{\rm tot}(x,y,z) \propto e^{ik\sqrt{(R+z)^2+x^2+y^2}} + e^{ikR}e^{ik\sqrt{x^2+y^2+z^2}} \approx$$
$$\approx e^{ik(R+z)}e^{ik\frac{x^2+y^2}{2(R+z)}} + e^{ik(R+z)}e^{ik\frac{x^2+y^2}{2z}}. \tag{10.4}$$

The heterodyne part $I_{\rm het}$ of the single-particle interferogram is then

$$I_{\rm het} \propto \cos\left[\frac{k(x^2+y^2)}{2}\left(\frac{1}{z+R}-\frac{1}{z}\right)\right]. \tag{10.5}$$

For SR wavefronts with radius of curvature R at the sample position, the Talbot oscillations at a distance z downstream the colloid are described in term of the effective

distance

$$z_{\text{eff}} = \frac{1}{z+R} - \frac{1}{z} \approx \frac{1}{R} - \frac{1}{z}, \tag{10.6}$$

where in the last passage we have reasonably assumed $R \gg z$.

Since this relation is non-linear, the wavefront curvature can be measured by comparing z_{eff} (fitted from the position of Talbot maxima and minima) to the nominal z (known by the position of the translation stage). Results are reported in Fig. 10.7 and the fitted value for the radius of curvature according to Eq. 10.6 is $R \approx 15$ m, corresponding to the nominal distance of the scattering cell from the center of the bending dipole. However, due to the low signal caused by the monochromator, data are widely scattered and affected by large uncertainties. As a result, we can only conservatively provide a lower limit of 5 m to the value of the radius of curvature.

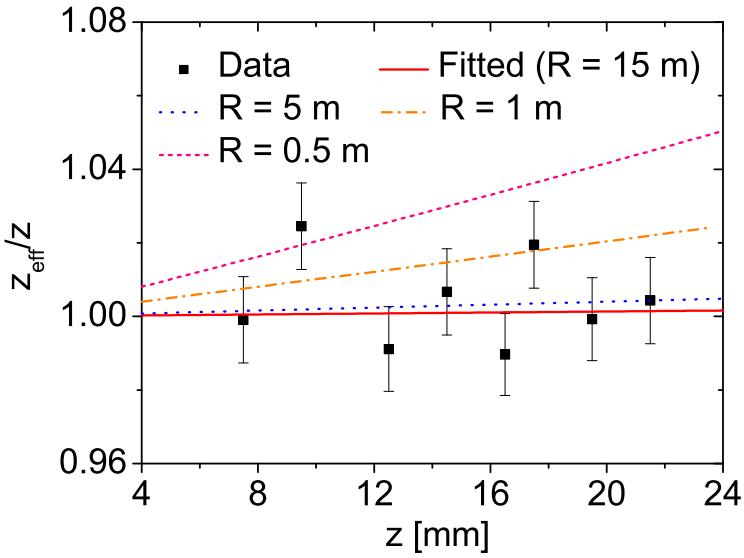

Figure 10.7: The periodicity of the Talbot oscillations is affected by a non-vanishing curvature of the coherence areas. Since for visible wavelength the coherence areas at the sample position behave as far field speckles, they carry the same curvature as the SR wavefront. Data are compatible with a radius of curvature larger than 5 m.

10.2.2 Temporal coherence of white SR beams

Temporal coherence of white SR beams is probed with the same experimental setup upon removal of the bandpass filter. Compared to the case of narrowband SR beams, power spectra exhibit less Talbot oscillations, thus implying a shorter longitudinal coherence length. The temporal master curve obtained by means of the scaling of Eq. 4.31 is reported in Fig. 10.8. The good superposition of the power spectra and the matching of the Talbot oscillations is a clear signature of limited temporal coherence.

Figure 10.9 shows the measured squared modulus of the radiation CDC obtained by averaging the upper and lower envelopes of the Talbot oscillations, reported in the inset

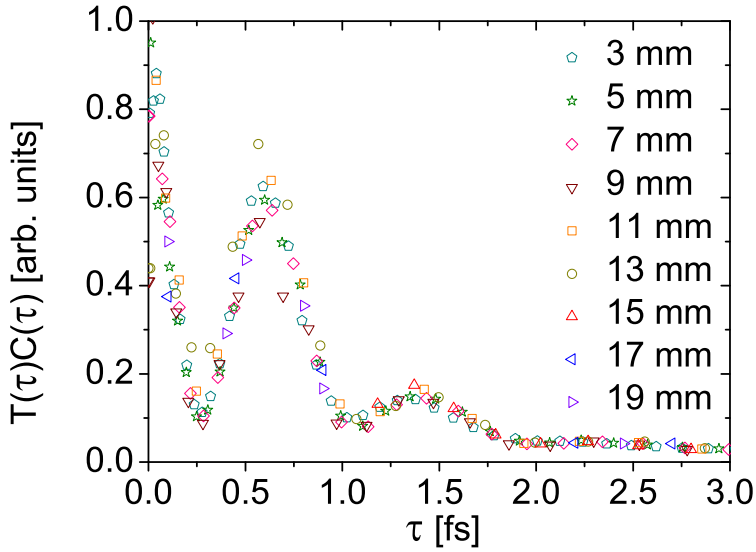

Figure 10.8: Broadband power spectra fit the master curve under the scaling of Eq. 4.31. The 9 probed distance are indicated in the figure legend and range between 3 mm and 19 mm.

from completeness. Data are much less scattered compared to the narrowband case of Fig. 10.6 due to the enhanced signal on the CCD camera without any monochromator. The decay of Talbot oscillations is entirely due to the limited temporal coherence, since the tapering effect observed for narrowband SR is absent. In fact, it can be noticed how the lower envelope (minima of Talbot oscillations) lies at almost zero level and it merges the upper envelope (maxima of Talbot oscillations) when power spectra decay to zero.

Integration of the master curve as yields a coherence time of 1.7 ± 0.4 fs, corresponding to a FWHM bandwidth of the incident SR power spectral density $\Delta\lambda = 240$ nm at an average wavelength $\bar{\lambda} = 350$ nm (fitted through the periodicity of the Talbot trasfer function by knowing the sample detector distance z from the position of the micrometer translational stage).

We can now verify *a posteriori* the validity of the stationary phase approximation, which allows to measure the coherence properties of the incoming SR directly from the decay of the power spectra. In fact the longitudinal coherence length $l_c = c\tau_{\mathrm{coh}} = 0.51$ μm is larger than $\bar{\lambda}/2 = 0.175$ μm and the requirements for the stationary phase approximation are then fulfilled. Furthermore, the measured coherence time is much shorter than the bunch duration, implying that temporal coherence properties of the emitted radiation are determined by the SR spectrum. Since we can only access the modulus of the radiation CDC, we cannot directly apply the Wiener-Kintchine theorem to retrieve the SR spectrum at the sample position. However, assuming that the SR spectrum is roughly symmetric around the peak wavelength, we can factorize the radiation CDC in the simple form [36]

$$\gamma(\tau) = |\gamma(\tau)|e^{i\bar{\nu}\tau}, \tag{10.7}$$

where $\bar{\nu} = c/\bar{\lambda}$ is the average frequency. The Wiener-Khinchine theorem takes the modi-

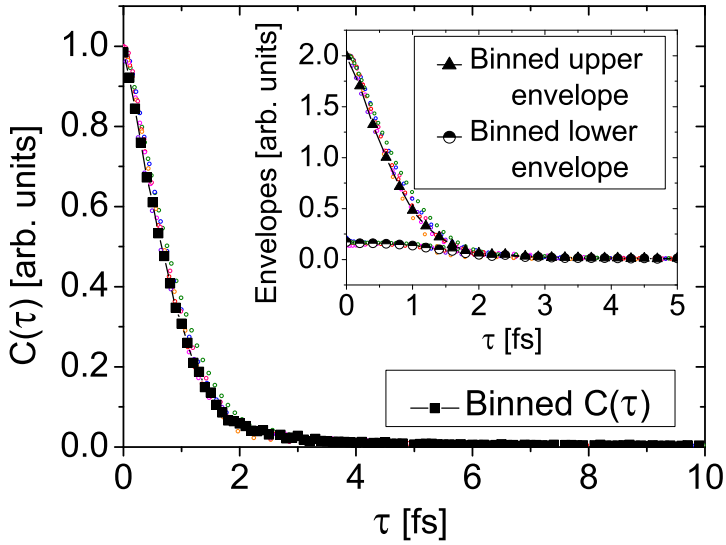

Figure 10.9: Squared modulus of the radiation CDC as measured with the HNFS technique. Data from the 9 different sample-detector distances have been merged through Eq. 4.31 and binned. Inset shows the corresponding upper and lower envelopes. By contrast with Fig. 10.6, the short coherence time of the radiation makes any tapering effect negligible, as the loss of Talbot visibility and the decay of power spectra to shot noise level are entirely due to the radiation CDC.

fied form [62]

$$S(\nu) = \int_0^{+\infty} 2|\gamma(\tau)| \cos\left[(\nu - \bar{\nu})\tau\right] \, \mathrm{d}\tau = \int_0^{+\infty} 2\sqrt{C(\tau)} \cos\left[(\nu - \bar{\nu})\tau\right] \, \mathrm{d}\tau. \tag{10.8}$$

Figure 10.10 shows the power spectral density (PSD) obtained by applying Eq. 10.8 to the measured curve $C(\tau)$ of Fig. 10.9. Comparison with independent measurements (red line in Fig. 10.10) performed with a standard spectrometer shows how the overall shape of the SR spectrum at the detection position is satisfactorily reproduced. Furthermore, the measured coherence time is compatible within the experimental error with the value of 1.4 fs obtained from the inverse bandwidth (at FWHM) of the SR spectrum as measured with the spectrometer. The three narrow peaks are missing in the retrieved spectrum mainly due to shotnoise limitations. In fact, since their width is less than one half of the spectrum FWHM, they are expected to contribute the modulus of the radiation CDC with some echoes at temporal delays larger than $\tau \approx 2\tau_{\mathrm{coh}} = 3.4$ fs, where the decay of Talbot oscillations has already reached the shotnoise level, as can be seen in Fig. 10.8, and where sampling is not properly done due to the quadratic relation of Eq. 4.31. Moreover, we also stress that $C(\tau)$ is computed by interpolation on a small number of Talbot maxima and minima and that we assumed specific symmetry properties for the SR spectrum in order to write Eq. 10.8. Although this approach allows to correctly retrieve larger structures of the SR power spectral density, it is currently a limiting factor for the detection of finer details. Nonetheless, the measured FWHM spectral bandwidth,

conveying the information on the SR coherence time, is correctly retrieved (250 nm to be compared with $\sim$ 300 nm from spectrometry measurements).

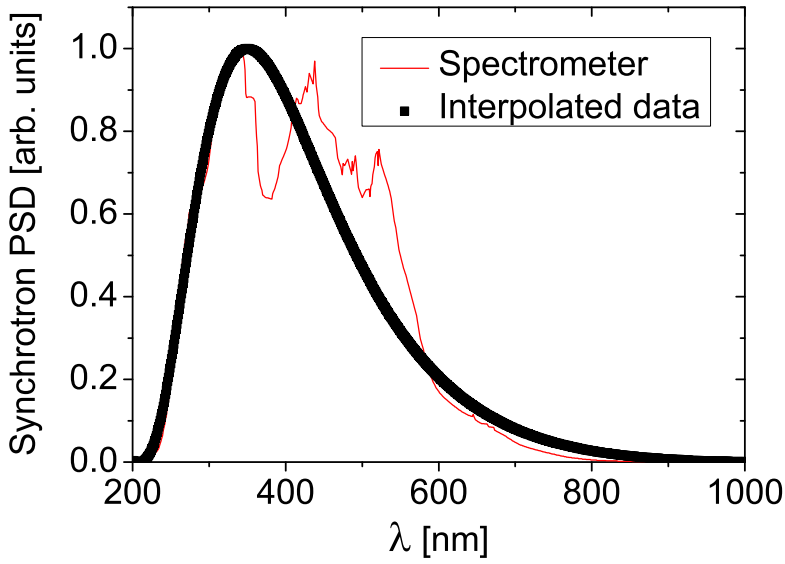

Figure 10.10: Synchrotron power spectral density PSD retrieved with the HNFS technique (squares) and measured with a spectrometer (red solid curve). The overall shape of the spectrum has been satisfactorily reproduced, despite the three narrow peaks have not been retrieved (see text for details).

A closing remark is worth mentioning regarding the SR power spectral density at the detection plane reported in Fig. 10.9 as a red line. Comparison with Fig. 10.11(b) representing the measured SR spectrum upstream the HNFS setup evidences how the two spectra are slightly different. This is due to the presence of the scattering cuvette, of the scattering sample, of the magnifying optics and of the CCD sensor altering the spectral density of the incoming radiation. Dealing with polychromatic light, we need to account the effects of the system transmission. Since the system will generally act as a band-pass filter, these effects can be modeled as the multiplication of the radiation spectrum by a Spectral Calibration Function (SCF). In the HNFS technique, for each wavelength it is given by the product of the scattering amplitude, the transmissivity of the liquid of the suspension and the walls of the cuvette and the spectral response of the CCD, as shown in Fig. 10.11(a) (each curve has been normalized to a maximum value 1). The term $|S(0)|$ can be computed from the exact Mie theory of light scattering, since spherical nanoparticles are used [56]. Transmission of the liquid and the scattering cell can be measured by means of a standard spectrometer, while the quantum efficiency of the sensor is provided by the CCD constructor.

Due to the relation between temporal coherence properties and power spectral density of the radiation, the shape of the measured CDC is influenced by the SCF of the experimental setup. The impact of a finite spectral bandwidth on different coherence-based experiments with SR is a very important topic that has to be treated at the appropriate accuracy level in each particular case. However, in many of such experiments one

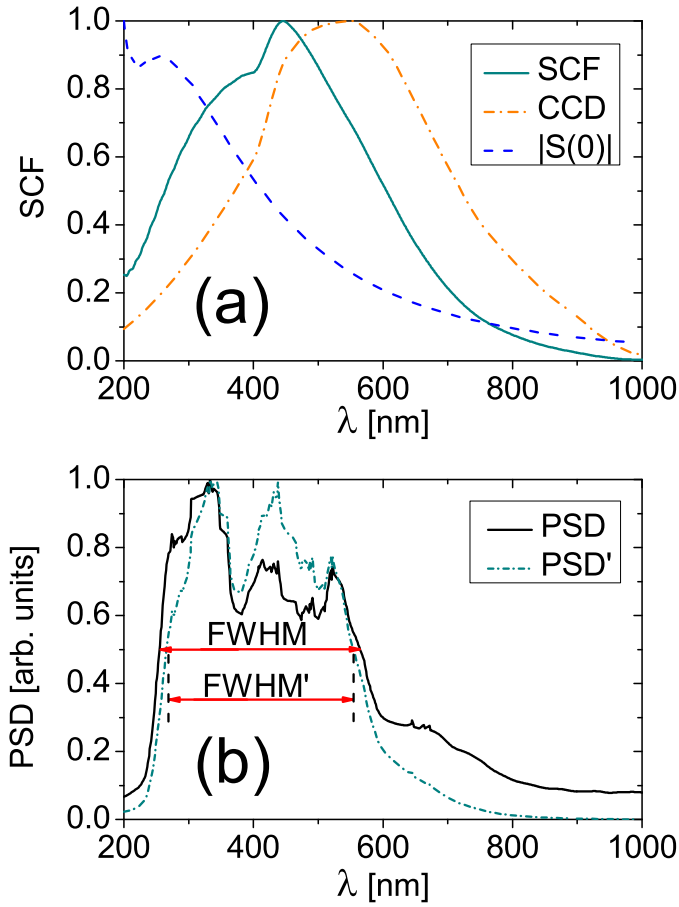

Figure 10.11: (a) Spectral calibration function SCF (solid cyan curve) taking into account the dependence of the forward scattering amplitude $|S(0)|$ on wavelength (dashed blue curve) and the quantum efficiency of the CCD sensor (dash-dot orange curve). The measured transmissivity of the liquid in the cuvette and of the cell walls is almost constant over the wavelength range indicated and it is not displayed. (b) Comparison between the incoming power spectral density of SR radiation measured with a spectrometer (PSD, solid black curve) and the detected spectrum (PSD', dash-dot cyan curve) obtained by means of multiplication for the SCF. Its effects on the radiation bandwidth are negligible, since the two spectra have full width at half maximum $FWHM = 310$ nm and $FWHM' = 290$ nm, respectively.

is interested in the coherence time of the SR rather than in the exact shape of the temporal coherence function. Since the coherence time is of the order of the inverse bandwidth of the radiation spectrum [36, 37], referring to Fig. 10.11 we can conclude that for the experiments at the ALBA bending dipole the effects of the SCF on the coherence time of the radiation are negligible and that the decay of the Talbot oscillations provides a significant measure of the temporal coherence of the incoming SR.

Following the same reasoning, the presence of the optical components of the extraction line prior to the scattering sample might introduce some changes in the SR spectrum and related coherence properties. This certainly occurs for the ALBA case, as it can be seen by comparing the theoretical spectrum plotted in Fig. 10.2 with the spectral density

measured with the spectrometer upstream the HNFS setup and reported in Fig. 10.11. For coherence-based experiment the presence of the extraction line is of no concern as the coherence properties of the SR beam at the sample position are of interest, regardless of the previous optical components. Opposite to this case, the reader should be aware that for coherence-based electron beam diagnostics it is mandatory that the extraction line be absent or at least its spectral response be characterized, in order to retrieve properties of the electron bunch from the measured coherence functions.

CHAPTER 11

Probing spatial coherence of Undulator Radiation

11.1 The NCD beamline (BL11)

Preliminary spatial coherence measurements with the HNFS technique have been performed at the Non-Crystalline Diffraction beamline at ALBA (NCD beamline or BL11) with the aim of retrieving the transverse size of the electron beam. The beamline is dedicated to Small Angle X-ray Scattering (SAXS) and Wide Angle X-ray Scattering (WAXS) experiments to provide structural and dynamic information of proteins, polymers and colloids.

Undulator radiation is generated by an in-vacuum undulator and a narrow photon energy range is selected with a double crystal Si-111 monochromator. The radiation wavelength can be tuned over the range 0.9 Å- 1.9 Åby adjusting the gap of the insertion device, variable between 5 mm and 30 mm. The optical layout is designed to deliver a high-photon flux onto the sample located in the experimental hutch at 34 m from the undulator center. A safety shutter placed 30 m downstream the insertion device in the separated optical hutch blocks the X-ray radiation, allowing direct operations on the sample.The schematic of the beamline is reported in Fig. 11.1, while the main parameters are summarized in Tab. 11.1. During operations, the undulator gap was tuned at its minimum value and the Si-111 monochromator selected a photon energy of 12 keV ($\lambda =$ 1 Å).

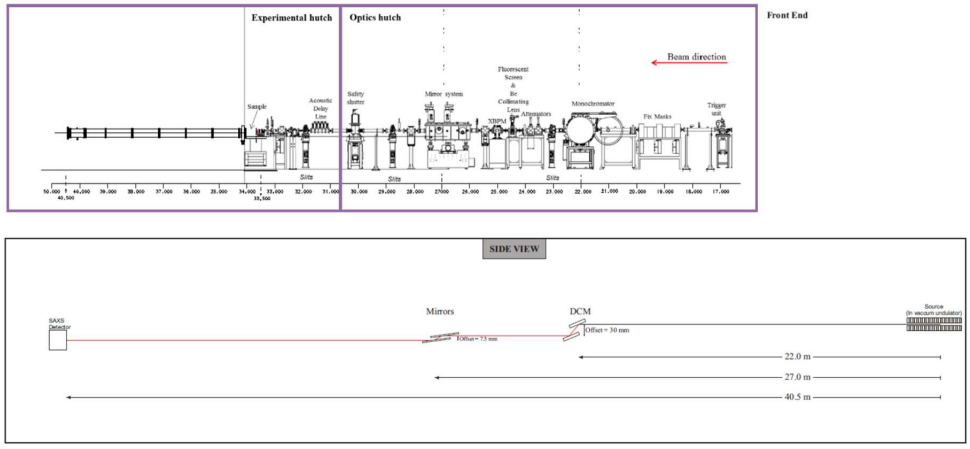

Figure 11.1: Schematic of the NCD beamline at ALBA.

Beamline specification		
Wavelength range	λ	0.9 Å- 1.9 Å
Energy range	-	6.5 keV - 13 keV
Flux at sample position	-	$2 \cdot 10^{12}$ ph/s
Monochromator relative bandpass	$\Delta E/E$	$< 10^{-4}$
Undulator source		
Wiggler wavelength	λ_w	21.3 mm
Number of wigglers	N_w	92
K at minimum gap	$K_{\min}$	1.6
Hor. beam size (FWHM)	σ_x	309 μm
Ver. beam size (FWHM)	σ_y	18 μm
Hor. divergence (FWHM)	σ'_x	112 μrad
Ver. divergence (FWHM)	σ'_y	28-22 μrad

Table 11.1: Main parameters specifying the NCD beamline and the in-vacuum plane undulator. The flux at the sample position refers to a photon energy of 10 keV and to a beam current of 100 mA.

The HNFS diagnostics has been installed in the experimental hutch at 34 m from the undulator center. It consists of a scattering cell made of mica storing silica nanospheres with a diameter of 500 nm. With respect to the measurements at the Xanadu beamline, both the mica cuvette and the silica sample are effective in enhancing the detected signal. The volume fraction of the sample was 10% w/w and the sample was periodically shaked in order to resuspend the scattering particles. X-ray heterodyne speckle fields are acquired and converted to visible wavelengths by a YAG phosphor 100 μm in thickness. The rear surface is imaged onto a Basler sc1300-32cm/gc CCD camera by means of a 20X magnifying microscope objective. To avoid direct exposure of the camera sensor to the residual X-ray beam, a mirror is inserted at 45 degrees in order to deflect the visible radiation perpendicularly with respect to the direction of propagation of the X-ray photons.

11.2 Preliminary results and discussion

11.2.1 Power spectra instability and treatment in data analysis

Preliminary measurement at the NCD beamline were aimed at validating the technique as a beam size monitoring method for the particle beams. We performed measurements in free propagation conditions at three different distances, namely 15.5 cm, 35.5 cm and 55.5 cm, in order to check the Talbot master curve for spatial coherence.

Opposite to the case of visible SR treated in the previous Chap. 10, images have been processed with the SFA data reduction algorithm in order to properly deal with the issue of power spectra instabilities. With this expression we mean the empirical observation that power spectra within the same sequence of acquired frames exhibit shot-to-shot

variations[1]. An example of the phenomenon is reported in the instability map of Fig. 11.2(a), where a collection of vertical profiles of power spectra corresponding to different single frames is shown. It can be compared in Fig. 11.2(b) with a similar map obtained for the case of the narrowband SR beam probed at the Xanadu beamline, showing stable and reproducible working conditions.

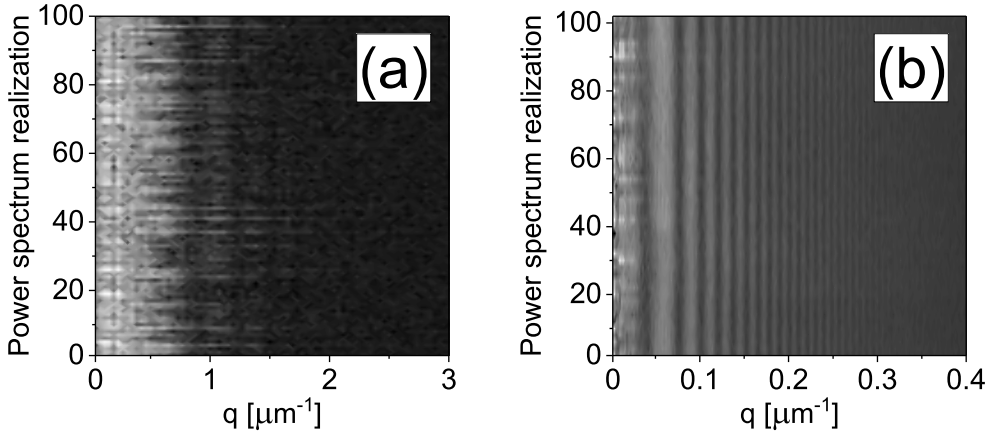

Figure 11.2: (a) Instability map of power spectra at the NCD beamline. A set of $N = 100$ single-frame vertical profiles from the same image sequence is plotted. The vertical axis labels each profile of the collection, while the horizontal scale refers to the wavevector coordinates. Shot-to-shot fluctuations can be clearly recognized from the varying number and features of the visible Talbot oscillations. (b) Instability map for the narrowband SR beam probed at the Xanadu beamline. Features of single-shot power spectra are homogeneous across the collection, thus indicating stable operating conditions.

Instabilities may be caused by the source or by the experimental apparatus(the beamline optics or the HNFS setup). In the former case, it would correspond to fluctuations in the transverse coherence properties of the undulator radiation hence the phenomenon would exhibit some dependence on the sample-detector distance (i.e. the instabilities would pertain to the real space). In the latter case, instabilities would arise in the Fourier space and the phenomenon would not exhibit any z-dependent feature. This would be the case for example of some mechanical vibrations causing a relative shift of the camera with respect to the radiation beam. A deeper survey of the phenomenon was not possible due to the lack of beamtime. However, the fundamental fact holds that the presence of such instabilities prevents data at different distances to properly fit the master curve for the spatial coherence scaling by naively averaging the power spectra of each collection. This issue can be circumvented by processing a strict selection of power spectra, namely the ones with the highest average values over a wavevector range $(q_{\min}, q_{\max})$. In particular, we sort power spectra corresponding to each single image by this criterion and we then average only the ones whose average values in the chosen wavevector range lie within 10% of the highest value. This corresponds to averaging a few number of power spectra, typically 2 or 3.

[1]Power spectra instabilities also affected previous HNFS spatial coherence measurements at the ESRF undulator [30], as extensively reported by Manfredda [29].

11.2.2 Spatial coherence measurements

Vertical profiles are reported in Fig. 11.3 for the three different sample-detector distances. By comparing Fig. 11.3(a) and Fig. 11.3(b), we can appreciate the accuracy of the power spectra selection in superimposing the upper and lower envelopes of Talbot oscillations. This allows to build the master curve in q-space corresponding to the instrumental transfer function of the phosphor screen, as shown in 11.4. Furthermore, data have been fitted with a negative exponential transfer function [] from which we can infer the characteristic wavevector of the YAG screen $q^* = 0.83\ \mu\text{m}^{-1}$ limiting power spectra in the vertical direction. Incidentally, the good fit to the q-vector master curve implies that the large vertical coherence areas could not be probed with the current configuration. With reference to Fig. 11.4, since the phosphor master curve is fitted up to roughly $q_{\max} = 2\ \mu\text{m}^{-1}$ and it causes the decay of Talbot oscillations to shotnoise level, we can conclude that the vertical coherence length is larger than $\sigma^{\max}_{\text{coh,v}} = q_{\max} z/k = 17.7\ \mu$m (the largest distance $z = 55$ cm has been used for the calculation).

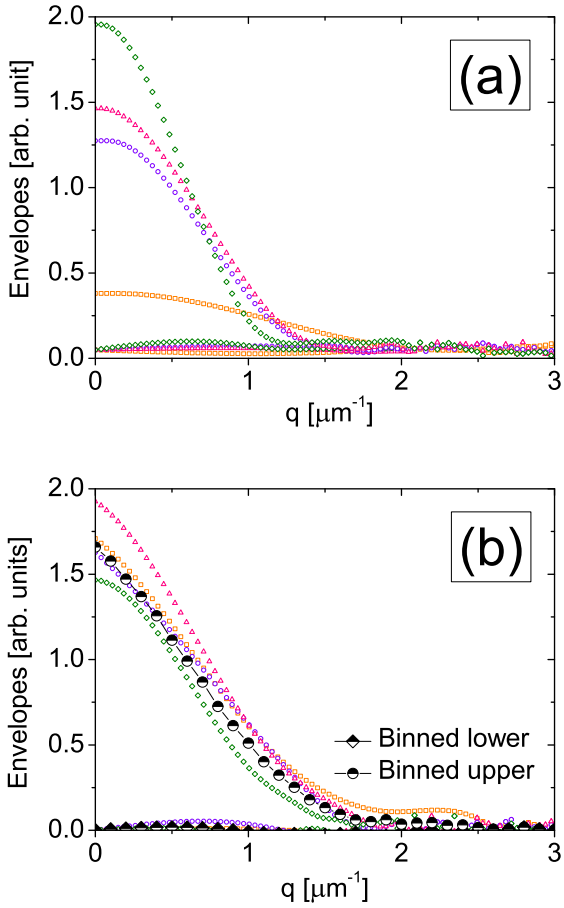

Figure 11.3: Vertical profiles of HNFS power spectra for the three probed sample-detector distances. (a) Upper and lower envelopes of Talbot oscillations fail to superimpose in q-space due to power spectra instabilities unless (b) only the best power spectra are selected.

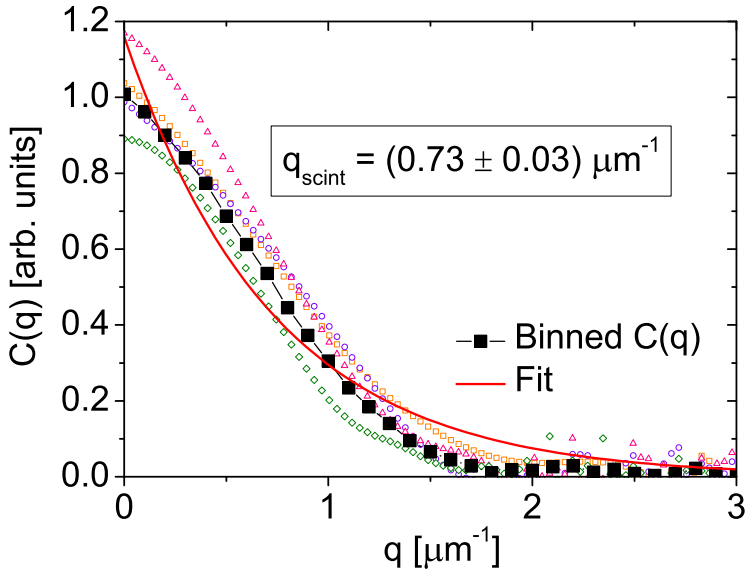

Figure 11.4: Averages of the upper and lower envelopes in Fig. 11.3 effectively build the master curve for the instrumental transfer function. A negative exponential fit is also reported, yielding the characteristic phosphor wavevector $q^* = (0.73 \pm 0.03)\ \mu\text{m}^{-1}$.

Figure 11.5 presents data regarding the horizontal profiles of power spectra. The instrumental transfer function $H(q)$ measured from the vertical profiles is used to properly reduce the horizontal curves. From Fig. 11.5(a) and Fig. 11.5(b) it can be noticed how the selection of power spectra ensures the good fit to the spatial master curve, as shown in Fig. 11.6. From the measured squared modulus of the radiation CCF, we derive a transverse coherence length equal to

$$\sigma_{\text{coh,x}} = 2 \int_{-\infty}^{+\infty} |\mu(\Delta x)|^2 \, \mathrm{d}\Delta x = (6.94 \pm 1.3)\ \mu\text{m}. \tag{11.1}$$

Experiments were carried with an unexpected low signal, likely due to the detuning of the monochromator central wavelength with respect the undulator resonant frequency or to some absorption effects by the cuvette walls. Therefore, raw data are quite noisy and this prevents to obtain a master curve as good as the temporal one for the case of visible SR beams. However, the dispersion of data around the binned curve is comparable to what has been reported elsewhere [29], thus validating our results.

11.2.3 Simulation of UR spatial coherence and discussion

Based on the theory of transverse coherence for third-generation light sources discussed in Chap. 3, we developed a $C/C++$ code for the simulation of the spatial coherence properties of undulator radiation. The software computes the ensamble average defining the spectral degree of coherence of the radiation as in Eq. 3.10 by adding the contributions of the fields emitted by a user-defined number of electrons N without any further assumption. We implemented the near field formula of the electric field for an

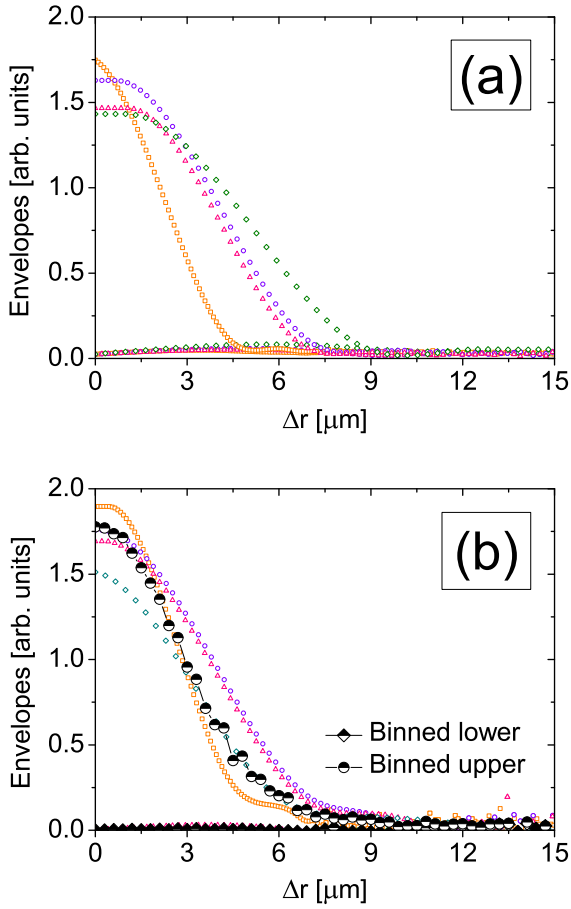

Figure 11.5: Horizontal profiles of HNFS power spectra for the three probed sample-detector distances. (a) Upper and lower envelopes of Talbot oscillations fail to superimpose in Δr-space due to power spectra instabilities unless (b) only the best power spectra are selected.

electron with offset and deflection under the assumption of perfect resonance, generalized to the h-th odd harmonics:

$$\hat{E}_h\left(\hat{z}_o,\vec{\hat{\theta}},\vec{\hat{\eta}},\vec{\hat{l}}\right)=e^{i\frac{\hat{z}_o}{2}\left|\vec{\hat{\theta}}-\frac{\vec{\hat{l}}}{\hat{z}_o}\right|^2}\Psi_h\left(\hat{z}_o,\left|\vec{\hat{\theta}}-\frac{\vec{\hat{l}}}{\hat{z}_o}-\vec{\hat{\eta}}\right|\right), \tag{11.2}$$

where we define

$$\Psi_h\left(\hat{z}_o,\alpha\right)=e^{-i\frac{\hat{z}_o\alpha^2}{2}}\left\{\mathrm{Ei}\left[\frac{i\hat{z}_o^2\alpha^2}{2\hat{z}_o-1}\right]-\mathrm{Ei}\left[\frac{i\hat{z}_o^2\alpha^2}{2\hat{z}_o+1}\right]\right\}. \tag{11.3}$$

As it can be seen, modifications are minimal for the odd harmonics and one only has to remember the new normalization $\hat{E}_h=[-2c^2\gamma/(K\omega eA_{\mathrm{JJ,h}})]\tilde{E}_h$ in passing from dimensionless to dimensional units, which however give no effects on the field correlation

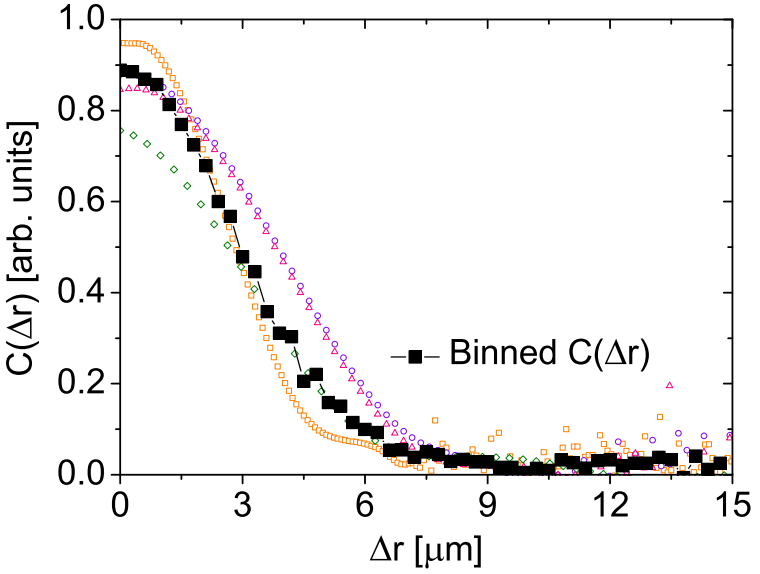

Figure 11.6: Averages of the upper and lower envelopes in Fig. 11.5 effectively build the master curve for the radiation CCF along the horizontal direction. The corresponding transverse coherence length is $\sigma_{\mathrm{coh,x}} = (6.94 \pm 1.3)\ \mu$m.

function. Here for completeness

$$A_{\mathrm{JJ,h}} = (-1)^{\frac{h-1}{2}} \left[J_{\frac{h-1}{2}} \left(\frac{hK^2}{4+2K^2} \right) - J_{\frac{h+1}{2}} \left(\frac{hK^2}{4+2K^2} \right) \right]. \tag{11.4}$$

Based on the reduced parameters given as an input, the code samples the desired transverse phase space of the electron beam by a Monte Carlo simulation coupled to Sobol sequences in order to avoid the formation of particle clusters. The user can choose between computing the two-dimensional transverse coherence function at a fixed distance or following the free propagation evolution of the transverse coherence length (in both horizontal and vertical direction) from the undulator exit. The transverse coherence length is computed in units of the diffraction length $(cL_w/\omega)^{1/2}$, while the distance from the undulator exit is normalized by the undulator length L_w.

The code has then been accelerated with CUDA in order to run on GPUs of commercially available laptops. Parallel computation of the electric field from different particles results in a speed-up of roughly 700X with respect to the serial implementation of the same code. This drastically reduces the computation time of the spectral degree of coherence of undulator radiation. The current version of the code is able to deal with 10^6 particles in less than 300 s on a 128×128 grid.

Benchmark of the code is reported in Fig. 11.7, where we compare the results of our simulation with the analytical results given in Eq. 3.13 and valid for $\hat{N} \gg 1$ and $\hat{D} \gg 1$. The good agreement between analytic results and actual simulations proves the validity of our code. We also report the asymptotic Van Cittert-Zernike's theorem ($\hat{z}_o \to +\infty$) and the Near Field limit at the undulator exit ($\hat{z} \to 1/2$).

Finally, we computed the evolution of the transverse coherence properties of the undulator radiation for the ALBA case. Results are shown in Fig. 11.8(a) and Fig. 11.8(b)

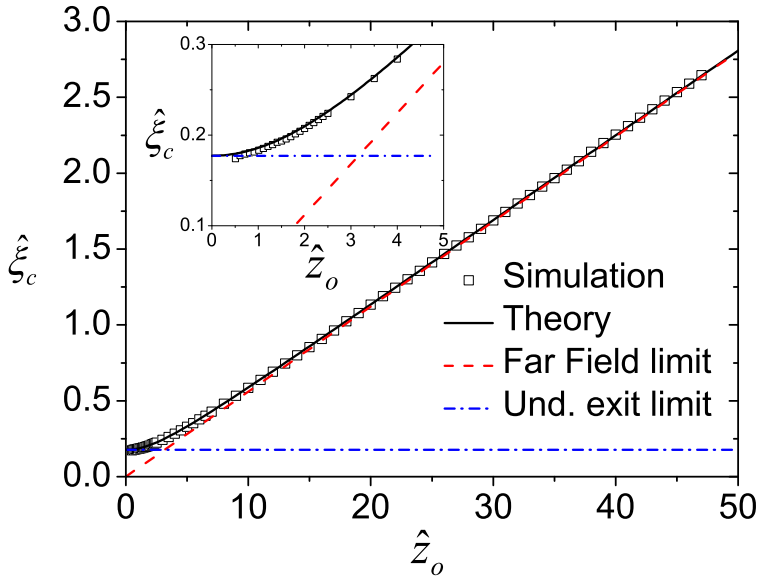

Figure 11.7: Benchmark of the GPU-based simulation code of undulator transverse coherence in the case $\hat{N} \gg 1$, $\hat{D} \gg 1$. Actual simulations (squared dots) and analytic expression (solid black line) for the reduced transverse coherence length $\hat{\xi}$ as a function of the normalized distance $\hat{z}_o$ are in good agreement. We also report the asymptotic Van Cittert-Zernike's theorem ($\hat{z}_o \to +\infty$, dashed red line) and the Near Field limit at the undulator exit ($\hat{z} \to 1/2$, dash-dotted blue line).

for the horizontal and vertical transverse coherence length, respectively. At the position of the HNFS diagnostics at $\hat{z}_o \approx 15$, the expected reduced transverse coherence length are $\hat{\xi}_{\mathrm{c,x}} = 1.1$ and $\hat{\xi}_{\mathrm{c,y}} = 18.0$. In normalized units $((cL_w/\omega)^{1/2} = 5.5$ μm at $\lambda = 1$ Å), $\sigma^{\mathrm{sim}}_{\mathrm{coh,x}} = 6.05$ μm and $\sigma^{\mathrm{sim}}_{\mathrm{coh,x}} = 100$ μm. It can be seen how the horizontal coherence properties measured with the HNFS technique are in agreement with theoretical expectations (relative error $(\sigma_{\mathrm{coh,x}} - \sigma^{\mathrm{sim}}_{\mathrm{coh,x}})/\sigma^{\mathrm{sim}}_{\mathrm{coh,x}}$ is less than 15%). Regarding vertical coherence properties, since the current setup is limited by the phosphor transfer function up to $q_{\max} = 2$ $\mu\mathrm{m}^{-1}$ at $z = 55$ cm, we could only measure transverse coherence length smaller than 17.7 μm. By properly rescaling the dimensionless parameters used in the simulation, this implies that the current setup could only probe electron beams with a vertical size larger than 40 μm, roughly 6 times larger than the nominal beam at NCD.

Finally, we would like to remark that these preliminary measurements were strongly affected by the low signal. A new experimental shift is scheduled to optimize the setup in terms of light yield by implementing new optical components and by replacing the scattering cuvette with much thinner capillaries. An enhanced detected signal might give access to a wider range of wavevector q (hence to a wider range of transverse displacements Δr) despite the presence of the phosphor, which currently determines the decay of power spectra to shotnoise level along the vertical direction. Furthermore, we could adopt an imaging geometry by means e.g. of compound refractive lenses to probe coherence properties of the X-ray radiation closer to the undulator exit where the transverse coherence length is expected to be shorter.

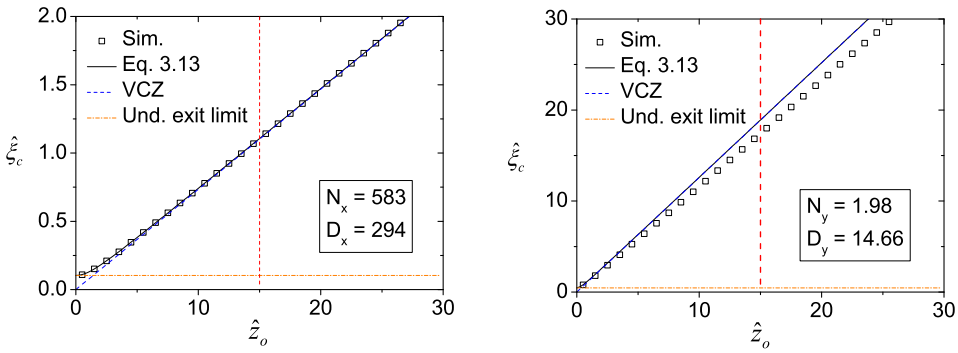

Figure 11.8: Simulated transverse coherence length as a function of the distance from the undulator exit (square black dots). Dimensionless quantities $\hat{\xi}_c$ and $\hat{z}_o$ are reported. The vertical dash red curve determines the position of the HNFS diagnostics. We also show for comparison the analytic results of Eq. 3.10 (solid black line), the Van Cittert-Zernike prediction (dashed blue line) and the undulator exit limit (dash-dotted orange line). It is worth noticing how the Van Cittert-Zernike's theorem yield incorrect result for the vertical transverse coherence length.

Conclusions and perspectives

In this thesis we have developed a diagnostics technique for partially coherent synchrotron radiation beams based on the Heterodyne Near Field Speckle (HNFS) approach. It relies on the Fourier analysis of the speckle fields generated by the staggered interference between the strong transmitted incident beam and the weak spherical waves scattered by nanoparticles suspended in a solution. Firstly introduced in 2009 by the Optics Laboratory of the University of Milan, so far it has been concerned with the study of spatial coherence. Here we show that the spatial power spectrum of near field speckle fields provides a direct measurement of the squared-modulus of the spatio-temporal coherence function of the incoming radiation, thus improving the existing theory and providing a complete and unified theoretical background of the HNFS method as a coherence diagnostics. The conditions for quantitatively assessing spatial and temporal coherence separately have been also discussed. In particular, a criterion based on master curves of data under two different scaling laws for the spatial and the temporal coherence has been introduced. Despite coherence properties can in principle be gauged with a single acquisition at a fixed distance, measurements at different distances endow the technique with robustness and versatility and they provide strong self-consistency to the experimental results.

The technique is ultimately wavelength independent and the experimental setup is minimal and free of any severe alignment requirement. Furthermore, the method can be easily operated at X-ray wavelengths, remarkably without any *ad hoc* engineered device or dedicated optics. Data processing is model independent and free from any external parameter. Finally, one of the most fashinating aspects of the HNFS technique is the possibility of directly measuring the two-dimensional spatial coherence function, as well as the entire temporal coherence function.

The technique has been tested with broadband table-top sources (halogen lamps and LEDs) to deduce temporal coherence properties in the simple case of visible thermal light, a paradigmatic system within the framework of Statistical Optics providing a solid benchmark for the technique. The measured coherence time of the white sources are in good agreement with the inverse bandwidth of the radiation, according to the Wiener-Khinchine's theorem and to independent measurements with a grating spectrometer. This proves the sensitivity of the technique to very short longitudinal coherence lengths of the order of a few wavelengths. Interestingly, for the case of the radiation emitted by the LEDs the measured temporal coherence function shows echoes at a characteristic time of 7 fs, revealing the double-peak structure of the emitted power spectral density with a wavelength separation of roughly 100 nm. Results are confirmed by independent

measurements with a grating spectrometer. This shows how HNFS can be advantageously implemented to characterize broadband sources.

We have also applied the technique to characterize the coherence properties of the second harmonic of a pulsed High Harmonic Generation (HHG) laser at the Laser Laboratory at the ELETTRA synchrotron, Trieste (Italy). We have proven that the laser pulses are endowed with limited transverse and longitudinal coherence lengths, since data failed to fit either the spatial or the temporal master curve. Close to the scattering sample, data succeeded in effectively building the temporal master curve. The measured coherence time $\tau_{\mathrm{coh}} = 190$ fs is comparable to the pulse duration $\sigma_T = 300$ fs and it corresponds to the presence of two longitudinal modes per pulse. We have also experimentally evidenced how the spatio-temporal coherence function of the laser pulses reduces to the product of the measured temporal master curve and of a spatial master curve describing transverse coherence properties. A transverse coherence length $\sigma_{\mathrm{coh}} = 3.83$ mm is found, comparable to the transverse beam size $\sigma_{\mathrm{beam}} = 5$ mm and corresponding to a degree of transverse coherence $\zeta = 0.77$. Finally, we have been able to reconstruct the two-dimensional spatio-temporal coherence function of the pulses from the simultaneous knowledge of the spatial and temporal master curves. It is worth noticing that, at variance with the case of classical thermal light, the system cannot be modelled as a quasi-stationary stochastic process and the Wiener-Khinchine's theorem does not hold anymore. The temporal master curve is thus expected to convey the information on both the temporal coherence of the radiation and the temporal intensity profile of the laser pulses, but a deeper and more detailed study of the phenomenon was not possible due to the lack of beamtime. Further analysis is currently ongoing.

In the last part of the thesis we have focused our attention to the meaningful scientific case of coherence characterization of partially coherent synchrotron radiation at the ALBA Synchrotron Light Source, Barcelona (Spain). We have performed for the first time measurements of temporal coherence of synchrotron radiation from a bending dipole (FE01 end station) with both narrowband and white beams. In the former case, a coherence time of 40 ± 10 fs has been measured, compatible with the filter inverse linewidth (expected value 43 fs). The high quality of the temporal master curve proves full spatial coherence over the accessed transverse scale of 1 mm, in agreement with independent Synchrotron Radiation Interferometry measurements. Since for visible wavelengths the sample lies in the far field of the source, coherence patches are homotetic, meaning that they propagate carring the information about the wavefront curvature. By studying the periodicity of the Talbot oscillations as the sample-detector distance is varied, we have estimated a wavefront radius of curvature larger than 5 m. Less conservatively, the fitted value is compatible with the nominal distance of 15 m from the center of the bending dipole. By contrast, it is worth noticing that for X-ray wavelengths the transition to the far field of the electron beam occurs after tens or hundreds meters and the scattering sample would always be in the Fresnel zone of the source. Coherence areas would then behave as diffraction-limited wavefronts with a Rayleigh range of the order of some meters, much larger than the sample-detector distances typically scanned during a HNFS experiment. The scattered spherical waves would thus be heterodyned by a wavefront carrying vanishing curvature. Regarding white beams, the decay of speckle power spectra yields a coherence time of 1.6 ± 0.4 fs, related to a radiation bandwidth of 240 nm at an average wavelength of 350 nm. From the measured squared modulus of the radiation Complex Degree of Coherence, we have retrieved the synchrotron power spectral density by applying the modified Wiener-Kintchine theorem. Results are in good agreement with independent measurements performed with a spectrometer, showing how HNFS can be effectively implemented as a powerful diagnostics technique.

Finally, we have performed preliminary measurements of the spatial coherence of an X-ray undulator beam at the BL11 beamline in free-propagation geometry, aimed at retreiving the transverse emittance of the electron beam. From the measured horizontal coherence length, a beam size $\sigma_x = 270$ μm has been obtained, with a good agreement with the nominal value of 309 μm. Measurements of the spatial coherence in the vertical directions have not been possible due to the unexpected low signal and to the predominant transfer function of the phosphor screen dictating the decay of power spectra to shotnoise level. While this is not the first application of HNFS for the analysis of transverse coherence of undulator radiation, it represents the first time that a direct measurement of the transverse beam size is attempted. In this view, since in many practical situations the conditions for the applicability of the Van Cittert-Zernike's theorem may not be satisfied, we have developed a simulation code based on the theory of transverse coherence of third-generation light sources as recently refurbished by G. Geloni *et al*. Given the four parameters σ_x, σ_y, $\sigma_x{}'$ and $\sigma_y{}'$ characterizing the electron beam size and divergence, the code fills the transverse phase space via Monte Carlo sampling for a given number N of particles. It then computes the propagated fields exploiting analytic expressions valid for the near zone as well as for the far zone and accounting for the correct phase terms for a particle with offset and deflection. The definition of the field correlation function is then applied in order to compute the two-dimensional spatial coherence function at a fixed distance or alternatively to follow the evolution of the transverse coherence length (both in the horizontal and in the vertical direction) as a function of the distance from the undulator exit. The code has been accelerated by CUDA in order to run on commercially available GPUs, computing the electric field of each particle concurrently and making such computing-demanding simualtions feasible to be executed on personal computers. A laptop equipped with a NVIDIA GEFORCE 940MX graphic card can deal with $N = 10^6$ particles in less than 300 s at a spatial resolution of 128$\times$128. A speedup of roughly 700X is observed compared to serial codes. The simulation software has been benchmarked with known cases and it was able to predict the correct transverse coherence length measured in our experiments. Extensions to include detuning and energy spread effects have already started.

As a closing remark, measurements have evidenced time-varying modulations of single-shot power spectra likely caused by relative vibrations of the camera with respect to the photon beam. Despite this issue has not been completely surveyed, it represents another valuable outcome of the technique, i.e. the possibility to perform time-resolved measurements. More generally, such characterization is expected to be of interest for coherence-based X-ray technique, being suitable to study the dynamics of photon beams as well as coherence fluctuations.

Appendices

APPENDIX A

Synchrotron Radiation: solution based on Paraxial Green's function

Let $\vec{E}_\perp(z_o, \vec{r}_{\perp o}, t) = \vec{\tilde{E}}_\perp(z_o, \vec{r}_{\perp o}, \omega)e^{-i\omega t}$ be the complex representation of a monochromatic wave of angular frequency ω. Here $\vec{r}_{\perp o} = (x_o, y_o)$ denotes the transverse coordinates of an observer at the longitudinal position z_o and $\vec{\tilde{E}}_\perp$ describes the complex amplitude of the wave. It satisfies the following differential equation in the space-frequency domain:

$$c^2\nabla^2\vec{\tilde{E}}_\perp + \omega^2\vec{\tilde{E}}_\perp = 4\pi c^2\vec{\nabla}\bar{\rho} - i4\pi\vec{\tilde{j}}, \tag{A.1}$$

where $\bar{\rho}(\vec{r}_\perp, z, \omega)$ and $\vec{\tilde{j}}(\vec{r}_\perp, z, \omega)$ are the Fourier transforms of the charge density $\rho(\vec{r}_\perp, z, t)$ and of the current density $\vec{j}(\vec{r}_\perp, z, t)$, respectively. Considering a single electron and introducing the curvilinear abscissa $s = vt$, where $v = |\vec{v}(t)|$ is assumed constant, the charge density and the current density take the form

$$\begin{aligned}
\rho(\vec{r}_\perp, z, t) &= -e\delta[\vec{r}_\perp - \vec{r}'_\perp(t)]\delta[z - z'(t)] = \\
&= -\frac{e}{v_z(z)}\delta[\vec{r}_\perp - \vec{r}'_\perp(z)]\delta\left[\frac{s(z)}{v} - t\right] \\
\vec{j}(\vec{r}_\perp, z, t) &= -e\vec{v}(t)\delta[\vec{r}_\perp - \vec{r}'_\perp(t)]\delta[z - z'(t)] = \\
&= -\frac{e}{v_z(z)}\vec{v}(z)\delta[\vec{r}_\perp - \vec{r}'_\perp(z)]\delta\left[\frac{s(z)}{v} - t\right],
\end{aligned} \tag{A.2}$$

where $(\vec{r}'_\perp(t), z'(t)) = (x'(t), y'(t), z'(t))$ and $\vec{v}(t)$ are the position and the velocity of the particle at a given time t, respectively. In the frequency domain the expressions for the charge density and for the current density correspond to

$$\begin{aligned}
\bar{\rho}(\vec{r}_\perp, z, \omega) &= -\frac{e}{v_z(z)}\delta(\vec{r}_\perp - \vec{r}'_\perp(z))\exp\left[i\omega\frac{s(z)}{v}\right] \\
\vec{\tilde{j}}(\vec{r}_\perp, z, \omega) &= -\frac{e}{v_z(z)}\vec{v}(z)\delta(\vec{r}_\perp - \vec{r}'_\perp(z))\exp\left[i\omega\frac{s(z)}{v}\right].
\end{aligned} \tag{A.3}$$

We introduce the slowly-varying envelope of the field

$$\vec{\tilde{\mathcal{E}}}_\perp = \vec{\tilde{E}}_\perp \exp\left(-i\omega\frac{z}{c}\right), \tag{A.4}$$

which satisfies the following general equation:

$$\left(\nabla^2 + \frac{2i\omega}{c}\frac{\partial}{\partial z}\right)\vec{\tilde{E}}_\perp = \frac{4\pi e}{v_z(z)}\exp\left\{i\omega\left(\frac{s(z)}{v} - \frac{z}{c}\right)\right\}\times$$
$$\times\left\{\frac{i\omega}{c^2}\vec{v}(z)\delta[\vec{r}_\perp - \vec{r}'_\perp(z)] - \vec{\nabla}\delta[\vec{r}_\perp - \vec{r}'_\perp(z)]\right\}. \tag{A.5}$$

In the ultrarelativistic approximation ($1/\gamma_z^2 \ll 1$), the radiation formation length is much longer than the wavelength and $\vec{\tilde{E}}_\perp$ does not vary appreciable on a scale comparable to the radiation wavelength λ: $|\partial_z\vec{\tilde{E}}_\perp| \ll (\omega/c)|\vec{\tilde{E}}_\perp|$. The second derivative with respect to z in ∇^2 can be neglected with respect to the first-order one and we can apply the paraxial approximation yielding to the following paraxial Maxwell's equation in space-frequency domain:

$$\left(\nabla_\perp^2 + \frac{2i\omega}{c}\frac{\partial}{\partial z}\right)\vec{\tilde{E}}_\perp = \frac{4\pi e}{c}\exp\left\{i\omega\left(\frac{s(z)}{v} - \frac{z}{c}\right)\right\}\times$$
$$\times\left\{\frac{i\omega}{c^2}\vec{v}_\perp(z)\delta[\vec{r}_\perp - \vec{r}'_\perp(z)] - \vec{\nabla}_\perp\delta[\vec{r}_\perp - \vec{r}'_\perp(z)]\right\}. \tag{A.6}$$

The solution to this equation is found by introducing the Green's function

$$G(z_o - z', \vec{r}_{\perp o} - \vec{r}'_\perp) = -\frac{1}{4\pi(z_o - z')}\exp\left\{i\omega\frac{|\vec{r}_{\perp o} - \vec{r}'_\perp|^2}{2c(z_o - z')}\right\} \tag{A.7}$$

and it takes the form

$$\vec{\tilde{E}}_\perp(z_o, \vec{r}_{\perp o}, \omega) = -\frac{e}{c}\int_{-\infty}^{+\infty}\mathrm{d}z'\,\frac{1}{z_o - z'}\times$$
$$\times\int\mathrm{d}\vec{r}'_\perp\left\{\frac{i\omega}{c^2}\vec{v}_\perp(z')\delta[\vec{r}'_\perp - \vec{r}'_\perp(z')] - \vec{\nabla}'_\perp\delta[\vec{r}'_\perp - \vec{r}'_\perp(z')]\right\}\times$$
$$\times\exp\left\{i\omega\left[\frac{|\vec{r}_{\perp o} - \vec{r}'_\perp|^2}{2c(z_o - z')} + \left[\frac{s(z')}{v} - \frac{z'}{c}\right]\right]\right\}. \tag{A.8}$$

The integration over the transverse coordinates can be performed straighforwardly, leading to the final expression

$$\vec{\tilde{E}}_\perp(z_o, \vec{r}_\perp, \omega) = -\frac{i\omega e}{c^2}\int_{-\infty}^{+\infty}\mathrm{d}z'\,\frac{e^{i\Phi_T}}{z_o - z'}\times$$
$$\times\left[\left(\frac{v_x(z')}{c} - \frac{x_o - x'(z')}{z_o - z'}\right)\hat{x} + \left(\frac{v_y(z')}{c} - \frac{y_o - y'(z')}{z_o - z'}\right)\hat{y}\right], \tag{A.9}$$

where the total phase Φ_T is given by

$$\Phi_T = \omega\left[\frac{s(z')}{v} - \frac{z'}{c}\right] + \omega\left[\frac{(x_o - x'(z'))^2 + (y_o - y'(z'))^2}{2c(z_o - z)}\right]. \tag{A.10}$$

APPENDIX B

Fourier Optics approach to classical electrodynamics

We now couple the theory of Synchrotron Radiation with Fourier Optics, a branch of physical optics suitable for the description of laser beams. This parallelism stems for the fact that both the radiation from an ultrarelativistic electron in a magnetic configuration and laser beams are solution of the wave equation under paraxial conditions. In particular, undulator radiation from an ultrarelativistic electron appears as a laser-like beam generated by a virtual source endowed with a plane wavefront. Remarkably, the electric field distribution of this virtual source is related to the Fourier transform of the far-field angular pattern.

The free-space evolution of the slowly-varying envelope of a monochromatic electromagnetic field is determined by the following source-free paraxial Maxwell's equation in space-frequency domain:

$$\left(\nabla_{\perp}^{2} + \frac{2i\omega}{c}\frac{\partial}{\partial z}\right)\vec{\tilde{E}}_{\perp} = 0. \tag{B.1}$$

It describes the propagation law for the complex envelope of the radiation field $\vec{\tilde{E}}_{\perp}(z, \vec{r}'_{\perp}, \omega)$ from a plane z to the plane of observation at z_o. The solution of this Cauchy-like problem for a fixed polarization component is given by

$$\tilde{E}_{\perp}(z_o, \vec{r}_{\perp o}, \omega) = \frac{i\omega}{2\pi c(z_o - z)} \int \mathrm{d}\vec{r}'_{\perp}\, \tilde{E}_{\perp}(z, \vec{r}'_{\perp}, \omega) \exp\left[\frac{i\omega|\vec{r}_{\perp o} - \vec{r}'_{\perp}|^2}{2c(z_o - z)}\right]. \tag{B.2}$$

We now introduce the spatial Fourier transform of the electric field by means of the following relations:

$$\begin{aligned} F(z, \vec{u}) &= \int \mathrm{d}\vec{r}_{\perp}\, \tilde{E}_{\perp}(z, \vec{r}_{\perp}, \omega) \exp\left[i\vec{r}_{\perp} \cdot \vec{u}\right] \\ \tilde{E}(z, \vec{r}_{\perp}, \omega) &= \frac{1}{4\pi^2} \int \mathrm{d}\vec{u}\, F(z, \vec{u}) \exp\left[-i\vec{r}_{\perp} \cdot \vec{u}\right]. \end{aligned} \tag{B.3}$$

It satisfies the following differential equation

$$\left(-|\vec{u}|^2 + \frac{2i\omega}{c}\frac{\partial}{\partial z}\right) F(z, \vec{u}) = 0 \tag{B.4}$$

whose solution is given by

$$F(z, \vec{u}) = F(0, \vec{u}) \exp\left[-\frac{ic|\vec{u}|^2 z}{2\omega}\right]. \tag{B.5}$$

The spatial Fourier transfomr of the electric field exhibits a trivial behavior during free-space propagation along the z-direction, while the same arguments do not generally hold for the electric field itself. This property is strictly related with the Fourier Optics interpretation of the spatial Fourier transform of the electric field (also known as the angular spectrum of the optical disturbance) as the superposition of many plane waves propagating along different directions and thus suffering different phase shifts.

Considering the far field case, defined by $z_o \to +\infty$ with a constant ratio $\vec{r}_\perp / z_o$, and expanding the exponential factor, we obtain

$$\tilde{E}_\perp(z_o, \vec{r}_{\perp o}, \omega) = \frac{i\omega}{2\pi c z_o} \int \mathrm{d}\vec{r}'_\perp \, \tilde{E}_\perp(z, \vec{r}'_\perp, \omega) \exp\left[\frac{i\omega}{2cz_o}\left(|\vec{r}_{\perp o}|^2 - 2\vec{r}_{\perp o}\cdot\vec{r}'_\perp + \frac{z}{z_o}|\vec{r}_{\perp o}|^2\right)\right]. \tag{B.6}$$

Exploiting the definition of the angular spectrum of the electric field and the propagation law of Eq. B.4 and Eq. B.5 and letting $\vec{\theta} = \vec{r}_\perp / z_o$, the far field expression of the electric field is expressed as

$$\tilde{E}_\perp(\vec{\theta}) = \frac{i\omega}{2\pi c z_o} \exp\left[\frac{i\omega|\theta|^2}{2c} z_o\right] F\left(0, -\frac{\omega\vec{\theta}}{c}\right). \tag{B.7}$$

The far field expression of the electric field is given by the spatial Fourier transform of the electric field at any position, apart for proportionality constants and phase factors. We can always interpret $F(0, \vec{u})$ as the spatial Fouier transform of a virtual source. Assuming that it is placed at $z = 0$, the virtual source is defined by the fact that it produces the same electric field distribution under study at any distance along the beamline.

We can also compute the electric field at the virtual source position by Fourier-inverting the previous relation:

$$\tilde{E}_\perp(0, \vec{r}_\perp, \omega) = \frac{i\omega z_o}{2\pi c} \int \mathrm{d}\vec{\theta} \exp\left[-\frac{i\omega|\theta|^2}{2c} z_o\right] \tilde{E}_\perp(\vec{\theta}) \exp\left[\frac{i\omega}{c}\vec{r}_\perp \cdot \vec{\theta}\right]. \tag{B.8}$$

Remarkably, the field at the virtual source position is related to the inverse Fourier trasform of the far field angle distribution. This allows to characterize the virtual source from the far field expression of the electric field.

APPENDIX C

Free-space evolution of undulator transverse coherence in the case $\hat{N} \gg 1$ and $\hat{D} \gg 1$

We now specialize the theory of the cross-spectral density of Synchrotron Radiation to the case of an undulator source. Restricting our analysis to the case of the system tuned at resoance with the first harmonic, we recall that under the resonant approximation the following expression is valid for the undulator reduced field $\tilde{E}_\perp$ emitted by a single electron with offset and deflection:

$$\hat{E}_\perp(\vec{\hat{l}}, \vec{\hat{\eta}}, \hat{z}, \vec{\hat{r}}_{\perp o}, \hat{C}) = \hat{z}_o \int_{-1/2}^{+1/2} \mathrm{d}\hat{z}' \, \frac{1}{\hat{z}_o - \hat{z}'} \exp\left\{ i \left[\left(\hat{C} + \frac{|\vec{\hat{\eta}}|^2}{2} \right) \hat{z}' + \frac{|\vec{\hat{r}}_{\perp o} - \vec{\hat{l}} - \vec{\hat{\eta}}\hat{z}'|^2}{2(\hat{z}_o - \hat{z}')} \right] \right\}, \tag{C.1}$$

where the normalized parameters are define as

$$\begin{aligned}
\hat{E}_\perp &= -\frac{c^2 z_o \gamma}{K \omega e L_w A_{\mathrm{JJ}}} \tilde{E}_\perp \\
\vec{\hat{\eta}} &= \vec{\eta} \sqrt{\frac{\omega L_w}{c}} \\
\hat{C} &= L_w C = 2\pi N_w \frac{\omega - \omega_0}{\omega_0} \\
\vec{\hat{r}}_{\perp o} &= \vec{r}_{\perp o} \sqrt{\frac{\omega}{c L_w}} \\
\vec{\hat{l}} &= \vec{l} \sqrt{\frac{\omega}{c L_w}} \\
\hat{z} &= \frac{z}{L_w}.
\end{aligned} \tag{C.2}$$

It can be shown that the electric field can be rewritten in the following general form:

$$\hat{E}_\perp\left(\hat{C},\hat{z}_o,\vec{\hat{\theta}}-\frac{\vec{\hat{l}}}{\hat{z}_o}-\vec{\hat{\eta}}\right)=\int_{-1/2}^{+1/2}\mathrm{d}\hat{z}'\,\frac{\hat{z}_o}{\hat{z}_o-\hat{z}'}\times$$

$$\times\exp\left\{i\left[\Phi_U+\hat{C}\hat{z}'+\frac{\hat{z}_o\hat{z}'}{2(\hat{z}_o-\hat{z}')}\left(\vec{\hat{\theta}}-\frac{\vec{\hat{l}}}{\hat{z}_o}-\vec{\hat{\eta}}\right)^2\right]\right\}=$$

$$=\exp(i\Phi_U)\,S\left[\hat{C},\hat{z}_o,\left(\vec{\hat{\theta}}-\frac{\vec{\hat{l}}}{\hat{z}_o}-\vec{\hat{\eta}}\right)^2\right]. \tag{C.3}$$

We introduce a version of G_ω defined as a function of normalized variables:

$$\hat{G}(\hat{z}_o,\vec{\hat{\theta}}_1,\vec{\hat{\theta}}_2,\hat{C})=\left\langle\hat{E}_\perp\left(\hat{C},\hat{z}_o,\vec{\hat{\theta}}_1-\frac{\vec{\hat{l}}}{\hat{z}_o}-\vec{\hat{\eta}}\right)\hat{E}^*_\perp\left(\hat{C},\hat{z}_o,\vec{\hat{\theta}}_2-\frac{\vec{\hat{l}}}{\hat{z}_o}-\vec{\hat{\eta}}\right)\right\rangle=$$

$$=\left(\frac{c^2z_o\gamma}{K\omega eL_wA_{\mathrm{JJ}}}\right)^2G_\omega. \tag{C.4}$$

We next substitute Eq. C.3 into Eq. C.4 and we expand thecomplex exponent. We then rephrase the ensamble average in terms of integration over the beam distribution functions, yielding to

$$\hat{G}(\hat{z}_o,\vec{\hat{\theta}}_1,\vec{\hat{\theta}}_2,\hat{C})=\exp\left[i\left(\vec{\hat{\theta}}_1^2-\vec{\hat{\theta}}_2^2\right)\frac{\hat{z}_o}{2}\right]\int\mathrm{d}\vec{\hat{l}}\,\mathrm{d}\vec{\hat{\eta}}\,F_{\vec{\hat{l}},\vec{\hat{\eta}}}(\vec{\hat{l}},\vec{\hat{\eta}})\exp[i(\vec{\hat{\theta}}_2-\vec{\hat{\theta}}_1)\cdot\vec{\hat{l}}]\times$$

$$\times S\left[\hat{C},\hat{z}_o,\left(\vec{\hat{\theta}}_1-\frac{\vec{\hat{l}}}{\hat{z}_o}-\vec{\hat{\eta}}\right)^2\right]S^*\left[\hat{C},\hat{z}_o,\left(\vec{\hat{\theta}}_2-\frac{\vec{\hat{l}}}{\hat{z}_o}-\vec{\hat{\eta}}\right)^2\right]. \tag{C.5}$$

The phase space distributions can be expressed in normalized units as

$$F_{\hat{\eta}_x}(\hat{\eta}_x)=\frac{1}{\sqrt{2\pi\hat{D}_x}}\exp\left(-\frac{\hat{\eta}_x^2}{2\hat{D}_x}\right)$$

$$F_{\hat{\eta}_y}(\hat{\eta}_y)=\frac{1}{\sqrt{2\pi\hat{D}_y}}\exp\left(-\frac{\hat{\eta}_y^2}{2\hat{D}_y}\right)$$

$$F_{\hat{l}_x}(\hat{l}_x)=\frac{1}{\sqrt{2\pi\hat{N}_x}}\exp\left(-\frac{\hat{l}_x^2}{2\hat{N}_x}\right)$$

$$F_{\hat{l}_y}(\hat{l}_y)=\frac{1}{\sqrt{2\pi\hat{N}_y}}\exp\left(-\frac{\hat{l}_y^2}{2\hat{N}_y}\right), \tag{C.6}$$

where $\hat{N}_{\mathrm{x,y}}$ and $\hat{D}_{\mathrm{x,y}}$ represent the normalized rms transverse dimension and angular spread of the electron bunch:

$$\hat{N}_{\mathrm{x,y}} = \sigma^2_{\mathrm{x,y}} \frac{\omega}{L_w c} \qquad\qquad \hat{D}_{\mathrm{x,y}} = \sigma'^2_{\mathrm{x,y}} \frac{\omega L_w}{c}. \tag{C.7}$$

At perfect resonance ($\hat{C} = 0$) we thus obtain the following general expression:

$$\begin{aligned}
\hat{G}(\hat{z}_o, \vec{\hat{\theta}}_1, \vec{\hat{\theta}}_2) = & \frac{\exp\left[i\left(\vec{\hat{\theta}}_1^2 - \vec{\hat{\theta}}_2^2\right)\frac{\hat{z}_o}{2}\right]}{4\pi^2\sqrt{\hat{D}_x\hat{D}_y\hat{N}_x\hat{N}_y}} \times \\
& \times \int_{-\infty}^{+\infty} \mathrm{d}\hat{\eta}_x \, \exp\left(-\frac{\hat{\eta}_x^2}{2\hat{D}_x}\right) \int_{-\infty}^{+\infty} \mathrm{d}\hat{\eta}_y \, \exp\left(-\frac{\hat{\eta}_y^2}{2\hat{D}_y}\right) \times \\
& \times \int_{-\infty}^{+\infty} \mathrm{d}\hat{l}_x \, \exp\left(-\frac{\hat{l}_x^2}{2\hat{N}_x}\right) \int_{-\infty}^{+\infty} \mathrm{d}\hat{l}_y \, \exp\left(-\frac{\hat{l}_y^2}{2\hat{N}_y}\right) \times \\
& \times S\left[\hat{z}_o, \left(\vec{\hat{\theta}}_1 - \frac{\vec{\hat{l}}}{\hat{z}_o} - \vec{\hat{\eta}}\right)^2\right] S^*\left[\hat{z}_o, \left(\vec{\hat{\theta}}_2 - \frac{\vec{\hat{l}}}{\hat{z}_o} - \vec{\hat{\eta}}\right)^2\right] \exp[i(\vec{\hat{\theta}}_1 - \vec{\hat{\theta}}_2)\cdot\vec{\hat{l}}].
\end{aligned} \tag{C.8}$$

1-D model of undulator radiation

We now assume that the vertical emittance is much smaller than the horizontal one. This implies that we can neglect the terms in $\hat{\eta}_y$ and $\hat{l}_y$. We will also restrict our attention to the correlation function in the horizontal plane, for which $\hat{\theta}_{y_1} = \hat{\theta}_{y_2}$. Introducing the variables

$$\begin{aligned}
\Delta\hat{\theta} &= \frac{\hat{\theta}_{x_1} - \hat{\theta}_{x_2}}{2} \\
\bar{\theta} &= \frac{\hat{\theta}_{x_1} + \hat{\theta}_{x_2}}{2}
\end{aligned} \tag{C.9}$$

and performing the following changes of variables

$$\begin{aligned}
\hat{\eta}_x &\to \hat{\eta} + \bar{\theta} \\
\frac{\hat{l_x}}{\hat{z}_o} &\to \hat{\phi} - \hat{\eta}
\end{aligned} \tag{C.10}$$

yields to

$$\begin{aligned}
\hat{G}(\hat{z}_o, \bar{\theta}, \Delta\hat{\theta}) = & \frac{\exp(i2\bar{\theta}\Delta\hat{\theta}\hat{z}_o)}{2\pi\sqrt{\hat{D}\hat{N}/\hat{z}_o^2}} \exp\left(-\frac{\bar{\theta}^2}{2\hat{D}}\right) \int_{-\infty}^{+\infty} \mathrm{d}\hat{\phi} \left[\exp\left(-\frac{\phi^2}{2\hat{N}/\hat{z}_o^2}\right) \times\right. \\
& \times \exp(-2i\Delta\hat{\theta}\hat{z}_o\phi) S^*[\hat{z}_o, (\hat{\phi} - \Delta\hat{\theta})^2] S[\hat{z}_o, (\hat{\phi} + \Delta\hat{\theta})^2] \times \\
& \left. \times \int_{-\infty}^{+\infty} \mathrm{d}\hat{\eta} \, \exp\left(-\frac{\hat{N}/\hat{z}_o^2 + \hat{D}}{2\hat{D}\hat{N}/\hat{z}_o^2}\hat{\eta}^2 + \frac{\hat{\phi}}{\hat{N}/\hat{z}_o^2} - \frac{\bar{\theta}}{\hat{D}}\hat{\eta} + 2i\Delta\hat{\theta}\hat{z}_o\hat{\eta}\right)\right].
\end{aligned} \tag{C.11}$$

The integral in $\hat{\eta}$ can be performed analytically leading to

$$\begin{aligned}\hat{G}(\hat{z}_o,\bar{\theta},\Delta\hat{\theta}) = &\frac{\exp(i2\bar{\theta}\Delta\hat{\theta}\hat{z}_o)}{\sqrt{2\pi(\hat{N}/\hat{z}_o^2+\hat{D})}}\times\\ &\times\exp\left[-\frac{\bar{\theta}^2+4\hat{N}\Delta\hat{\theta}^2\hat{D}+4i(\hat{N}/\hat{z}_o^2)\bar{\theta}\Delta\hat{\theta}}{2(\hat{N}/\hat{z}_o^2+\hat{D})}\right]\times\\ &\times\int_{-\infty}^{+\infty}\mathrm{d}\hat{\phi}\,\exp\left[-\frac{\hat{\phi}^2+2\hat{\phi}(\theta+2i(\bar{\hat{N}}/\hat{z}_o)\Delta\hat{\theta}}{2(\hat{N}/\hat{z}_o+\hat{D})}\right]\times\\ &\times S^*[\hat{z}_o,(\hat{\phi}-\Delta\hat{\theta})^2]S[\hat{z}_o,(\hat{\phi}+\Delta\hat{\theta})]. \end{aligned}\tag{C.12}$$

We now make the non-restrictive assumptions $\hat{N}\gg 1$ and $\hat{D}\gg 1$ and define $\hat{A}=\hat{N}/\hat{z}_o^2$, which represent the angular size of the source at the observer position in dimensionless units. Under the assumptions on $\hat{N}$ and $\hat{D}$, the term $2\hat{A}\hat{z}_o^2\hat{D}/(\hat{A}+\hat{D})$ is always much greater than one. The exponential factor outside of the integral sign implies that $\hat{G}(\hat{z}_o,\bar{\theta},\Delta\hat{\theta})$ is different from zero only for (very) small values of $\Delta\hat{\theta}$. As a result,we can neglet the terms $\Delta\hat{\theta}$ inside $S(\cdot)$ and $S^*(\cdot)$. We can also neglect the exponential factor $\exp[-(\hat{\phi}^2+2\hat{\phi}\bar{\theta})/(2\hat{A}+2\hat{D})]$ since its argument takes values of order unity for $\hat{\phi}\gg 1$ where the function $S(\cdot)$ cuts off the integrand. The integral reduces to the Fourier transform of $f(\hat{\phi})=|S(\hat{z}_o,\hat{\phi}^2)|^2$ expressed as a function of the variable $2\hat{A}\hat{z}_o\Delta\hat{\theta}/(\hat{A}+\hat{D})$. Since $f(\hat{\phi})$ is non-negligible for $\hat{\phi}$ of order unity or smaller, the integral gives non-negligible contributions only up to some maximum value of $|\Delta\hat{\theta}|$:

$$|\Delta\hat{\theta}|_{\max}\approx\frac{1}{2\hat{z}_o}\left(1+\frac{\hat{D}}{\hat{A}}\right).\tag{C.13}$$

At the same time, the exponential factor outside the integral requires $|\Delta\hat{\theta}|$ to take values smaller than or of the same order as

$$|\Delta\hat{\theta}|_{\max}2\approx\frac{1}{2\hat{z}_o}\left(\frac{1}{\hat{D}}+\frac{1}{\hat{A}}\right)^{1/2}.\tag{C.14}$$

For any values of $\hat{z}_o$, $|\Delta\hat{\theta}_{\max}|\gg|\Delta\hat{\theta}_{\max 2}|$ in the limit $\hat{D}\gg 1$. The Fourier transform is significant only for values of $2\hat{A}\hat{z}_o\Delta\hat{\theta}/(\hat{A}+\hat{D})$ almost null and it thus contributes to $\hat{G}(\hat{z}_o,\bar{\theta},\Delta\hat{\theta})$ with the inessential factor

$$\int_{-\infty}^{+\infty}\mathrm{d}\hat{\phi}|S[\hat{z}_o,\hat{\phi}^2]|^2=\textbf{const}.\tag{C.15}$$

We finally arrive to the following expression for the spectral degree of coherence of undulator radiation:

$$g(\hat{z}_o,\bar{\theta},\Delta\hat{\theta})=\exp(i2\bar{\theta}\hat{z}_o\Delta\hat{\theta})\exp\left[-\frac{2i\hat{A}\bar{\theta}\hat{z}_o\Delta\hat{\theta}}{\hat{A}+\hat{D}}\right]\exp\left[-\frac{2\hat{A}\hat{D}\hat{z}_o^2\Delta\hat{\theta}}{\hat{A}+\hat{D}}\right].\tag{C.16}$$

Following Mandel and defining the transverse coherence length ,normalized to the diffraction length $\sqrt{L_w c/\omega}$, as follows

$$\hat{\xi}_c(\hat{z}_o) = 2 \int_{-\infty}^{+\infty} |g(\Delta\hat{\theta})|^2 \, \mathrm{d}(\hat{z}_o \Delta\hat{\theta}), \tag{C.17}$$

we obtain

$$\hat{\xi}_c(\hat{z}_o) = \sqrt{\pi} \left(\frac{1}{\hat{A}} + \frac{1}{\hat{D}} \right)^{1/2}. \tag{C.18}$$

Bibliography

[1] D. Mills, *Third Generation Hard X-ray Synchrotron Radiation Sources* (John Wiley and Sons, Inc., New York, 2002).

[2] A. Hofmann, *The Physics of Synchrotron Radiation* (Cambridge University Press, Cambridge, United Kingdom, 2004).

[3] E. L. Saldin, E. A. Schneidmiller, and M. V. Yurkov, *The Physics of Free Electron Lasers* (Springer-Verlag, Berlin, 2000).

[4] Z. Huang, and K.-J. Kim, "Review of X-ray free-electron laser theory", *Phys. Rev. ST Accel. Beams* **10**, 034801 (2007).

[5] A. K. Nugent, "Coherent methods in the X-ray sciences", *Adv. Phys.* **59**, 1 (2010).

[6] T. Naito, and T. Mitsuhashi, "Very small beam-size measurement by a reflective synchrotron radiation interferometer", *Phys. Rev. ST Accel. Beams* **9**, 122802 (2006).

[7] L. Torino, and U. Iriso, "Transverse beam profile reconstruction using synchrotron radiation interferometry", *Phys. Rev. Accel. Beams* **19**, 122801 (2016).

[8] G. Kube, "Review of synchrotron radiation based diagnostics for transverse profile measurements", in *Proceeding of 8^{th} European workshop on beam Diagnostics and Instrumentation of Particle Accelerators (DIPAC 2007)*.

[9] T. Mitsuhashi, "Recent trends in beam size measurements using the spatial coherence of visible synchrotron radiation", in *Proceedings of 6^{th} International Particle Accelerator Conference (IPAC 2015)*.

[10] H. Wiedemann, *Particle Accelerator Physics* (Springer-Verlag, Berlin, 2007).

[11] S. Corde, K. Ta Phuoc, G. Lambert, R. Fitour, V. Malka, A. Rousse, A. Beck, and E. Lefebvre, "Femtosecond X-rays from laser-plasma accelerators", *Rev. Mod.Phys.* **85**, 1 (2013).

[12] A. Rousse, K. T. Phouc, R. Shah, A. Pukhov, E. Lefebvre, V. Malka, S. Kiselev, F. Burgy, J.-P. Rousseau, D. Umstadter, and D. Hulin, "Production of a keV X-Ray Beam from Synchrotron Radiation in Relativistic Laser-Plasma Interaction", *Phys. Rev. Lett.* **93**(13), 135005 (2004).

[13] S. Cipiccia *et. al.*, "Gamma-rays from harmonically resonant betatron oscillations in a plasma wake", *Nat. Phys.* **7**, 867 (2011).

[14] B. Paroli, E. Chiadroni, M. Ferrario, A. Mostacci, V. Petrillo, M. A. C. Potenza, A. R. Rossi, and L. Serafini, "Coherence properties and diagnostics of betatron radiation emitted by an externally-injected electron beam propagating in a plasma channel", *Nucl. Instrum. Methods Phys. Res., Sect. B* **355**, 217 (2015).

[15] A. Curcio, M. Anania, F. Bisesto, E. Chiadroni, A. Cianchi, M. Ferrario, F. Filippini, D. Giulietti, A. Marocchino, M. Petrarca, V. Shpakov, and A. Zigler, "Trace-space reconstruction of low-emittance electron beams through betatron radiation in laser-plasma accelerators", *Phys. Rev. Accel. Beams* **20**, 012801 (2017).

[16] B. Paroli, E. Chiadroni, M. Ferrario, V. Petrillo, M. A. C. Potenza, A. R. Rossi, L. Serafini, and V. Shpakov, "Asymmetric lateral coherence of betatron radiation emitted in laser-driven light sources", *EPL* **111**, 44003 (2015).

[17] T. Ditmire, E. T. Gumbrell, R. A. Smith, J. W. G. Tisch, D. D. Meyerhofer, and M. H. R. Hutchinson, "Spatial Coherence Measurement of Soft X-ray Radiation Produced by High Order Harmonic Generation", *Phys. Rev. Lett.* **77**, 4756 (1996).

[18] V. Kohn, I. Snigireva, and A. Snigirev, "Direct Measurement of Transverse Coherence Length of Hard X-rays from Interference Fringes", *Phys. Rev. Lett.* **85**, 2745 (2000).

[19] D. Paterson, B. E. Allman, P. J. McMahon, J. Lin, N. Moldovan, K. A. Nugent, I. McNulty, C. T. Chantler, C. C. Retsch, T. H. K. Irving, and D. C. Mancini, "Spatial coherence measurement of X-ray undulator radiation", *Opt. Commun.* **195**, 79 (2001).

[20] J. P. Sutter, T. Ishikawa, U. Kuetgens, G. Materlik, Y. Nishino, A. Rostomyan, K. Tamasaku, and M. Yabashi, "An X-ray BBB Michelson interferometer", *J. Synchrotron Radiat.* **11**, 378 (2004).

[21] V. Hilbert, A. Blinne, S. Fuchs, T. Feigl, T. Kampfer, C. Rodel, I. Uschmann, M. Wunsche, G. G. Paulus, E. Forster, and U. Zastrau, "An extreme ultraviolet Michelson interferometer for experiments at free electron lasers", *Rev. Sci. Instrum.* **84**, 095111 (2013).

[22] M. Masaki, and S. Takano, "Two-dimensional visible synchrotron light interferometry for transverse beam-profile measurement at the SPring-8 storage ring", *J. Synchrotron Radiat.* **10**, 295 (2003).

[23] J. J. A. Lin, D. Paterson, A. G. Peele, P. J. McMahon, C. T. Chantler, K. A. Nugent, B. Lai, N. Moldovan, Z. Cai, D. C. Mancini, and I. McNulty, "Measurement of the Spatial Coherence Function of Undulator Radiation using a Phase Mask", *Phys. Rev. Lett.* **90**, 074801 (2003).

[24] F. Pfeiffer, O. Bunk, C. Schulze-Briese, A. Diaz, T. Weitkamp, C. David, J. F. van der Veen, I. Vartanyants, and I. K. Robinson, "Shearing Interferometer for Quantifying the Coherence of Hard X-Ray Beams", *Phys. Rev. Lett.* **94**, 164801 (2005).

[25] X. Shi, S. Marathe, M. J. Wojcik, N. G. Kujala, A. T. Macrander, and L. Assoufid, "Circular grating interferometer for mapping transverse coherence area of Xray beams", *Appl. Phys. Lett.* **105**, 041116 (2014).

[26] M. Lyubomirskiy, I. Snigireva, and A. Snigirev, "Lens coupled tunable Young's double pinhole system for hard X-ray spatial coherence characterization", *Opt. Express* **24**, 13679 (2016).

[27] F. Ferri, D. Magatti, D. Pescini, M. A. C. Potenza, and M. Giglio, "Heterodyne near-field scattering: A technique for complex fluids", *Phys. Rev. E* **70**, 041405 (2004).

[28] D. Magatti, M. D. Alaimo, M. A. C. Potenza, and F. Ferri, "Dynamic heterodyne near field scattering", *Appl. Phys. Lett.* **92**, 241101 (2008).

[29] M. Manfredda, "Probing Synchrotron RAdiation Coherence: the Heterodyne Speckle Approach", Ph.D. thesis, University of Milan (2012).

[30] M. D. Alaimo, M. A. C. Potenza, M. Manfredda, G. Geloni, M. Sztucki, T. Narayanan, and M. Giglio, "Probing the Transverse Coherence of an Undulator X-ray Beam Using Brownian Particles", *Phys. Rev. Lett.* **103**, 194805 (2009).

[31] M. D. Alaimo *et al.*, "Mapping the transverse coherence of the self amplified spontaneous emission of a free-electron laser with the heterodyne speckle method", *Opt. Express* **22**, 30013 (2014).

[32] M. Siano, B. Paroli, E. Chiadroni, M. Ferrario, and M. A. C. Potenza, "Measurement of power spectral density of broad-spectrum visible light with heterodyne near field scattering and its scalability to betatron radiation", *Opt. Express* **23**, 32888 (2015).

[33] M. Siano, B. Paroli, M. A. C. Potenza, U. Iriso, A. A. Nosych, L. Torino, S. Mazzoni, G. Trad, and A. N. Goldblatt, "Characterizing temporal coherence of visible synchrotron radiation with heterodyne near field speckles", *Phys. Rev. Accel. Beams* **20**, 110702 (2017).

[34] R. Cerbino, L. Peverini, M. A. C. Potenza, A. Robert, P. Bosecke, and M. Giglio, "X-ray scattering information obtained from near-field speckle", *Nat. Phys.* 4, 238 (2008).

[35] Y. Kashyap, H. Wang, and K. Sawhney, "Two-dimensional transverse coherence measurement of hard-X-ray beams using near-field speckle", *Phys. Rev. A* **92**, 033842 (2015).

[36] J. W. Goodman, *Statistical Optics* (Wiley-Interscience, New York, 2000).

[37] L. Mandel, and E. Wolf, *Optical Coherence and Quantum Optics* (Cambridge University Press, New York, 1995).

[38] A. Hofmann, *The Physics of Synchrotron Radiation* (Cambridge University Press, Cambridge, United Kingdom, 2004).

[39] J. A. Clarke, *The Science and Technology of Undulators and Wigglers* (Oxford University Press Inc., New York, 2004).

[40] G. Geloni, E. Saldin, E. Schneidmiller, and M. Yurkov, "Fourier Optics Treatment of Classical Relativistic Electrodynamics", in *Proceedings of FEL 2006*.

[41] G. Geloni, E. Saldin, E. Schneidmiller, and M. Yurkov, "Fourier treatment of near-field synchrotron radiation theory", *Opt. Commun* **276**, 167 (2007).

[42] G. Geloni, E. Saldin, E. Schneidmiller, and M. Yurkov, "Transverse coherence properties of X-ray beams in third-generation synchrotron radiation sources", *Nucl. Instrum. Methods Phys. Res., Sect. A* **588**, 463 (2008).

[43] M. Siano, B. Paroli, M. Manfredda, M. D. Alaimo, and M. A. C. Potenza, "Measure of the transverse coherence of a self amplified spontaneous emission of a free electron laser with the heterodyne speckles method", in *Proceeding of SPIE Optics + Optoelectronics 2015, Volume 9512: Advances in X-ray Free-Electron Lasers Instrumentation III*.

[44] M. Siano, B. Paroli, E. Chiadroni, M. Ferrario, and M. A. C. Potenza, "Note: Nanosecond LED-based source for optical modeling of scintillators illuminated by partially coherent X-ray radiation", *Rev. Sci. Intrum.* **87**, 126104 (2016).

[45] M. Siano, B. Paroli, M. A. C. Potenza, U. Iriso, A. A. Nosych, L. Torino, S. Mazzoni, G. Trad, and A. N. Goldblatt, "Transverse Beam Size Diagnostics Using Brownian Nanoparticles at ALBA", in *Proceedings of the 2016 International Beam Instrumentation Conference (IBIC 2016)*.

[46] M. Born and E. Wolf, *Principles of Optics* (Pergamon Press Ltd, London, 1970).

[47] J. W. Goodman, *Introduction to Fourier Optics* (Roberts and Company Publishers, New York, 2004).

[48] O. Chubar, P. Elleaume, and A. Snigirev, "Phase analysis and focusing of synchrotron radiation", *Nucl. Instr. Meth. Res. Sect. A* **435**, 495 (1999).

[49] J. W. Goodman, *Speckle Phenomena in Optics* (Roberts and Company Publishers, New York, 2008).

[50] J. C. Dainty, *Laser Speckle and Related Phenomena* (Springer-Verlag, Berlin, 1975).

[51] M. Giglio, M. Carpineti, and A. Vailati,"Space Intensity Correlation in the Near Field of the Scattered Light: A Direct Measurement of the Density Correlation Function $g(r)$", *Phys. Rev. Lett.* **85**, 1416 (2000).

[52] M. Giglio, M. Carpineti, A. Vailati, and D. Brogioli, "Near-field intensity correlation of scattered light", *Appl. Opt.* **40**, 4036 (2001).

[53] D. Brogioli, A. Vailati, and M. Giglio, "Heterodyne near-field scattering", *Appl. Phys. Lett.* **81**, 4109 (2002).

[54] F. Ferri, D. Magatti, D. Pescini, M. A. C. Potenza, and M. Giglio, "Heterodyne near field scattering: A technique for complex fluids", *Phys. Rev. E* **70**, 041405 (2004).

[55] D. Magatti, M. D. Alaimo, M. A. C. Potenza, and F. Ferri, "Dynamic heterodyne near field scattering", *Appl. Phys. Lett.* **92**, 241101 (2008).

[56] H. C. van de Hulst, *Light Scattering by Small Particles* (Dover Publications Inc., New York, 1981).

[57] M. Ferrario *et al.*, "SPARC LAB present and future", *Nucl. Instrum. Meth. Phys. Res. Sect. B* **309**, 183 (2013).

[58] M. Giglio, D. Brogioli, M. A. C. Potenza, and A. Vailati, "Near field scattering", *Phys. Chem. Chem. Phys.* **6**, 1547 (2004).

[59] S. Mazzoni, M. A. C. Potenza, M. D. Alaimo, S. J. Veen, M. Dielissen, E. Leussink, J. L. Dewandel, O. Minster, E. Kufner, G. Wegdam, and P. Schall, "SODI-COLLOID: A combination of static and dynamic light scattering on board the International Space Station", *Rev. Sci. Instrum.* **84**, 043704 (2013).

[60] M. A. C. Potenza, K. P. V. Sabareesh, M. Carpineti, M. D. Alaimo, and M. Giglio, "How to Measure the Optical Thickness of Scattering Particles from the Phase Delay of Scattered Waves: Application to Turbid Samples", *Phys. Rev. Lett.* **105**, 193901 (2010).

[61] A. Gatti, D. Magatti, and F. Ferri, "Three-dimensional coherence of light speckles: Theory", *Phys. Rev. A* **78**, 063806 (2008).

[62] E. Wolf, *Introduction to the Theory of Coherence and Polarization of Light* (Cambridge University Press, Cambridge, England, 2007).

Ringraziamenti

Vorrei ringraziare innanzitutto il mio supervisore, Marco Potenza, per avermi dato la possibilità di entrare a far parte del suo gruppo di ricerca. Questi tre anni sono stati per me una fonte inesauribile di apprendimento sull'ottica, sulla fisica e sul metodo scientifico in generale.

Un ringraziamento speciale merita il mio correlatore, Bruno Paroli: fin dai primi giorni della mia tesi magistrale ha avuto un ruolo fondamentale nella mia crescita professionale, insegnandomi molto senza rendersene conto. Ma oltre che un ottimo mentore, è soprattutto un ottimo amico e le giornate in laboratorio non sarebbero le stesse senza la consueta frase "*Mi sa che è ora*" delle 11:00.

Ringrazio chi ha fatto parte del mio percorso universitario condividendo la fatica degli esami e dei laboratori, ma anche i momenti piacevoli di pausa dallo studio. In particolare ringrazio Andrea e Giuseppe, gli amici fedelissimi della "*Orange Juice*".

Parlando di amici, non posso non menzionare Andrea, uno dei primi ad accogliermi nel Laboratorio di Ottica. Indimenticabili resteranno gli scherzi a Sara e le battute di basso (bassissimo!!!) livello che facevamo, ma soprattutto le rimpatriate per una cena o un beach volley.

Ringrazio gli amici della VdB che ormai da più di 8 anni fanno parte della mia quotidianità. Nonostante le sconfitte restino al momento più delle vittorie, tutto passa in secondo piano pensando alle meravigliose persone che ho conosciuto.

Una menzione particolare va a Mirco perché "*affonda pure quanto vuoi, tanto sarò li per tirarti su*" è una cosa rara da trovare in una persona, e di questo gli sarò sempre grato.

Un enorme ringraziamento va a Gerardo, Ornella, Elvira (o Carolina???) e Yarin: neanche lo immaginano, ma c'è molto di loro in questo lavoro. Il supporto che mi hanno sempre dato e l'affetto che non mi hanno mai fatto mancare sono sempre stati per me fonte inesauribile per andare avanti e cercare di raggiungere i miei obiettivi. E se oggi sto scrivendo queste parole, devo ringraziare soprattutto loro.

Infine, il mio ultimo ringraziamento va alla persona che, proprio come questa tesi, rappresenta per me il presente e il futuro: Stefania.